NIFS-PROC-96

Summary Report of Japan-US Joint Project (TITAN) (FY 2007-2012)

(Eds.) K. Okuno and T. Muroga

Jan. 30, 2014

Summary Report of Japan-US Joint Project (TITAN)
(FuY 2007-2012)

Edited by
K. Okuno and T. Muroga

This report summarizes the scientific accomplishments achieved through the TITAN Japan-US Collaboration Program. The TITAN collaboration (**T**ritium, **I**rradiation and **T**hermofluid for **A**merica and **N**ippon) has been carried out through six years (FuY 2007-2012) under the collaboration implemented by establishing Annex I to the NIFS-ORNL Agreement on Academic and Scientific Exchange.

The TITAN collaboration was established to obtain fundamental understanding for the control of tritium and thermofluid in first wall, blanket and recovery systems with particular emphasis on their interfacial issues. The experiments were designed for testing under conditions specific to fusion, such as intense irradiation, high heat/particle flux, and circulation in a high magnetic field. The results have been applied using integrated modeling to advance the design of tritium and heat control in MFE and IFE systems.

Key words: Japan-US Collaboration, fusion reactors, first wall, blanket, neutron irradiation, tritium transport, mass transport, thermofluid, synergistic effects, joining and coating, irradiation creep, system integration modeling.

Summary Report of Japan-US Joint Project (TITAN)
(FY 2007-20012)

1. Preface

(K. Okuno)

1-1 Introduction

The TITAN collaboration (**T**ritium, **I**rradiation and **T**hermofluid for **A**merica and **N**ippon) was carried out through six years (FY 2007-2012). The preceding project was the JUPITER-II project (2001-2006) under Phase 4 of the collaboration implemented by Amendment 4 of Annex I to the MEXT (Ministry of Education, Culture, Sports, Science and Technology)-DOE (United States Department of Energy) Cooperation. This program followed the RTNS-II Program (Phase 1: 1982-1986), the FFTF/MOTA Program (Phase 2: 1987-1994) and the JUPITER Program (Phase 3: 1995-2000). At the end of JUPITER-II collaboration, however, the Annex I to the MEXT-DOE Cooperation expired. The TITAN collaboration was therefore implemented by establishing Annex I to the NIFS-ORNL Agreement on Academic and Scientific Exchange.

All the collaborations have been carried out, including planning, execution and summarizing, by a research group organized in NIFS, which is composed of Japanese University researchers. In TITAN collaboration, the university people in wide areas from fusion engineering fields gathered in response to the widening scope of the project.

This publication is the final report of the TITAN collaboration collecting the project overview, summary of the research tasks, some detailed scientific reports and statistics.

The purpose of the collaboration is to obtain fundamental understanding for establishing tritium and thermofluid control for fusion systems. The experiments were designed for testing under conditions specific to fusion, such as intense irradiation, high heat/particle flux, and circulation in a high magnetic field. The results will be applied using integrated modeling to advance the design of tritium and heat control in MFE and IFE systems.

In addition to the scientific achievements to be reported in the subsequent chapters, the collaboration has contributed to promoting fusion engineering research through (1) organization of research groups composed of materials, blanket, tritium, PWI, and thermofluid people collaborating for promotion of the project, (2) developing a new research phase for system integration of the fusion nuclear systems, (3) enhancing Japanese domestic fusion engineering research activity as supporting or complementary researches of TITAN collaboration, and (4) education of young scientists in this field.

Acknowledgements

This collaboration has been started by creating a new framework under NIFS-ORNL agreement. The efforts made for establishing the framework by NIFS and relating people are highly acknowledged. Thanks go to Japan-US Collaboration Research Planning Committee for supporting the collaboration, especially Professors O. Motojima and A. Komori, the former and present committee Chairman, respectively, Professor S. Sudo, secretary to the committee, the committee members, and the TITAN project advisories. Post Irradiation Examination carried out in Japan is the debt of the cooperation by Oarai Center of IMR, Tohoku University. Needless to say, success of this project is thanks to the cooperation of the people of the US side from DOE, ORNL, INL, UCLA, UCSD and so on.

TITAN LOGO

2. Project overview

(T. Muroga)

2.1 Progress in JAPAN-US collaboration

2.1.1 RTNS-II, FFTF/MOTA and JUPITER Projects

The Japan–USA fusion cooperation program has a history of more than 30 years. Five joint projects have been carried out within this framework. Table 1 summarizes the history of the US-Japan joint projects [1,2]. The collaboration was started in FY(Japanese Fiscal Year starting April) 1981, and the first phase was the RTNS-II (Rotating Target Neutron Source-II) project, followed by the second phase known as the FFTF/MOTA (Fast Flux Test Facility/Materials Open Test Assembly) project from FY 1987. In the RTNS-II program, fusion neutron irradiation experiments using the D-T neutron source of the U.S.A. were carried out. Though the maximum irradiation dose was limited to about 0.1 dpa, Japanese advanced technologies on microstructure observation by electron microscopy and mechanical property evaluation by testing miniaturized specimens were utilized to obtain numerous highly precise data on the generation and accumulation processes of defects induced by the D-T neutrons as well as on the microstructure-strength correlation. Irradiation of breeding materials, superconducting materials and device materials were also carried out in the project.

Table 1. History of the Joint Project in Japan-USA Fusion Cooperation Program. (*JFY: Japanese Fiscal Year starts April and ends March of the next year)

Project Name	Period (JFY*)	Representatives & Coordinators	Major Test Facilities	Core Subjects
RTNS-II	1981~1986	M. Cohen D. Doran/ K. Kawamura K. Sumita	RTNS-II	Low dose D-T neutron irradiation
FFTF/MOTA	1987~1994	T. Reuther F. Garner/ A. Miyahara S. Ishino A. Kohyama	FFTF EBR-II	High fluence neutron irradiation
JUPITER	1995~2000	F. Wiffen R. Jones/ K. Abe A. Kohyama	HFIR ATR HFBR	Temperature variation effects Transient effects for ceramics Radiation creep
JUPITER-II	2001~2006	S. Berk G. Nardella S. Zinkle D.K. Sze/ K. Abe A. Kohyama S. Tanaka	HFIR STAR MTOR	Key issues for advanced blankets
TITAN	2007~2012	G. Nardella B. Sullivan P. Pappano D.K. Sze/ K. Okuno T. Muroga	HFIR TPE/STAR MTOR PISCES	Mass and heat transfer Irradiation-tritium synergism Coating/joining

The main theme in the FFTF/MOTA project was to explore the effects of high-dose neutron irradiation up to 100 dpa, which was the expected life time for fusion reactor materials. A more fundamental approach, compared to conventional irradiation tests, was promoted and a thorough understanding of the entire microstructural evolution process under irradiation covering low dose

to high dose irradiation regimes was obtained.

The irradiation experiments in the above projects were performed under relatively simple and steady irradiation conditions. The JUPITER project [3], started in FY 1995, focused on dynamic radiation effects detectable only during irradiation and effects of variable and combined irradiation conditions. This included radiation-induced conductivity of ceramic insulators, varying temperature irradiation effects, and combined transmutation effects. These experiments extracted valuable information on materials response in fusion relevant environments.

2.1.2 JUPITER-II Project

The projects before JUPITER-II focused on materials performance under irradiation and materials development based on the knowledge gained from the irradiation experiments. In fusion blankets, materials will be used as joined or coated materials (materials systems). In addition, the use of materials in blankets involves new issues associated with the interaction with breeders and coolants. Thus basic technological studies and their integration are essential. The issues are better specified with the progress in the blanket design.

JUPITER-II project [4] aimed at (1) developing key technology for fabrication and operation of "self-cooled liquid blankets" and "high temperature gas-cooled blankets" which are combinations of low activation structural materials and breeder/coolants which are capable of high tritium breeding ratio and

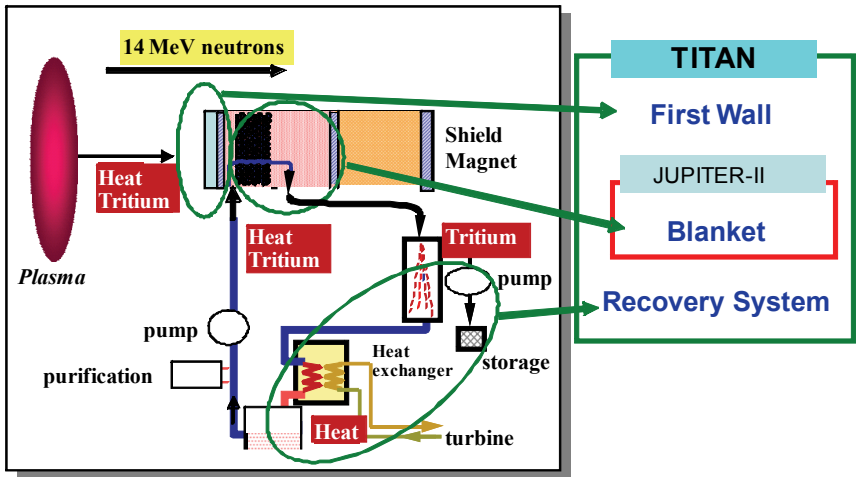

Fig. 1. Schematic illustration showing the scope of the TITAN project compared with that of JUPITER-II project.

high coolant exit temperature, and (2) evaluation of the irradiation performance of the materials system which is a key feasibility issue for blanket development. Overall evaluation of blankets and materials systems based on modeling, and orientation of the development towards the commercialization of the system were also carried out in this project [4].

2.2 Outline of TITAN project

2.2.1 Objectives

Fig. 1 schematically shows a comparison between the TITAN and the JUPITER-II projects. The JUPITER-II project focused its efforts on several critical issues regarding advanced blankets such as molten salt Flibe blankets, liquid lithium blankets with a vanadium alloy structure, and high-temperature gas-cooled blankets with a SiC/SiC composite structure.

The TITAN project extended the scope of the JUPITER-II project by including not only first wall issues but also focusing on interface issues among the first wall, blanket, and recovery system. Particular interest was placed on obtaining fundamental understanding for establishing tritium and thermofluid control. The experiments were designed for testing under conditions specific to fusion, such as intense irradiation, high heat/particle flux, and circulation in a high magnetic field. The results will be applied using integrated modeling to advance the design of tritium and heat control in MFE and IFE systems.

Table 2. Task structure and research subjects of the TITAN project.

Task	Subtask	Facilities	Research subjects
Task1 Transport phenomena	1-1 Tritium and mass transfer in first wall (concluded March 2010)	STAR/TPE PISCES	Tritium retention and transfer behavior and mass transfer in first wall
	1-2 Tritium behavior in blanket systems	STAR	Tritium behavior through elementary systems of liquid blankets
	1-3 Flow control and thermofluid modeling	MTOR	Flow control and thermofluid modeling under strong magnetic fields
Task2 Irradiation synergism	2-1 Irradiation-tritium synergism	HFIR STAR	Irradiation effects on tritium retention and transfer behavior in first wall and structural materials
	2-2 Joining and coating integrity	HFIR	Synergy effects of simultaneous production of tritium and helium on healthiness of joining and coating integrity
	2-3 Dynamic deformation	HFIR	Effects of irradiation and simultaneous production of tritium and helium on dynamic deformation of structural materials
Common Task System integration modeling	MFE/IFE system integration modeling		Integration modeling for mass transfer and thermofluid through first wall, blanket and recovery systems of MFE/IFE

Table 2 summarizes the tasks, subtasks, facilities, and research subjects. The project has three tasks and seven subtasks. Task 1 is about transport

phenomena that consider mass and heat flow in the first wall, blanket, and recovery system. Special emphasis is placed on mass transfer during the interaction of mixed plasma of D/He/Be with the first wall, tritium transfer in liquid breeders, and the thermofluid control in liquid breeders in a magnetic field. Task 2 focuses on the irradiation effects of materials with an emphasis on the synergistic effects of irradiation and tritium or other impurities including transmutation-induced helium. The common task is a unique group organized by those who are engaged in other tasks and take care of the modeling. This task performs integration modeling of materials performance, thermofluids in magnetic fields, tritium and mass transfer for the enhancement of reactor system design, including the evaluation of the available modeling codes and the enhancement of reactor system designs.

The following US facilities are used.

(a) STAR (Safety and Tritium Applied Research) [INL] Established at the Idaho National Laboratory in 2001, with an allowable tritium inventory of 16,000 Ci, STAR includes the Tritium Plasma Experiment (TPE) and various facilities for testing tritium behavior in blanket conditions. Unique features of the facility include use of Be and neutron-irradiated materials.

(b) HFIR (High Flux Isotope Reactor) [ORNL] HFIR is a 100MW mixed spectrum research reactor, currently operated at 85MW, which is planned to remain in operation until 2035. The HFIR is a unique irradiation facility with the potential for high environmental and temperature control during irradiation, and very low to high flux irradiation. Some of the HFIR-irradiated specimens were shipped to Oarai Center of Tohoku University for Post Irradiation Examinations and others were tested at ORNL radiological facilities.

(c) MTOR (Magneto-Thermofluid Omnibus Research Facility) [UCLA] The facility includes a magnet of homogeneous field to 2T in an area 15cm wide and 1m long, which can be used for testing the fluid dynamics of liquid metals and MHD flow for high Prandtl number stimulant fluids using electrolytes.

(d) PISCES (Plasma Interactive Surface Component Experimental Station) [UCSD] A linear plasma simulator which can produce high-density plasmas with H, D, He and Be. Pulsed lasers are equipped for synergistic plasma exposure and pulse heating studies. Plasma diagnostics and surface characterization systems are furnished.

Note that unique equipment has been installed in these facilities, some of which were fabricated in Japan and shipped to experimental sites. Installed equipment include facilities for testing of mechanical properties in the ORNL PIE area and tritium solubility testing in STAR, a miniaturized specimen holder for tritium plasma irradiation in TPE, a liquid metal circulation facility in MTOR, and pulse heating facilities for PISCES. Fig. 2 shows the pulse heat loading conditions designed for PISCES. With the two

operation modes of the newly installed pulse lasers, plasma-wall interaction tests are performed in pulse heat loading conditions, which are close to those of Disruption, ELM, and IFE wall. In addition, it is noteworthy that some of the neutron-irradiated specimens are shipped to the Oarai Center in Tohoku University for PIE using the unique Japanese facilities.

The TITAN project supports MFE/IFE common technology research including the performance of ablation plumes of the first wall by pulse heat loading.

Table 3 shows the organization of the TITAN project, which includes Representatives, Program

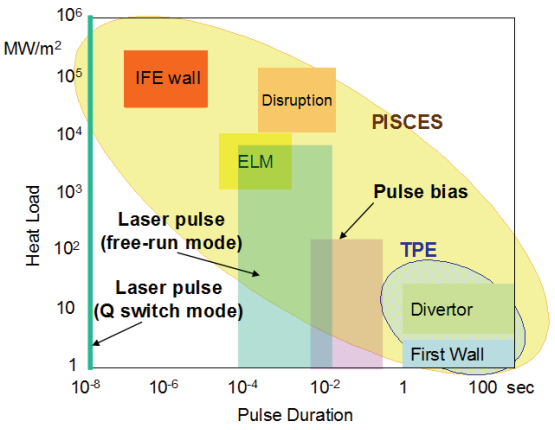

Fig. 2. Pulse heat load conditions in PISCES using pulse lasers.

Table 3. Organization of the TITAN project.

Representatives Coordinators		JP : K. Okuno (Shizuoka U.) JP : T. Muroga (NIFS)		US : P. Pappano(USDOE) US : P. Pappano(USDOE)		
Task	**Subtask**	**Facility**	**TC (JP)**	**STC/Deputy (JP)**	**TC (US)**	**STC/Deputy (US)**
Task 1 Transport phenomena	1-1 Tritium and mass transfer in first wall	TPE PISCES	T. Terai (U.Tokyo)	Y. Ueda (Osaka U.)/ N. Ohno (Nagoya U.) K. Tokunaga (Kyushu U.)	P. Pappano (USDOE)	R. Doerner (UCSD)
	1-2 Tritium behavior in blanket systems	STAR		T. Terai (U. Tokyo)/ S. Fukada (Kyushu U.) S. Konishi (Kyoto U.)		B. Merrill (INL)
	1-3 Flow control and thermofluid modeling	MTOR		T. Kunugi (Kyoto U.)/ T. Yokomine (Kyoto U.)		S. Smolentsev (UCLA)/ K. Messadek (UCLA)
Task 2 Irradiation synergism	2-1 Irradiation-tritium synergism	HFIR STAR	A.Kimura (Kyoto U.)	Y. Hatano (Toyama U.)/ Y. Oya (Shizuoka U.)	R. Kurtz (PNNL)	Y. Katoh (ORNL)/ B. Merrill(INL)
	2-2 Joining and coating integrity	HFIR ORNL-HL (incl. T-test)		A. Kimura (Kyoto U.)/ N. Hashimoto (Hokkaido U.) T. Nagasaka (NIFS)		T. Yamamoto (UCSB)/ Y. Katoh (ORNL)
	2-3 Dynamic deformation			A.Hasegawa (Tohoku U.)/ T. Hinoki (kyoto U.)		Y. Katoh (ORNL)
Common Task System integration modeling	MFE/IFE system integration modeling		A.Sagara (NIFS)	A. Sagara (NIFS)/ H. Hashizume (Tohoku U) T. Norimatsu (Osaka U.)	R. Nygren (SNL)	R. Nygren (SNL)
Laboratory Liaisons	ORNL : INL : IMR-Oarai (Tohoku) :	Y. Katoh (ORNL) B. Merrill (INL) T. Shikama (Tohoku U.)				
IFE Liaisons			K. Tanaka (Osaka U.)	Kodama(Osaka U.) Yoneda(UTC)	M. Tillack (UCSD)	

Coordinators, Task Coordinators (TCs), Subtask Coordinators (STCs), and Deputies. Many scientists from various universities and institutes in Japan and US are also part of the project. In addition, liaisons for the Laboratories and IFE are nominated to facilitate the communication among scientists and facility personnel and enhance the common MFE/IFE technology research, respectively.

The TITAN project started in April 2007. The budget available for the project (~1.0 M$ from each side) was almost steady in the first three years with a minor decline. However, sizable budget reduction occurred in FY2010 (down to ~0.74 M$ each). Re-planning of the project, including downsizing of test matrices and tasks restructuring, was made to accommodate budget cuts. Task 1-1 was decided to be concluded as of March 2010. The TPE part of the task was merged to Task 2-1, and some of the research projects in PISCES continued outside the TITAN budget by Japanese scientists assigned to UCSD. Two journal papers [5,6] were published reporting status of the Project at the midpoint and after the fifth year, respectively.

2.3 Research highlights (reproduced from Chapter 3)

2.3.1 Task 1-1 : Tritium and mass transfer in first wall

The purpose of the task is to clarify tritium and mass transfer in the first walls of blankets by using tritium plasma, Be and He seeded plasma, and pulsed laser system. The objectives of this task are as follows; (1) To investigate tritium retention and diffusion behavior in tungsten and tungsten coated reduced activation ferritic steel (F82H) by an imaging plate (IP) technique. Tritium plasma irradiation was performed in TPE at INL. (2) To investigate production processes of material mixing layers and D retention by Be/He/D mixed plasma irradiation to tungsten under high temperature (~1100 K) and low temperature (~600 K) conditions. Mixed plasma irradiation was performed in PISCES at UCSD. (3) To investigate erosion of Be/W mixed materials under simultaneous irradiation of high density plasma and pulsed laser in PISCES.

Effects of mixed ion (D+He+Be) irradiation to tungsten and diffusion of hydrogen isotope in the bulk tungsten were performed. Small amount of impurity species (He and Be) greatly affects hydrogen isotope retention and surface morphology changes. New technique of bulk T diffusion and retention was proved to be effective. Behavior of eroded Be by pulsed heat could include chemical reactions in the plasma.

2.3.2 Task 1-2 : Tritium behavior in blanket systems

This task has two goals: 1) to estimate the solubility of hydrogen isotopes in lead–lithium eutectic (LLE); and 2) to evaluate tritium permeation in structural materials, including the characterization of permeation barriers at very low-permeation flux levels.

Solubility of hydrogen isotopes including tritium in a Li-Pb eutectic alloy (LLE) was experimentally investigated in order to clarify tritium behavior in the Li-Pb blanket system. Precise experiment was carried out by means of a constant volume method to elucidate the reasons why wide scattering appears in previous data, and discussion is made with focusing on the four effects on solubility; (i) Li preferential evaporation from Li-Pb, (ii) thermal convection in liquid, (iii) reaction in a reaction tube or crucible and especially (iv) difference in crucible materials among Al_2O_3, SiO_2 and W.

Another important issue of the blanket system is to develop a new ceramic coating to decrease tritium permeation rate. Tritium permeation reduction factor was determined using Er_2O_3 coated on reduced-activation F82H steel. The permeation reduction factor achieved here was higher than 10^3. Isotope effects in solubility and diffusivity between H and D were determined within a Japanese domestic work. No isotope effect in solubility was observed between H and D, and the H diffusivity was 1.4 times larger than the D one. Experiment to determine tritium solubility in Li-Pb is performed under the collaboration work with INL.

2.3.3 Task 1-3 : Flow Control and Thermofluid Modeling

LLE flow in a fusion blanket interacts with the plasma-confining magnetic field, and eventually the flow structure is strongly affected by a MHD (magneto-hydrodynamics) effect. Especially, LLE flows under the strong magnetic field including the flow instabilities and the flow distribution in a coolant channel such as a manifold may determine the heat removal, the hot spots, the corrosion and the tritium transport. Therefore, the understanding of MHD themofluid behavior and the flow control are key issues for fusion blanket research and development. This task has been studying characteristics of the thermofluid under the strong magnetic field and modeling the MHD phenomena. This task conducts

some MHD experiments using the MTOR, which is able to make a uniform magnetic field of maximum 2T in a rectangular gap of 15 cm in width and 1m in length by constructing new test apparatus MaPLE.

To investigate the flow characteristic of high temperature LLE flow under strong magnetic field, HT-UDV and DP sensor has been developed. The pressure drop measurement of a rectangular channel with the 3-surface–multi-layered as the insulation walls was tested, and decreased 1/10 compared to the theoretical value in the same size rectangular channel without any insulation wall. This is the first demonstration of pressure drop reduction using the LLE at high temperature in the world.

2.3.4 Task 2-1 : Irradiation-tritium synergism

Retention and release of hydrogen isotopes in/from plasma-facing materials (PFMs) is an important issue from the viewpoints of in-vessel tritium inventory, waste managements and tritium accountancy. However, the effects of neutron-irradiation on hydrogen isotope retention have been scarcely examined. The objective of this study is to examine trapping of hydrogen isotope at defects induced by neutron irradiation. Tungsten (W) is selected as reference material of PFMs for DEMO reactors. Small specimens of pure W were irradiated with neutrons in HFIR. The irradiated specimens were shipped to INL and exposed to high flux deuterium (D) plasma in a linear plasma machine called TPE. Then, D retention and release were examined by means of nuclear reaction analysis (NRA) and thermal desorption spectroscopy (TDS).

Neutron irradiation of W resulted in significant increase in hydrogen isotope retention due to strong trapping effects by radiation-induced defects. The concentration of trapped D in the specimen irradiated to 0.3 dpa reached 0.8 and 0.4 at.% at 200 and 500 ºC, respectively. In addition, deep penetration of D (50−100 μm) with filling up traps was observed at 500 ºC. These observations suggest the significant increase in tritium inventory in W is possible after neutron irradiation. Thermal desorption of D from neutron-irradiated specimen continued up to 900 ºC, whereas that from non-irradiated specimen was completed at around 400 ºC. The release of D from neutron-irradiated W was controlled by long-range diffusion process under strong trapping effects. The activation energy for detrapping was evaluated from thermal desorption spectra to be about 1.8 eV. These results indicate that removal of tritium from neutron-irradiated W by baking at moderate temperatures in vacuum is difficult, and development of tritium removal technique, e.g. isotope exchange, is necessary.

2.3.5 Task 2-2 : Joining and coating integrity

In this task, irradiations of joints and coating of oxide dispersion strengthened (ODS) steel and reduced activation ferritic steel (F82H) were performed in HFIR for the purpose of studying the irradiation performance of joints and coating of structural components of blankets. The experimental objectives are to a) evaluate feasibility of electron beam welding for F82H by means of mechanical property measurement after neutron irradiation. Irradiation effects on tensile properties and hardness were investigated for F82H joints, b) investigate irradiation effects on vacuum plasma spray (VPS)- W coating on ODS steel and F82H to assess the feasibility of VPS-W as a first wall of blanket, c) examine the irradiation performance of friction stir processed (FSP) ODS steel, d) develop solid state diffusion bonding (SSDB) technology of ODS steel without significant change in the dispersion morphology of oxide particles, and e) perform a limited investigation of synergistic effect of helium/hydrogen with irradiation effects on mechanical properties of F82H using hydrogen cathodic charging tensile test method after irradiation. Effects of helium on microstructure of ODS steel and F82H were investigated by means of isotope tailoring method newly developed in this research.

Joining/coating technology development and assessment of joint/coating performance under neutron irradiation were performed using HFIR in ORNL. VPS-W coating with high performance was successfully obtained by a newly developed masking method during spraying. Irradiation hardening was observed in VPS-W after irradiation at 500°C, which has never been observed in ferritic steels. Application feasibility was checked for FSP-ODS steel and it was proved that FSP was adequate method joining ODS steel without drastic changes in nano-sized oxide particle distribution morphology. A feasible SSDB technology was developed for ODS steels and the bonding fracture strength as high as that of base metal was successfully achieved. Hydrogen and helium effects were investigated by a newly developed irradiation technique.

2.3.6 Task 2-3: Dynamic deformation

In this task, (1) dynamic deformation behavior called irradiation creep of SiC and (2) synergistic effects of tritium implantation and displacement damage production on the tritium distribution behavior in SiC were studied. As for the irradiation creep, it often determines irradiated lifetime of metallic structural components of nuclear reactors, but it may also be beneficial for inherently brittle materials like ceramics for functional applications, because creep may relax or redistribute the stresses. For silicon

carbide (SiC)-based nuclear components, the latter function of irradiation creep may be important, in particular when a significant temperature gradient exists and the secondary stresses developed by differential swelling can be severe. Flow channel insert in liquid metal blankets of fusion energy systems is an example of such applications.

To establish an effective tritium recovery scheme in a fusion reactor, it is important to examine synergistic effects on the behavior of tritium in structural material such as SiC under irradiation with neutrons and energetic particles, including tritons created by nuclear reactions of $^{6}Li(n, \alpha)T$ in breeder materials. The second objective of this study is to evaluate tritium distribution in SiC under irradiation at high temperature using the imaging plate (IP) technique, which is a powerful tool for measuring the tritium distribution on and in the bulk region of materials.

The irradiation creep experiments using Bend Stress Relaxation (BSR) capsule in HFIR were carried out. It was found that the stress exponent of SiC under irradiation was unity. This is the first time that the stress exponent was explicitly determined for the neutron irradiation creep of ceramic materials. The creep behavior of SiC materials used in advanced SiC/SiC composites was also clarified. Synergistic effect of neutron irradiation and tritium implantation to SiC at 1073K was also examined, and showed that the in-situ injected tritium did not undergo long-range diffusion into the bulk during the 1073 K irradiation over a duration of 3000 h. PIE of irradiated specimens are being continues both in the US and Japan by their domestic programs.

2.3.7 Common Task : MFE/IFE system integration modeling

The final goal of Common Task is to create a self-consistent model by integrating the separate systems of tritium, heat, and thermofluid. At the same time, via feedback of important considerations to each task, the validity of our experimental results is assessed in the interfaces between research goals in each task, in order to promote the development of an integrated system modeling methodology. In this report, we focus on material research in Tasks 1-1; 1-2; and 2-1, 2-2, 2-3. The common critical issue in MFE and IFE in terms of fuel self-sufficiency and environmental safety is tritium mass transfer through the heat exchangers. Therefore, a typical heat-exchanger system, designed to identify appropriate boundary conditions for material researches, is also discussed.

The common task identifies cross-linked considerations in the blanket system modeling on the basis of the material research in each task. The results are summarized as follows:

(1) The helium effects on hydrogen isotope retention in tungsten were investigated by reviewing the results of previous studies and by conducting D^+ He mixed plasma exposure experiments in PISCES. These results reveal that D retention is reduced by high-density He bubbles forming in the near surface region.

(2) Research into permeability, diffusivity, and solubility of hydrogen isotopes in a Pb-Li alloy as a tritium breeder is summarized. The blanket design must achieve a low tritium leak to the outside and high tritium recovery from a breeder loop.

(3) A simulation code to model the accumulation and release of hydrogen isotopes interacting with vacancies in tungsten was developed using a Monte Carlo technique. Simulation results revealed that the behavior of hydrogen isotopes depends strongly on the mode of irradiation (i.e., whether the specimen is ion- or neutron-irradiated).

(4) Multiscale modeling of microstructural changes in a binary compound material during irradiation has elucidated the nucleation and growth processes of defect clusters.

(5) Tritium permeation through a heat exchanger equipped with double tubes filled with an oxidizer can be reduced to $1/10^4$ that of bare stainless tubes, without degrading the heat exchange rate.

2.4 Conclusion

The TITAN collaboration successfully completed its sixth year with excellent progress toward its initial objectives and with significant scientific accomplishments that address key issues for several attractive first wall and blanket systems of common interest to Japan and the U.S. The types of systematic experimental and theoretical studies of the first wall and blanket being conducted under TITAN are important and essential elements toward realizing attractive fusion energy options.

References

[1] Twenty Year Report for Activities Regarding Japan/US Fusion Research Collaboration, June 2000, Japan/US Coordination Committee on Fusion Energy.

[2] Special Report on the Occasion of the 30th Anniversary of the Japan/U.S. Fusion Research Collaboration, March 2011, Japan/US Coordination Committee on Fusion Energy.

[3] K. Abe, A. Kohyama, C. Namba, F. W. Wiffen, R. H. Jones, J. Nucl. Mater. **258-263** (1998) 2075-2078.

[4] K. Abe, A. Kohyama, S. Tanaka, C. Namba, T. Terai, T. Kunugi, T. Muroga, A. Hasegawa, A. Sagara, S. Berk, S.J. Zinkle, D.K. Sze, D.A. Petti, M.A. Abdou, N.B. Morley, R.J. Kurtz, L.L. Snead, N.M. Ghoniem, Fusion Engineering and Design, **83** (2008) 842-849.

[5] T. Muroga, D.K. Sze, K. Okuno et al., Fusion Sci. & Tech. 60 (2011) 321-328.

[6] T. Muroga, D.K. Sze, K. Okuno, Fusion Eng. Des. 87 (2012) 613-619.

3. Task summaries

3-1 Task 1-1: Tritium and mass transfer in first wall

(Y. Ueda, N. Ohno, K. Tokunaga, R. Doerner)

3-2 Task 1-2: Tritium behavior in blanket systems

(T. Terai, S. Fukada, S. Konishi, B. Merrill)

3-3 Task 1-3: Flow control and thermofluid modeling

(T. Kunugi, T. Yokomine, S. Smolentsev)

3-4 Task 2-1: Irradiation-tritium synergism

(Y. Hatano, Y. Oya, Y. Katoh, B. Merrill)

3-5 Task 2-2: Joining and coating integrity

(A. Kimura, N. Hashimoto, T. Nagasaka, M.A. Sokolov, T. Yamamoto)

3-6 Task 2-3: Dynamic deformation behavior

(A.Hasegawa, T. Hinoki, Y. Katoh, L. L. Snead)

3-7 Common Task : MFE/IFE system integration modeling

(A. Sagara, H. Hashizume, T. Norimatsu, R. Nygren))

3-1 Task 1-1: Tritium and Mass Transfer in first wall

(Y. Ueda, N. Ohno, K. Tokunaga, R. Doerner)

3-1-1 Objectives of the Task

In Task 1-1 of TITAN, the purpose is to clarify tritium and mass transfer in the first walls of blankets by using tritium plasma, Be and He seeded plasma, and pulsed laser system. The objectives of this task are followings; (1) To investigate tritium retention and diffusion behavior in tungsten and tungsten coated reduced activation ferritic steel (F82H) by an imaging plate (IP) technique. Tritium plasma irradiation was performed in TPE at INL. (2) To investigate production processes of material mixing layers and D retention by Be/He/D mixed plasma irradiation to tungsten under high temperature (~1100 K) and low temperature (~600 K) conditions. Mixed plasma irradiation was performed in PISCES at UCSD. (3) To investigate erosion of Be/W mixed materials under simultaneous irradiation of high density plasma and pulsed laser in PISCES.

3-1-2 Participants to the Task

Y. Ueda (Osaka Univ.), N. Ohno, S. Kajita (Nagoya Univ.), M. Miyamoto, K. Ono (Shimane Univ.), K. Tokunaga, T. Otsuka, N. Yoshida, T. Tanabe (Kyushu Univ.), H. Kurishita (Tohoku Univ.)

R. Doerner, M. Baldwin, D. Nishijima, K. Umstadter, Jonathan Yu (UCSD) P. Sharpe, M. Shimada (INL)

3-1-3 Research Highlights

(a) Surface modifications of tungsten and formation of re-deposited layer by Be seeded D-He mixture plasma exposure

Be-seeded low energy and high-flux D/He mixture plasma exposure experiments on W have been performed to simulate W wall materials erosion/modification and deposition phenomena. Fig. 1 shows an SEM image of a cross section of UFG W-0.5wt%TiC/H_2 after the irradiation. SEM observation of the surface and cross section of the irradiated samples indicated that a nanostructure layer formed near the surface as well as by the D-He mixture plasma without Be exposure.

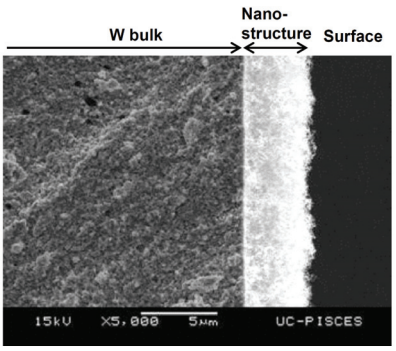

Fig. 1 Cross sections of the nano-structured layer on UFG W-TiC. The UFG-W was exposed to D/0.2He plasmas with Be at 1123 K

Fig. 2 shows nano-structured layer thickness as a function of the square root of the plasma exposure time. The thickness of the nanostructured layer increased with increasing exposure time, similar to the result for exposure to the D-He plasma without Be. The set of nanostructured layer thickness data as a function of the square root of the plasma exposure time tended to have some deviations with a fitted $t^{1/2}$ dependence and the straight line fit did not pass through zero. The $t^{1/2}$ axial intercepts may be an indication of a short incubation or saturation time that precedes nanostructuring. The analysis results indicate that Be exists in a very thin area near the sample surface. In addition, it is considered that the Be layer thickness is thin enough, and He implantation depth was greater than the Be layer thickness, leading to the formation of He bubbles in the W, which are believed to drive the nanostructure formation process.

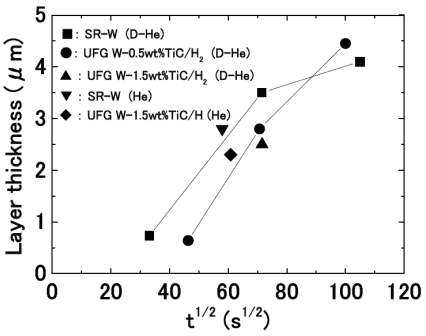

Fig. 2 Nano-structured layer thickness as a function of the square root of the plasma exposure time

(b) D+He+Be mixture plasma exposure experiments in the linear divertor plasma simulator PISCES

Mixture plasma (D+He+Be) exposure experiments were performed in the linear divertor plasma simulator PISCES to predict plasma-wall interaction phenomena under the in the ITER divertor region.

Fig. 3 shows SEM images of the W samples exposed to various mixture plasmas at 573 K. High density micron-sized blisters are formed on the surfaces of W exposed to pure D plasma. The seeding He and/or Be into D plasma caused significant influence on these blisters formation. For the W sample exposed to D+He

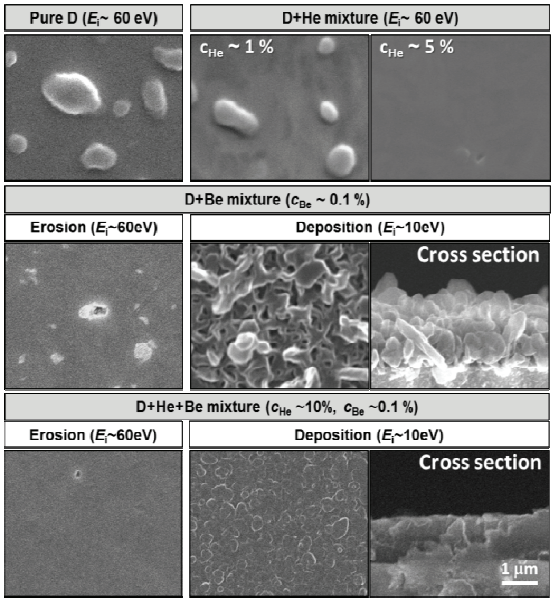

Fig.3 SEM images of the W samples exposed to various plasmas at the fluence of 5×10^{25} m^{-2} and T_s ~573 K. For the samples exposed to the plasma at the Be deposition condition, cross-sectional images are also displayed.

mixture plasma, the blister formation was suppressed even at a low He^+ ion concentration of c_{He^+} ~1 %, and not observed at c_{He^+} ~5 %. In case of Be seeding at E_i ~60 eV, most of incoming Be onto the W surface was re-sputtered and SIMS analysis revealed the formation of a mixed Be/W layer of a few nm in thickness. The sample exposed to D+Be+He mixture plasma at E_i ~60 eV looks as comparably smooth as an unexposed surface. At a lower E_i of ~10 eV, deposited Be is not re-sputtered, and a thick Be layer of ~ 1 μm was observed.

In Fig. 4, thermal desorption spectra of D_2 from the W samples exposed to various plasmas at the fluence of 5×10^{25} m^{-2} and T_s ~ 573 K are displayed. D retention in the sample exposed to D+He mixture plasma was significantly lower than that in the pure D exposed sample. High density He bubbles are observed in the sample exposed to D+He mixture plasma, and cross sectional observation revealed that the damaged layer with He bubbles was much thicker than the He ion range of a few nm. Since the volume fraction of He bubbles exceeds the percolation threshold, the desorption mechanism that injected D atoms diffuse back to the surface through the percolating bubbles is suggested.

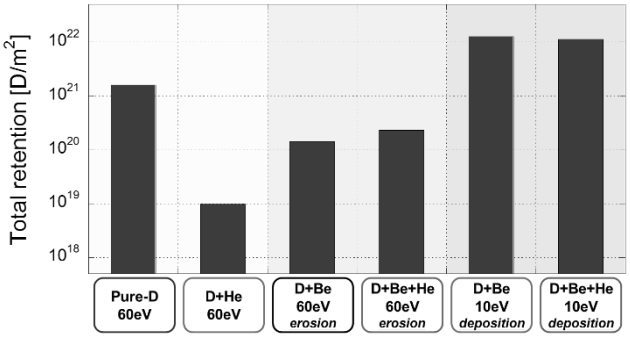

Fig.4 The total retention of D for W samples exposed to various plasmas. The fluence of D is unified to be the fluence of 5×10^{25} m^{-2} for the all samples.

The D-retention in the W samples exposed to D+Be and D+He+Be plasmas at the Be erosion condition (E_i ~60 eV) was about an order of magnitude smaller than the sample exposed to pure D plasma. Because the thickness of Be/W mixed layer is roughly equal to the implantation depth of incident D, the thin Be/W mixed layer may obstruct the diffusion of D into the bulk. In contrast, at the Be deposition condition (E_i ~10 eV), the D retention was about an order of magnitude higher than that in the pure-D exposed sample. Assuming that all retained D atoms uniformly distribute only within the Be deposition layers, the D/Be ratio is estimated to be ~0.03. This high ratio of D/Be seems to be caused by the strong D trapping efficiency of Be, resulting from the formation of D bubbles as shown in the TEM observations. It was also found that He seeding to D+Be plasma had little influence on D retention regardless of the conditions of erosion and deposition, as opposed to He mixture to pure D plasma. Thus, it can be said that Be seeding has a more dominant influence on the D retention behavior in plasma-exposed W than He seeding.

(c) Diffusion and retention behavior of tritium loaded in tungsten materials from plasma

Depth profiles of tritium (T) loaded into pure tungsten (W) at various temperatures were measured by means of tritium imaging plate technique (TIPT) [6] to examine T diffusion and retention behaviors in pure W. The T loading experiments were conducted with a linear plasma device (TPE) located at Idaho National Laboratory (INL).

A surface side of the disk covered by a mask made of W with four holes (6 mm in diameter) was exposed to D(T) plasma for 2 h at 473K and 773K. The T/D ratio of the D(T) mixture gas was 0.5 %. Plasma parameters in TPE were described elsewhere [7] in details; briefly, incident ions were assumed to be singly ionized species (D^+ or T^+), and their energy is 100 eV that was determined by the potential difference between the bias voltage and the plasma space potential. The incident ion flux was estimated to be 10^{22} m^{-2} s^{-1}.

After the T loading, the sample was cooled down to RT with the cooling rate of around 1 K s^{-1}. T distribution on the T-loaded surface was measured by TIPT for 1 h at room temperature (RT).

Figure 5 (a) shows T distribution on (a) the T-loaded surface and (b) the cross-section surface for the sample loaded at 473 K for 2 h. In the figure, T concentration is higher as the color changes from blue, green, yellow to red. In Fig. 5 (a), one can see 4 circular areas with uniform and high T concentration caused by T loading. The corresponding cross sectional view of T distribution is shown in Fig. 5 (b).

Figure 6 shows the T depth profile of the sample loaded at (a) 473 K and (b) 773 K. In the figure, one can see deeper T penetration by the loading at higher temperature. Solid curves indicate theoretical curves fitted to the experimental data for the bulk component.

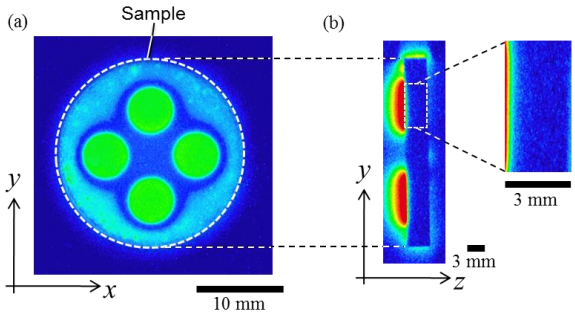

Fig.5. T distribution on (a) the plasma-loaded surface and (b) the cross-section surface for the sample loaded at 423 K for 2 h.

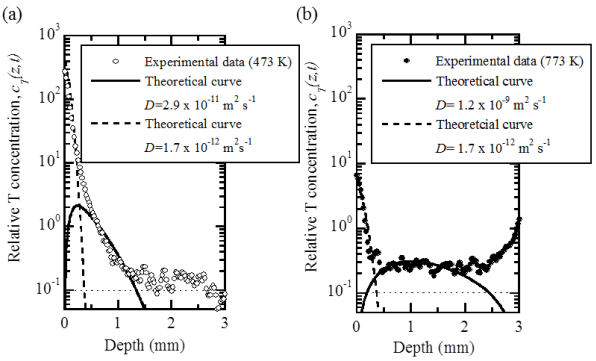

Fig. 6. T depth profile of the sample loaded at (a)473 K and (b)573 K. Dot and solid curve indicates theoretical curves numerically calculated for the near-surface component and the bulk component, respectively.

The determined hydrogen diffusion coefficients in the present study [6] and the previous study [8] are plotted as grey circles and black squares in Fig. 7 and compared with the literature data. The hydrogen diffusion coefficients for the bulk component are in good agreement with the extrapolation of Frauenfelder's data [9] obtained at higher temperatures than 1198 K to the present temperature range. This indicates that the bulk component is caused by diffusion penetration of dissolved hydrogen in pure W at the loading temperature. On the other hand, the hydrogen diffusion coefficients for the near-surface component are two orders of magnitude smaller than those for the bulk component. The reason could be trapping probably by surface oxide layers, lattice defects induced by hydrogen plasma loading. [10].

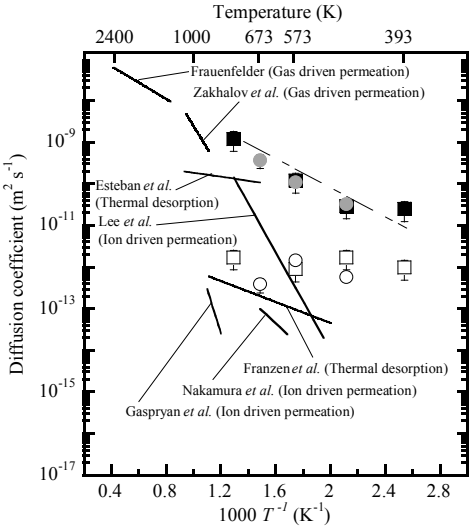

Fig. 7. Hydrogen diffusion coefficient in pure W

(d) Beryllium erosion induced by transient heat loads

The effects of transient heat loads on erosion of a Be target are experimentally investigated in the linear divertor plasma simulator PISCES-B using a pulsed laser irradiation to mimic edge localized modes (ELMs). Light emissions from Be atoms and beryllium deuteride (BeD) molecules are simultaneously observed in front of the target during the laser irradiation with two fast framing cameras. A Nd:YAG laser (NEC: M801C) irradiate a Be target, while the target is exposed to a steady-state deuterium plasma. In front of the cameras, optical filters were placed to detect light emission of the Be I line at 457.3 nm (2^1P-3^1D) and the $A^2\Pi$-$X^2\Sigma^+$ band of BeD. The profile of BeI, showing that BeI emission is intense just in front of the target. On the other hand, BeD profile was broader than that of BeI. The detailed Be release process and transport were discussed in ref. [11] from a numerical calculation of the surface temperature evolution.

Evaporation is thought to be the dominant erosion process of Be during the transients (0.1 - 4MJ m^{-2} at 1-10 ms). Since the surface is heated by the transients, BeD molecules are not directly ejected from the surface, but created in the plasma through the atomic and molecular processes. The following reaction chain was proposed for the volumetric formation of BeD molecules:

$Be + e \rightarrow Be^+ + e + e$,
and then,
$Be^+ + D_2 \rightarrow BeD + D^+$.

Although only a bulk Be target was used in this study, deposited Be layers will be formed on Be as well as on C and W divertor target surfaces, and Be-C and Be-W mixed materials can be created in ITER. Thus, it is of significant importance to explore the interaction of the deposited Be layers and mixed materials with transients.

3-1-4 Summary

Effects of mixed ion (D+He+Be) irradiation to tungsten and diffusion of hydrogen isotope in the bulk tungsten were performed. Small amount of impurity species (He and Be) greatly affects hydrogen isotope retention and surface morphology changes. New technique of bulk T diffusion and retention was proved to be effective. Behavior of eroded Be by pulsed heat could include chemical reactions in the plasma.

[1] M.J. BALDWIN, et al., J. Nucl. Mater., **390**, 886 (2009).
[2] K. TOKUNAGA et al., J. Nucl. Mater. **417**,528 (2011).
[3] K. TOKUNAGA et al., J. Nucl. Mater. **442**, S313 (2013).
[4] G. DE TEMMERMAN, , Nucl. Fusion. **48**, 075008 (2008).
[5] M. MIYAMOTO, et al., J. Plasma Fusion Res. **89**, 335 (2013), in Japanese.
[6] T. OTSUKA, Phy. Scri., **T136**, 014052 (2009).
[7] M. SHIMADA, *et al.* , Rev. Sci. Instrum. 82, 083503 (2011);
[8] T, OTSUKA, *et al.*, J. Nucl. Mater, **417** issue 1-3 1135-1138, (2011).
[9] R. FRAUENFELDER, J. Vac. Sci. Technol., **6**, 388-395 (1968).
[10] T. OTSUKA, *et al.*, Fusion Sci. Technol., **60**, 1539-1542 (2011).
[11] S. KAJITA, et al., J. Nucl. Mater. **420** (2012) 252-257.

3-2 Task 1-2 Tritium behavior in blanketsystems

(T. Terai, S. Fukada, S. Konishi, B. Merrill)

3-2-1 Objectives of task 1-2

Solubility of hydrogen isotopes including tritium in a$Li_{15.7}Pb_{84.3}$ eutectic alloy was experimentally investigated in order to clarify tritium behavior in the Li-Pb blanket system.Precise experiment was carried out by means of a constant volume method to elucidate the reasons whywide scatteringappearsin previous data, and discussion is made with focusing onthe four effects on solubility; (i) Li preferential evaporation fromLi-Pb, (ii) thermal convection in liquid, (iii) reaction in a reaction tube or crucible and especially (iv) difference in crucible materials among Al_2O_3, SiO_2 and W. Another important issue of the blanket system is to develop a new ceramic coating to decrease tritium permeation rate. Tritium permeation reduction factor was determinedusing Er_2O_3 coated on reduced-activation F82H steel. The permeation reduction factor achieved here was higher than 10^3. Isotope effects in solubility and diffusivity between H and D were determined within a Japanese domestic work. No isotope effect in solubility was observed between H and D, and the H diffusivity was 1.4 times larger than the D one. Experiment to determine tritium solubility in Li-Pbis performed under the collaboration work with INL.

3-2-2 Participants to task 1-2

Japan side; T. Terai, T. Chikada (U. Tokyo), S. Fukada, K. Katayama, Y. Edao (Kyushu U.), S. Konishi, Y. Yamamoto, K. Noborio (Kyoto U.),U. S. side; B. Merrill, M.Shimada, P. Sharpe, P.Calderoni, B.Denny, R.Pawelko, S.Schuetz (INL), D.K. Sze, R.Doerner (UCSD)

3-2-3Research highlights

(a) Research background of task 1-2

It is an important issue to clarify and control the behavior of tritium mass transfer in a fusion reactor from viewpoints of safety and reliability of D-T fuel cycle. Understanding behavior of the tritium transfer in a blanket of a fusion reactor is aninevitableissue todesign a cycle of self-sufficient tritiumsupply within onereactor system which is manipulatedproperly with a highly safety. A full system of tritium cycle can be divided into the three parts of plasma-interface region, tritium breeding region and tritium recovery region.Although the three parts can be designed independently,

tritium transfer is continuous and the three regions contact with each other.Therefore, we need to know the tritium behavior correctly not only in normal operation and in maintenance manipulation but also in accidental cases. In addition,we need to reflect the results to tritium system design. Solubility and diffusivity of tritium in breeders are the most important factors to elucidate them. $Li_{15.7}Pb_{84.3}$ eutectic alloy is the most expected material among fusion liquid blanket ones. However, there is a large scattering in solubility of hydrogen isotopes of H and D, which raw data distribute in the range of four orders.In addition, there is no reliable data for tritium one. Therefore, we cannot estimate a reliable integrated blanket system under the present circumstance and cannot design the blanket of a fusion reactor correctly.

In the present task 1-2 of the TITAN project, we focused on the interaction between Li-Pb and surrounding materials, and tested Li-Pbmelted in various materials such as Al_2O_3, SiO_2, Mo and W crucibles or reaction tubes. Solubility of H isotopes in Li-Pbis determined by means of a constant volume method. Discussion is focused on the four effects on solubility; (i) Li preferential evaporation from Li-Pb, (ii) thermal convection in liquid, (iii) chemical interaction in a reaction tube or crucible and (iv) difference in crucible materials among Al_2O_3, SiO_2 and W. Tritium solubility experiment is also performed in this task. Another important work is to develop a low permeation material of Er_2O_3 oxide film to decrease tritium leak to outside. Tritium has an ability of permeation through various materials at high-temperature regions in fusion rectors. Control of tritium permeation through structural material of reduced-activation F82H steel with Er_2O_3oxide coating is measured, and the permeation reduction factor is determined. The present task 1-2 is performed in the STAR facilities of the Idaho National Laboratory to perform tritium experiment. Results obtained under the Japan-US collaboration work and its contribution and importance to the overall blanket technology are summarized here.

(b) Experiment to determine solubility of hydrogen isotopes in Li-Pb

The experimental apparatus set up for the present task is schematically shown in Fig. 1. Hydrogen solubility is determined by means of a constant volume method. The whole system is composed of the three parts of (i) material enclosure with heater, (ii)

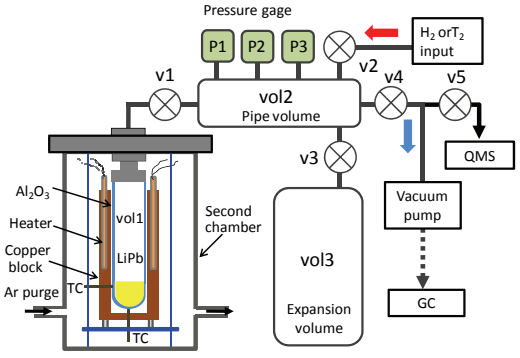

Fig.1 Schematic diagram of experimental apparatus to determine H absorption in Li-Pb

pressure detection in expansion volume and (iii) evacuation. Solubility is determined from pressure difference between the initial value and equilibrium one by using three diaphragm gauges, each of which has a different measurement range.

At first, Li and Pb metals which are adjusted to an atomic composition ratio with Li:Pb=15.7:84.3 corresponding to the eutectic composition are melted in a crucible, which is composed of anyone among Mo, Al_2O_3, SiO_2 and W. The materials are selected because they will be used in actual fusion reactor systems. Two methods to insert Li-Pbinto the reaction tube are tested; (i) a direct method to pour melted Li-Pb directly from a crucible and (ii) a particle packing method to insert solid alloy particles which are made up in a crucible beforehand. The two methods are compared based on detectable differences in solubility data. Heating is supplied by an electric resistance method for Al_2O_3 and SiO_2, by an induction method for W crucible or external electric heating for Mo. The initial H_2 pressure is in the range of 10Pa to 100kPa and temperature in the range of 300^{o}C to 650^{o}C.After Li-Pb contacted with H_2 gas for a sufficient time, pressure difference before and after the contact is read, which is called an absorption method. After Li-Pb is initially saturated with $H_2$where equilibrium state is confirmed, an amount of desorbed gas is measured in the constant volume part, which is called a desorption method. Composition included in the desorbed gas is measured by a quadru-pole mass spectrometer or gas chromatography, and it is confirmed that desorbed gas is only H_2.

Correction of dead space is important to enhance the accuracy of solubility of Li-Pb. The dead space correction is repeated to measure the apparent absorption amount when no Li-Pbis present in a reaction tube. The correction includes effects of adsorption on the tube material, temperature difference and so on along with volume expansion.

Fig.2 shows summary of H absorption in Li-Pb when an Al_2O_3crucible is used, along with previous data. All the solubility data obtained here are correlated to the Sieverts' law described by $C = K\sqrt{P_{H_2}}$, where p_{H2} is

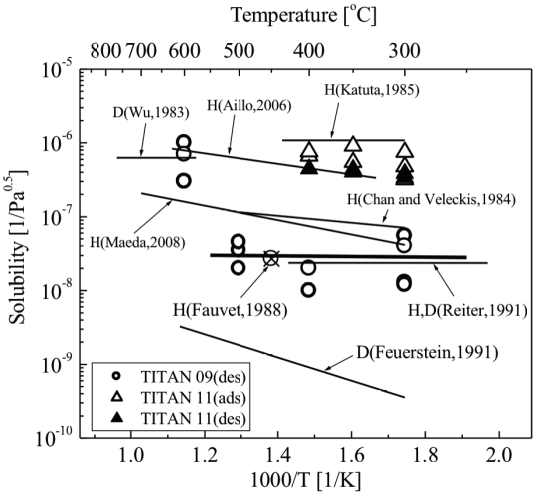

Fig. 2 Summary of H solubility in Li-Pb

equilibrium H_2 pressure in Pa, *C* is the H/Li-Pb ratio in atomic ratio and *K* is the solubility.As seen in the figure, the 2009 Al_2O_3data which are poured by the direct method showed lower values than the 2011 W ones where the particle packing method is used. This may be because the latter one has less possibility to contact with impurity. The 2009 solubility at 600°C shows higher values, because the Al_2O_3 crucible may react with Li-Pb.

When a SiO_2crucible is used, it was cracked after 16 hours heating at 300°C because of direct reaction between Li-Pb and SiO_2. SiO_2cannot be used under conditions where Li-Pb contacts with it.

Since W crucible has good compatibility with Li-Pb and has a property of low permeability for H_2, it is expected to work as a good Li-Pb crucible. However, when it is heated to 600°C, the top part of the reaction tube was covered with a black material. This is because preferential evaporation of Li and Li-Pbthermal convection are enhanced due to large temperaturedifferences between W and SiO_2. Li evaporated from Li-Pbdeposited on the cooled top part of the reaction tube.

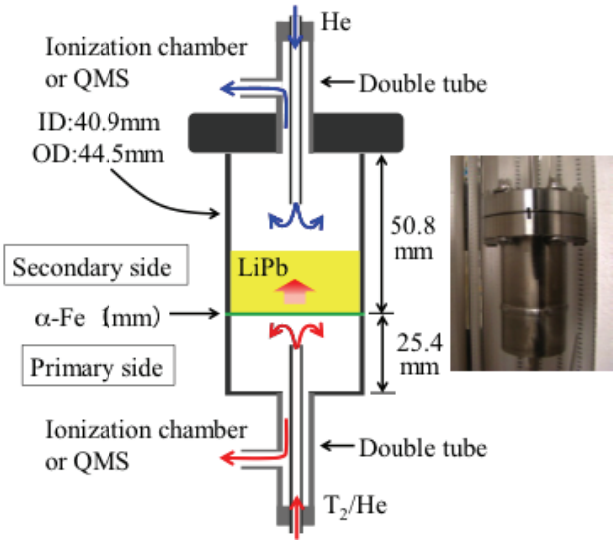

Fig. 3 Experimental apparatus to measuretritium permeation through Li-Pb

Tritium permeability, solubility and diffusivity in Li-Pb are determined by using the experimental apparatus show in Fig. 3. When a T_2/He gas mixture including anyone of the T_2 partial pressures of 10^{-3}, 0.15 and 2.4 Pa is introduced in to the permeation pot, the overall permeation flux obtained is plotted in Fig. 4. Differences in the overall permeation behavior with or without Li-Pb on aα-Fe plate are clearly compared.

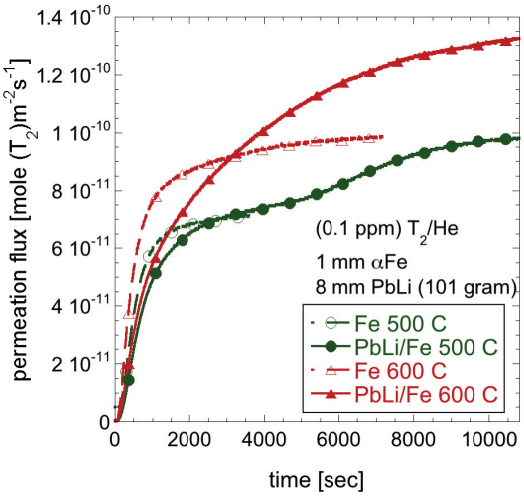

Fig. 4 T_2 permeation rate through Li-Pb

(c) Tritium permeation through RAFM steel tube and Er_2O_3 coating for permeation barrier

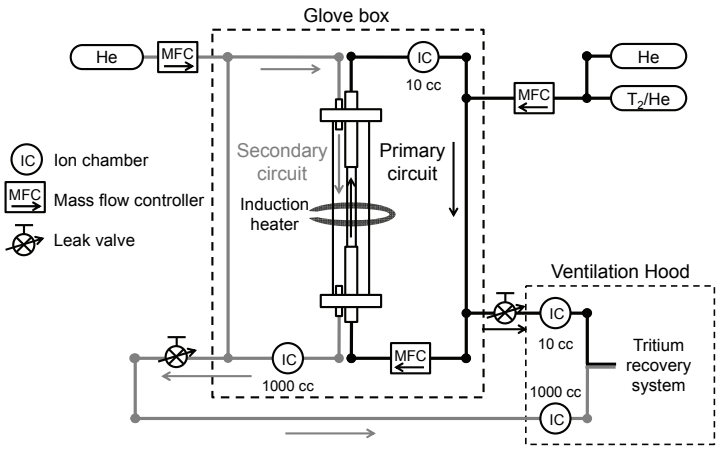

Fig. 5 Schematic view of the tritium permeation

A conceptual diagram of the tritium permeation system is described in Fig. 5. The sample assembly was mounted in a quartz tube. Sample heating was conducted using an induction heater with a 1-turn, 5 inch diameter coil made of copper. Tritium-helium mixture gas was introduced in a circuit (primary circuit) and flew through the tubular sample at a rate of 1000 sccm (standard cm^3 min^{-1}) using a mass flow controller. Tritium that permeated outward through the sample was purged by a pure helium flow of 1000 sccm in another circuit (secondary circuit). The tritium concentrations in the primary and secondary circuits were examined with 10 and 1000 cm^3 ion chambers, respectively. After passing through the ion chambers, the circulating gas in both circuits was partly discharged at a rate of 15 sccm from the primary circuit and 100 sccm from the secondary circuit, to a tritium recovery system placed in a ventilation hood.

The permeation phenomenon of hydrogen isotopes from the primary circuit which contains a known concentration to the secondary circuit with a negligible small concentration are represented by the following equation:

$$J = P\frac{p^{0.5}}{d}, \qquad (1)$$

where J is the permeation flux, P is named permeability which is an intrinsic parameter for the sample, p is the partial pressure of the hydrogen isotope introduced into the primary circuit, and d is the thickness of the sample. The pressure exponent represents permeation regime: the value of 0.5 indicates the rate-limiting process is diffusion of hydrogen isotope atoms, and the value of more than 0.5 means a contribution of molecular reactions such as surface effects. For a simple comparison with past results of deuterium permeation, Eq. (1) was applied for the calculation of tritium permeability in this study.

Temperature dependence of tritium permeability is shown in Fig. 6. The uncoated sample tested with 1.2 ppm tritium at the setting temperature of 380–420 °C (average temperature: 361–393 °C) showed one order of magnitude lower permeability than that of the reference data with 100% deuterium. In addition, the permeation measurements with 40 ppm tritium were more than twice larger than that with 1.2 ppm tritium. However, after the measurements at 400 and 420 °C with 40 ppm tritium, the permeability at 380 °C decreased to the level similar to the result with 1.2 ppm tritium probably due to the oxidation of the sample. A permeability comparable to the reference is supposed with higher tritium concentration, indicating a surface effect on the permeation at the low tritium concentration. The tritium permeability similar to the reference is expected with higher concentrations.

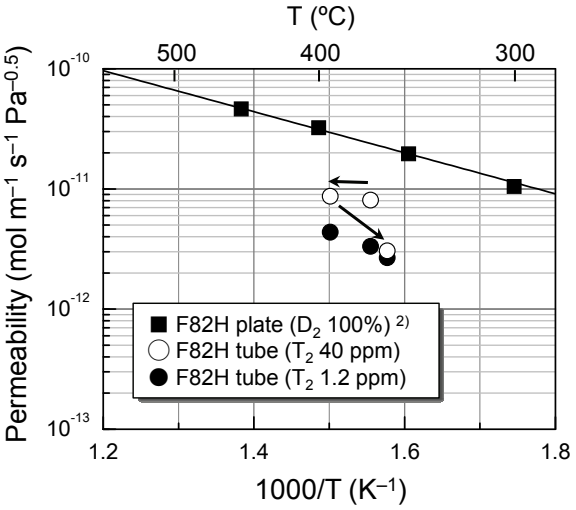

Fig. 6 Arrhenius plots of tritium permeability of the uncoated F82H samples.

The tritium permeability of the uncoated and coated sampled with reference data of deuterium permeability with plate samples are shown in Fig. 7. The coated tubular sample showed two orders of magnitude lower permeability than that of the uncoated one. Compared with the result of the coated plate sample tested with 100% deuterium, the permeability of the coated tubular sample tested with 1.2 ppm tritium also reduced to one-third or one-fourth, which is accorded with the trend in the results of the uncoated samples.

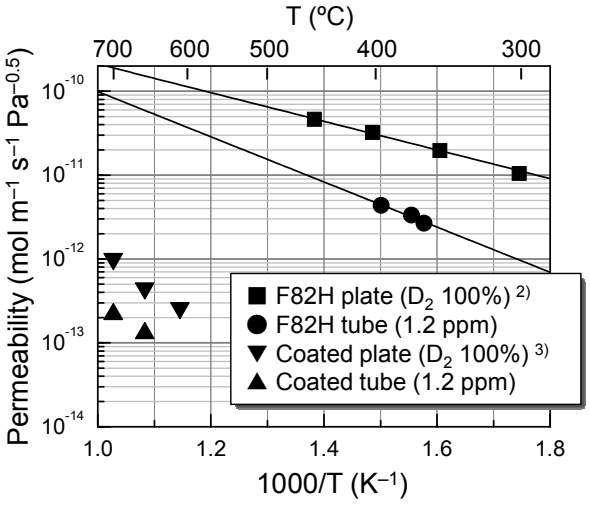

Fig. 7 Arrhenius plots of tritium permeability of the uncoated and Er_2O_3-coated F82H tubular samples.

Because several scratches were observed on the outer side of the coating after the welding process to prepare the sample assembly, the inner coating mainly contributed to the permeation reduction. Therefore, it is proved that the inner coating with a good uniformity and surface coverage has been achieved by the dip-coating process. In addition, the tritium permeability of the coating under the practical condition in a fusion reactor will be smaller than expected from the permeation data with high partial pressure hydrogen isotopes due to the contribution of the surface effect.

3-3 Task 1-3: Flow Control and Thermofluid Modeling

(T. Kunugi, T. Yokomine, S. Smolentsev)

3-3-1 Objectives of the Task

Liquid metal (LM) flow in a fusion blanket interacts with the plasma-confining magnetic field, and eventually the flow structure is strongly affected by a MHD (magneto-hydrodynamics) effect. Especially, LM flows under the strong magnetic field including the flow instabilities and the flow distribution in a coolant channel such as a manifold may determine the heat removal, the hot spots, the corrosion and the tritium transport. Therefore, the understanding of MHD themofluid behavior and the flow control are key issues for fusion blanket research and development. This task has been studying characteristics of the thermofluid under the strong magnetic field and modeling the MHD phenomena. This task conducts some MHD experiments using the MTOR, which is able to make a uniform magnetic field of maximum 2T in a rectangular gap of 15 cm in width and 1m in length.

3-3-2 Participants to the Task

T. Kunugi, T. Yokomine, Y. Ueki (Kyoto U.), H. Hashizume, S. Ebara, M. Aoyagi (Tohoku U.), S. Satake (Tokyo U. Sci.), K. Yuki (Yamaguchi Tokyo U. Sci.)
S. Smolentsev, F-Ch Li, K. Messadek, N. Morley, M. Abdou, T. Sketchley, V. Naveen, J. Young, D. Sutevski (UCLA)

3-3-3 Research Highlights

(a) Liquid metal flow distribution under strong magnetic field

Flow distribution of LM in the coolant manifold under strong magnetic field was studied, which consists of three parallel channels with the electrically insulating walls. The working fluid was mercury, and electrical potential probes were used to measure the flow rates in each channel. As results, a uniform distribution was achieved in the case of the ratio of a magnetic force (Ha) and an inertia force (Re): $N = Ha^2/Re > 90$. Furthermore, in order to investigate the transition of turbulence from three-dimensional to quasi-two-dimensional state due to string magnetic field, the innovative instrumentation technique, where a Printed Circuit Board populated with hundreds of potential probes is used, has been tested and calibrated.

(b) Development of lead-lithium eutectic (LLE) flow diagnostic and interfacial effects

LLE is chosen as the working fluid in this task because it is one of the candidate LM coolants for fusion blanket designs. In order to grasp the LLE flow field, we have been developing a High-Temperature Ultrasonic Doppler Velocimetry (HT-UDV). To do this, LLE acoustic properties necessary for the HT-UDV were obtained and a tracer particle for LLE flow was investigated. On the other hand, for the object to be measured, the interfacial phenomenon related to the LLE wettability may affect the MHD flows. This task has made the quantitative evaluations of the interfacial effects by measuring the contact angles of a LLE droplet on a silicon carbide (SiC) surface, and also measuring an electrical contact resistivity at a SiC/LLE interface.

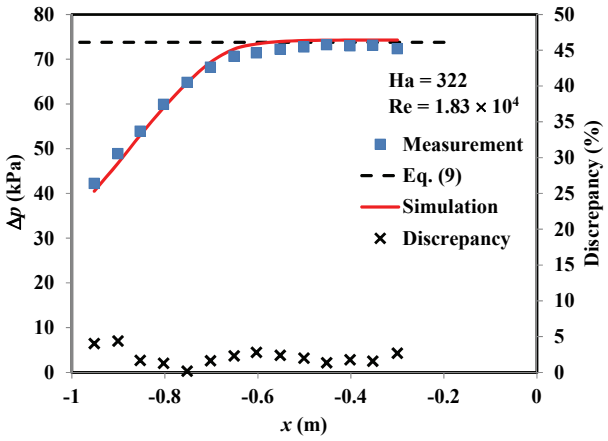

Fig. 1 High magnetic field pressure drop: experiment versus computations

On the other hand, flow diagnostics in hot-temperature LLE, including pressure or differential pressure (DP) measurements, is significantly limited because of the aggressive high-temperature environment, in particular because of corrosion. An indirect approach has then been proposed for measurements of the differential pressure by utilizing a normal gas-pressure DP transducer. Figure 1 shows the measured pressure drop Δp as a function of axial distance in the fringing magnetic field, together with the numerical simulation results by HIMAG, which has been developed specifically for the MHD flows in the environment of nuclear fusion devices. Theoretical estimations of Δp for fully developed MHD flow in the uniform magnetic field are also plotted for reference. As seen from Fig. 1, experimental and numerical simulation results are in fairly good agreement with each other, with less than a 5% discrepancy.

(c) LLE Loop Construction and Performance Test

In order to address the issues related to LLE turbulent flow under magnetic flow via a series of experiments, MaPLE (Magnetohydrodynamic PbLi Experiment) has been newly constructed as a MTOR complementation apparatus as shown in Fig. 2. The main components of this facility include a flow circuit, electromagnetic (EM) pump, EM flow meter, electromagnet and a glove box. The flow circuit, including a melting tank and pipelines, are made of stainless steel SUS304. The maximum

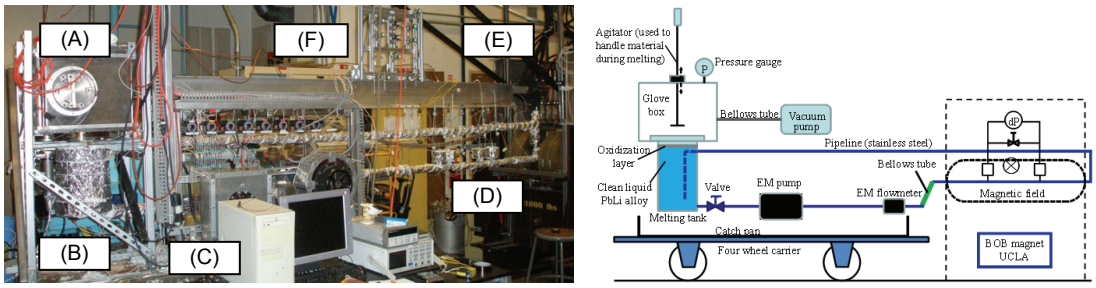

Fig. 2 Photograph and schematic diagram of MaPLE: (A) Glove box, (B) Melting tank, (C) Data sampling system, (D) Test section, (E) Strong magnetic field, (F) Differential pressure sensors

inventory of LLE in the loop is now about 200 kg. The loop is currently operated at 350 ^{o}C maximum as required by the temperature limit of the pump. Figure 3 shows the typical result of performance test, in which EM pump was tested by changing flow rate under strong magnetic field. From the results, it is confirmed that MaPLE can conduct the MHD experiment with LLE under strong magnetic field. With the construction of MaPLE and a series of performance tests with LLE, we can accumulate the valuable technical know-how for performing the LLE MHD experiment, including the preparation and treatment of LLE.

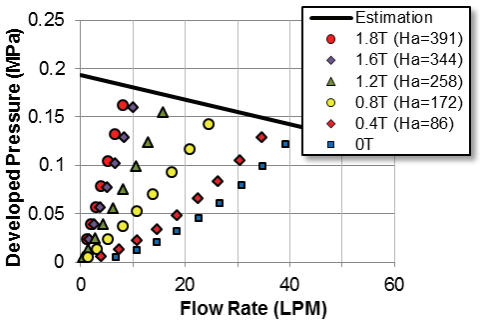

Fig. 3 The characteristic curve measured for the reference EM conduction pump

(d) Development of MHD pressure drop reduction technique

MHD pressure drop reduction is one of the most important R&D issues in LM fusion blankets. A three-surface-multi-layered channel is one of the advanced concepts to reduce the MHD pressure drop, where only three sides of the duct are electrically insulated, while the fourth one that faces the plasma does not carry any insulation. In this way, the MHD pressure drop can be significantly reduced by breaking the cross-sectional current circuit. At the same time, the non-insulated wall is made thinner compared to other three walls to reduce thermal resistance to the surface heat flux. In order to verify this concept, LLE flow experiment has been conducted by means of MaPLE. A test-section (Fig. 4) was fabricated in Japan at Tohoku University and brought to the US for testing. The host duct made of SUS316 steel has a length of 80 cm, a width of 2 cm and a height of 0.8 cm. In the experiments, the applied magnetic field is perpendicular to the short walls. The three insulated walls are 0.5 cm thick, while the

fourth one, non-insulated, is 0.3 cm thick. The two short walls and one of the long walls are painted inside with liquid silica. Figure 5 shows the pressure drop obtained by the experiment and the calculations in the case of 300 °C and 1.8 T. The experimental result is almost corresponding to the calculation for the three-surface-multi-layered channel indicated by a thin line and is one-tenth the value of the calculation for the conducting channel without insulating coating indicated by a dashed line. This result represents the MHD pressure drop is reduced drastically by the three-surface-multi-layered channel.

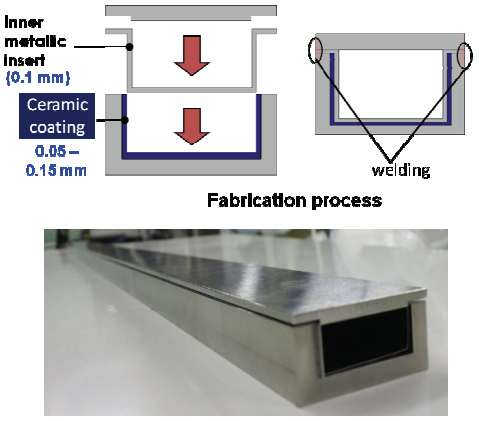

Fig. 4 Three-surface-multi-layered channel tested in MaPLE: fabrication process and photograph of assembled test section

Another solution to reduce the MHD pressure drop is a flow channel insert (FCI). FCI samples of foam-based SiC are fabricated by Ultramet, Inc., USA and delivered to UCLA for testing in LLE. The series of experiments to demonstrate the foam-based FCI is now ongoing by means of MaPLE at UCLA.

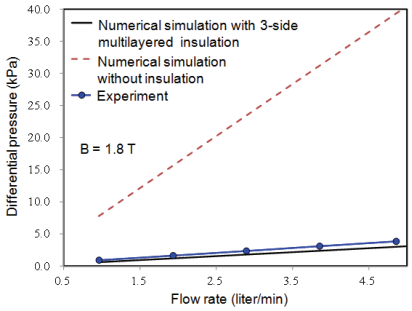

Fig. 5 High magnetic field pressure drop

(e) MHD modeling and numerical simulation

In order to establish the MHD flow control behavior, some MHD models and numerical simulations have been performed and the MHD turbulent effects on the heat transfer have been studied.

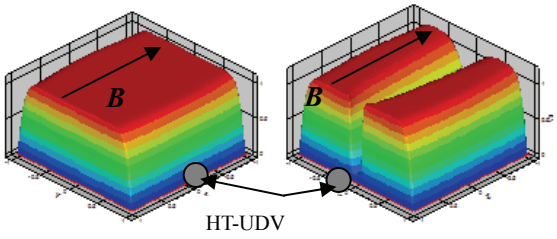

Fig. 6 Numerical estimation of the impact of HT-UDV probe on LLE MHD flow field

Thanks to the developed numerical model, we could access the possible effects of the location of the HT-UDV probe in the duct on the induced electric currents and velocity field. The additional circuit due to installation of HT-UDV may cause significant disturbances of the flow field around the probe. Thus the location of the probe in the duct is important. The

modeling results as shown in Fig. 6 demonstrate almost no probe effect on the flow when the probe is located on the side wall. On the other hand, the probe located on the Hartmann wall causes significant changes in the electric current distribution and as a result leads to drastic changes in the velocity filed in the form of the velocity deficit zone. The practical recommendation is therefore not to install the probe on the Hartmann wall.

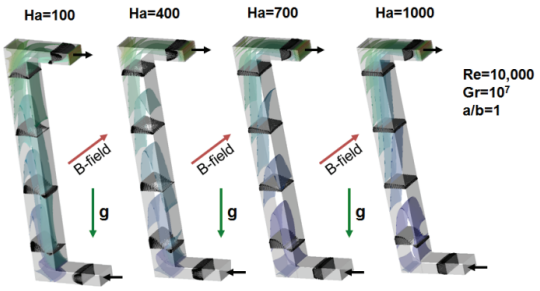

Fig. 7 Simulation results of MHD mixed convection in poloidal duct of DCLL blanket: occurrence of reverse flow due to buoyancy

On the other hand, a mixed convection which consists of both a forced convection driven by pump and a natural convection due to the buoyancy under the strong magnetic field is one of the key issues for the blanket designs. This task has numerically simulated the MHD quasi-two-dimensional flows based on the developed model and obtained the detailed understandings on the complex thermofluid where strong magnetic field and the buoyancy force interact as shown in Fig. 7.

In addition to these main tasks, the opportunities of this collaboration have led to many small-scales but important research cooperation that has been the topics of Master students' projects and theses. These include measurements of contact angle and wetting characteristics of LLE on SiC, electrical contact resistance at SiC/LLE interfaces, simulations of surface slip impact on MHD flow and heat transfer, and many other advanced simulation projects on LM MHD flow, heat and mass transfer that have improved our understanding of blanket function and design immensely.

3-4-4 Summary

This task has been studying characteristics of the thermofluid under the strong magnetic field and modeling the MHD phenomena. This task conducts some MHD experiments by constructing new test apparatus MaPLE installed in the MTOR. To investigate the flow characteristic of high temperature LLE flow under strong magnetic field, HT-UDV and DP sensor has been developed. The pressure drop measurement of a rectangular channel with the 3-surface–multi-layered as the insulation walls was tested, and decreased 1/10 compared to the theoretical value in the same size rectangular channel without any insulation wall. This is the first demonstration of pressure drop reduction using the LLE at high temperature in the world.

3-4 Task 2-1: Irradiation-Tritium Synergism

(Y. Hatano, Y. Oya, Y. Katoh, B. Merrill)

3-4-1 Objectives of the Task

Retention and release of hydrogen isotopes in/from plasma-facing materials (PFMs) is an important issue from the viewpoints of in-vessel tritium inventory, waste managements and tritium accountancy. However, the effects of neutron-irradiation on hydrogen isotope retention have been scarcely examined. The objective of this study is to examine trapping of hydrogen isotope at defects induced by neutron irradiation. Tungsten (W) is selected as reference material of PFMs for DEMO reactors. Small specimens of pure W were irradiated with neutrons in High Flux Isotope Reactor (HFIR) at Oak Ridge National Laboratory (ORNL). The irradiated specimens were shipped to Idaho National Laboratory (INL) and exposed to high flux deuterium (D) plasma in a linear plasma machine called TPE. Then, D retention and release were examined by means of nuclear reaction analysis (NRA) and thermal desorption spectroscopy (TDS).

3-4-2 Participants to the Task

Y. Hatano, M. Hara, K. Zhang (U. Toyama), Y. Oya, M. Kobayashi, K. Okuno (Shizuoka U.), T. Oda (U. Tokyo), K. Sato (Kyoto U.), T. Ohtsuka (Kyushu U.) B. Merrill, M. Shimada, J. P. Sharpe, P. Calderoni (INL), G. Cao (U. Wisconsin), Y. Katoh, M. A. Sokolov (ORNL), T. Yamamoto (UCSB)

3-4-3 Research Highlights

(a) Development of Miniature Specimen Testing Techniques

Due to limited irradiation volume in HFIR and radioactivity induced by neutron irradiation, disk-type miniature specimens (6 mm in diameter and 0.2 mm in thickness) were used in this study. The size of the miniature specimens is 1/18 in surface area and 1/90 in volume of that of standard specimen used in TPE (1 inch in diameter and 1 mm in thickness). First, fabrication of holder was necessary to accommodate those small specimens. Because the surface area of sample was far smaller than the size of plasma, the majority of incident plasma particles interact not with specimen but with specimen holder. Therefore, sputtering of holder material and re-deposition on the specimen surface could be a problem. In addition, because of brittleness of W at around room

temperature, the thin specimens were frequently broken at the initiation of discharge due to heat flux from plasma. A thermocouple pressed onto the back of specimen for temperature measurement was a main source of stress. In order to solve the first problem, a specimen holder made of W with 4 mm-diameter opening was prepared by discharge machining as indicated by an arrow in Fig. 1 (a). In addition, a thermocouple was mounted on a micrometer-driven linear-motion feedthrough to minimize the stress induced by a thermocouple as indicated in Fig. 1 (b). The exposure of miniature specimens without fracture became possible by developments of these specimen holder and micrometer-driven linear-motion feedthrough.

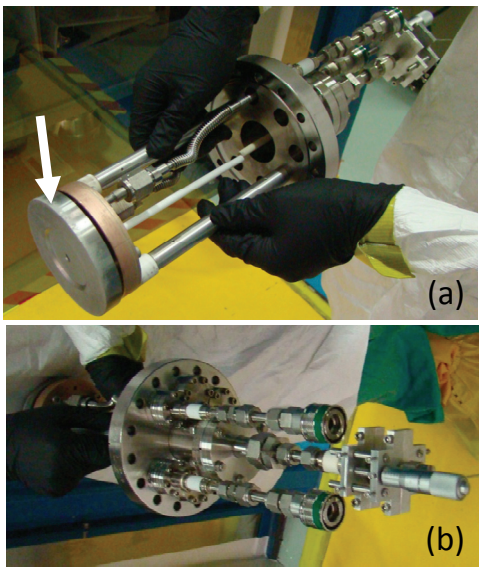

Fig. 1. Holder for plasma exposure of miniature W specimens.

(b) Deuterium Retention in Neutron-Irradiated Tungsten

The disk-type specimens of W were irradiated in HFIR at coolant temperature of the reactor (~50 ºC) to 0.025 and 0.3 displacement per atom (dpa) using perforated rabbit capsules and Mo envelopes. After shipping to INL, the specimens were exposed to D plasma in TPE at 200 and 500 ºC. Flux and fluence of D were (5–7) × 10^{21} D $m^{-2}s^{-1}$ and (5–7) × 10^{25} D m^{-2}, respectively. Then, measurements of depth profiles of D by means of NRA were performed in the University of Wisconsin, Madison. A 3.5 MeV ^{3}He beam was used as a probe. Non-irradiated W specimens were also examined for comparison.

Fig. 2 shows depth profiles of D in non-irradiated specimens and neutron-irradiated specimens (0.025 and 0.3 dpa). Deuterium retention in the near surface region of non-irradiated specimen was 0.1 at.% at 200 ºC and 0.01 at.% at 500 ºC. As described below, the total retention of D at 200 ºC evaluated by TDS was significantly larger than that at 500 ºC. Hence, the lower D concentration at 500 ºC is due to enhanced reemission at the surface and not the diffusion into deeper region.

Deuterium concentrations in neutron-irradiated specimens were clearly higher than those in non-irradiated specimens, and it increased with increase in damage level. The concentration of D in the near surface region after plasma exposure at 200 ºC reached 0.3 at.% at 0.025 dpa and 0.8 at.% at 0.3 dpa. The concentration of D started to

decrease at a depth of 3 μm after the exposure to plasma at 200 ºC. After the plasma exposure at 500 ºC, the D concentration was slightly lower than 200 ºC cases, and it was 0.2 at.% at 0.025 dpa and 0.4 at.% at 0.3 dpa. On the other hand, the penetration depth of D at 500 ºC was clearly larger than that at 200 ºC due to enhanced diffusion; D diffused beyond the detection limit of NRA (about 5 μm under the present conditions). These observations clearly indicated that strong traps for hydrogen isotopes were formed by neutron irradiation, and the concentration of those traps increased with increase in neutron dose.

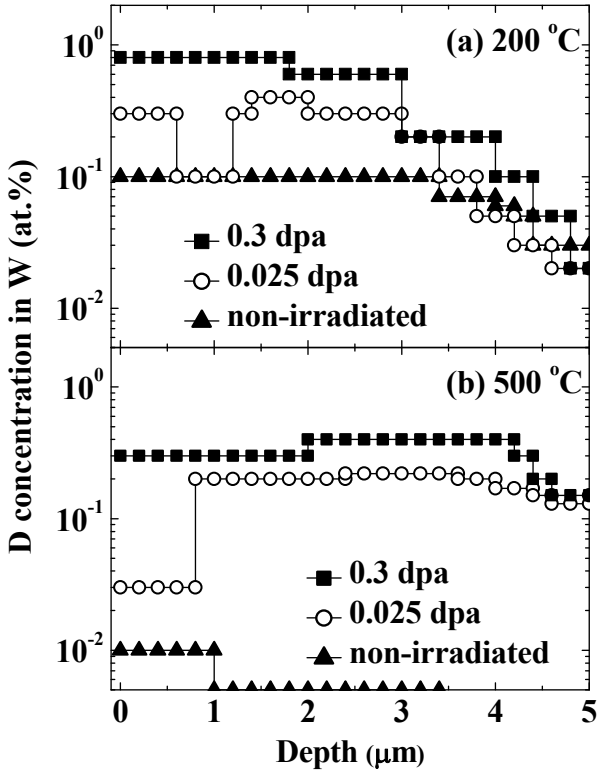

Fig. 2. Depth profiles of D in non-irradiated and neutron-irradiated (0.025 and 0.3 dpa) W specimens.

Although the damage level increased by an order of magnitude, the concentrations of D after neutron irradiation to 0.3 dpa were only higher by a factor of 2 than those at 0.025 dpa at 200 and 500 ºC. According to Roth and Schmid [Phys. Scr., **T145**(2011)014031] who summarized the correlation between damage level and trap density in W irradiated with high-energy heavy ions at room temperature, the density of traps sharply rises at dpa values <0.1 and ceases to increase at around 0.7 dpa and a D concentration of 1.0–1.4 at.%. Alimov et al. [J. Nucl. Mater., **441**(2013)280] also observed such saturation at around 0.1 dpa. It is plausible that saturation with traps also takes place with neutron irradiation, and the trap density after irradiation to 0.3 dpa was close to the saturation level. However, measurements of D retention after neutron irradiation to higher damage levels are necessary to draw a final conclusion.

(c) Desorption of Deuterium from Neutron-Irradiated Tungsten

Fig. 3 shows thermal desorption spectra of D from non-irradiated and neutron-irradiated W (0.025 dpa) after exposure to the plasma at 200 and 500 ºC. The ramp rate of specimen temperature was set to 10 ºC/min. After the exposure to the plasma at 200 ºC, the desorption from non-irradiated specimen was completed at around 400 ºC. In contrast, desorption from the neutron-irradiated specimen continued up to 900 ºC. The retention of D in non-irradiated specimen after the plasma exposure at 500 ºC was significantly smaller than that after the exposure at 200 ºC due to enhanced reemission. On the other hand, large retention was observed for neutron-irradiated specimen even after plasma exposure at 500 ºC due to trapping effects by defects. The amounts of D retained in the neutron-irradiated specimens after the plasma exposure at 200 and 500 ºC were 2.4 × 10^{21} and 6.4 × 10^{21} D m^{-2}, respectively. Interestingly, the D retention at 500 ºC was larger than that at 200 ºC, although the concentration of D in the near surface regions was higher at 200 ºC. Such large retention at 500 ºC can be ascribed to the deep penetration of D into the bulk. The concentration of D evaluated by NRA was 0.1–0.2 at.% corresponding to 6.3–12.6 × 10^{25} D m^{-3} after the plasma exposure at 500 ºC. By assuming that this level

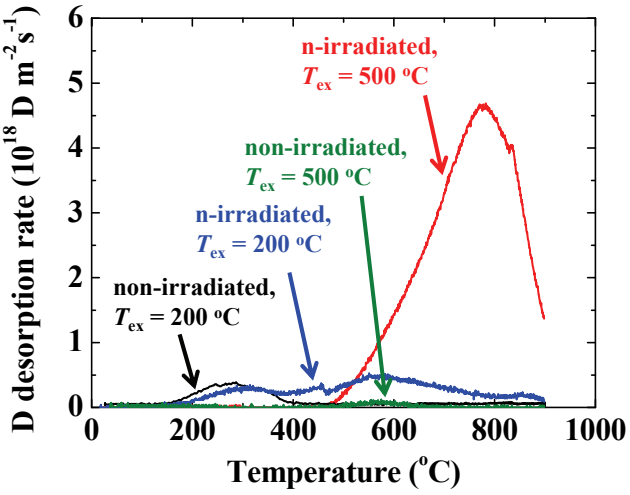

Fig. 3. Thermal desorption spectra of D from non-irradiated and neutron-irradiated W (0.025 dpa) after exposure to D plasma at 200 and 500 ºC. T_{ex} in the figure indicates temperature for plasma exposure.

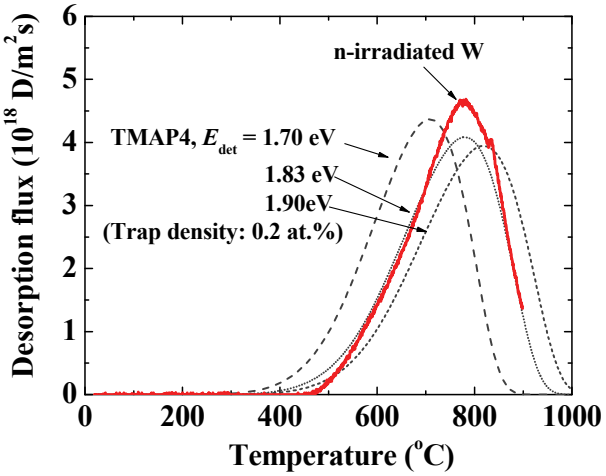

Fig. 4. Simulation of thermal desorption spectrum of D from neutron-irradiated specimen (0.025 dpa) after plasma exposure at 500 ºC using TMAP4 program.

of D concentration continued to deeper region, the penetration depth of D at 500 ºC was evaluated to be 50–100 μm as the quotient of the amount of retained D (6.4×10^{21} D m^{-2}) and D concentration ($6.3–12.6 \times 10^{25}$ D m^{-3}).

The result of a simulation run using the TMAP4 program is shown in Fig. 4. In this simulation, the thickness of the specimen was adjusted to 100 μm because D penetrated up to this depth, as described above. The real specimen thickness was 200 μm, but the presence of remaining 100 μm zone without trapped D was neglected. This is because the effects of this zone were observed in a simulation run only above 700 ºC, and exact simulation at such high temperatures was difficult without consideration on annihilation of defects. The simulated-spectrum agreed with the experimental result with trap concentration of 0.2 at.% and the activation energy for detrapping E_{det} = 1.83 eV. Neutron-irradiation should induce various types of defects with different E_{det}. Hence, 1.83 eV should be considered as the average value for several different types of traps. A more detailed analysis is required to determine exact values of E_{det} for each type of traps. Nevertheless, the result of simulation run also indicated the presence of strong traps.

3-4-4 Summary

Neutron irradiation of W resulted in significant increase in hydrogen isotope retention due to strong trapping effects by radiation-induced defects. The concentration of trapped D in the specimen irradiated to 0.3 dpa reached 0.8 and 0.4 at.% at 200 and 500 ºC, respectively. In addition, deep penetration of D (50−100 μm) with filling up traps was observed at 500 ºC. These observations suggest the significant increase in tritium inventory in W is possible after neutron irradiation. Thermal desorption of D from neutron-irradiated specimen continued up to 900 ºC, whereas that from non-irradiated specimen was completed at around 400 ºC; The release of D from neutron-irradiated W was controlled by long-range diffusion process under strong trapping effects. The activation energy for detrapping was evaluated from thermal desorption spectra to be about 1.8 eV. These results indicate that removal of tritium from neutron-irradiated W by baking at moderate temperatures in vacuum is difficult, and development of tritium removal technique, e.g. isotope exchange, is necessary.

3-5 Task 2-2: Joining and coating integrity

(A. Kimura, N. Hashimoto, T. Nagasaka, M.A. Sokolov, T. Yamamoto)

3-5-1 Objectives of the Task

In this task, irradiations of joints and coating of oxide dispersion strengthened (ODS) steel and reduced activation ferritic steel (F82H) were performed in HFIR for the purpose of studying the irradiation performance of joints and coating of structural components of blankets. The experimental objectives are to a) evaluate feasibility of electron beam welding for F82H by means of mechanical property measurement after neutron irradiation. Irradiation effects on tensile properties and hardness were investigated for F82H joints, b) investigate irradiation effects on vacuum plasma spray (VPS)- W coating on ODSS and F82H to assess the feasibility of VPS-W as a first wall of blanket, c) examine the irradiation performance of friction stir processed (FSP) ODS steel, d) develop solid state diffusion bonding (SSDB) technology of ODS steel without significant change in the dispersion morphology of oxide particles, and e) perform a limited investigation of synergistic effect of helium/hydrogen with irradiation effects on mechanical properties of F82H using hydrogen cathodic charging tensile test method after irradiation. Effects of helium on microstructure of ODS steel and F82H were investigated by means of isotope tailoring method newly developed in this research.

3-5-2 Participants to the Task

A. Kimura, S.H. Noh, R. Kasada, K. Yabuuchi, H. Noto (Kyoto U.), N. Hashimoto, S. Ohnuki, H. Oka (Hokkaido U.), T. Muroga, T. Nagasaka (NIFS), H. Watanabe, K. Tokunaga, N. Yoshida (Kyushu U.)
M.A. Sokolov, Y. Katoh (ORNL), T. Yamamoto (UCSB)

3-5-3 Research Highlights

(a) Hardness distribution and tensile properties in an electron-beam-welded F82H irradiated in HFIR

F82H-IEA and its EB-weld joint were irradiated at 573 and 773 K up to 9.6 dpa in the HFIR and the irradiation effect on its mechanical properties and microstructure were investigated. A hardness profile across the weld joint before irradiation showed the

hardness in transformed region (TR) was high and especially that in the edge of TR was the highest (high hardness region: HHR) compared to base metal (Fig. 1). This hardness distribution corresponds to grain size distribution. After irradiation, hardening in HHR was small compared to other region in the sample. In tensile test, the amount of hardening in yield strength and ultimate tensile strength of F82H EB-weld joint was almost similar to that of F82H-IEA but the fracture position of EB-weld joint was at the boundary of TR and BM. Therefore, the TR/BM boundary is the structural weak point in F82H EB-weld joint after irradiation. As the plastic instability was observed, the dislocation channeling deformation can be expected though the dislocation channel was not observed in this study.

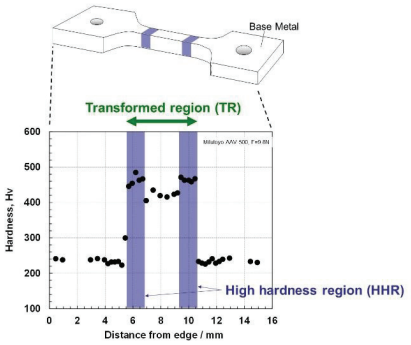

Fig. 1 The distribution of hardness in an unirradiated F82H EB-weld joint.

(b) Effects of Neutron Irradiation on VPS-W Coating on ODS Ferritic Steels

In present study, the effects of neutron irradiation on the hardness of W-coated ODS steels were investigated. Vacuum plasma spraying (VPS) technique was employed to fabricate W layer on the surface of substrates. Substrate materials were K1-, K4-ODS ferritic steels and F82H steel, which are 3mm thick plates. Tungsten powder of 99.9% high purity was used for VPS process. The powders were sprayed by the plasma jet of argon and hydrogen mixture to the surface of substrates pre-annealed at 773K. VPS-W coated specimens, which was obtained with high density of more than 90% (Fig.2), were irradiated at 723K to 1.6, 2.7 dpa in the High Flux Isotope Reactor (HFIR), respectively. To investigate the effect of neutron irradiation on joint area, the hardness distributions were evaluated on the cross section using a micro Vickers hardness tester. Microstructure analysis revealed that W was successfully coated on each

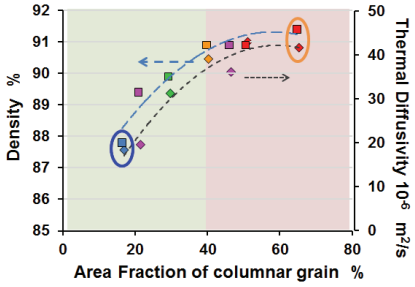

Fig. 2 The dependence of density and thermal diffusivity on area fraction of columnar grain in VPS-W.

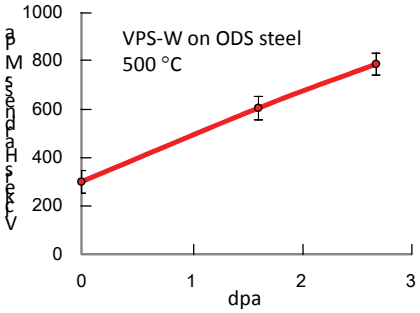

Fig. 3 Irradiation dose dependence of the hardening in VPS-W.

substrate by VPS process, in spite of mismatch of the CTE between these materials. The hardness of W was significantly varied because inhomogeneous cooling rate during the process. After irradiations, a remarkable irradiation hardening was occurred in the VPS-W from Hv=260 to almost 800, while substrate materials did not.

(c) Hardness Distribution and Effect of Irradiation in FSP-ODS Ferritic Steels

Oxide dispersion strengthened ferritic steels (ODS-FS) have been considered as one of the most promising structural materials for advanced nuclear systems such as fusion reactors and next generation fission reactors, because of its excellent elevated temperature strength, corrosion and radiation resistance. Especially, irradiation resistance is a critical issue for the high performance of ODS-FS. In this study, effects of the irradiation on hardness properties of friction stir processed (FSP) ODS-FS were investigated (Fig. 4). FSP technique was employed on ODS-FS. A plate specimen was cut out from the cross section and irradiated to 1.2 dpa at 573K in the High Flux Isotope Reactor (HFIR). To investigate the effect of neutron irradiation on processed area, the hardness distributions were evaluated on the cross section. Hardness of FSP ODS-FS was various with each microstructure after irradiation to 1.2 dpa at 573K. The increase of Vickers hardness (Fig. 5) was significant in the stirred zone and heat affected zone. Base material exhibited the lowest hardening about 38HV. Since nano-oxide particles in stirred zone showed identical mean diameter and number density, it is considered that hardening differences between stirred zone and base material is due to differences in initial dislocation density.

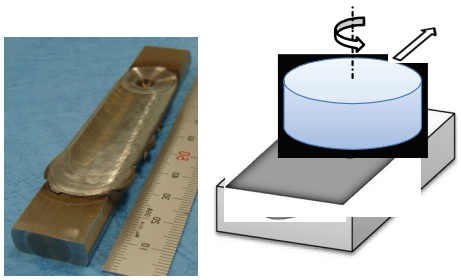

Fig. 4 Friction stir processing of ODS steel

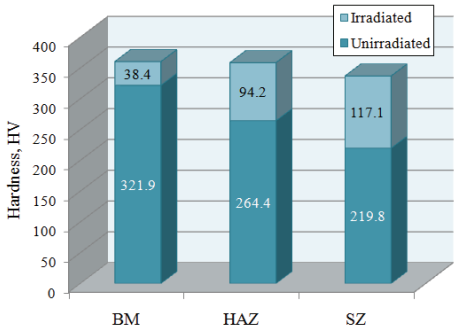

Fig. 5 Irradiation hardening of each region

(d) Development of Solid State Diffusion Bonding of ODS Ferritic Steels

Solid-state diffusion bonding (SSDB) was employed to join high-Cr oxide dispersion strengthened (ODS) ferritic steel (Fe-15Cr-2W-0.2Ti-0.35Y_2O_3) blocks under uniaxial hydrostatic pressure using a high vacuum hot press, and the microstructure and mechanical properties of the joints were investigated. High-Cr ODS ferritic steels were

successfully diffusion bonded at 1200 °C for 1 h, without precipitates and micro-voids at the bonding interface or degradation in the base materials (fig. 6). TEM observation revealed that the nano-oxide particles near the bonding interface were uniformly distributed in the matrix and that the chemical composition across the bonding interface was virtually constant. At room temperature, the joint had nearly the same tensile properties and exhibited anisotropic behavior similar to that of the base material. The tensile strength of the joint region at elevated temperatures is nearly the same as that of the base material, with necking behavior at several μm from the bonding interface (Fig. 7). The total elongation of the joint region slightly decreased at 700 °C, with an exfoliation fracture surface at the bonding interface. Although a small ductile-brittle transition temperature (DBTT) shift was observed in the joints, the upper shelf energy (USE) was fully reserved in the case of joints with the L-R bonding orientation, for which cracks did not propagate on the bonding interface. Therefore, it is concluded that SSDB can be potentially employed as a joining method for high-Cr ODS ferritic steel owing to the excellent mechanical properties of the joints.

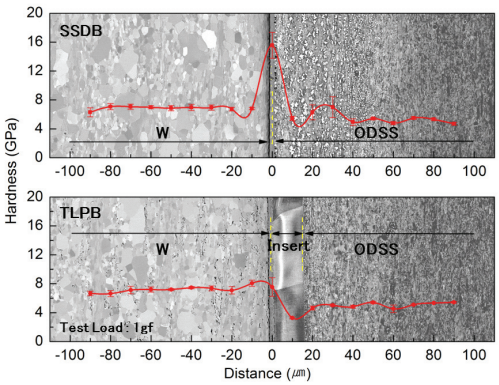

Fig. 6 Microstructure and hardness distribution of SSDB and TLPB (transient liquid phase bonding).

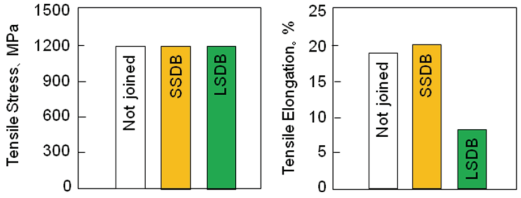

Fig. 7 Tensile stress and elongation of the ODS steel with and without joining.

(e) Effect of hydrogen and helium on swelling in electron-irradiated pure iron

Ion irradiation of Fe^{3+} and H^{+} at 400°C for pure iron resulted in the formation of relatively large voids in matrix. While, voids observed in both base metal (BM) and a heat affected zone (HAZ) of EB-welded F82H indicated smaller than that in pure iron. This behavior of void formation seemed a similar tendency to that of dislocation loop formation. The ion-irradiated F82H indicated the formation of smaller voids with higher number density compared to that in pure iron. In addition, voids observed in the HAZ appeared to be smaller and the number density was higher than that in the BM of F82H. The synergistic effects of hydrogen and helium on swelling for pure iron under electron

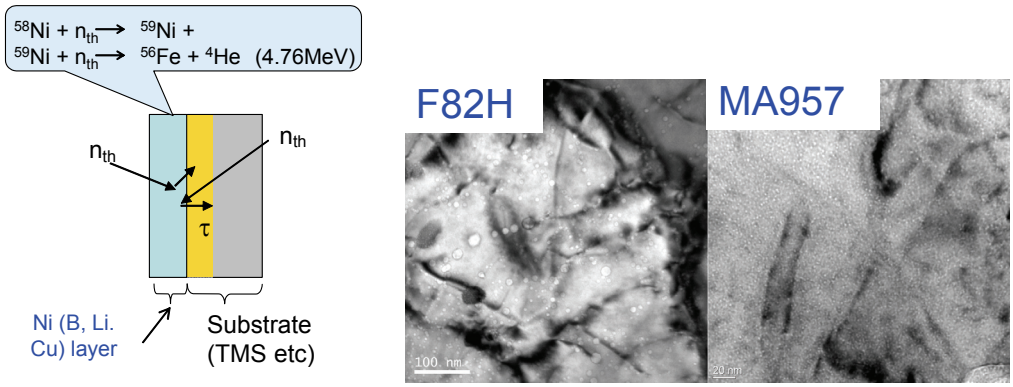

Fig. 8 New technique to evaluate helium effect on void swelling behavior and helium bubbles formed by irradiation in HFIR.

irradiation have been investigated. A new technique to evaluate helium effect on void swelling behavior and helium bubbles was developed and evaluated by irradiation in HFIR. The helium bubbles were formed by isotope tailoring, which indicates that the method is effective to monitoring transmutation helium (Fig. 8). The dual beam irradiation of H^+ and electron was performed at 623 K to 5 dpa after He^+ pre-injection of 100 appm at room temperature. In the pure iron pre-doped with 100 appmHe, the electron irradiation exhibited the formation of cavities with high number density. In addition, the presence of H^+ enhanced swelling about 30% at a maximum. Dislocation densities were increasing with increasing H^+ concentration at the same dose. From those results, it is suggested that the existence of H^+ would lead to the reduction of dislocation bias.

3-5-4 Summary

Joining/coating technology development and assessment of joint/coating performance under neutron irradiation were performed using HFIR in ORNL. VPS-W coating with high performance was successfully obtained by a newly developed masking method during spraying. Irradiation hardening was observed in VPS-W after irradiation at 500°C, which has never been observed in ferritic steels. Application feasibility was checked for FSP-ODS steel and it was proved that FSP was adequate method joining ODS steel without drastic changes in nano-sized oxide particle distribution morphology. A feasible SSDB technology was developed for ODS steels and the bonding fracture strength as high as that of base metal was successfully achieved. Hydrogen and helium effects were investigated by a newly developed irradiation technique.

3-6 Task 2-3:Dynamic Deformation Behavior

(A.Hasegawa, T.hinoki, Y.Katoh, L.L.Snead)

3-6-1 Objective of the task

In this task, (1) dynamic deformation behavior called irradiation creep of SiC and (2) synergistic effects of tritium implantation and displacement damage production on the tritium distribution behavior in SiC werestudied.As for the irradiation creep, it often determines irradiated lifetime of metallic structural components of nuclear reactors, but it may also be beneficial for inherently brittle materials like ceramics for functional applications, because creep may relax or redistribute the stresses. For silicon carbide (SiC)-based nuclear components, the latter function of irradiation creep may be important, in particular when a significant temperature gradient exists and the secondary stresses developed by differential swelling can be severe. Flow channel insert in liquid metal blankets of fusion energy systems is an example of such applications.

To establish an effective tritium recovery scheme in a fusion reactor, it is important to examine synergistic effects on the behavior of tritium in structural material such as SiC under irradiation with neutrons and energetic particles, including tritons created by nuclear reactions of $^{6}Li(n, \alpha)T$ in breeder materials.The second objective of this study is to evaluate tritium distribution in SiC under irradiation at high temperature using the imaging plate (IP) technique, which is a powerful tool for measuring the tritium distribution on and in the bulk region of materials.

3-6-2 Participants to the Task

A. Hasegawa, S. Nogami, T.Shikama(Tohoku U.), T.Hinoki, S.Kondou (Kyoto U.)
Y. Katoh, L.L.Snead (ORNL)

3-6-3 Research Highlights

(a) Development of Bend Stress Relaxation technique for irradiation creep study

The objective of this study is to investigate irradiation creep properties of SiC. Based on the previous works of the experimental technique and the recognized importance of the irradiation creep, a more detailed study on the BSR irradiation creep of SiC ceramics and composites was planned as the main focus of Task 2-3 on dynamic deformation of fusion materials. Figure 1 shows (a) a side view of the BSR fixture made of SiC, (b) top view of stacked and mounted the fixture and (c) bent specimen after

creep test. Controlling the bend elastic deformation loaded before irradiation and the thickness of the strip type specimen, test parameter of loaded stress can be changed. The characteristic points of this method are (1) elastic deformation can be loaded to even in brittle materials, (2) PIE is to measure a curvature of the specimen and this is very simple and (3)comparing the specimen lengths of before and after the irradiation, void swelling caused by its microstructure change can be estimated. On the other hand, to obtain elastically bent deformed specimen, the thickness must be less than 50 micrometers. Special specimen preparation technique to obtain the thin strip specimen from a bulk material with certain accuracy was required. The specimen preparation was carried out in Japan.The mounted BSR fixtures were inserted in a rabbit capsule. The rabbit capsule was filled with helium gas and cooled by reactor water through the helium gas. These rabbit capsules were irradiated in a hydraulic tube or fixed rabbit train in HFIR at ORNL. Irradiation temperatures were 573K, 773K, 1073K and 1473K and irradiation were 0.01dpa, 0.1dpa, 1dpa and 10dpa. The total number of irradiation conditionsperformed in TITAN was 16.

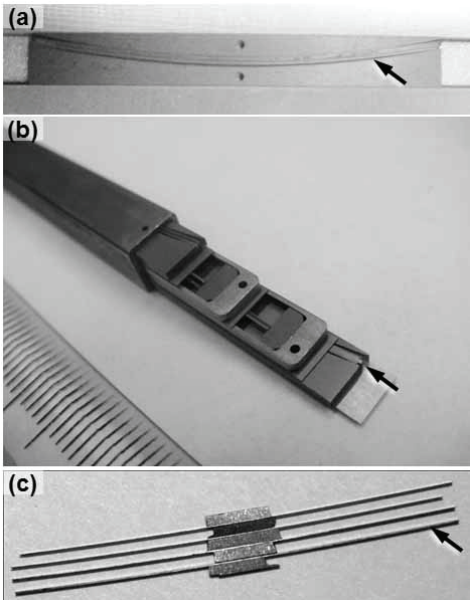

Figure 1 BSR apparatus for irradiation creep experiments

(b) Creep behavior of high purity SiC

The relationship between BSR ratio (m) and loaded flexural stress of SiC obtained after various temperature and dpa were plotted in Fig. 2. The BSR ratiom is equal to 1 at the beginning then it gradually decreases as the permanent strain due to creep deformation accumulates.The m is equal to zero means the initial stress relaxed completely by the creep deformation.The BSR ratio m is 0.9 at

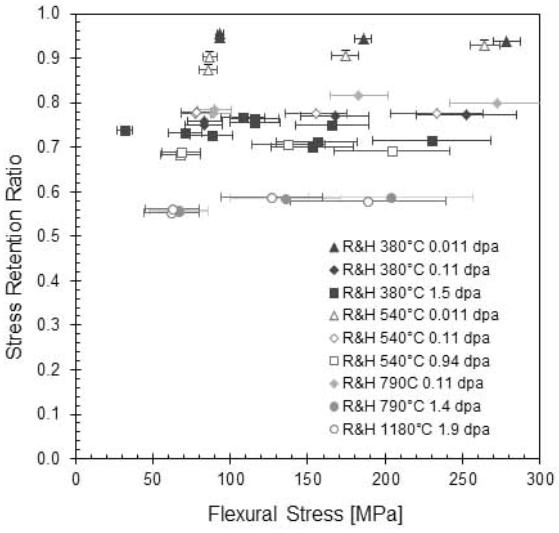

Figure 2 Relationship between BSR ratio and flexural stress of CVD SiC.

873K for loading stress of 65MPa and m is 0.85 at 1473K. Irradiation induced stress relaxation appeared significantly at high temperature region. In Fig. 2, the m values are plotted against the flexural stress magnitude for the three CVD materials irradiated in a range of fluence and temperatures. From Fig. 2the m values are clearly independent of the stress magnitude regardless of the material, the irradiation temperature, or the fluence level. The independence of m values from the stress magnitude at the same fluence levels within a range of evolving creep deformation indicates that the stress exponent (n) is unity. All the proposed irradiation creep models and the vast majority of the irradiation creep data indicate a value of unity for a wide range of materials for which irradiation creep was previously understood, including metalsand graphite. However, this is in contrast to the common understanding for thermally activated creep that gives significantly greater n values.This is the first time that the stress exponent was explicitly determined for the neutron irradiation creep of ceramic materials.

(c) Creep behavior of NITE SiC

Figure 3 shows relationship between BSR ratio and irradiated fluence of CVD-SiC and LPS-SiC.The SiC fabricated by liquid phase sintering (LPS), which wasthe same material for NITE-SiC composite matrix, had remained sintering additive at grain boundaries and triple junctions and showed significant large amount of creep compared to the high purity CVD-SiC. The reduced sintering additives were used for LPS-2 SiC, which was half of the sintering additives used for LPS-1. Effect of the amount of sintering additive on creep wasn't observed.

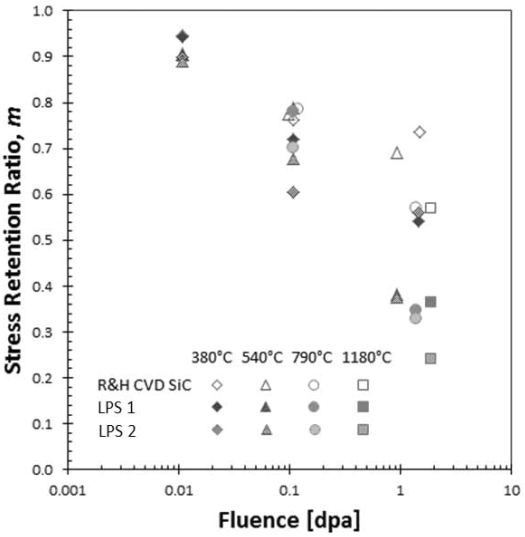

Figure 3 Relationship between BSR ratio and irradiated fluence of CVD-SiC and LPS-SiC

Relationship between the creep behavior and microstructure will be clarified after microstructural observation of these irradiated samples which will be performed in Japan.

(d) Tritium distribution in SiC during reactor irradiation

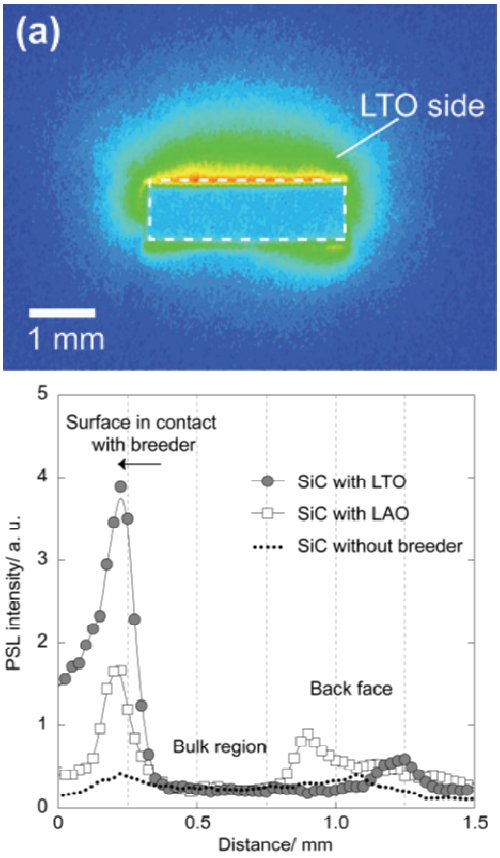

Figure 4 Tritium distribution of irradiated SiC to 5dpa at 1073K. (a) result of IP, (b) depth distribution of PSL intensities in irradiated SiC.

IP images of cross sections of SiC irradiated in the HFIR with ceramic breeder materials are shown in Fig.4. The upper areas of samples in images of (a) correspond to the face of SiC in contact with the solid breeder disk. A significantly higher photo-stimulated luminescence (PSL) intensity is observed near the incident surface that had been in contact with lithium titanate ($Li_{2x}TiO_{3-y}$: LTO)or lithium aluminate ($Li_{1x}AlO_{2-x}$: LAO) during the irradiation. The PSL in the bulk region was observed but was quite lower than that in the vicinity of the incident surface. Figure4(b) depicts PSL intensities of the SiC samples in the direction from the ceramic breeder side to the back faces approximately at the center vertical lines. The PSL intensities in the near-surface regions on the sides of the solid breeders were significantly higher than those on the other sides for SiC samples with both LTO and LAO, although short-range depth profiles in the order of μm could not be obtained from the IP measurement owing to its spatial resolution limitation of 25μm and the contribution of β-rays traveling in air to the PSL intensities. In the bulk region of the SiC in contact with solid breeders, the PSL intensities were similar to those in the reference SiC sample. This means that the in-situ injected tritium did not undergolong-range diffusion into the bulk during the 1073 K irradiation over a duration of 3000 h.

SiC at the initial stage of irradiation within 200 h, while the displacement damage by neutrons was accumulated over 3000 h. Therefore, the tritons and a particles (rather than neutrons) could induce defects, interacting with tritium trapping in the vicinity of the incident surface of SiC. The interaction between tritium and defects induced by the injection of MeV-energy tritons and a particles from the adjoining breeder material may result in the apparent tritium retention in the vicinity of the incident surface of SiC

in the present IP study. The PSL intensity could not simply be converted to tritium concentration owing to the absorption of b-rays in SiC and β-rays traveling in air from the SiC surface beforetheir detection by the IP. Further quantitative studies are required to explain tritium transport processes, including detrapping, diffusion into bulk, and recombination.

4 Summary

The irradiation creep experiments using BSR capsule in HFIR were carried out. It was found that the stress exponent of SiC under irradiation was unity. This is the first time that the stress exponent was explicitly determined for the neutron irradiation creep of ceramic materials. The creep behavior of SiC materials used in advanced SiC/SiC composites was also clarified. Synergistic effect of neutron irradiation and tritium implantation to SiC at 1073Kwas also examined, and showed that the in-situ injected tritium did not undergo long-range diffusion into the bulk during the 1073 K irradiation over a durationof 3000 h. PIE of irradiated specimens are being continues both in the US and Japan by their domestic programs.

3-7 Common Task :MFE/IFE system integration modeling

(A. Sagara, H. Hashizume, T. Norimatsu, R. Nygren)

3-7-1 Objectives of the Task

The final goal of common task is to create a self-consistent model by integrating the separate systems of tritium, heat, and thermofluid. At the same time, via feedback of important considerations to each task, the validity of our experimental results is assessed in the interfaces between research goals in each task, in order to promote the development of an integrated system modeling methodology.In this summary, we focus on material research in Tasks 1-1; 1-2; and 2-1, 2-2, 2-3. The common critical issue in MFE and IFE in terms of fuel self-sufficiency and environmental safety is tritium mass transfer through the heat exchangers. Therefore, a typical heat-exchanger system, designed to identify appropriate boundary conditions for material researches, is also discussed.

3-7-2 Participants to the Task

A. Sagara(NIFS), H. Hashizume(Tohoku U), T. Norimatsu (Osaka U),
R. Nygren(SNL), M. Miyamoto(Shimane U), D. Nishijima(UCSD),
R. Doerner(UCSD), S. Fukada(Kyushu U), Y. Oya(Shizuoka U),
T. Oda(U of Tennessee), K. Morishita(Kyoto U), F. Gao(PNL), T. Yamamoto(UCSB),
S. Sharafat(UCSD), T. Terai(U of Tokyo), A. Kimura, T. Hinoki, S. Konishi(Kyoto U),
Y. Hatano(Toyama U), S. Smolentsv, N. Morley, A. Ying(UCLA), P. Calderoni,
M. Shimada (INL), R. Raffray(UCSD), T. Kunugi, K. Yokomine(Kyoto U),
Y. Ueda(Osaka U), D.K. Sze(UCSD), T. Muroga(NIFS), K.Okuno(Shizuoka U)

3-7-3 Research Highlights

(a)Helium (He) effect on deuterium (D) retention in tungsten

A critical consideration in fusion reactor design is the tritium recycling properties of the first wall of the fusion blanket.The effects of helium on the retention of hydrogen isotopes in tungsten seems strongly depend upon experimental conditions.The results of several previous studies are shown in Fig. 1.Results for D retention by energetic ion implantation (open symbols in Fig. 1) are consistent across studies, with D retention saturating at around 3×10^{20} D^+ m^{-2}, even for He^+fluence as large as 10^{22} He^+ m^{-2}.While He bubble formation and radiation damages create potential D trapping sites,

higher density and larger He bubbles may enhance desorption of D by suppressing its diffusion toward the bulk tungsten.

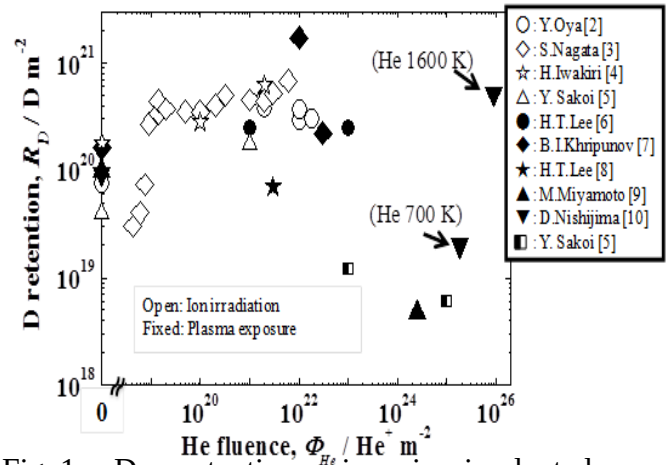

Fig. 1 D retention in ion-implanted or plasma-exposed tungsten, as a function of He^+fluence.

(b)Tritium absorption and diffusion in Pb-Li

Task 1-2 of the TITAN project is the quantitative analysis of tritium absorption and diffusion in a promising blanket cooling material (Pb-Li). in our study, solubility measurements were carried out by two different methods: 1) a constant volume method at the Idaho National Laboratory (INL) and 2) a transient permeation method at Kyushu University. The former experiment determined T solubility in Pb-Li, while the latter determined the solubility and diffusivity of H and D in Pb-Li.The results are presented in a separate Task 1-2 paper of the special issue: “Clarification of tritium behavior in Pb-Li blanket system”. The second task is system design integration, with the application of a Pb-Li breeding material to the fusion reactor systems.In Japan, a water-cooled ceramic (Li_2TiO_3) breeder blanket is used as the ITER–TBM. Blanket designs using Pb-Li as coolant and breeder of magnetic fusion have not been considered previously. On the other hand, a wet-wall Pb-Li design is proposed for the Koyo-fast commercial fusion reactor.A schematic of this design, with a list of design parameters, is shown in Fig. 2.

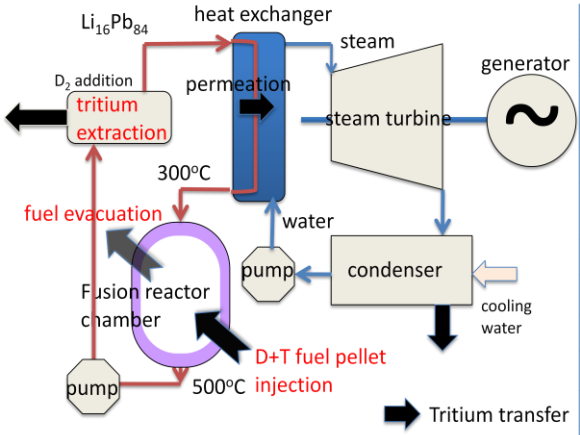

Total power	1 GWt
$Li_{16}Pb_{84}$ inlet temp.	300 °C
$Li_{16}Pb_{84}$ outlet temp.	500 °C
$Li_{16}Pb_{84}$ mass flow rate	18.4 t/s
T generation rate	1.43 MCi/day
T concentration in $Li_{16}Pb_{84}$	8.6×10^{-9} T/$Li_{16}Pb_{84}$
T partial pressure in LiPb	1.8×10^{-3} Pa
Heat transfer coefficient of heat exchanger	5.0×10^3 W/m^{2}K
Surface area of het exchanger	690 m^2
Logarithmic temperature difference in heat exchanger	290 °C
Estimated T leak rate	255 Ci/day
Rate-determining step	T permeation through tube wall

Fig. 2 $Li_{16}Pb_{84}$ loop and steam Rankine cycle in a Laser fusion reactor.

Pb-Li flows into the top of the reactor chamber to protect the metal chamber from damage by heavy neutron irradiation. Besides its role as a tritium breeder, Pb-Li receives heat from particles created by D-T fusion and the n-6Li reaction within the blanket. The energy conversion and tritium recovery systems in the external Pb-Li flow for IFE are essentially same as those for MFE, except that the flowing Pb-Li directly comes in contact with the high-temperature plasma on the wet wall of the vacuum chamber.Tritium concentration in the Pb-Li flow is controlled by the tritium generation rate in the chamber and by the Pb-Li flow rate. Majority of the tritium is recovered by a Pb-Li-He counter-current flowing system, but a small portion escapes from the outlet of the recovery system into the heat exchanger. Tritium balance and permeation rate through heat-exchanger tubes were initially estimated as 255 Ci/day. We consider that this comparatively high tritium permeation rate can be mitigated by coating the heat exchanger tubes with ceramic. A 1000-fold reduction in permeation implies a tritium leakage rate below 1 Ci/day, which complies with the safety standards. Experimental verification of permeation reduction is presented in the Task 1-2 section of the abovementioned paper.

(c)Effect of radiation on tritium retention in tungsten exposed to ion and neutron irradiations

Radiation damage is likely to increase tritium retention. Accurate prediction of tritium retention in fusion reactors requires careful analysis and interpretation of these experimental results. In Task 2-1, the effects of neutron and ion irradiation were investigated by computer simulations as well as by irradiation experiments with neutrons and ions.

We developed a simulation code based on the Monte Carlo technique for modeling the accumulation and release behaviors of hydrogen isotopes interacting with vacancies in tungsten. The code utilizes the results of first-principle calculations as well as data obtained in previous experiments. It can integrate systems containing vacancies from external sources, for example, from TRIM code. We then evaluated the behavior of hydrogen loaded by plasma exposure or ion irradiation. The results are presented as depth profiles in tungsten and thermal desorption spectra. From the simulation results, hydrogen introduced by plasma exposure was found to be localized in a region of high defect density created by ion irradiation of tungsten. In contrast, in neutron-irradiated tungsten, hydrogen was spread over a wide region (Fig. 3). Thermal desorption behavior of introduced hydrogen also differed between ion-irradiated and neutron-irradiated samples, consistent with the experiment. These differences are attributed to a difference

in the vacancy distribution between ion-irradiated (localized distribution) and neutron-irradiation (uniform distribution) systems.

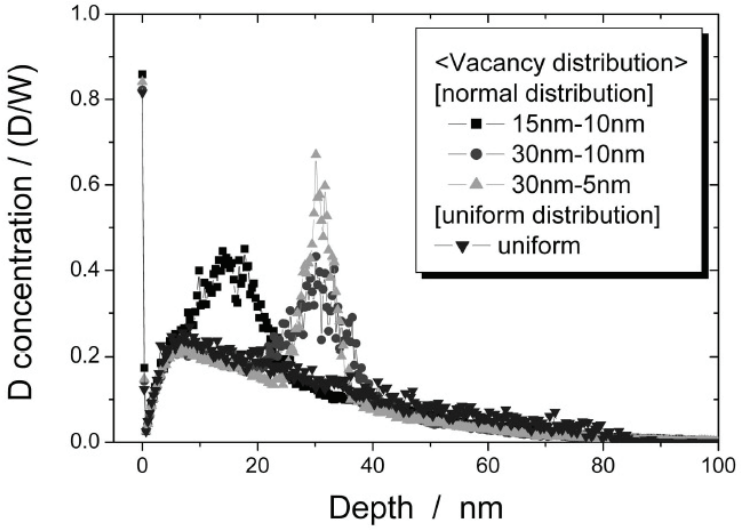

Fig. 3Monte Carlo simulation results on distribution of deuterium implanted into ion-irradiated or neutron irradiated tungsten at 473 K. Deuterium implantation depth is around 5 nm, corresponding to a plasma exposure of 200 eV deuterium. The label "15–10 nm" signifies that the vacancy distribution is centrally localized at 15 nm with FWHM 10 nm (assuming normal distribution), and "uniform" signifies a uniform distribution of defects. The localized and uniform distributions correspond to ion and neutron irradiation, respectively. The peak trap concentration is set to 4% for all conditions.

(d)Multiscale modeling of microstructural change in SiC during irradiation

The main component of SiC/SiC composites, used as blanket structural materials for nuclear fusion reactors, is cubic silicon carbide (β-SiC). Fusion reactor materials are subject to various point defects such as vacancies (V), self-interstitial atoms (SIAs), and those induced by helium and hydrogen atoms displaced by high-energy incident neutrons from the fusion core plasma. Modeling defect cluster formation in a compound material requires special care, as discussed below.

First, the formation, binding, and migration energetics of β-SiC defects were investigated by classical molecular dynamics (MD) and molecular statics (MS), combined with the method of Gao–Weber empirical interatomic potential. In the MD and MS calculations, the formation energy of the most energetically favorable SIA clusters was derived as a function of size and chemical composition ratio (Si/C) of the clusters. Knowledge of the formation energy is crucial for evaluating binding energy

between defects since the binding energy corresponds to the thermal stability of the defects. Migration energies of isolated silicon and carbon interstitials (SIAs) were also derived).

On the basis of the defect energetics obtained from the atomistic calculations, the nucleation and growth processes of SIA clusters were then investigated by the kinetic Monte Carlo (KMC) method. Here the KMC model constructed allows for statistical fluctuations in the inflow/outflow of isolated SIAs into/from an SIA cluster. In the KMC simulations, the ratios of the diffusion fluxes between silicon and carbon interstitials (DISiCISi: DICCIC) were set as 1:1, 1:10, and 1:100, while the total diffusion flux (DISiCISi + DICCIC) was kept constant at 1.0×10^{19} m^2/s. The formation kinetics of SIA clusters in β-SiC during irradiation were roughly classifiable into two temperature-dependent classes. At relatively high temperatures, the thermal stability of an SIA cluster is crucial, and the chemical composition of the cluster is almost stoichiometric (i.e., Si/C = 1), as shown in Fig. 4-(a). In contrast, at relatively low temperatures, where cluster thermal stability is no longer crucial, the composition of SIA clusters can deviate markedly from stoichiometric (Fig. 4-(b)).

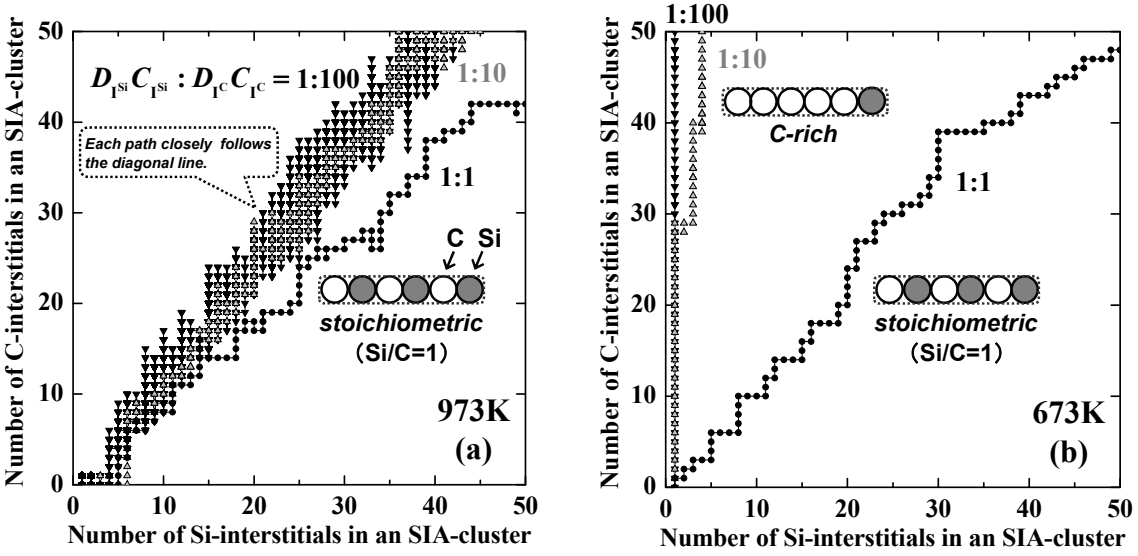

Fig. 4 KMC simulations of nucleation and growth path of SIA clusters in β-SiC at (a) 973 K and (b) 673 K.

(f)Leakage control of tritium through heat cycles of fusion reactor

Tritium leakage by diffusion through heat exchangers occurs in both MCF and IFE. While retaining the system efficiency, the tritium leakage must be reduced by a factor of $1/10^{10}$ to reach that of a current fission plant. To reduce tritium permeation from the

primary liquid metal or sodium loop into the secondary water loop, a heat exchanger incorporating small-diameter tubes containing an oxidizer was proposed. An inert gas containing a small amount of oxidizer flows through the tubes, oxidizing tritium intercepted from the primary liquid metal coolant.

Evaluation of this design indicated that the tritium leakage through the heat exchanger was reduced by $1/10^5$, with an acceptable increase in the size of the heat exchanger. This scheme is compatible with the coating technique, using compounds such as Er_2O_3 and ZrO_2, which may further reduce permeation by a factor of $1/10^4$.

3-7-4 Summary

The common task in the US-J TITAN project identifies cross-linked considerations in the blanket system modeling on the basis of the material research in each task. The results are summarized as follows:

(1) The helium effects on hydrogen isotope retention in tungsten were investigated by reviewing the results of previous studies and by conducting D^+ He mixed plasma exposure experiments in PISCES. These results reveal that D retention is reduced by high-density He bubbles forming in the near surface region.

(2) Research into permeability, diffusivity, and solubility of hydrogen isotopes in a Pb-Li alloy as a tritium breeder is summarized. The blanket design must achieve a low tritium leak to the outside and high tritium recovery from a breeder loop.

(3) A simulation code to model the accumulation and release of hydrogen isotopes interacting with vacancies in tungsten was developed using a Monte Carlo technique. Simulation results revealed that the behavior of hydrogen isotopes depends strongly on the mode of irradiation (i.e., whether the specimen is ion- or neutron-irradiated).

(4) Multiscale modeling of microstructural changes in a binary compound material during irradiation has elucidated the nucleation and growth processes of defect clusters.

(5) Tritium permeation through a heat exchanger equipped with double tubes filled with an oxidizer can be reduced to $1/10^4$ that of bare stainless tubes, without degrading the heat exchange rate.

4. Research reports

4-1 Task 1-1

(1) Tritium and mass transfer in first wall

4-2 Task 1-2

(1) Tritium permeation through reduced activation ferritic/martensitic steel tube and erbium oxide coating

(2) Clarification of behavior of tritium release from liquid Li-Pb blanket and tritium recovery

(3) Measurement of solubility of hydrogen isotopes in Li-Pb by adsorption and desorption method

(4) Development of a low tritium partial pressure permeation system for mass transport measurement in lead lithium eutectic

(5) Research activities for measurement of hydrogen solubility in LiPb

(6) Solubility of Hydrogen Isotopes in Liquid LiPb

4-3 Task 1-3

(1) Electrical insulation test of alumina coating fabricated by sol-gel method in molten PbLi pool

(2) Acoustic properties of Pb-17Li alloy for ultrasonic doppler velocimetry

(3) Velocity profile measurement of lad-lithium flows by high-temperature ultrasonic doppler velocimetry

(4) Construction and initial operation of MHD PbLi facility at UCLA

(5) Verification test of three-surface-multi-layered channel for MHD pressure drop reduction

4-4 Task 2-1

(1) Design and construction of thermal desorption measurement system for

tritium contained materials

(2) Measurement of tritium retained in neutron-irradiated molybdenum using imaging plate and beta-ray induced x-ray spectrometry

(3) Comparison of deuterium retention for ion-irradiated and neutron-irradiated tungsten

(4) Influence of displacement processes on the formation of irradiation defects and deuterium retention in tungsten

(5) Dose dependence of deutrium retention in neutron-irradiated tungsten

4-5 Task 2-2

(1) Hardness distribution and tensile properties in an electron-beam-welded F82H irradiated in HFIR

(2) Effects of neutron irradiation on VPS-W coated ODS ferritic steels

(3) Hardness distribution and effect of irradiation in FSW-ODS ferritic steels

(4) Development of solid state diffusion bonding of ODS ferritic steels

(5) Effect of hydrogen and helium on swelling in electron-irradiated pure iron

(6) Solubility of hydrogen isotopes in liquid LiPb

4-6 Task 2-3

(1) Study on stress relaxation behavior of silicon carbide by BSR method

(2) Irradiation creep of nano-powder sintered silicon carbide at low neutron fluences

(3) Effects of neutron Irradiation on mechanical properties of silicon carbide composites fabricated by nano-infiltration and transient eutectic-phase process

(4) Tritium tapping in silicon carbide in contact with solid breeder under high flux isotope reactor irradiation

4-7 Common Task

(1) Integrated material system modeling of fusion blanket

4-1 Task 1-1(1) Tritium and mass transfer in first wall

K. Tokunaga[1], M. Miyamoto[2], T. Ohtsuka[3], S. Kajita[4], Y. Ueda[5], N. Ohno[6], M. Shimada[7], D. Nishijima[8], M.J. Baldwin[8], R. Doerner[8]

[1] *Research Institute for Applied Mechanics, Kyushu University, Kasuga, Fukuoka 816-8580, Japan, tokunaga@riam.kyushu-u.ac.jp*
[2] *Department of Material Science, Shimane University, Matsue, Shimane 690-8504, Japan, miyamoto@riko.shimane-u.ac.jp*
[3] *Interdisciplinary Graduate School of Engineering and Science, Kyushu University, Japan, t-otsuka@nucl.kyushu-u.ac.jp*
[4] *EcoTopia Science Institute, Nagoya University, Nagoya 464-8603, Japan, kajita@ees.nagoya-u.ac.jp*
[5] *Graduate School of Engineering, Osaka University, Suita, Osaka 565-0871, Japan, yueda@eei.eng.osaka-u.ac.jp*
[6] *Graduate School of Engineering, Nagoya University, Nagoya 464-8603, Japan, ohno@ees.nagoya-u.ac.jp*
[7] *Fusion Safety Program, Idaho National Laboratory, Idaho Falls, ID, USA, masashi.shimada@inl.gov*
[8] *Center for Energy Research, University of California at San Diego, 9500 Gilman Drive, La Jolla, CA 92093-0417, USA, dnishijima@ferp.ucsd.edu, rdoerner@ucsd.edu,*

Under th US-Japan collaboration project TITAN, studies on erosion, surface modification and tritium retention of tungsten under D/He/Be combined ion irradiation environment were performed. Mixed materials formation of W and Be and its impact on blistering and D retention as well as on He bubble formation were studied for the first time. Since Be inclusion in plasmas significantly affects retention and surface morphology changes. it is necessary to evaluate Be effects correctly in ITER and beyond. Bulk tritium distribution after tritium plasma exposure was measured by IP (Imaging Plate) technique, which is proved to be a powerful tool for a bulk retention study. Be erosion by ELM-simulated pulsed heat was observed.

I SURFACE MODIFICATION OF TUNGSTEN AND FORMATION OF RE-DEPOSITED LAYER BY BE SEEDED D-He MIXTURE PLASMA EXPOSURE

Co-deposition of H isotopes with material eroded from plasma facing components in deposition dominated areas in fusion devices will influence tritium retention, recycling of H isotopes and diffusion to bulk material. In the ITER reactor, a clear understanding of the properties and tritium retention of the Be co-deposited layer is of the highest importance for reliable prediction of the in-vessel retention and also for the development of tritium removal techniques. In the present study, Be-seeded low energy and high-flux D/He mixture plasma exposure experiments on W have been performed to simulate W ITER divertor erosion/modification and deposition phenomena [1, 2, 3].

Powder metallurgy tungsten (PM-W) and ultrafine grain (UFG) W‐0.5 wt%TiC were used in the present experiments. The samples were irradiated by plasma in the UCSD PISCES-B. The exposure conditions were fixed ion energy of 60 eV and flux of 3‐6 x $10^{22}/m^2/s$. The sample temperature was kept at 1123 K and exposure times spanned 1050‐10,100 s. The typical ratio of He/D ions was 0.2. A Be impurity flux is generated in PISCES-B through the use of an evaporative source. In the present experiments, the Be content was 0.2%. Glassy carbon plates were installed on a witness plate manipulator to collect eroded material during the W exposure.

Fig. 1 shows an SEM image of a cross section of UFG W-0.5wt%TiC/H_2 after the irradiation. SEM observation of the surface and cross section of the irradiated samples indicated that a nanostructure layer formed near the surface as well as by the D‐He mixture plasma without Be exposure.

Fig. 2 shows nano-structured layer thickness data as a function of the square root of the plasma exposure time. The thickness of the nanostructured layer increased with increasing exposure time, similar to the result for exposure to the D-He plasma without Be. The set of nanostructured layer thickness data as a function of the square root of the plasma exposure time tended to have some deviations with a fitted $t^{1/2}$ dependence and the straight line fit did not pass through zero. The $t^{1/2}$ axial intercepts may be an indication of a short incubation or

saturation time that precedes nanostructuring. The analyses results indicate that Be exists in a very thin area near the sample surface. In addition, it is considered that the Be layer thickness is thin enough, and He implantation depth was greater than the Be layer thickness, leading to the formation of He bubbles in the W, which are believed to drive the nanostructure formation process. In these conditions, deposited Be on the W target by the Be seeded D/He plasma irradiation was also sputtered by D/He irradiation. However, when energy decreases, for example, to 15 eV, a BeW alloy layer is formed that depends on the temperature, and the nano-structure is not formed.

A fraction of the re-eroded Be from the W target is deposited on a glassy carbon plate with line of sight to the tungsten target. The Be redeposit layer is in the form of laminae and includes D, He, H and W. The obtained D/Be values are plotted in Fig. 3. This is the first report of co-deposition data formed in this way, and the results ought to be relevant and applicable to specific areas of the ITER divertor where W fuzz may grow. That is, the experimentally obtained D/Be value is plotted against that predicted by the De Termmerman scale [4]. Plotting the data in this way gives an indication of the level of agreement of the current co-deposit D/Be ratios with the known experimental database.

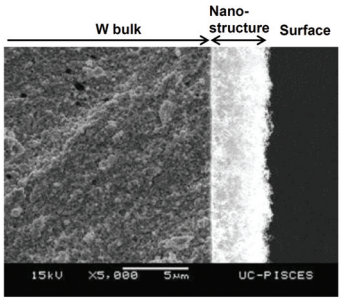

Fig. 1 SEM images of cross sections of the nano-structured layer on UFG W-0.5 wt%TiC/H_2 alloy after plasma exposure. The UFG-W was exposed to D-0.2He plasmas with Be at 1123 K for 10,100 s.

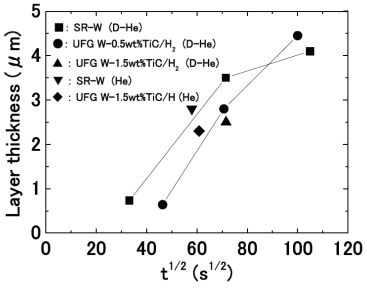

Fig. 2 Nano-structured layer thickness as a function of the square root of the plasma exposure time

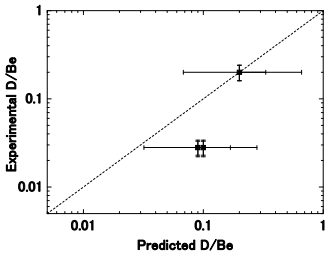

Fig.3 D/Be values of the current study plotted against the expectation value of the empirical De Temmerman scale in Ref. [4].

II. D+He+Be mixture plasma exposure experiments in the linear divertor plasma simulator PISCES

This section outlines the results of the mixture plasma exposure experiments performed in the linear divertor plasma simulator PISCES to predict plasma-wall interaction phenomena under the in the ITER divertor region. See Ref. [5] for more information.

The stress-relieved and mirror-polished W samples were exposed to mixed-species (D+He, D+Be and D+He+Be) plasmas as well as pure D plasma. Subsequent to the plasma exposures, surface morphology and internal microstructures were examined using a scanning electron microscope (SEM) and a transmission electron microscope (TEM), respectively. In addition, to investigate D retention properties, gas-desorption profiles were measured using a thermal desorption spectroscopy (TDS) system.

Fig. 4 shows SEM images of the W samples exposed to various mixture plasmas at 573 K. High density micron-sized blisters are formed on the surfaces of W exposed to pure D plasma. It is found from the EBSD measurements that more blisters are prone to be formed in grains with the sample surface direction close to <111>, which is the most open direction in the bcc lattice. Since D ions may have a deeper penetration range at the most open direction, more blistering can take place. The recent report, which also shows the strong correlation between surface modifications and crystal orientations for W exposed to high flux He plasma in NAGDIS, points out the influence of the angle between a split face and a surface of crystal grain [6]. The seeding He and/or Be into D plasma caused significant influence on these blisters formation. For the W sample exposed to D+He mixture plasma, the blister formation was suppressed even at a low He^+ ion concentration of c_{He+} ~1 %, and not observed at c_{He+} ~5 %. In case of Be seeding at E_i ~60 eV, most of incoming Be onto the W surface was re-sputtered and SIMS analysis revealed the formation of a mixed Be/W layer of a few nm in thickness. On the D+Be plasma exposed surface, submicron-sized blisters and their

exfoliations were observed. On the other hand, the sample exposed to D+Be+He mixture plasma at E_i ~60 eV looks as comparably smooth as an unexposed surface. This He seeding effect on the surface morphology is consistent with the case of D+He mixture plasma exposure with no Be. At a lower E_i of ~10 eV, deposited Be is not re-sputtered, and a thick Be layer of ~ 1 μm was observed.

In Fig. 5, thermal desorption spectra of D_2 from the W samples exposed to various plasmas at $\Phi_D \sim 5\times10^{25}$ m^{-2} and T_s ~ 573 K are displayed. D retention in the sample exposed to D+He mixture plasma was significantly lower than that in the pure D exposed sample. As shown in Fig. 6, high density He bubbles are observed in the sample exposed to D+He mixture plasma, and cross sectional observation revealed that the damaged layer with He bubbles was much larger than the He ion range of a few nm. Since the volume fraction of He bubbles exceeds the percolation threshold, the desorption mechanism that injected D atoms diffuse back to the surface through the percolating bubbles is suggested. This dramatic decrease of D retention was also observed even at a low He^+ ion concentration of c_{He+} ~1 % in a PISCES plasma. In a machine such as like ITER, where the incident He fluxes to the walls will be even greater, significant reduction of tritium inventory are expected. In the sample exposed to Be seeding plasma, D retention property differ widely according to presence or absence of Be deposition layer. The D-retention in the W samples exposed to D+Be and D+He+Be plasmas at the Be erosion condition (E_i ~60 eV) was about an order of magnitude smaller than the sample exposed to pure D plasma. Because the thickness of Be/W mixed layer is roughly equal to the implantation

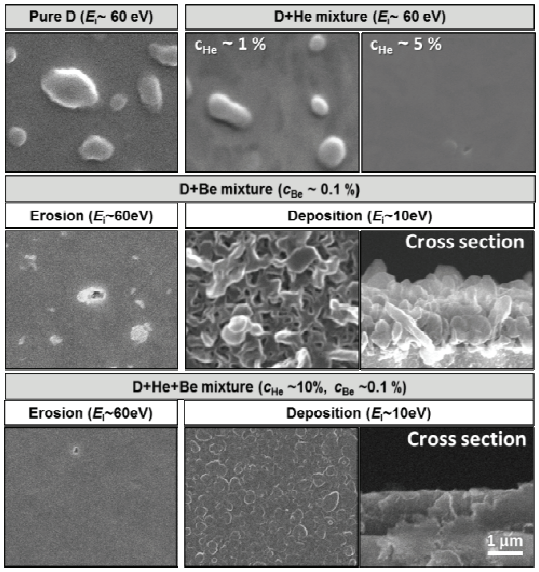

Fig.4 SEM images of the W samples exposed to various plasmas at Φ_D ~5×10^{25} m^{-2} and T_s ~573 K. For the samples exposed to the plasma at the Be deposition condition, cross-sectional images are also displayed.

depth of incident D, the thin Be/W mixed layer may

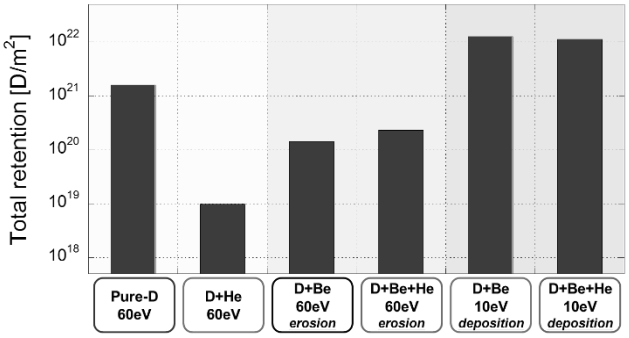

Fig.5 The total retention of D for W samples exposed to various plasmas. The fluence of D is unified to be Φ_D ~5×10^{25} m^{-2} for the all samples.

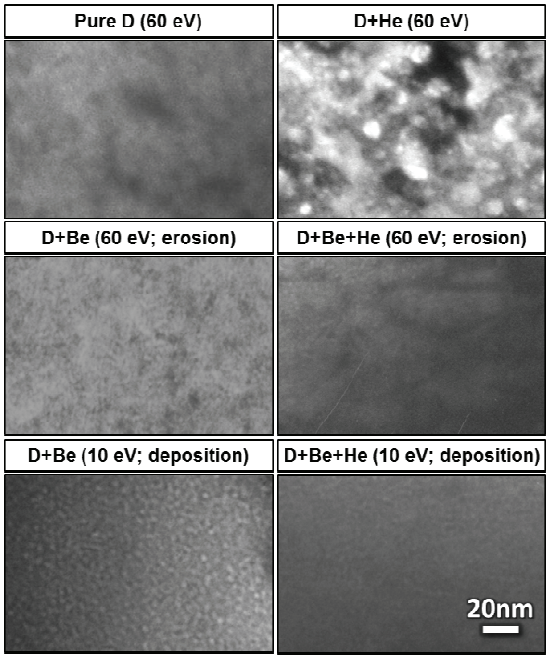

Fig.6 Internal microstructures of pre-thinned W samples exposed to various plasmas. In these image conditions, cavities are observed as white contrasts if they are present.

obstruct the diffusion of D into the bulk. In contrast, at the Be deposition condition (E_i ~10 eV), the D retention was about an order of magnitude higher than that in the pure-D exposed sample. Assuming that all retained D atoms uniformly distribute only within the Be deposition layers, the D/Be ratio is estimated to be ~0.03. This high ratio of D/Be seems to be caused by the strong D trapping efficiency of Be, resulting from the formation of D bubbles as shown in the TEM observations (Fig. 6). It was also found that He seeding to D+Be plasma had little influence on D retention regardless of the conditions of erosion and deposition, as opposed to He mixture to pure

D plasma. Thus, it can be said that Be seeding has a more dominant influence on the D retention behavior in plasma-exposed W than He seeding. Note that all the experiments presented here were executed at T_s ~573 K to better clarify the effects of the mixture of He and Be. For a better prediction of the tritium retention, the T_s dependence of D retention and the high energy neutron irradiation effect in W exposed to D+Be and D+He+Be mixture plasma should be investigated.

III. DIFFUSION AND RETENTION BEHAVIORS OF TRITIUM LOADED IN TUNGSTEN MATERIALS FROM PLASMA

In the present study, depth profiles of tritium (T) loaded into pure tungsten (W) at various temperatures were measured by means of tritium imaging plate technique (TIPT) [7] to examine T diffusion and retention behaviors in pure W. The T loading experiments were conducted with a linear plasma device (TPE) located at Idaho National Laboratory (INL) in US.

The sample used was 1 inch disk (3 mm thick) of stress-relieved polycrystalline pure W (A.L.M.T.). Figure 7 shows a schematic geometry during T loading in TPE. A surface side of the disk covered by a mask made of W with four holes (6 mm in diameter) was exposed to D(T) plasma for 2 h at 473K and 773K. The T/D ratio of the D(T) mixture gas was 0.5 %. Plasma parameters in TPE were described elsewhere [8] in details; briefly, incident ions were assumed to be singly ionized species (D^+ or T^+), and their energy is 100 eV that was determined by the potential difference between the bias voltage and the plasma space potential. The incident ion flux was estimated to be 10^{22} m^{-2} s^{-1}.

After the T loading, the sample was cooled down to RT with the cooling rate of around 1 K s^{-1}. T distribution on the T-loaded surface was measured by TIPT for 1 h at room temperature (RT). Then, the sample was bisected perpendicular to the T loaded surface to appear a cross-section. This bisection process was done using a diamond-wire saw in a ventilated

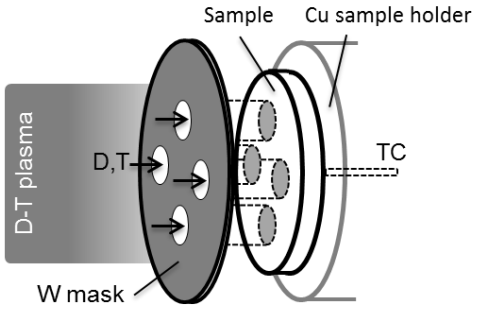

Fig.7. A schematic geometry during T loading in TPE

glove box and finished within 2 h at RT. TIPT was then applied to measure T distribution on the cross-section surface for 24 h at RT.

Figure 8 (a) shows T distribution on (a) the T-loaded surface and (b) the cross-section surface for the sample loaded at 473 K for 2 h. In the figure, T concentration is higher as the color changes from blue, green, yellow to red. In Fig. 8 (a), one can see 4 circular areas with uniform and high T concentration caused by T loading. The corresponding cross-sectional view of T distribution is shown in Fig. 8 (b). Magnified image of T distribution clearly indicates T penetration towards a depth direction along a z axis described in the figure.

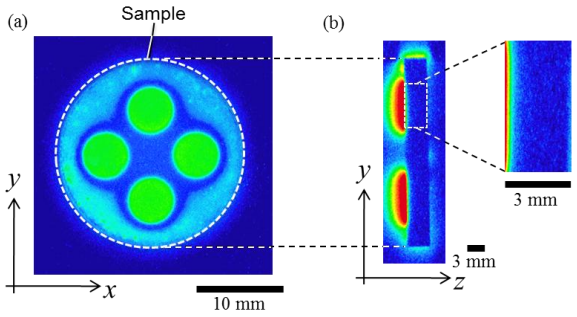

Fig.8. T distribution on (a) the plasma-loaded surface and (b) the cross-section surface for the sample loaded at 423 K for 2 h.

Digitizing averaged T concentration at each depth of 50μm (a spatial resolution of TIP) and plotting them against the depth, T depth profile was obtained. Figure 9 shows T depth profiles with (a) a linear and (b) a logarithmic scale of T concentration. In Fig. 9 (a), one can see T concentration was very high indicating a large amount of T localized near surface region within 0.5 mm in depth (hereinafter referred as a near-surface component). In addition, a tiny amount of T, of which concentration was 3 orders of magnitude smaller than that of the near-surface component, penetrated into deeper region of the bulk around 1.5 mm in

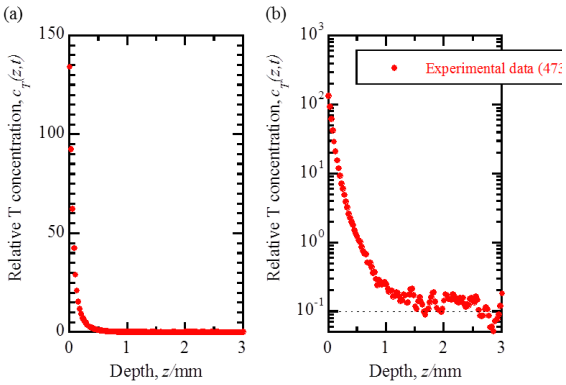

Fig. 9. T depth profile for the sample loaded at 473 K for 2 h, plotted with (a) a linear and (b) a logarithmic scale of the T concentration as a vertical axis.

depth (hereinafter referred as a bulk component).

From the T depth profiles, apparent hydrogen diffusion coefficients for the near-surface component and the bulk component are determined as follows. Note that the isotopic effects would be so small as to be indivisible as compared to experimental errors in the present data. We assume that hydrogen concentration at the T-loaded surface was constant during the loading due to a balance of an incoming flux and a release flux, and hydrogen penetrated into the deeper region by diffusion. After the plasma termination, hydrogen concentration of the T-loaded surface instantaneously became zero and hydrogen was rapidly released by diffusion at the loading temperature during the cooling periods. Both the apparent hydrogen diffusion coefficient and the hydrogen concentration at the T-loaded surface were determined by fitting the numerical solution of Fick's diffusion equation (hereinafter referred as a theoretical curve) to the experimental data.

Figure 10 shows the T depth profile of the sample loaded at (a) 473 K and (b) 773 K. In the figure, one can see deeper T penetration by the loading at higher temperature. Solid curves indicate theoretical curves fitted to the experimental data for the bulk component.

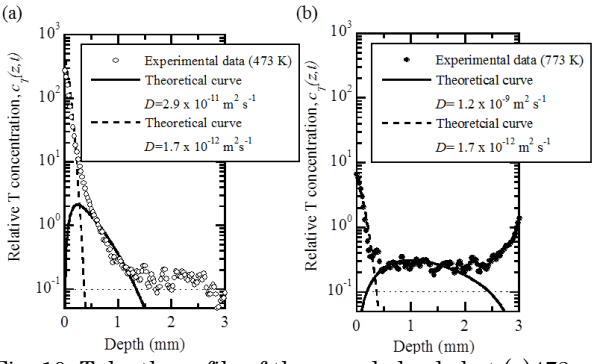

Fig. 10. T depth profile of the sample loaded at (a)473 K and (b)573 K. Dot and solid curve indicates theoretical curves numerically calculated for the near-surface component and the bulk component, respectively.

The determined apparent hydrogen diffusion coefficients in the present study [7] and the previous study [9] are plotted as grey circles and black squares in Fig. 11 and compared with the literature data. The apparent hydrogen diffusion coefficients for the bulk component are in good agreement with the extrapolation of Frauenfelder's data obtained at higher temperatures than 1198 K to the present temperature range. This indicates that the bulk component is caused by diffusion penetration of dissolved hydrogen in pure W at the loading temperature. On the other hand, the apparent hydrogen diffusion coefficients for the near-surface component are two orders of magnitude smaller than those for the bulk component. The cause could be trapping probably by surface oxide layers, lattice defects induced by hydrogen plasma loading. Since the data for the near-surface component are similar to the other literature data, trapping effect would be difficult to be eliminated in thermal release or permeation experiments.

In a practical fusion reactor, trapping effects in the bulk as well as near surface region will become significant due to defects formation induced by neutron irradiation. To understand retention behaviors of T in in the bulk during operation and maintenance, temperature and time dependences of T depth profiles in the deeper region, i.e. mm in depth, should be examined [11] as well as near the surface region.

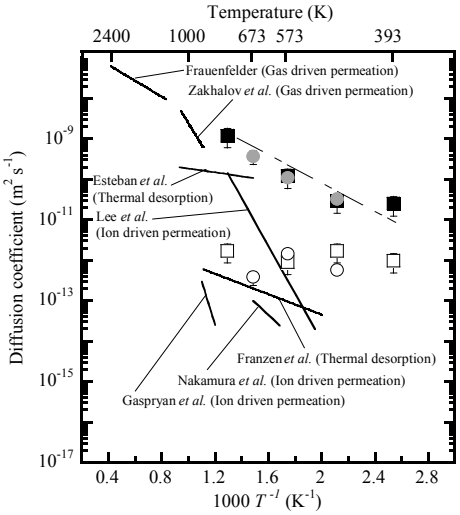

Fig. 11. Hydrogen diffusion coefficient in pure W

IV. BERYLLIUM EROSION INDUCED BY TRANSIENT HEAT LOADS

The effects of transient heat loads on erosion of a Be target are experimentally investigated in the linear divertor plasma simulator PISCES-B using a pulsed laser irradiation to mimic edge localized modes (ELMs). Light emissions from Be atoms and beryllium deuteride (BeD) molecules are simultaneously observed in front of the target during the laser irradiation with two fast framing cameras. A Nd:YAG laser (NEC: M801C) irradiate a Be target, while the target is exposed to a steady-state deuterium plasma. In front of the cameras, optical filters were placed to detect light emission of the Be I line at 457.3 nm (2^1P-3^1D) and the $A^2\Pi$-$X^2\Sigma^+$ band of BeD.

Fig. 12 shows typical emission profiles of BeD and Be I. Laser was introduced from the right hand side and a Be target was located on the left of the image.

Fig. 12(b) shows the profile of BeI, showing that BeI emission is intense just in front of the target. On the other hand, BeD profile was broader than that of BeI. The detailed Be release process and transport were

discussed in ref. [12] from a numerical calculation of the surface temperature evolution.

Evaporation is thought to be the dominant erosion process of Be during the transients (0.1 - 4MJ m^{-2} at 1-10 ms). Since the surface is heated by the transients, BeD molecules are not directly ejected from the surface, but created in the plasma through the atomic and molecular processes. The following reaction chain was proposed for the volumetric formation of BeD molecules:

$$Be + e \dashrightarrow Be^{+} + e + e,$$

and then,

$$Be^{+} + D_2 \dashrightarrow BeD + D^{+}.$$

Although only a bulk Be target was used in this study, deposited Be layers will be formed on Be as well as on C and W divertor target surfaces, and Be-C and Be-W mixed materials can be created in ITER. Thus, it is of significant importance to explore the interaction of the deposited Be layers and mixed materials with transients.

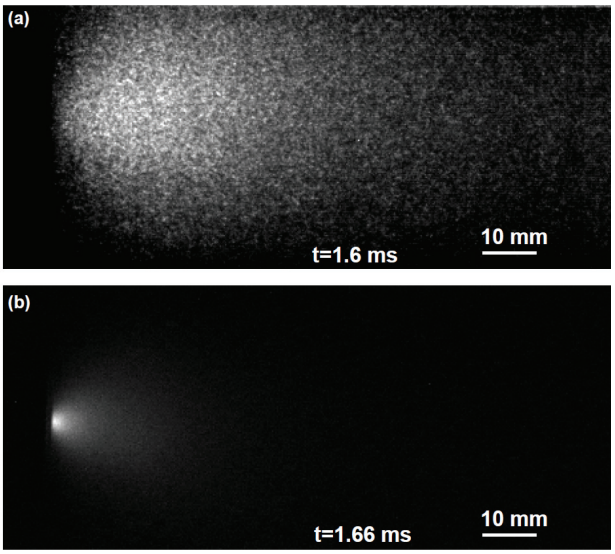

Fig. 12 Typical emission profiles of (a) the A-X band of BeD and (b) Be I at 457.3 nm.

REFERENCES

[1] M.J. BALDWIN, R.P. DOERNER, D. NISHIJIMA et al., "The effects of high fluence mixed-species (deuterium, helium, beryllium) plasma interactions with tungsten", *J. Nucl. Mater.*, **390**, 886 (2009).

[2] K. TOKUNAGA M.J. BALDWIN B, R.P. DOERNER et al., "Nanoscale surface morphology of tungsten materials induced by Be-seeded D-He plasma exposure" J. Nucl. Mater. **417**,528 (2011).

[3] K. TOKUNAGA, M.J. BALDWIN B, D. NISHIJIMA et al., "Properties of deposited layer formed by interaction with Be seeded D–He mixture plasma and tungsten", J. Nucl. Mater. **442**, S313 (2013).

[4] G. DE TEMMERMAN, M.J. BALDWIN, R.P. DOERNER et al.," An empirical scaling for deuterium retention in co-deposited beryllium layers", Nucl. Fusion. **48**, 075008 (2008).

[5] M. MIYAMOTO, D. NISHIJIMA, M.J. BALDWIN et al., "Microstructure and Deuterium Retention Property of W in D-He-Be Mixture Plasma Environment", J. Plasma Fusion Res. **89**, 335 (2013), in Japanese.

[6] N. OHNO, Y. HIRAHATA, M. YAMAGIWA et al., "Influence of crystal orientation on damages of tungsten exposed to helium plasma", J. Nucl. Mater. **438**, S879 (2013).

[7] T. OTSUKA, T. HOSHIHIRA, T. TANABE, "Visualization of hydrogen depth profile by means of tritium imaging plate technique", Phy. Scri., **T136**, 014052 (2009).

[8] M. SHIMADA, R. D. KOLASINSKI, J. P. SHARPE *et al.*," Tritium plasma experiment: Parameters and potentials for fusion plasma - wall interaction studies", Rev. Sci. Instrum. 82, 083503 (2011);

[9] T, OTSUKA, T. TANABE, K. TOKUNAGA *et al.*, "Application of tritium tracer techniques to observation of hydrogen on surface and in bulk of F82H", J. Nucl. Mater., **417** issue 1-3 1135-1138, (2011).

[10] R. FRAUENFELDER, "Permeation of Hydrogen through Tungsten and Molybdenum", J. Vac. Sci. Technol., **6**, 388-395 (1968).

[11] T. OTSUKA, M. SHIMADA, T. TANABE *et al.*, "Behavior of Tritium near Surface Region of Metals Exposed to Tritium Plasma", Fusion Sci. Technol., **60**, 1539-1542 (2011).

[12] S. KAJITA, D. NISHIJIMA, R. DOERNER, et al., "Beryllium erosion induced by transient heat loads and subsequent reactions in a deuterium plasma", J. Nucl. Mater. **420** (2012) 252-257.

4-2 Task 1-2 (1) TRITIUM PERMEATION THROUGH REDUCED ACTIVATION FERRITIC/MARTENSITIC STEEL TUBE AND ERBIUM OXIDE COATING

T. Chikada[1], M. Shimada[2], R.J. Pawelko[2], T. Terai[1], T. Muroga[3]

[1]*The University of Tokyo, 2-11-16 Yayoi, Bunkyo-ku, Tokyo 113-8656 Japan, chikada@nuclear.jp, tera@n.t.u-tokyo.ac.jp*

[2]*Idaho National Laboratory, 2525 Fremont Ave., Idaho Falls, Idaho ID 83401, USA, masashi.shimada@inl.gov, robert.pawelko@inl.gov*

[3]*National Institute for Fusion Science, 322-6 Oroshi, Toki, Gifu 502-5292, Japan, muroga@nifs.ac.jp*

Low concentration tritium permeation experiments have been performed on uncoated F82H and Er_2O_3-coated tubular samples in the framework of the Japan-US TITAN collaborative program. The tritium permeability of the uncoated sample with 1.2 ppm tritium showed one order of magnitude lower than that with 100% deuterium. The permeability of the sample with 40 ppm tritium was more than twice higher than that of 1.2 ppm, indicating a surface effect at the lower tritium concentration. The Er_2O_3-coated sample showed two orders of magnitude lower permeability than the uncoated sample, and lower permeability than that of the coated plate sample with 100% deuterium. It was found that the memory effect of ion chambers in the primary and secondary circuits was caused by tritiated water vapor that was generated by isotope exchange reactions between tritium and surface water on the coating.

I. INTRODUCTION

Understanding tritium migration behaviors in a fusion blanket is a key technology for the establishment of a fusion reactor fuel cycle. In a framework of the Tritium, Irradiation and Thermofluid for America and Nippon (TITAN) Japan-US collaborative program conducted in fiscal year 2007–2012, tritium permeation in fusion reactor materials including a tritium permeation barrier (TPB) has been investigated[1]. One of the remaining issues in tritium behaviors in the fusion materials is to clarify the permeation behavior at low partial pressure tritium for the interpolation to practical fusion blanket conditions. Regarding the TPB coatings, erbium oxide (Er_2O_3) thin films have recently shown remarkable permeation reduction factors using a physical vapor deposition method[2]. Moreover, Er_2O_3 coatings have been fabricated on plate substrates by not only spin-coating but also dip-coating process with a metal-organic decomposition (MOD) method[3,4]. However, the establishment of plant-scale fabrication of the coating, for example on a tubular substrate, is challenging. In this study, low concentration tritium permeation experiments have been carried out using reducing activation ferritic/martensitic (RAFM) steel tubular substrates and Er_2O_3 coatings fabricated by the liquid-phase method.

II. EXPERIMENTAL

II.A. Sample preparation

Electrolytically-polished RAFM steel F82H (8Cr-2W) tubes with dimensions of 150-mm length, 8-mm inner diameter, and 1.5-mm thickness were used as substrates. The MOD coating procedure is described in detail in the previous study[4]. First, the tube substrate was dipped into an Er_2O_3 coating precursor (Kojundo Chemical Laboratory Co., Ltd. Er-03®) without addition of thinner, and then withdrawn at a constant speed of 1.2 mm s^{-1} using a dip-coater. Second, the sample was placed in a dry oven set at 120 °C for 10 min to turn the solvent into a gel. Finally, the sample was heat treated in an infrared image furnace to decompose organic residues and to crystallize the Er_2O_3 coating. The heat-treatment condition was determined from the previous study[4]: at 700 °C for 10 min in hydrogen (purity: 99.9999%, O_2: < 0.02 ppm, H_2O: < 0.5 ppm) with approximately 0.6% moisture. The flow rate is less than 10 cm^3 min^{-1}, and the rate of temperature increase and decrease is 100 and 30 °C min^{-1}, respectively. Moisture was added to the hydrogen flow by passing it through ice-chilled water. The coating process was repeated three times in order to increase coating thickness and reduce unevenness of the coating. The thickness of the coating was estimated as 0.3 μm on both inner and outer surfaces of the sample by the previous result[3]. Both ends of uncoated and coated samples were welded to prepare sample assemblies for the installation in a tritium permeation system which is describe in the next section.

II.B. Permeation setup

A conceptual diagram of the tritium permeation system is described in Fig. 1. The sample assembly was mounted in a quartz tube. Sample heating was conducted using an induction heater with a 1-turn, 5 inch diameter coil made of copper. Tritium-helium mixture gas was introduced in a circuit (primary circuit) and flew through the tubular sample at a rate of 1000 sccm (standard cm^3 min^{-1}) using a mass flow controller. Tritium that permeated outward through the sample was purged by a pure helium flow of 1000 sccm in another circuit (secondary circuit). The tritium concentrations in the primary and secondary circuits were examined with 10 and 1000 cm^3 ion chambers, respectively. After passing

through the ion chambers, the circulating gas in both circuits was partly discharged at a rate of 15 sccm from the primary circuit and 100 sccm from the secondary circuit, to a tritium recovery system placed in a ventilation hood.

The procedure of a gas-driven tritium permeation measurement is described as follows. After setting a test temperature using the induction heater, the system was conditioned for 2 h until the signals of ion chambers became stable. Then the pure helium flow in the primary circuit was switched to the tritium-helium mixture. The tritium concentration in the mixture gas cylinders was originally prepared as 3 and 65 ppm; however, it was actually measured as 1.2 and 40 ppm using ion chambers before and after a series of experiments. It took approximately 2 h to reach the steady state tritium concentration after introducing the tritium-helium mixture. The length of the work day limited the duration of the permeation experiments to less than 6 h.

One of the important issues in the evaluation of tritium permeation through tubular samples is how to determine a temperature distribution. The induction heating power was controlled by a thermocouple inserted in the center of the sample with its head touching the inner wall. In this study, an infrared camera and a pyrometer were used to measure the temperature profile of the sample surface. The infrared camera could automatically store the temperature data only at more than 600 °C in two-dimensional display. On the other hand, the uncoated sample was measured by the pyrometer because lower test temperatures were required to avoid surface oxidation. The temperature profile at the permeation section was manually measured with vertically moving the position. The temperature distribution was calculated by Gaussian fitting to the surface temperature data.

The permeation phenomenon of hydrogen isotopes from the primary circuit which contains a known concentration to the secondary circuit with a negligible small concentration are represented by following equation[5]:

$$J = P\frac{p^{0.5}}{d}, \qquad (1)$$

where J is the permeation flux, P is named permeability which is intrinsic parameter for the sample, p is the partial pressure of the hydrogen isotope introduced into the primary circuit, and d is the thickness of the sample. The pressure exponent represents permeation regime: the value of 0.5 indicates the rate-limiting process is diffusion of hydrogen isotope atoms, and the value of more than 0.5 means a contribution of molecular reactions such as surface effects. For a simple comparison with past results of deuterium permeation, Eq. (1) was applied for the calculation of tritium permeability in this study.

III.RESULTS AND DISCUSSION

III.A. Uncoated sample

Figure 2 is a representative example of the tritium permeation experiments and illustrates temporal changes

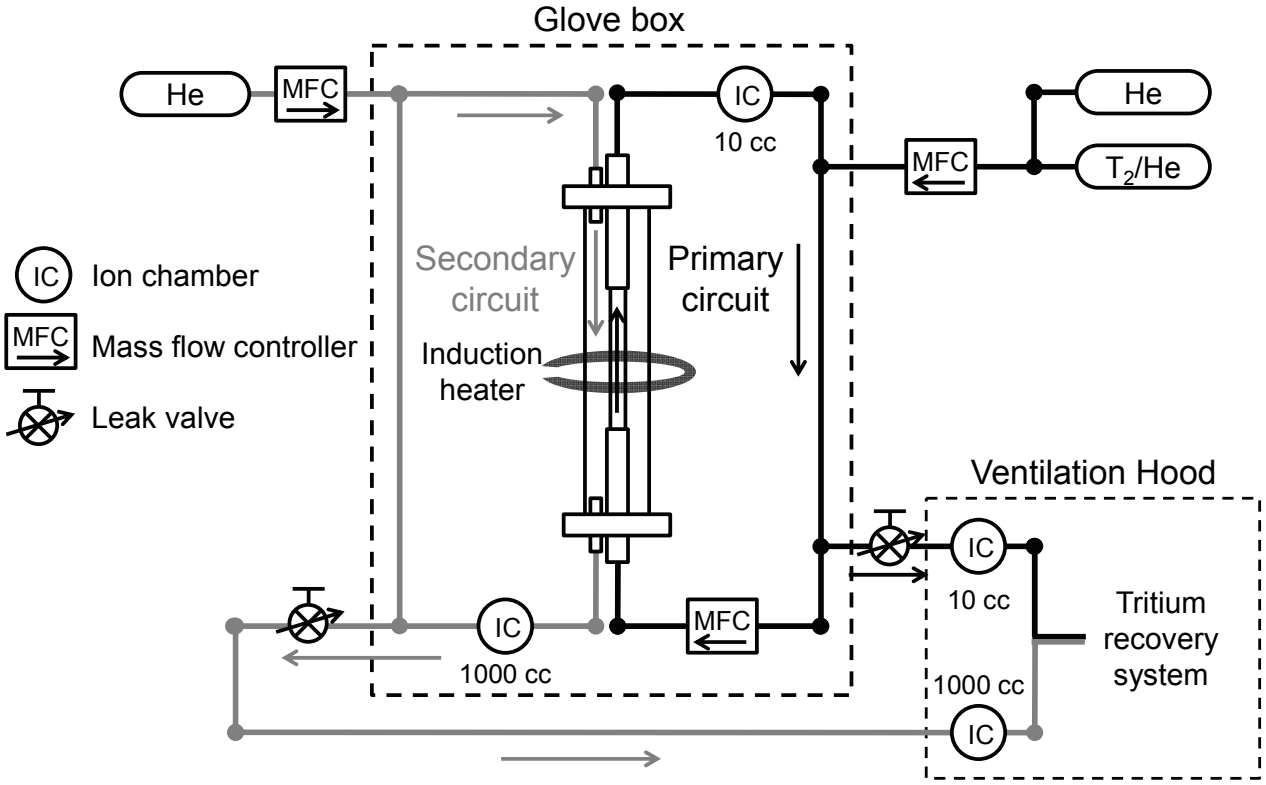

Fig. 1. Schematic view of the tritium permeation system.

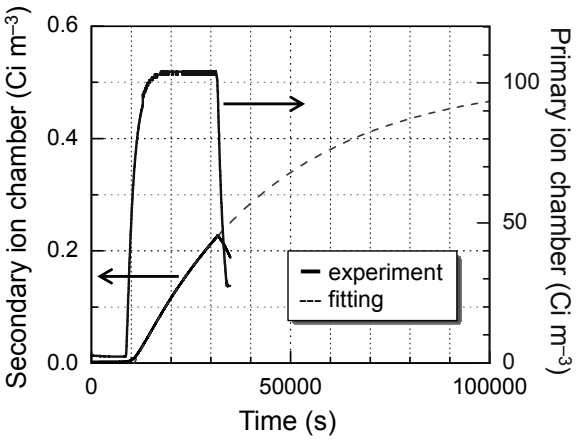

Fig. 2. Temporal changes and a fitting curve of ion chamber outputs at primary and secondary circuits on the permeation measurement of the uncoated F82H sample with 1.2 ppm tritium. The setting temperature was 400 °C, and the average temperature in the test section was 378 °C.

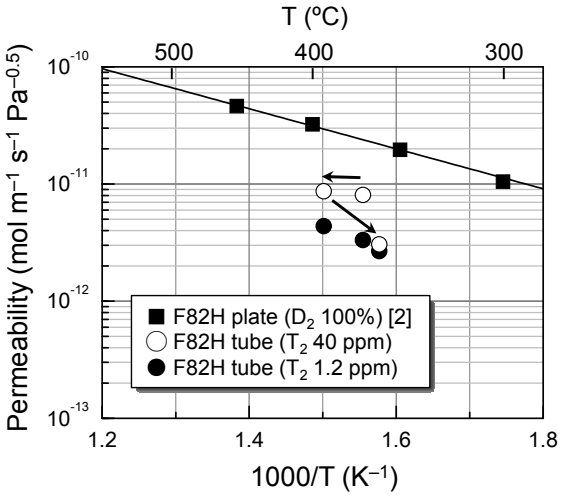

Fig. 3. Arrhenius plots of tritium permeability of the uncoated F82H samples. Deuterium permeability of the F82H plate sample is also presented[2].

to the ion chamber concentrations with 40 ppm tritium in the primary and a temperature setting of 400 °C. Although the signal at the primary circuit reached steady state, the tritium concentration in the secondary circuit continuously increased. Since the permeation flux that finally achieves equilibrium with the rate of discharge can be expressed by an exponential function, the tritium permeation flux at the steady state was determined by fitting the secondary permeation flux.

Temperature dependence of tritium permeability is shown in Fig. 3. The uncoated sample tested with 1.2 ppm tritium at the setting temperature of 380–420 °C (average temperature: 361–393 °C) showed one order of magnitude lower permeability than that of the reference data with 100% deuterium[2]. In addition, the permeation measurements with 40 ppm tritium were more than twice larger than that with 1.2 ppm tritium. However, after the measurements at 400 and 420 °C with 40 ppm tritium, the permeability at 380 °C decreased to the level similar to the result with 1.2 ppm tritium probably due to the oxidation of the sample. A permeability comparable to the reference is supposed with higher tritium concentration, indicating a surface effect on the permeation at the low tritium concentration. The tritium permeability similar to the reference is expected with higher concentrations.

III.B. Coated sample

The tritium permeation experiments on the Er_2O_3-coated sample were performed at the setting temperature of 400–750 °C. However, no permeation signal was detected in a test duration at 600 °C or less because of a small permeation flux and a long diffusion time. Fig. 4 shows temporal changes of the ion chamber outputs in the glove box and ventilation hood during the measurement with 1.2 ppm tritium at the setting temperature of 750 °C. The signals of both ion chambers in the glove box continuously increased at accelerated rates during the measurement, which is not probable especially in the primary circuit. This phenomenon had reproducibility in the measurements at 650 and 700 °C. It is reported that the memory effect is mainly caused by the tritium transfer to surface water on an electrode wall in the ion chamber via adsorption and isotope exchange reactions[6]. Since the phenomenon did not appear in the measurements on the uncoated sample, the surface water existed on the Er_2O_3 coating in this case. Therefore, the process of the memory effect can be explained as follows: tritium adsorbed or permeated through the coated sample, reacted and desorbed as tritiated water vapor, and adsorbed to the electrodes of the ion chambers in both circuits. When the fraction of desorption species (HTO, HT and T_2) at the coating on the primary and secondary circuit sides is presumed same, the permeability can be estimated using the outputs of the ion chambers in the ventilation hood, where HT and T_2 are mainly detected. The tritium permeability of the uncoated and coated sampled with reference data of deuterium permeability with plate samples are shown in Fig. 5[2],[4]. The coated tubular sample showed two orders of magnitude lower permeability than that of the uncoated one. Compared with the result of the coated plate sample tested with 100% deuterium, the permeability of the coated tubular sample tested with 1.2 ppm tritium also reduced to one-third or one-fourth, which is accorded with the trend in the results of the uncoated samples. Because several scratches were observed on the outer side of the coating after the welding process to prepare the sample assembly,

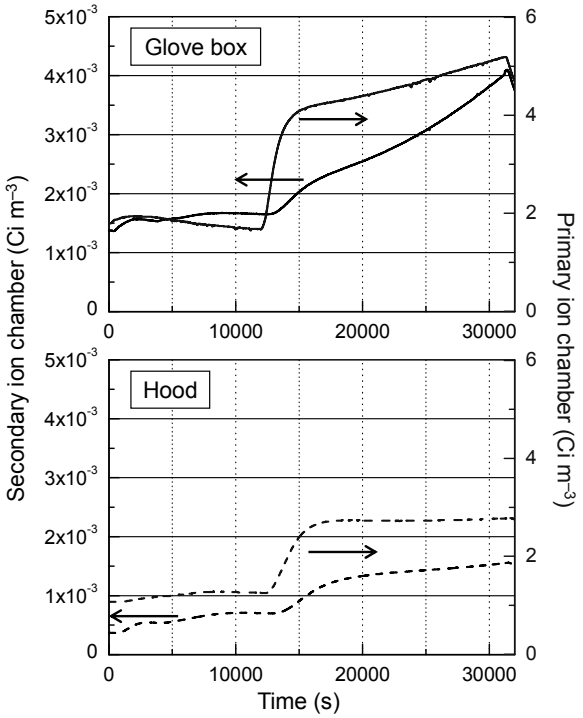

Fig. 4. Temporal changes of ion chamber outputs at primary and secondary circuits at the glove box and ventilation hood on the permeation measurement of the Er_2O_3-coated F82H sample tested with 1.2 ppm tritium. The setting temperature was 750 °C, and the average temperature in the test section was 720 °C.

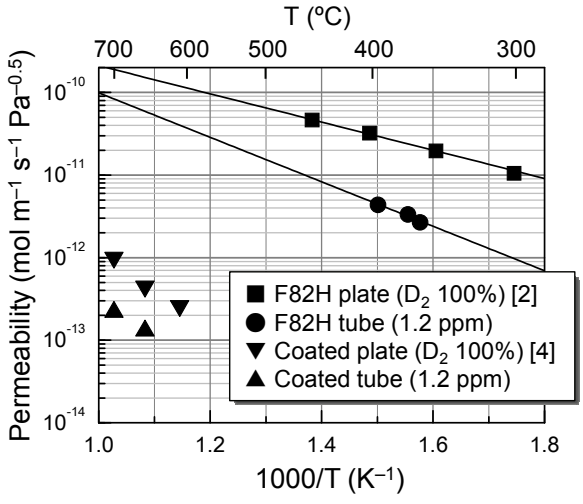

Fig. 5. Arrhenius plots of tritium permeability of the uncoated and Er_2O_3-coated F82H tubular samples. Deuterium permeabilities of the uncoated and coated plate samples are also presented[2],[4].

the inner coating mainly contributed to the permeation reduction. Therefore, it is proved that the inner coating with a good uniformity and surface coverage has been achieved by the dip-coating process. In addition, the tritium permeability of the coating under the practical condition in a fusion reactor will be smaller than expected from the permeation data with high partial pressure hydrogen isotopes due to the contribution of the surface effect.

IV.SUMMARY

Gas-driven permeation experiments with low concentration tritium have been performed on uncoated and Er_2O_3 coated F82H tubular samples. The uncoated sample tested with 1.2 ppm tritium showed one order of magnitude lower permeability than that of a plate sample with 100% deuterium. The permeability of the sample with 40 ppm was more than twice higher than that of 1.2 ppm, indicating a surface effect at the low tritium concentration. The Er_2O_3-coated sample with 1.2 ppm tritium showed two orders of magnitude lower permeability than the uncoated sample, and less permeability than that of the coated plate sample with 100% deuterium. It was found that the memory effect of ion chambers in both circuits was caused by tritiated water vapor which was generated by isotope reactions between tritium and surface water on the coating. An Er_2O_3 coating on the tubular sample with a good uniformity and surface coverage has been achieved by the dip-coating process.

ACKNOWLEDGMENTS

This work was conducted in the framework of the Japan-US TITAN collaborative program. The authors appreciate collaborators in Idaho National Laboratory for their supports on tritium permeation experiments.

REFERENCES

[1] T. MUROGA, D.K. SZE, and K. OKUNO, "Overview of the TITAN project," *Fusion Eng. Des.,* **87**, 613 (2012).

[2] T. CHIKADA, A. SUZUKI, C. ADELHELM et al., "Surface behaviour in deuterium permeation through erbium oxide coatings," *Nucl. Fusion* **51** 063023 (2011).

[3] T CHIKADA, A. SUZUKI, T. TANAKA et al., "Microstructure control and deuterium permeability of erbium oxide coating on ferritic/martensitic steels by metal-organic decomposition," *Fusion Eng Des.* **85** (2010) 1537–1541.

[4] T. CHIKADA, S. NAITOH, A. SUZUKI et al., "Deuterium permeation through erbium oxide coatings on RAFM steels by a dip-coating technique," *J. Nucl. Mater.*, **442**, 533 (2013).
[5] K.S. FORCEY, D.K. ROSS, J.C.B. SIMPSON, "Hydrogen transport and solubility in 316L and 1.49419 steels for fusion reactor applications," *J. Nucl. Mater.*, **160**, 117 (1988).
[6] M. NISHIKAWA, T. TAKEISHI, Y. YASUMOTO et al., "Ionization chamber system to eliminate the memory effect of tritium," *Nucl. Instr. Meth. Phys. Res.* **A278**, 525 (1989).

Task 1-2(2) Clarification of behavior of tritium release from liquid Li-Pb blanket and tritium recovery

Satoshi Fukada, Yuki Edao, Hiroaki Okitsu, Makoto Okada, Kenichi Katekari, Hidetaka Noguchi
Kyushu University, Hakozaki, Higashi-ku, Fukuoka 812-581, Japan, sfukada@nucl.kyushu-u.ac.jp

1. Introduction

$Li_{16}Pb_{84}$ eutectic alloy is a promising liquid blanket material as a tritium breeder of a fusion reactor. The breeding material is applied to the test blanket module of ITER as EU-HCLL or US-DCLL concept. Although the solubility and diffusivity of tritium in the Li-Pb alloy are important properties for the design of the fusion reactor blanket, there are some scatterings in previous data, and correct values have not been determined. In addition, the isotope effectsare not presented. In the present study, the solubility and diffusivity of H and D in $Li_{17}Pb_{83}$ are determined by using a permeation method. This research is performed under a cooperative study with Japan Atomic Energy Agency as a part of the Broader Approach R&D activities for tritium technologies to a demonstration reactor.

2. Experimental

The solubility and diffusivity of hydrogen isotopes in $Li_{17}Pb_{83}$ eutectic alloy were determined by the permeation method as shown in Fig. 1. A $Li_{17}Pb_{83}$layer is put on an □-Fe plate with 1mm in thickness in a 304 stainless-steel enclosure. The thickness of the $Li_{17}Pb_{83}$ layer is 1 cm. The full system is heated by an electric heater and controlled to a constant temperature. The bottom is supplied with a gas mixture of Ar+H_2, Ar+D_2 or H_2+D_2, which is purified with SAES getter or molecular sieve 5A adsorbent. H_2, HDand D_2 permeated in the upper part are purged by Ar. Their concentrationsare detected by gas chromatography and a quadrupole mass spectrometer.

3. Results and Discussion

Fig. 2 shows an example of H_2 build-up curve from the Li-Pb or □-Fe system. When the cell of□-Fe plate without the Li-Pb layer is supplied with H_2, the permeation rate is very fast, and its time response is quick. The overall permeation behavior is well simulated by the diffusivity and solubility of H in □-Fe, which was previously reported by A. Tahara*et al*. (Trans. Jap. Inst. Met. 26 (1985) 869). When Li-Pballoy is put on the □-Fe plate, the permeation rate drops toaround one-hundredth of the □-Fe case. Since the permeation rate is in reversal proportion to the thickness of the Li-Pb layer, the diffusion-limiting permeation is assured.

Fig. 3 shows an example of the dimensionless hydrogen concentration calculated for the system of the LiPb+□-Fe+sus304 permeation cell. Although the H atom concentration slightly decreases in the sus304 and □-Fe, the effect is very small. The one-dimensional permeation through the Li-Pb layer appears.The values of diffusivity, solubility and also permeability are determined from fitting the calculation to the experiment.

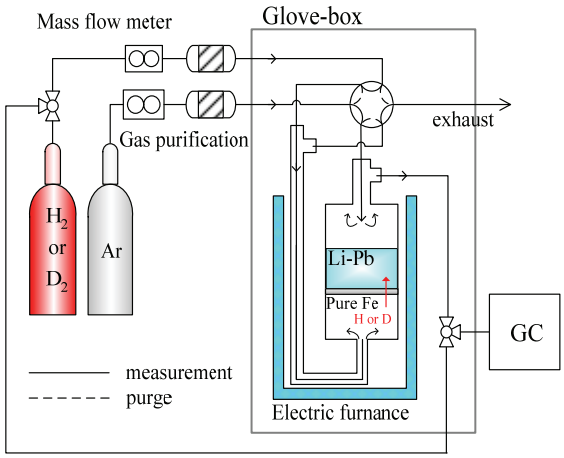

Fig. 1 Experimental apparatus of H or D permeation

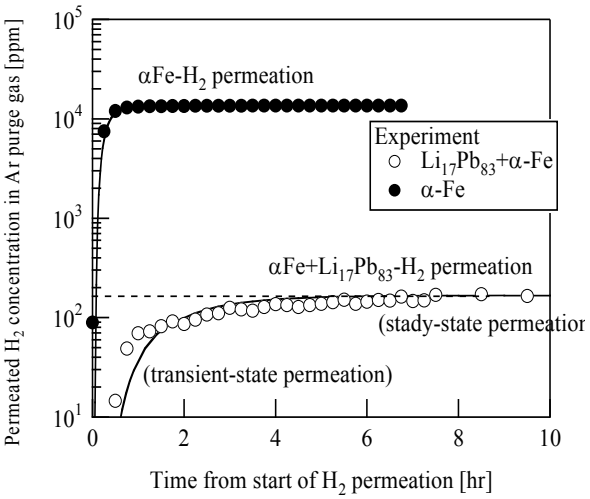

Fig. 2 H_2 build-up curve from Li-Pb permeation cell

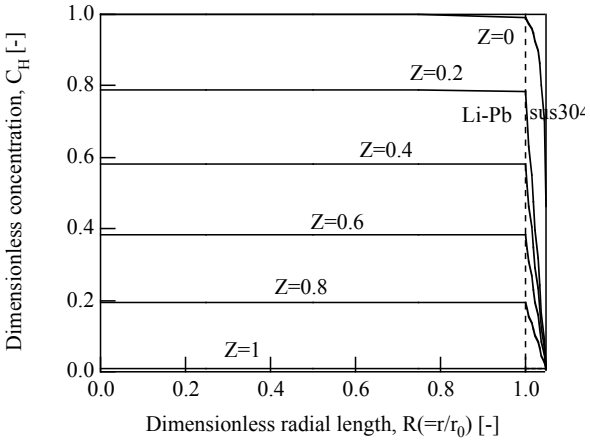

Fig. 3H concentration profile in Li-Pb and sus304

Fig. 4 shows typical H and D permeation curves when a H_2+D_2 mixture is supplied. Close agreement is obtained between experiment and calculation. The permeability is equal to a product of diffusivity and solubility, and therefore the effect of bubble formation at interface between solid □-Fe or sus304 and liquid Li-Pb is negligibly small.

Fig. 5 shows the results of simultaneous H and D permeation through Li-Pb. The steady-state permeabilitiesof H and D are plotted as a function of D/(H+D) atom fraction in the upstream gas. As seen in the figure, the H or D permeability is independent of the D/(H+D) atom fraction regardless of the presence of other components. The isotope effect of the permeability between H and D is around 0.7, which is equal to the mass ratio of H and D. Thus classical isotope effect is observed in the permeabilityof H and D through Li-Pb. This can lead to estimate the diffusivity and solubility of tritium in Li-Pb. Its value will be determined experimentally under this cooperative study of BA R&D program. Fig. 6 shows isotopic equilibrium constant of H_2+D_2=2HD at the downstream side. The experimental value is almost consistent with the isotopic equilibrium constant predicted by Urey.

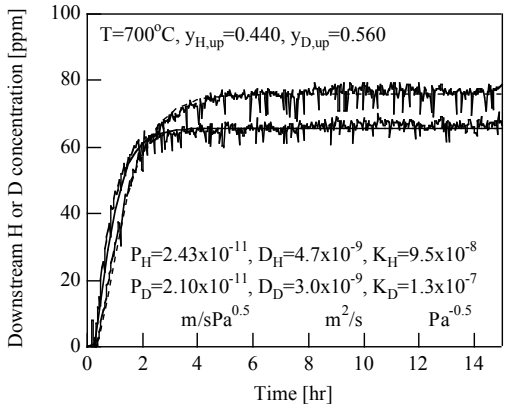

Fig. 4 Experiment (solid line) and calculation (broken line) of H and D permeation curves

4. Conclusions

(1) Permeability, diffusivity and solubility of H and D in $Li_{17}Pb_{83}$ alloy are determined.
(2) When H and D mixtures are present simultaneously, their permeabilities are correlated by the ideal solution model, and the solubility and diffusivity are determined in a similar way to the single component of H_2 or D_2.
(3) Isotope effects of solubility and diffusivity can be correlated by a harmonic oscillation model and vibration energies in solution site and transient site.
(4) The energy determined here is consistent with 1st principle numerical simulation for H behavior in $Li_{17}Pb_{83}$ eutectic alloy.
(5) Li activity and H energy in trap site for solubility in arbitral composition of Li+Pb alloys are correlated by the linear addition rule of Li and Pb atoms.

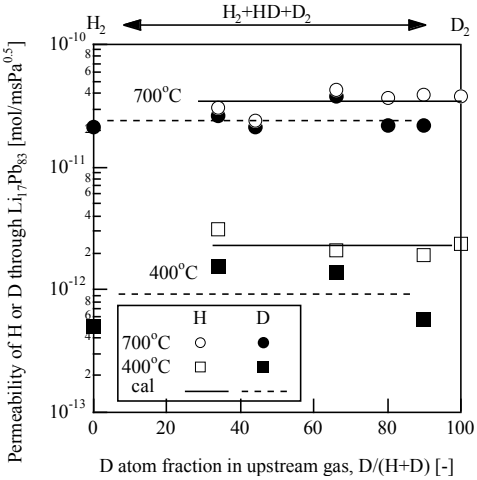

Fig. 5 H and D permeability through Li-Pb alloy as function of D/(H+D) ratio

Publication

1.Y. Edao, S. Fukada, S. Yamaguchi, H. Nakamura, "Tritium removal by Y hot trap for Li purification of IFMIF target", Fusion Engineering and Design, 85 (2010) 53-57.
2.Y. Edao, H. Noguchi, H. Okitsu, S. Fukada, "Permeation behavior of two-component hydrogen isotopes in lithium-lead eutectic alloy"Presented in International Conference on Tritium Science and Technology, Nara, (2010).
3.Y. Edao, H. Noguchi, S. Fukada, "Experiment of hydrogen isotopes permeating through Li-Pb with diffusion, dissolution and isotopic exchange", Proc. ICFRM-14, Sapporo, (2009) Sept. 7-11.
4.S. Fukada, Y. Edao, "Unresolved issues on tritium mass transfer in Li-Pb liquid blankets", Proc. ICFRM-14, (2009) Sept. 7-11.
5.D. Masuyama, T. Oda, S. Fukada, "Chemical state and diffusion behavior of hydrogen isotopes in liquid lithium-lead", Chemical Physics Letters, 483 (2009) 214-218.
6. Y. Edao, S. Fukada, H. Noguchi, Y. Maeda, K. Katayama, "Isotope effects of hydrogen isotope absorption and diffusion in $Li_{0.17}Pb_{0.83}$ eutectic alloy", Fusion Science and Technology, 56 (2009) 831-835.
7. S. Fukada, Y. Edao, A. Sagara, "Effects of simultaneous transfer of heat and tritium through Li-Pb or Flibe blanket", Fusion Engineering and Design, (2010) in printing.
8. Y. Edao, H. Noguchi, S. Fukada, "Isotopic exchange rate between hydrogen and deuterium in the process of permeating through $Li_{0.17}Pb_{0.83}$", Fusion Engineering and Design, (2010) in printing.

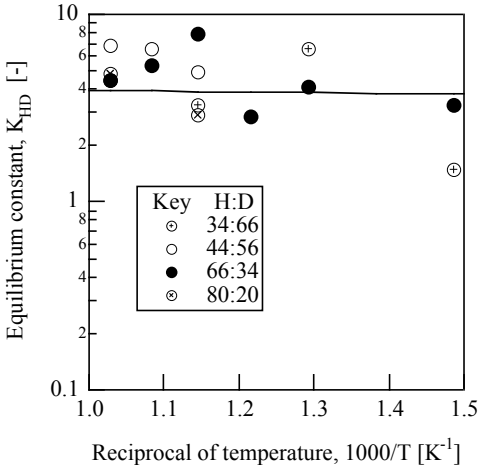

Fig. 6 H_2-HD-D_2 isotopic equilibrium in downstream side of permeation

Task 1-2(3) Measurement of solubility of hydrogen isotopes in Li-Pb by adsorption and desorption method

Y. Edao[1,2], K. Katayama[1], S. Fukada[1], T. Terai[3], S. Konishi[4], M. Shimada[5], B. Merrill[5], P. Calderoni[5], B. Denny[5], R. Pawelko[5]

[1]Kyushu University, 6-1 Kasuga-koen, Kasuga, Fukuoka 816-8580, Japan,
edao.yuki@jaea.go.jp, kadzu@nucl.kyushu-u.ac.jp, sfukada@nucl.kyushu-u.ac.jp
[2]Japan Atomic Energy Agency, 2-4 Shirane-shirakata, Tokai, Ibaraki 319-1195, Japan
[3]The University of Tokyo, Tokyo 113-8656, Japan
[4]Kyoto University, Kyoto 611-0011, Japan
[5]Idaho National Laboratory, Idaho Falls, Idaho, USA

Measurement of tritium solubility in lithium lead eutectic alloy (Li-Pb) has been performed under the Japan-US collaboration work of"TITAN".The present paper reports that results of H and D solubility in Li-Pb which melted in an alumina tube determined by means of a constant volume method, and also reports an experimental apparatus for measurement of tritium solubility in Li-Pbin a tungsten crucible is improved and examined in the STAR facility of the Idaho National Laboratory.It was shown that H solubility in Li-Pb was easily influenced by impurities, interaction withsurrounding materials and evaporated Li-Pb. The influences were suggested to be caused by large scattering among the previously reported data on solubility of hydrogen isotopes in Li-Pb.

I. INTRODUCTION

Liquidlithium lead eutectic alloy (Li-Pb) is one of the most promising candidates for advanced tritium breeding materials. It is important to understand tritium transfer behavior in liquid Li-Pb in order to construct a system of tritium recovery from liquid Li-Pb blanket in a fusion reactor. Some data on mass transfer properties of tritium in Li-Pb are reported such as permeability, diffusivity and solubility of hydrogen isotopes [1-12].

However, there is a large scattering among the previously reported solubility of hydrogen (H) and deuterium(D) in Li-Pb. Especially, there is no reliable data for tritium (T). The previous data on H or D solubility were determined using a constant volume method [1-6] or a permeation method [9-12].In measurement of solubility of hydrogen isotopes, Li-Pb was melted in various crucibles such as iron, quartz glass, stainless steel and so on.The interaction between Li-Pb and surrounding materials should be discussed to clarify a cause of the scattering and to determinesolubility of hydrogen isotopes precisely.

Therefore, in order toobtaintritium solubility in Li-Pb, an experimental apparatus was improved and examined in the STAR facility of the Idaho National Laboratory under the Japan-US TITANcollaboration work. Solubility of hydrogen isotopes in Li-Pbwhich melted in an alumina tube or a W crucible was measured by means of a constant volume method.

II. EXPERIMENTAL

II.A. Preparation of Li-Pb

Hydrogen desorption test in Li-Pb (Li:Pb = 15:85 at.%) was carried out. The Li-Pb pieces prepared previously were added into alumina tube in air. The total weight of Li-Pbin the alumina tube was 131.37 g. The liquid volume was 13.85 cc at 300 ^{o}C, and the tube was filled with liquid which height of 38mm from the bottom. The alumina tube was installed in the solubility measurement system and it heated up to 150 ^{o}C with evacuating for baking. After leak checking from the alumina tube, Li-Pb was melted by heating alumina tube slowly up to 350 ^{o}C with evacuating.

II.B. Experimental setup of solubility of hydrogen isotopes measurement system

A schematic diagram of the experimental setup is shown in Fig. 1. The test section of the alumina tube was heated by a ceramic heater, and thermal insulations were put around the heater. Temperature of a bottom thermocouple (TC4) was differed from side TCs(TC1, 2, 3), and temperature shown by TC4 was much lower than the others. When the temperature of Li-Pb was measured during cooling down after heating up to 400 ^{o}C, the eutectic temperature was confirmed.The temperature of Li-Pb was controlled by TC3 because it was shown the closest to eutectic temperature among the TCs. A line to a quadrupole mass spectrometer (QMS) was installed in order to investigate impurities leaking from air or in Li-Pb in the system. We conducted leakage checking in Vol 1+Vol 2+Vol 3 where charging helium (He) at 1.33×10^{5}Pa by a He leak tester, and confirmed no leakage. After that, air or carbon compounds peaks (Mass No.28, 32, 40, 44) were increased in QMS measurement when the TMP gate valve closed though they were a very small amount and there was no peak with evacuating by Turbo molecular pump (TMP). It was considered the impurities were included in Li-Pb and they were

released from the space of lead lithium. H_2 was charged into Li-Pb at 625 Pa in order to remove the impurities. Leakage of He gas through the alumina tube, flange, joints and valves were checked by a leak tester after Vol 1+Vol 2 was filled with high pressure He gas at 1.33×10^5 Pa. The alumina tube with a heater was covered with a plastic bag, where He leakage was checked. There was no leak through the alumina tube. Consequently, it was concluded that the impurities peaks were not leaked from Air to the experimental system but released from Li-Pb or other parts. We could treat the pressure increase in the system as background.

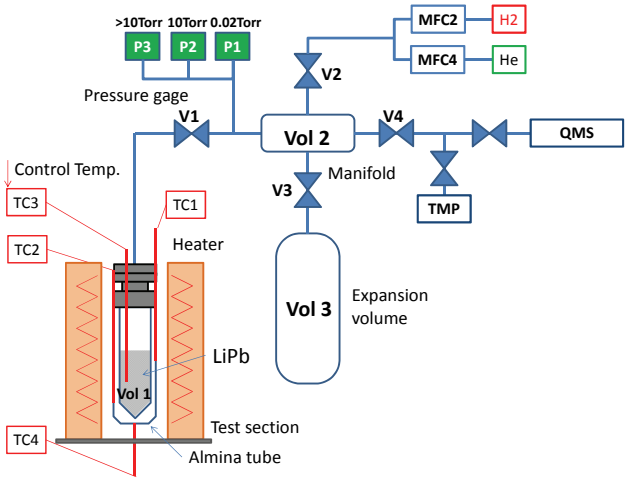

Fig. 1 Aschamatic diagram of the experimental setup of H solubility measurement

II.C. Measurement of H and D solubility in Li-Pb

An amount of hydrogen adsorbed or absorbed in Li-Pb was measured by two techniques of absorption and desorption. Adsorption and desorption test were performed at the temperature of 300, 350, 400 °C and under the pressure of 1330 Pa. Low temperature and low pressure charging of hydrogen was effective.

III. Results and discussion

Fig. 2 shows the results of adsorption at 300 °C. In adsorption tests, the amount of H adsorbed and absorbed in Li-Pb is decided from difference between an initial pressure and an equilibrium pressure after H_2 charging. The initial pressure means an expanded pressure in vol 1+vol 2 for 30 sec after V1 opened. In desorption tests, the amount of H_2 release is measured by opening V1 at intervals of 5 min. It confirmed that no impurity peaks were detected in desorption tests by QMS measurement, and H_2 release rates were measured simultaneously by pressure gauge and QMS measurement.

Fig. 3 shows the comparisons of hydrogen release rate from Li-Pb with that from the blank tube. The release rate from Li-Pb is larger than that from the tube. It is estimated that the amount of H_2 release from the tube is approximately 3% in that from Li-Pb for 200min.

The comparisons of H solubility among reported values from referencesare shown in Fig. 4. The solubility obtained by adsorption tests is larger than that of desorption tests in the same experimental conditions because desorption period is not long enough. In the adsorption measurement process, it is required more measurement time to reach to steady state of H_2 release. The solubility in this work is larger than that in a previous work of TITAN09. Three reasons were considered as the differences. First, the estimated solubility is not taken into consideration background of H_2 release from the alumina tube. Hydrogen is trapped in Kovar part of the alumina tube. Second, experimental conditions of heating and insulating are different. Third, operations of Li-Pb filling with a vessel were differed between a direct poured method (TITAN09) and a particle packing one (TITAN11). There is a possibility that some impurities, spaces or bubbles are present in Li-Pb where a large amount of hydrogen is trapped.

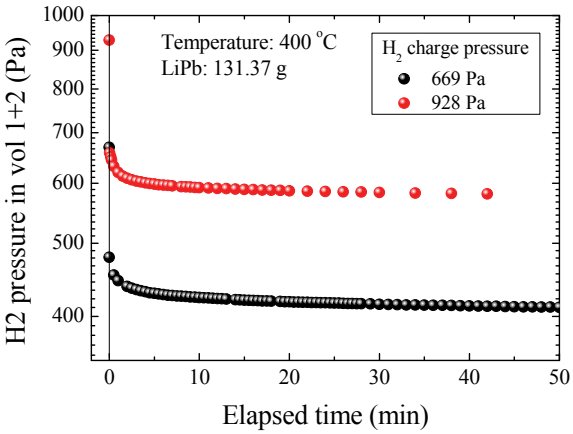

Fig. 2Result of adsorption test at 300°C

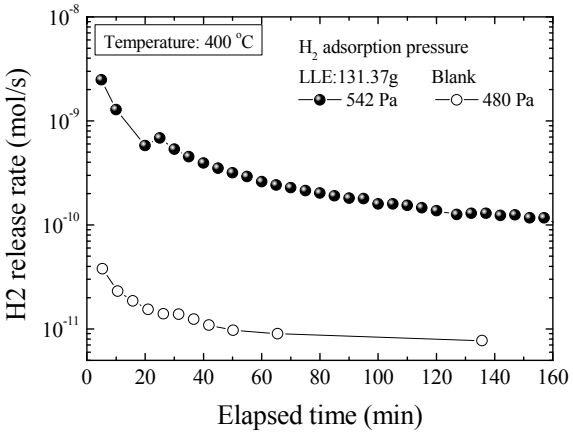

Fig. 3 H_2 release rates at 400°C

IV. Preliminary test for tritium solubility measurement of liquid Li-Pb

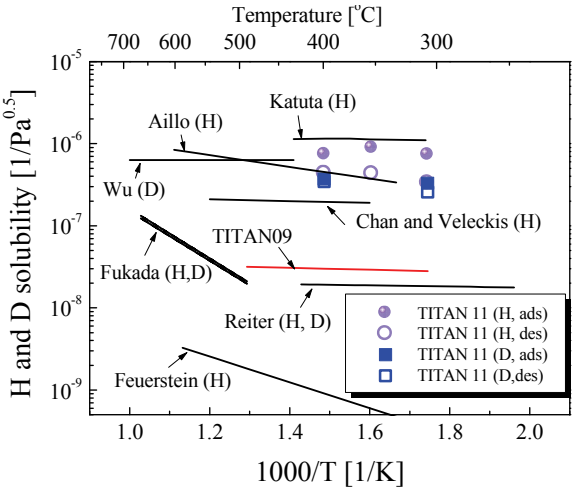

Fig. 4Solubility of H and D in Li-Pb

Preliminary experiment was conducted using by an experimental apparatus for measurement of T solubility in Li-Pb.

IV.A. Experimental setup for T solubility measurement

Fig.5 shows a schematic view of an experimental apparatus of tritium solubility measurement. Li-Pb is housed in a tungsten (W) crucible inside a quartz vessel and heated by induction coils. W crucible, which had a good compatibility with Li-Pb and low H solubility, was selected as a container of Li-Pb filling.A sealed part of the quartz vessel is cooling by a cold gun blowing N_2 in order to avoid heating up the seal material. The W crucible is heated by an induction heater.Allthe valve operations, temperature, pressure and gas flow rates are controlled by the Labview on PC put on externally.

The T solubility measurement system has three volumes of vol1, vol2 and vol3. The volumes in the measurementsystem were calibrated using by a calibrated volume.

Leak rates in the volumes of vol1, vol2 and vol3 were measured at room temperature of 22°C on average. Pressure increase in vol1+vol2 and vol1+vol2+vol3 for 5 min was measured with closing each valve. The leak rates confirmed to be small at room temperature.

Heating tests of a W crucible were conducted by an induction heater. Temperature of the W crucible is controlled by output power of the induction heater. Thermocouples are placed in a side wall of the W crucible, bottom of the quartz vessel, outside of vol2 and the seal part surrounding an O-ring. In addition, temperature of the W crucible is also measured by a pyrometer (Ircon infrared thermometer) which temperature range is 350-700°C. The pyrometer was calibrated by the thermocouple which contacted with the W crucible. Temperature of the W crucible indicated by the thermocouple agrees well with that by the pyrometer in the temperature range of 400-600°C. Temperature distribution in the W crucible was also observed.

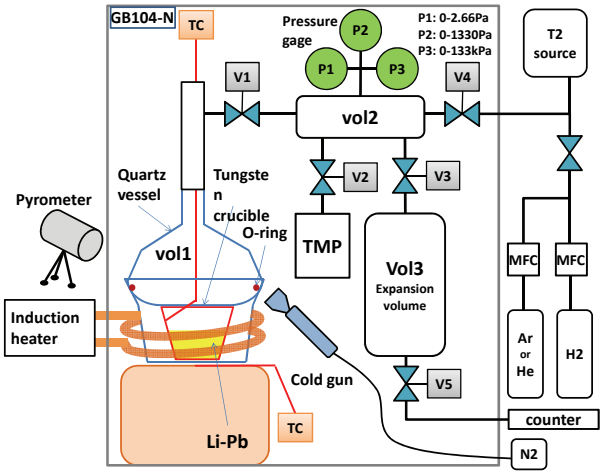

Fig. 5A schematic view of the experimental apparatus of T solubility.

IV.B. Blank test

H_2 adsorption and desorption tests of the W crucible without Li-Pbwere performed in the experimental apparatus at the temperature of 500°C and the H_2 charging pressure of 10-100Pa. Results of H_2 desorption test are shown in Fig.6.Regarding adsorption tests, pressure in vol1+vol2 became steady state within 15 min after charging 100PaH_2 to vol1 while pressure was not changed after charging 10Pa H_2 to vol1. Regarding desorption tests, H_2 released rate decreased slowly. It is considered that H_2 adsorbed in the walls of the W crucible and the quartz vessel was released. Therefore, the H_2 release rate has to be considered as background.

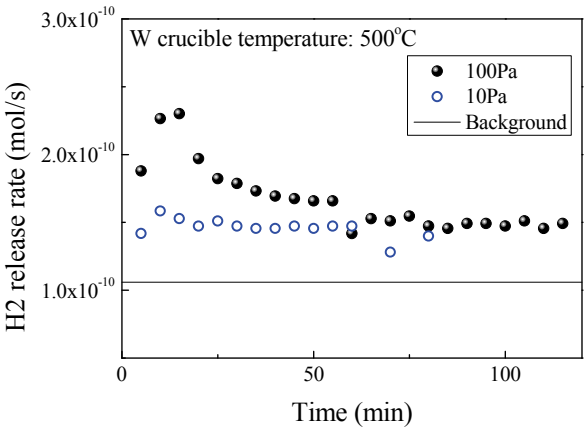

Fig. 6 Results of H_2desorption test without Li-Pb.

IV.C. Preliminary tests of H adsorption and desorption in Li-Pb

Li-Pb was prepared as Li:Pb=15:85 in a melting

pot in a glove box of He atmosphere. Li-Pb of 68g was put in the W crucible in a tritium-handling glove box (GB104-N). The W crucible with Li-Pb housed in aquartz vessel was evacuated to remove air. After the pressure in vol1+vol2+vol3 decrease lower than 0.001 Pa at room temperature and a leak rate is 4×10^{-5} Pa/s, the W crucible with Li-Pb was heated up to 150°Cslowly for baking. Li-Pbwas meltedat 250°C overnight after confirmed that pressure in the quartz vessel was lower than 0.001Pa. Since the Li-Pb was melted, it was heated up to 500°C. Although the quartz vessel was clear before heating up the Li-Pb, the vessel turned black gradually as seen in Fig.7. This is because Li or Li-Pb vaporized and covered inside the vessel, and they reacted with a very small amount of impurities such as nitrogen, oxygen or water at high temperature. A leak rate in vol1+vol2+vol3 at 500°C is 2.9×10^{-4} Pa/s after evacuating overnight at 500°C.The leak rate was small judging from the leak rate at room temperature and at 500°C.

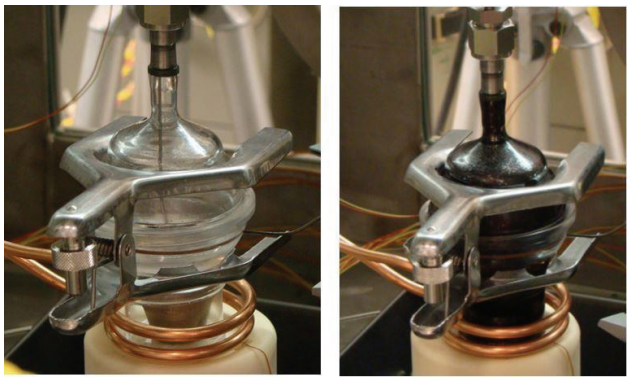

Fig. 7Observation of a quartz vessel which enclose W crucible with Li-Pb before heating (left) and after heating (right).

Preliminary tests were carried out in the conditions of H_2 charging pressure of 100Pa and 300Pa and the temperature of 500°C.

At first, H_2 adsorption experiment was conducted. V1 was opened after charging H_2 in vol2, and pressure decrease with H absorption into Li-Pb in vol1+vol2 was measured. The amount of H dissolution in Li-Pb was calculated from difference between H_2 pressure after V1 opening and equilibrium pressure.

After H_2 adsorption,H desorption rate was measured. H_2 release rates from Li-Pb were measured as rates of pressure change in vol1+vol2 for 5minafter evacuating H_2 gas in vol1 instantly. Fig. 8 shows time variations of H_2 release rate from Li-Pb. The H release rate from Li-Pb was higher than that from background.

H solubility in Li-Pbwas calculated roughly in this experiment. The solubility was 10 times larger than values obtained from other experiments using by the alumina tube. This is considered the amount of H absorption increases because H_2 release from the Li-Pb evaporated which covers with a quartz vessel. Since the evaporated Li-Pb was suspected to be caused by scattering among reported values, the amount of adsorption in evaporated Li-Pb was necessary to be estimated to obtain solubility of tritium precisely.

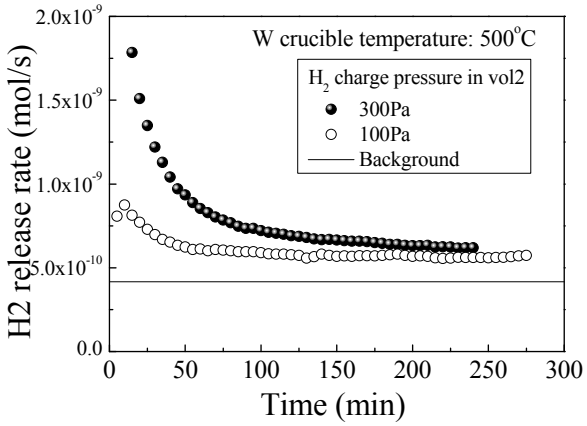

Fig. 8 H desorption from Li-Pb.

V. Conclusions

H and Dsolubility in Li-Pb were measured by two kinds of techniques of absorption and desorption at the temperature of 300, 350, 400 °C and under the pressure of 1330 Pa.Solubility of hydrogen isotopes was changed by difference of Li-Pb filling methods. A black material in a quartz vessel enclosed W crucible with Li-Pb was observed by heating up to 500 °C. The black one was supposed asevaporated Li-Pb. H_2 adsorption in or desorption from the evaporated Li-Pbwas suggested to be caused by scattering among the previouslyreported data.

ACKNOWLEDGMENTS

Authors are grateful for the support to all the membersin the Japan-US collaboration work of TITAN task 1-2.

REFERENCES

[1] F. Reiter,"Solubility and diffusivity of hydrogen isotopesin liquid Pb-17Li,"*Fus. Eng. Des*.,**14**, 207, (1991).

[2] Y. C. Chan and E. Veleckis.,"A thermodynamic investigation of dilute solutions of hydrogen in liquid Li-Pb alloys,"*J. Nucl. Mater*.,**122-123**, 935, (1984).

[3] H. Katsuta, H. Iwamoto and H Ohno,"Hydrogen solubility in liquid $Li_{17}Pb_{83}$,"*J. Nucl. Mater*.,**133-134**,167, (1985).

[4] C.H.Wu,"The solubility of deuterium in lithium-lead alloys," *J. Nucl. Mater.*,**114**, 30, (1983).

[5] H. Feuerstein, H. Gr bner, S. Horn and J. Oschinski,"Behavior of deuterium and rare gases in thermal convection loops with molten Pb-17Li,"*Fus. Eng. Des*. **14**, 261, (1991).

[6] A. Aiello, A. Ciampichetti and G. Benamati,"Determination of hydrogen solubility in leadlithium using sole device,"*Fus. Eng. Des*. **81**, 639, (2006).

[7] M. Okamoto, et al.,"Tritium recovery from neutron irradiated li-pb alloys,"*Fus. Eng. Des*.,**8**, 345, (1989).

[8] T. Terai, S. Nagai, T. Yoneoka, et al.,"Diffusion coefficient of tritium in molten lithium-lead alloy ($Li_{17}Pb_{83}$) under neutron irradiation at elevated temperatures,"*J. Nucl. Mater*.,**187**, 247, (1992).

[9] Y. Edao, H. Noguchi, H. Okitsu and S. Fukada, "Permeation behavior of two-component hydrogen isotopes in lithium-lead eutectic alloy," *Fus. Sci. Technol.*, **60**, 1163, (2011).

[10] Y.Edao, S.Fukada, H. Noguchi, et al., "Isotope Effects of Hydrogen Isotope Absorption and Diffusion in $Li_{0.17}Pb_{0.83}$ Eutectic Alloy," *Fus. Sci. Technol.*, **56**, 831, (2009).

[11] Y. Maeda, Y. Edao, S. Yamaguchi and S. Fukada, "Solubility, diffusivity, and isotopic exchange rate of hydrogen isotopes in Li-Pb," *Fus. Sci. Technol*. **54**, 131, (2008).

[12] Y. Edao, H. Noguchi and S. Fukada, "Experiments of hydrogen isotope permeation, diffusion and dissolution in Li–Pb," *J.Nucl.Mater*., **417**, 723, (2011).

Task 1-2(4)DEVELOPMENT OF A LOW TRITIUM PARTIAL PRESSURE PERMEATION SYSTEM FOR MASS TRANSPORT MEASUREMENT IN LEAD LITHIUM EUTECTIC

R.Pawelko[a,*], M. Shimada[a], K. Katayama[b], S. Fukada[b], and T. Terai[c]

[a]*Idaho National Laboratory, Idaho Falls, ID 83415, USA*
[b]*Kyushu University, Higashi-ku, Fukuoka, 812-8581, Japan*
[c]*University of Tokyo, Bunkyo, Tokyo 113-0032, Japan*

**robert.pawelko@inl.gov*

A new experimental system designed to investigate tritium mass transfer propertiesin materials important to fusion technology is operational at the Safety and Tritium Applied Research (STAR) facility located at the Idaho National Laboratory (INL). The tritium permeation measurement system was developed as part of the Japan/US TITAN collaboration to investigate tritium mass transfer properties in liquid lead lithium eutectic (LLE) alloy. The system is similar to a hydrogen/deuterium permeation measurement system developed at Kyushu University and also incorporates lessons learned from previous tritium permeation experiments conducted at the STAR facility.

This paper describes the experimental system that is configured specifically to measure tritium mass transfer properties at low tritium partial pressures. We present preliminary tritium permeation results for α-Fe and α-Fe/LLE samples at 600°C and at tritium partial pressures between 1.0E-3 and 2.4 Pain helium. The preliminary results are compared with literature data.

I. INTRODUCTION

Liquid lead lithium eutectic (LLE) alloy has been selected for the helium-cooled lead lithium (HCLL) Test Blanket Module (TBM) in ITER and thedual coolant lead lithium (DCLL) concept in future fusion demonstration (DEMO) reactor designs. The tritium partial pressure in these blanket systems is expected to be < 1000 Pa and therefore reliable data on the tritium mass transport properties (permeability, diffusivity, and solubility) in LLE at low tritium partial pressures are key parameters for the design of an effective and safe blanket system.

One task of the Japan/US TITAN collaboration is focused on investigating the tritium mass transport properties in liquid LLE at low tritium partial pressures. To accomplish this task a new tritium permeation measurement system was developed at the Safety and Tritium Applied Research (STAR) facility located at the Idaho National Laboratory (INL). The system is similar to a hydrogen/deuterium permeation measurement system at Kyushu University in which a permeation method was used to obtain the mass transport properties of hydrogen and deuterium in LLE.[1]

The tritium permeation measurement system, experimental method, and preliminary tritium permeation results for α-Fe and α-Fe/LLE are hereafter presented and discussed.

II. EXPERIMENTAL SYSTEM

The tritium permeation measurement system is housed in a ventilated enclosure and laboratory hood. Figure 1 provides a simplified schematic of the experimental system. The primary components of the system include the LLE permeation cell, two independent gas manifolds, a tritium capture system, and a National Instruments (NI) LabVIEW based control and data acquisition system. A brief description of the system's primary components follows:

1. The LLE permeation cell is shown in Figure 2. The cell is constructed of 304 stainless steel and is 4.1 cm in diameter. A 1 mm thick (13.0cm^2) α-Feplate separates the cell into two chambers and also forms the permeation interface separating the primary and secondary gas manifolds. A tube furnace maintains the permeation cell at uniform temperature ranging between 300 and 600°C with a temperature gradient across the cell of less than 5˚C.For the LLE experiments a 101.1 gram PbLisample was melted on the α-iron plate creating an approximately 8 mm thickliquid LLE layer. The permeation cell is replaceable to accommodate tritium permeation studies on metal, molten metal, and saltsamples.
2. The tritium test gas mixtures flow through the bottom chamber of the permeation cell and the primary manifold. A 0 to 100 sccm mass flow controller,pressure sensor, and a leak valve are used toestablish tritium test gas flow rates and pressures in the primary manifold.Tritium concentrations in the primary manifoldare measured with a10 ccTyne

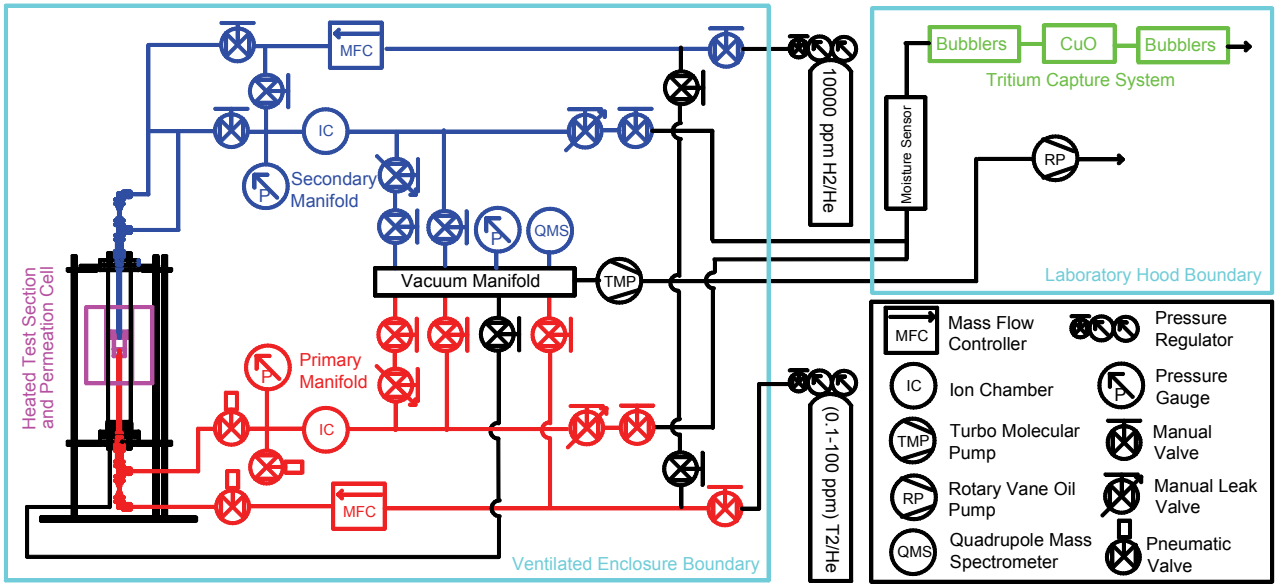

Fig. 1. Simplified schematic of the tritium permeation measurement system.

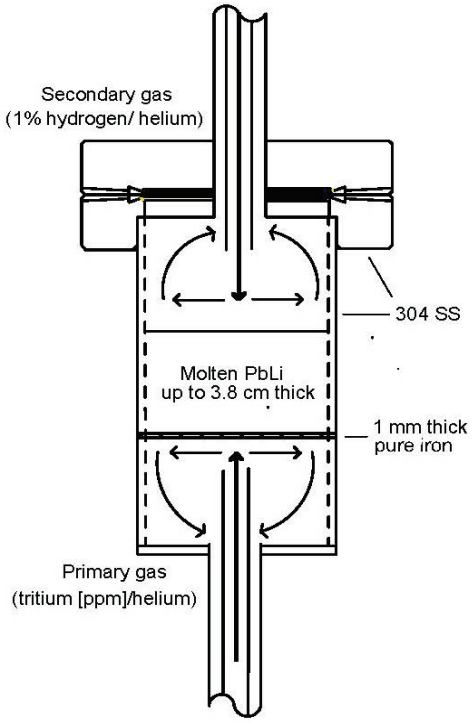

Fig. 2. Diagram of LLE permeation cell.

ion chamber with a detection range of 10^{-3} to 10^{6} Ci/m^3. A 1% hydrogen in helium (1% H_2/He) sweep gas flows through the top chamber of the permeation cell and the secondary manifold. The 1% H_2/He gas mixtureminimizes surface effects andalso reduces tritium losses and ion chamber background levels by saturating the secondary manifold's surfaces with H_2.A 0 to 200sccmmass flow controller, pressure sensor, and a leak valve are used to establish the sweep gas flow rates and pressures in the secondary manifold. Tritium concentrations in the secondary manifold are measured with a 1000 cc Tyne ion chamber with a detection range of10^{-6} to 10^{3} Ci/m^3.

3. The tritium capture system consists of a pair of ethylene glycol filled bubblers for capturing tritiated water (HTO). These are followed by a CuO catalyst bed at 600˚C that converts elemental tritium (HT and/orT_2) into tritiated water (HTO) which is then captured in a second pair of bubblers containing ethylene glycol. All manifold gas containing tritium flows through the capture system prior to being vented to the facility exhaust.

4. NI LabVIEW control and data acquisition software operates the tritium permeation measurement system.The software operates electro-pneumatic valves and mass flow controllers during experiments while continually recording the temperature, flow rate, pressure, and tritium concentration data.

Ancillary components include: a turbo molecular vacuum pump system, a quadrupole mass spectrometer, molecular sieve beds, and a moisture sensor to monitor H_2O concentrations in the manifolds.

III. TRITIUM TEST GAS MIXTURES

The tritium test gas mixtures are stored in large 49 liter internal volume cylinders that were originally made for the Tritium Migration, Infiltration and Scintillation Test (TMIST) program. At the end of the program the largely depleted cylinders became available and by

re-pressurizing the tanks with UHP helium it was possible to create cylinders with low tritium partial pressures. The cylinders were then assayed using a 10 cc Tyne ion chamber and found to contain T_2 partial pressures of 1.1E-3, 0.15, and 2.4 Pa. The large volume cylinders provide a constant tritium concentration gas supply that can be used for multiple extended run tests.

IV. LEAD LITHIUM EUTECTIC SAMPLE

The LLE sample used in these experiments was supplied by Atlantic Metals of the US. Thecomposition of the LLE was determined using inductively coupled plasma mass spectroscopy (ICP-MS) and optical emission spectroscopy (ICP-OES) analysis by sample dissolution in nitric acid conducted on batch samples at the INL analytical laboratories. ICP-MS analysis determined the LLE composition to be 85.04 mole% Pb and 14.90 mole% Li. ICP-OES analysis identified trace quantities of Bi, Sn, and Zn in the PbLi eutectic sample.

V. ANALYSIS ANDPRELIMINARY RESULTS

Tritium mass transfer experiments have been conducted on a 1 mm thick α-Fe plate attemperatures between 300 and 600°C and T_2partial pressures of 1.1E-3, 0.15, and 2.4 Pa. In addition, four experiments were conducted on the α-Fe platewithan 8 mm layer of liquid LLE at temperatures between 300 and 600°C and T_2 partial pressures between 2.2E-2 and 2.6E-3 Pa.

Prior to each experiment the permeation cell was heated to the test temperature and purged with a 1%H_2/He gas mixture to remove oxides and minimize surface effects. During experiments the secondary manifold was purged with a 1%H_2/He sweep gas to reduce tritium losses and ion chamber background levels by saturating the secondary manifold's surfaces with H_2.The effects of the 1%H_2/He sweep gas on the transport of low partial tritium in LLE isunder investigation at this time, and this will be the subject of subsequent publication.

The experimental technique hinges on the use of ion chambers to accurately measure tritium concentrations.Prior to conducting experiments, the Tyne ion chambers were electronically response checked to verify proper operation and to assure accuracy. Although ion chamber measurements cannot distinguish between T_2 and HT an effective tritium flux and partial pressure can be defined that correspond directly to the detectors measurements. In this report, the ion chamber's response corresponds to effective T_2 fluxes and partial pressures. Lastly, at low tritium concentrations, the ion chamber's signal to background ratio is small which disproportionately increases the uncertainty associated with thesemeasurements.

We present preliminary tritium permeation results for α-Feat temperatures ranging between 400 and 600°Cand α-Fe/LLE at 600°C.

V.A. α-Fe Sample

Figure 3 presentstritium permeation fluxesfor α-Feat 600°C as a function of time.A temperature gradient across the cell was measured to be less than 5°C. The traces represent T_2 partial pressures of 1.6E-3, 1.5E-1, and 2.4 Pa in the primary manifold.

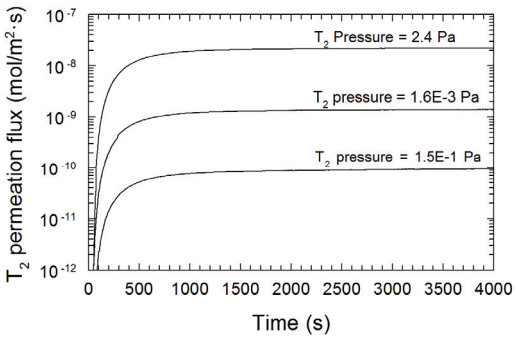

Fig. 3.Measured T_2permeation fluxes for α-Fe at 600°C.

Figure 4displays the steady state α-Fe tritium permeation flux valuesfor a series of isotherms as a function ofT_2input partial pressures**.**

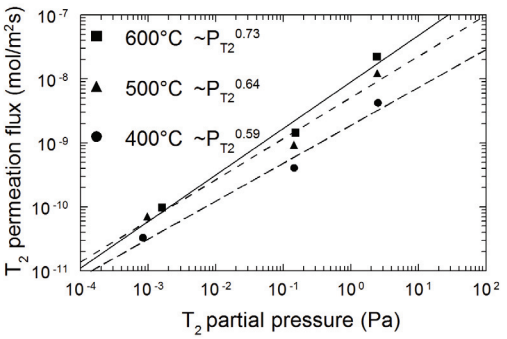

Fig. 4. Steady state T_2 permeation flux for α-Fe as a function ofT_2 input partial pressure.

Figure 4 depicts a relationship between the T_2 permeation flux and the T_2 input partial pressure that isroughly linear,with exponents ranging between 0.73 and 0.59. There is clearly no square root dependence that is a characteristic of diffusion-limited permeation at high partial pressures nor is there astrictly linear relationship that is characteristic of surface-limited permeation and is known to occur in metals at low partial pressures.The graph represents preliminary evidence that the data spans a transition region between the diffusion-limited regime and the surface-limited regime. Additional data points

arerequired to determine the existence and range of a surface-limited regime. Without this information a meaningful quantitative determination of the mass transport properties in α-Fe a low tritium partial pressures is not possible.

V.B. α-Fe/Molten LLE Sample

In Figure 5 tritium permeation fluxes for α-Fe and α-Fe/LLE at 600°C are presented as a function of time. The α-Fe trace represents tritiumpermeation through a 1 mm thick α-Feplate with aT_2inputpartial pressures of 1.6E-3 Pa. The α-Fe/LLE trace istritium permeation through the α-Fe plateand 8 mm layer of liquid LLE witha T_2 input partial pressure of 2.6E-3 Pa.

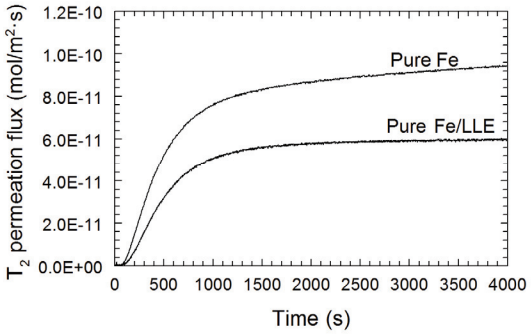

Fig. 5. T_2 permeation curves forα-Fe and α-Fe/LLE at 600°C.

The data presented in Figure 5is currently our only datathat compares the tritium permeation fluxes of α-Fe and α-Fe/LLE at comparable temperatures and T_2input pressures.The tritium permeation curves presented in Figure 5 are very different from H_2 permeation curves for α-Fe and α-Fe/LLE that have been reported in literature.[1] In the H_2 permeation studies the permeation resistance of α-Fe is two orders of magnitude lower than that of α-Fe/LLE and therefore can be considered negligible compared to that of the liquid LLE layer. However, our preliminary data indicates that atlow T_2partial pressure (< 2.5E-3 Pa), the steady state permeation flux for α-Fe is comparable to that of the α-Fe/LLE sample and therefore the permeation resistance of α-Fe must be accounted for when determining the permeation fluxof tritium in LLE.
Additional data isneeded to determine if the tritium permeation through the LLE is diffusion-limited or surface-limited at low T_2 partial pressures and to obtain the tritium mass transport properties in LLE.It is not clear that the diffusion-limited permeation reported inH_2 permeation experiments on α-Fe and on LLE conducted at significantly higher input pressures appliesto the currentlow tritium partial pressure studies .[3]

VI. CONCLUSIONS

In this paper, we have described a new system that has been developed to investigate tritium mass transfer properties in materials important to fusion technology at lowtritium partial pressures.The system is currently being used to conduct low tritium partial pressure permeation experiments onα-Fe and on LLE.Preliminary resultshave revealed differences between the H_2 permeation studies on α-Fe and α-Fe/LLE reported in literature and the low tritium partial pressure permeation studies currently being conducted.

Additional measurements are required to determine if the tritium permeation through LLE is diffusion-limited or surface-limited at low T_2 partial pressures.Data is also needed to determine the effect of the 1%H_2/He sweep gas on the transport of tritium in LLE. Finally,TMAP modeling is required to extract the LLE permeation flux from the α-Fe/LLE permeation flux.Once this information is obtained, thetritium mass transfer properties in LLE at low tritium partial pressures can be determined. Due to the reasons described above, determination of the tritium mass transport properties in LLE has become complex and is beyond the scope of this paper. Tritium behavior in LLE via Tritium Migration Analysis Program (TMAP) modeling will be investigated in the subsequent publication.

ACKNOWLEDGMENTS

This work was prepared for the U.S. Department of Energy, Office of Fusion Energy Sciences; under the DOE Idaho Field Office contract number DE-AC07-05ID14517.

REFERENCES

1. Y. EDAO, H. NOGUCHI, S. FUKADA, “Experiments of Hydrogen Isotope Permeation, Diffusion and Dissolution in Li-Pb,”*Journal of Nuclear Material*, **417,** 723, (2011).
2. P. CALDERONI et al., “Tritium Permeability of Incoloy 800H and Inconel 617,” INL/EXT-1-23265, Idaho National Laboratory.
3. H OKITSU et al., “Analysis of Diffusion and Dissolution of Two-Component Hydrogen (H+D) in Lead Lithium,” *Fusion Engineering and Design*, **87**, 1324, (2012).

Task 1-2(5) Research activities for measurement of hydrogen solubility in LiPb

K. Katayama[1], Y. Edao[1], S. Fukada[1], K. Noborio[2], Y. Yamamoto[2], S. Konishi[2], T. Terai[3], P. Calderoni[4], P. Sharpe[4], M. Shimada[4], B. Merrill[4], B. Denny[4], R. Pawelko[4], S. Schuetz[4]

[1]*Kyushu University, 6-1 Kasuga-koen, Kasuga, Fukuoka 816-8580, Japan, kadzu@nucl.kyushu-u.ac.jp*
[2]*Kyoto University, Uji Kyoto 611-0011 Japan,*
[3]*The University of Tokyo, 2-11-16 Yayoi, Bunkyo-ku, Tokyo 113-8656 Japan*
[4]*Fusion Safety Program, Idaho National Laboratory, Idaho Falls, USA*

Research activities for measurement of hydrogen solubilitya in LiPb has been conducted under the U.S.-Japan TITAN collaboration program at STAR facility in Idaho National Laboratory. The solubility test using a quartz crucible has been tried at 300 °C but the crack had been caused at about 15 hours after temperature reached 300 °C. This is caused by chemical reaction of LLE and SiO_2. Hydrogen solubility and apparent diffusivity has been estimated from data obtained by solubility tests using alumina crucible by fitting method assuming one dimensional diffusion. The estimated solubility in the range from 300 °C to 500 °C is close to Reiter's one. However, the value of solubility increased sharply at 600 °C. This seemed to be caused by chemical reaction of LLE and Al_2O_3.The estimated diffusivity was two orders of magnitude larger than literature data. This large difference may be due to natural convection of LLE in the alumina crucible.

I. INTRODUCTION

Measurements of hydrogen solubility in LLE (Lead-Lithium Eutectic) have been carried out in 2008-2009 under TITAN project using Al_2O_3 sample holder with different sample weight. Estimated solubility is close to Reiter's data [1] at 300 °C and 400 °C but it rose largely at 500 °C and 600 °C. This increment is considered to be due to the reaction of the LLE with the alumina crucible. Easy alternatives are to use metal crucibles such as a SS tube with W coating or a Mo tube and so on. However, a large amount of LLE will be necessary to estimate correct data because of a large H solubility in metals. A quartz crucible is one candidate because of low H solubility. An inductive heating system can be used for quartz tube, where liquid metal behavior can be seen directory. A quartz loop is one option for a small forced convection loop. However, the compatibility of quartz with LLE is uncertain. Potentially there is a concern about braking and cracking. In order to check compatibility and to obtain collect data at high temperature, H solubility test using quartz crucibles was tried in this work.

Hydrogen solubility and apparent diffusivity was estimated from data obtained by solubility tests using alumina crucible by fitting method assuming one dimensional diffusion. A numerical simulation of hydrogen permeation behavior in a small loop of LLE by using obtained solubility and apparent diffusivity.

II. EXPERIMENTAL

II.A Blank test in a quartz crucible

The experimental system was assembled as shown in Fig.1 and the blank test was begun before I arrived at INL. It is important to evaluate hydrogen sorption/desorption behavior from the experimental system as quantitatively as possible because the solubility of hydrogen in LLE is little as well known. The schematic diagram of experimental apparatus is shown in Fig.2, where LLE sample is just an image. V 1, V 2 and V 3 are pneumatic valves which can be controlled from PC. Hydrogen was charged overnight at high pressure or low pressure under each designed temperature. Before beginning the hydrogen desorption procedure, hydrogen emission rate

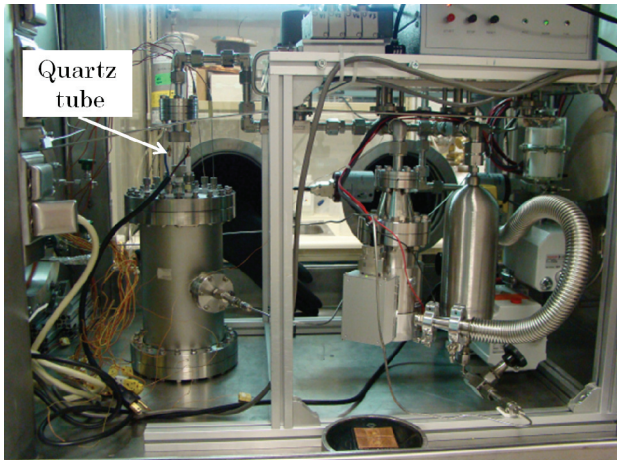

Fig.1 Photograph of experimental system 1 for the blank test using a quartz crucible.

from system material (Vol 2) was measured. Then, hydrogen left in the gas phase of Vol1 is quickly evacuated for about 1 min and V 1 was closed. Basically after waiting for 5 min, V 2 was closed and V 1 was opened for 30 second and then the pressure increase of Vol 2 was measured. This desorption procedure was continued until the hydrogen desorption rate became lower than the hydrogen emission rate from system materials.

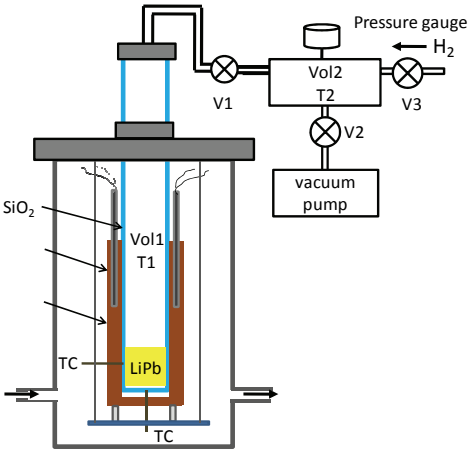

Fig.2 Schematic diagram of the heating system 1 used for blank test.

II.B Preparation of LLE

After blank test was completed, the preparation of sample was progressed. A quartz tube was cleaned by soaking HNO_3 overnight and it was installed in the inert gas box (see Fig.3). A $Li_{15}Pb_{85}$ block was input in the melting pot (see Fig.4). The inside of the box was significantly purged at 3 l/min by argon gas until oxygen concentration was 0.5 % and water vapor concentration was below 500 ppm and then heating was started. The temperature in the pot stopped rising at around 400 ^{o}C that suggests melting started. This temperature does not indicate the average temperature of LLE because it depends on the position of thermocouple in the melting pot. After melting was confirmed by dropping a little into the quartz tube, a designed amount of LLE was able to be poured successfully (see Fig.5). LLE contacting with the cold surface of the quartz was condensed one after another. Consequently horizontal stripes were formed at the side and a hole was formed at the top as shown in Fig.5. Weight of this sample was 117.2g. After successful pouring, heating was stopped but argon purging was continued until the temperature of LLE decreased to room temperature to avoid oxidation of LLE. The quartz with LLE was inserted into the second chamber and the flange with O ring was covered the top of the quartz. Finally when a horizontal pipe connecter was carefully fastened, the top of the quartz was broken because of mechanical

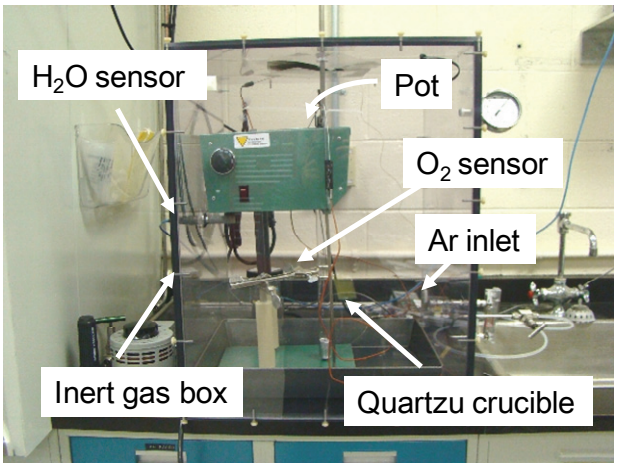

Fig.3 Photograph of the inert gas box.

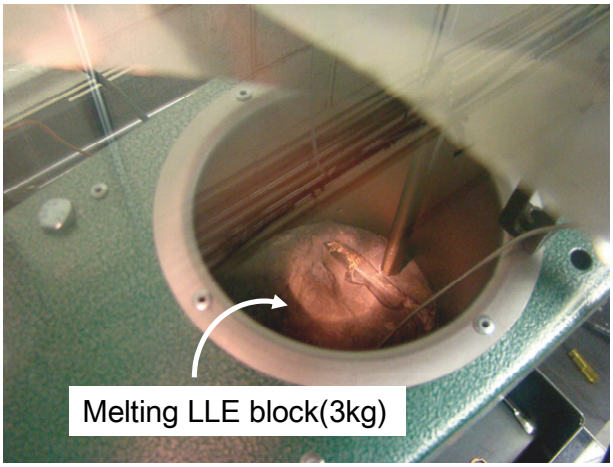

Fig.4 Photograph of melting LLE.

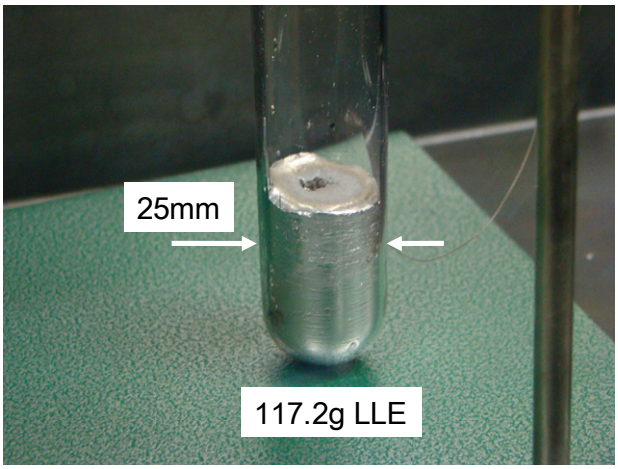

Fig.5 Photograph of LLE poured.

stress. In this heating system, it is not easy structurally to avoid the breaking of the quartz by a mechanical stress when a connector is fastened, though the setting of the quartz for the blank test was fortunately well done. In

order to allow the quartz to move, we decided to remove the second chamber. Because a copper block is awfully oxidized when it is heated in air, it is also removed and a simple heating system was constructed as shown in Fig.6.

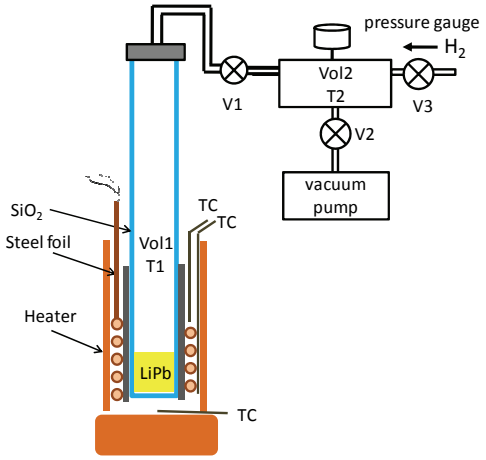

Fig.6 Schematic cdiagram of heating system 2.

III.RESULTS AND DISCUSSION

IV.III.A Blank test in a quartz crucible

The hydrogen desorption rate, which is obtained by dividing the pressure increase by the waiting and opening period (basically 330 second) were summarized in Fig.7. As shown in this figure, the desorption rate depends on the charge pressure but the obvious temperature dependence is not observed. This indicates that this hydrogen was released from not the heated quartz tube but the cylinder and piping system that are kept at room temperature. From the dependence of desorption rate on the charge pressure, I assumed that the desorption consists of the following three causes.

A) Dissolution, which is proportional to square root of the charge pressure.
B) Adsorption, which is proportional to the charge pressure.
C) Leakage, which is constant.

The following equation was assumed and then each constant was obtained by fitting like shown in Fig.8.

$$R(\mathrm{Pa/s}) = A\exp(-k_1 t)\cdot\sqrt{P_{H_2}} + B\exp(-k_2 t)\cdot P_{H_2} + C \qquad (1)$$

A:3.60×10^{-6} , k_1:1.15×10^{-3}, B:6.60×10^{-9}, k_2:1.48×10^{-4}, C:3.0×10^{-5}

Comparison of calculated desorption rates with experimental ones is shown in Fig.9. The calculated curves agree approximately with experimental curves.

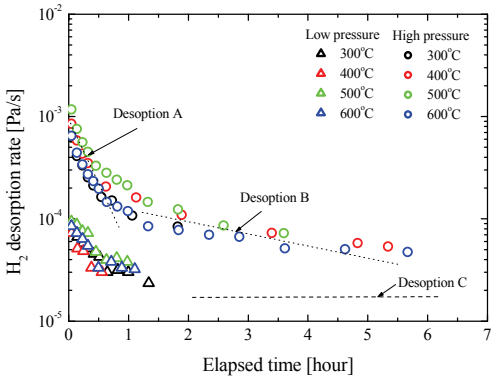

Fig.7 Hydrogen release rate in blank test.

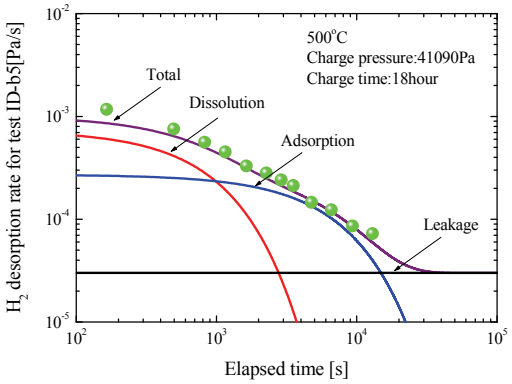

Fig.8 An example of fitting for desorption curve.

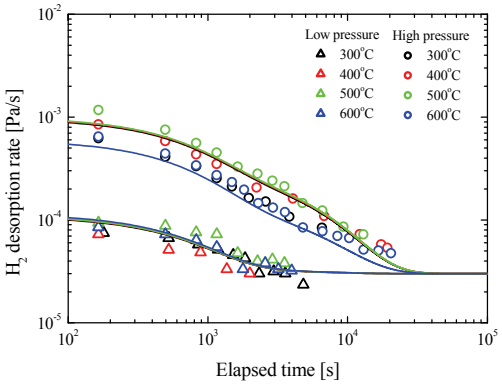

Fig.9 Comparison of estimated curves with experimental ones.

III.B Heating of LLE in a quartz crucible

At first, LLE sample (#2 129.5g) prepared again was heated without a steel foil at the heat load of 50%. Immediately after heating started, a crack was caused at the part where the heater contacts with the quartz. It was considered that LLE around heater melted partly by a large heat load pushed the quartz. Also the rate of temperature increase was as fast as about 1° C/sec. Thus, a steel foil was inserted between heater and the quartz and the heating test of an empty quartz tube was successfully performed. A small amount LLE sample (#3 34.7g) was prepared again and installed in the heating system. The temperature was slowly increased at about 1.25 °C/min (see Fig.10) to avoid a large heat load and reached at 300 °C after 4 hour without crack. In order to remove impurity, evacuating and heating was continued for a while (during weekend). On Monday, however, it was found that the crack had been caused at about 15 hours after temperature reached 300 °C. The history of the temperature and pressure is shown in Fig.11. Photograph of this broken sample are shown in Fig.12 comparing with sample #2.

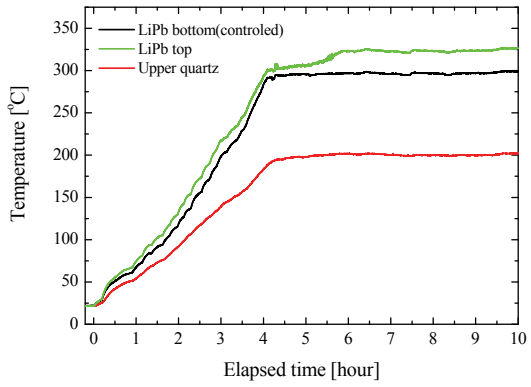

Fig.10 Temperatures of around LLE heated slowly at about 1.25°C/min.

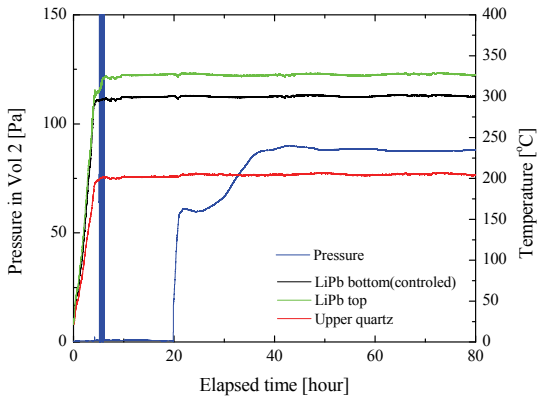

Fig.11 The history of the temperature and pressure during evacuating with heating for removal of impurity.

Fig.12 Photograph of samples after heating (#3). Sample #2 is original color of LLE.

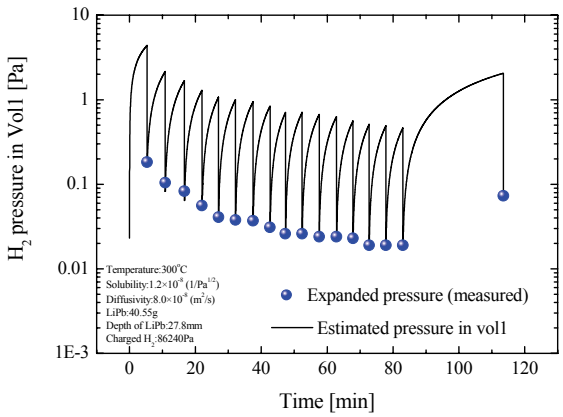

Fig.13 Fitting the calculated pressure in Vol 1 to the pressure measured.

Some materials with different color are observed. It seems that the crack was caused by the cchemical reaction of LLE with SiO_2. It can be said that the compatibility of LLE with SiO_2 is not good obviously. We decided not to try again the solubility test using a quartz tube until good countermeasure is found out. Discussion on next improving for solubility test was started. An alumina crucible with W or Mo coating is considered to be next candidate. Inductive heating will be used efficiently in next experiment.

III.C Estimation of solubility and apparent diffusivity

Hydrogen solubility tests using alumina crucible has been performed in Jun 2009. Rough estimated solubility is shown in Fig.1 as resent data. I tried to estimate apparent diffusivity from desorption curves assuming one dimensional diffusion. After H_2 charging, V 1 is opened periodically and then hydrogen accumulated in Vol 1 expands to Vol 1 + Vol 2 (refer Fig.2). I calculated the change of hydrogen pressure in Vol 1 numerically and fit it to experimental results varying solubility and diffusivity as parameters (Fig.13). Results are shown in Fig.14 (a) - (d). Large jumps at final measurement after a long waiting

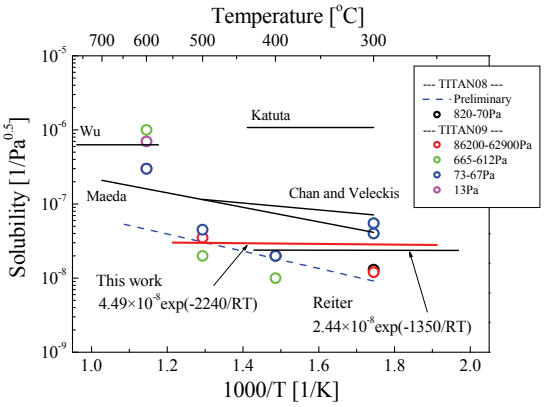

Fig.15 Estimated solubility and literature data [1-5].

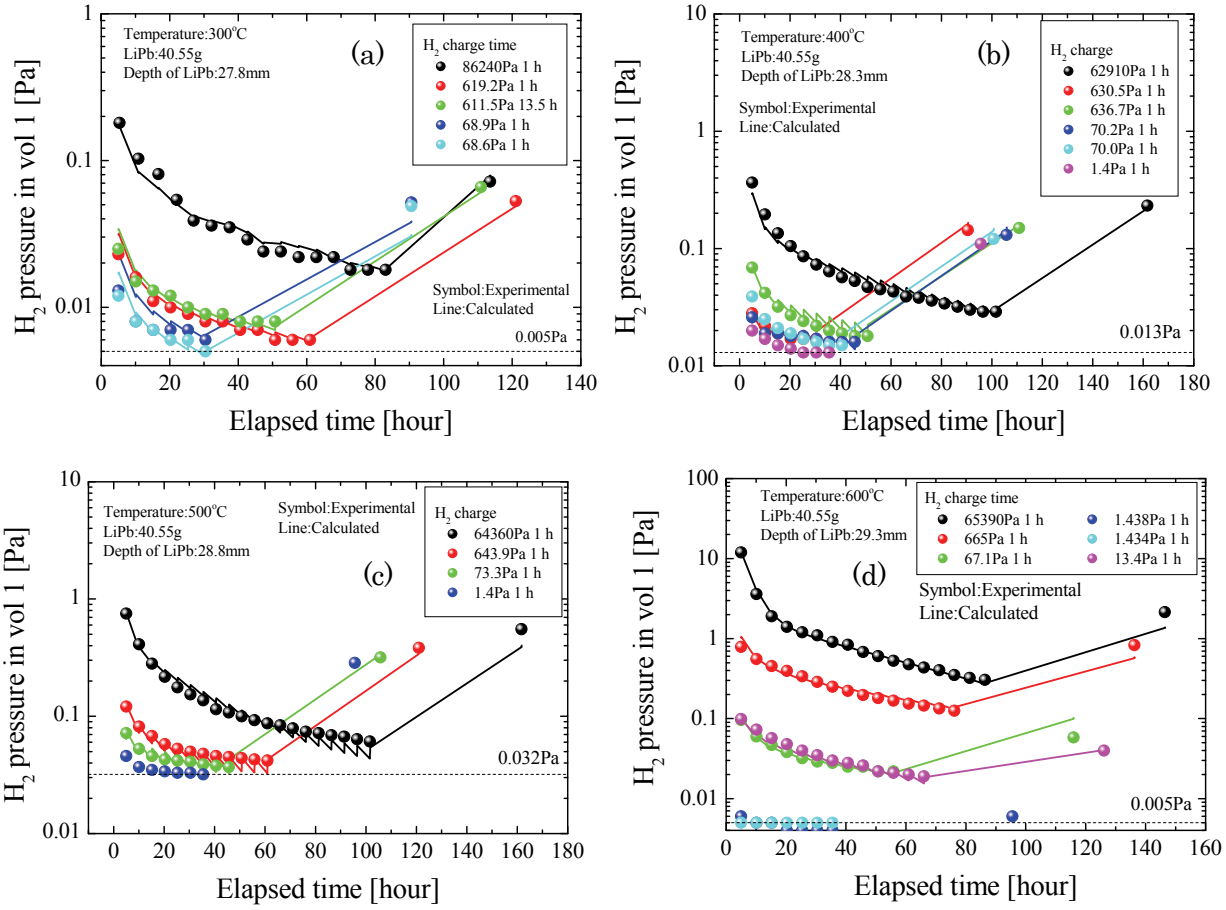

Fig.14 Comparison of calculated pressure with measured ones for 300°C(a), 400°C(b), 500°C(c), 600°C(d).

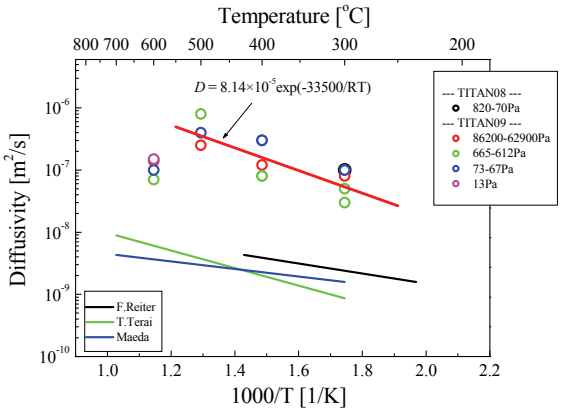

Fig.16 Estimated apparent diffusivity [1,5,6].

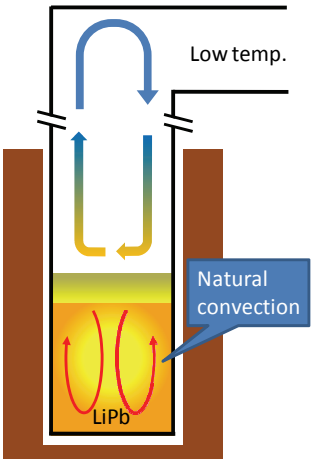

Fig.17 Natural mixing in crucible.

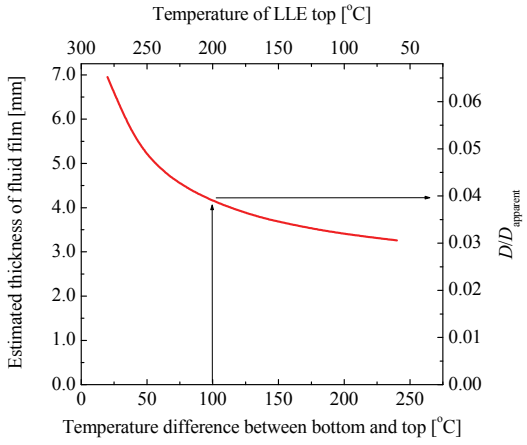

Fig.18 Estimated thickness of fluid film.

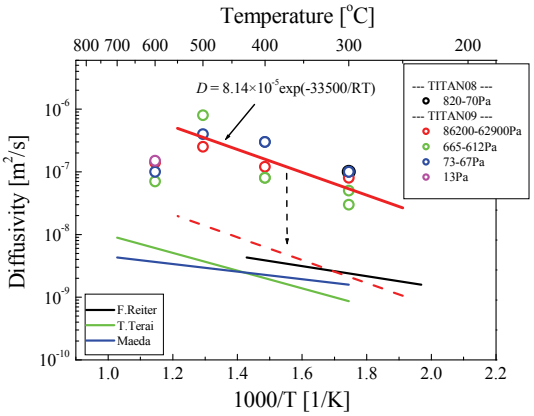

Fig.19 Diffusivity estimated assuming natural onvection of LLE.

time indicates that hydrogen desorption is keeping on even after the measurement was quitted. Estimated solubility and diffusivity are compared with literature data in Fig.15 and Fig.16, respectively. Solubility increases and diffusivity decreases sharply at 600 °C. This implies that the chemical reaction of LLE with Al_2O_3 occurred between 500 °C to 600 °C. Temperature dependence of solubility in the range from 300 °C to 500 °C is uncertain because data are scattered. But averaged value is close to Reiter's one. The following value is obtained as hydrogen solubility, S;

$$S = 2.44\times10^{-8}\exp(-1350/RT)\ \ [1/\mathrm{Pa}^{0.5}] \qquad (2)$$

Temperature dependence of estimated diffusivity in the range from 300 °C to 500 °C is close to literature data while the estimated value is two orders of magnitude large. This large difference may be due to natural convection of LLE in the alumina crucible. The copper block is kept at a

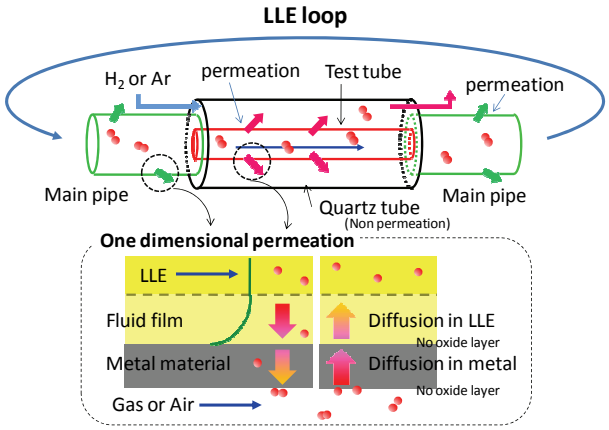

Fig.20 Calculation model for hydrogen behavior in flowing LLE.

designed temperature but the surface of LLE contacts with hydrogen gas cooled down at the top of Vol 1. Therefore, natural mixing of LLE as shown in Fig.17 is doubted. Therefore, the thickness of fluid film was roughly estimated using the following equation.

$$\overline{Nu} = 0.069 Ra^{1/3} Pr^{0.074} \quad (3)$$

$$3\times10^5 < Ra < 7\times10^9 \quad (4)$$

This is applied to heat transfer for a horizontal rectangular cavity heated below in enclosed spaces. I'm not sure that applying this equation to our experiment is appropriate. More suitable equation may have been proposed so far. On example of estimation of the thickness of liquid film is shown in Fig.18. In this estimation, the bottom of LLE is assumed 300 °C. The thickness decreases with increasing the temperature difference between top and bottom of LLE. When the temperature difference is 100 °C, the thickness is estimated 4 mm. The desorption rate of hydrogen with time depends on L2/D, where L is diffusion length and D is diffusion coefficient. When diffusion length is not 27.8 mm but 4 mm, diffusivity decreases to be 2×10-2Dapparent. That to say, diffusivity decreases about two orders of magnitude and it becomes close to literature data as shown in Fig.19. It is considered that a natural convection of LLE cannot be ignored when diffusivity is estimated from this experimental system. However, it is difficult to quantify the temperature difference between the top and bottom of LLE.

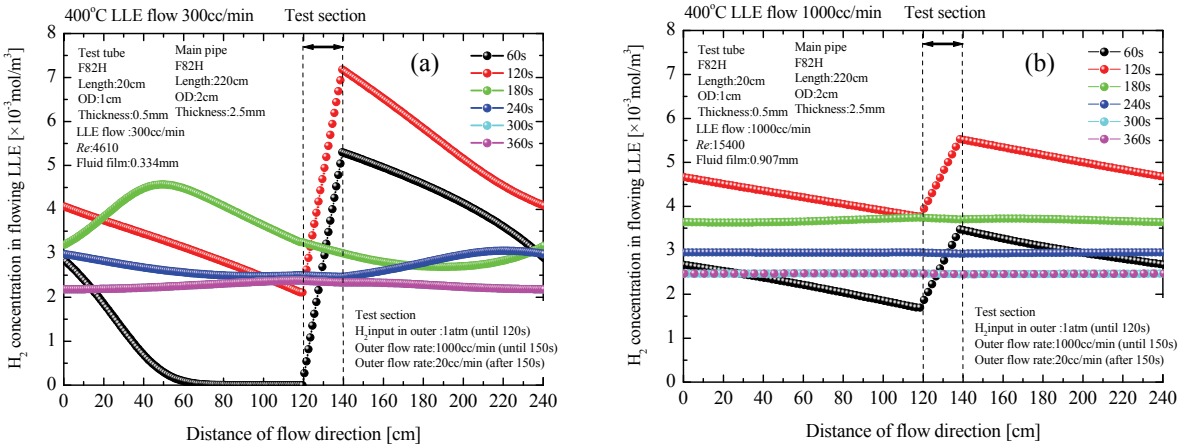

Fig.21 The change of distribution of hydrogen concentration in flowing LLE to flow direction with time. (a):LLE flow rate is 300cc/min, (b):LLE flow rate is 1000cc/min)

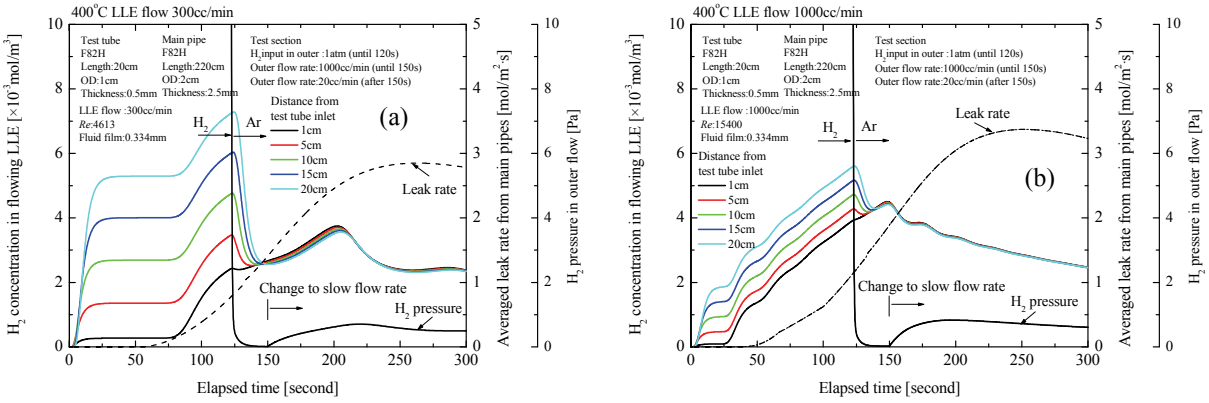

Fig.22 Hydrogen concentration in flowing LLE at the test section. Averaged leak rate from F82H main pipes to atmosphere. H_2 partial pressure in outer gas phase of the test section. (a) :LLE flow rate is 300cc/min, (b):LLE flow rate is 1000cc/min)

III.D **Permeation behavior in flowing condition**

Discussion on a loop design is one purpose of this visiting at first. In parallel with the solubility experiment, I began to make a numerical calculation code for useful discussions. The rough image of this calculation model is shown in Fig.20. A loop construction in Task 1-2 has been cancelled, however, the estimation of hydrogen in flowing LLE is useful for planning future experiment. Therefore I tried making it for a simulation of hydrogen behavior in a small loop of LLE by the numerical calculation based on the following assumptions:

(a) The thickness of fluid film of LLE is estimated from the following relationship:

$$Sh = 0.023 Re^{0.83} Sc^{1/3} \quad (5)$$

$$2100 < Re < 35000 \quad (6)$$

$$0.6 < Sc < 3000 \quad (7)$$

(b) No oxide layer on metal surface.
(c) This relationship of CLLE/SLLE = Cmetal/Smetal is hold at the interface between LLE and metal surface.
(d) One dimensional to radial direction and to flow direction, respectively.
(e) The solubility and diffusivity estimated in this work are used.

Two examples of numerical simulation are shown in Fig.21 and Fig.22, where main pipe is F82H (L:220cm, OD:2cm, Thickness:2.5mm) and test tube is also F82H (L:20cm, OD:1cm, Thickness:0.5mm).

V. CONCLUSIONS

It was concluded that a quartz crucible is unsuitable as a LLE container for hydrogen solubility measurement because of compatibility issue.

Hydrogen solubility was obtained in the temperature range from 300 ^{o}C to 500 ^{o}C. Hydrogen diffusivity estimated from hydrogen release rate from from LLE was two orders of magnitude larger than literature date. This implies that a natural convection of LLE occurs in alumina crucible.

ACKNOWLEDGMENTS

Authors are grateful for the financial support from the U.S. D.O.E., and the Japanese Ministry of Education, Culture, Sports, Science and Technology via TITAN collaboration.

REFERENCES

[1] F. REITER, Fuion Eng. Des., 14 (1991) 207-211.
[2] C.H. WU, J. Nucl. Mater., 114 (1983) 30-33.
[3] Y.C. CHAN and E. VELECKIS, J. Nucl. Mater., 122&123 (1984) 935-940.
[4] H. KATSUTA, H. IWAMOTO and H. OHNO, J. Nucl. Mater., 133&134 (1985) 167-170.
[5] Y. MAEDA, Y. EDAO, S. YAMAGUCHI and S. FUKADA, Fusion Sci. Tech., 54 (2008) 131-134.
[6] T. TERAI, S. NAGAI, T. YONEOKA and Y. TAKAHASHI, J. Nucl. Mater., 187 (1992) 247-253.

Task 1-2(6)Solubility of hydrogen isotopes in liquid LiPb

S. Konishi[1], Y. Yamamoto[2], K.Noborio[3], P. Calderoni[4], B. Merrill[4]

[1]*Kyoto University, Gokasho,Uji 611-0011 Japan,s-konishi@iae.kyoto-u.ac.jp*
[2]*Kansai University, 3-3-5, Yamate, Suita, 564-8680 Japan, yama3707@kansai-u.ac.jp*
[3]*Toyama University,Gofuku 3190,Toyama, 930-8555 Japan, noborio@ctg.u-toyama.ac.jp*
[4]*Fusion For Energy, Torres Diagonal Litoral B3,08019 Barcelona, Spain, pattrick.calderoni@f4e.europa.eu*

This research was performed mainly in the first half of the task 1-2 of TITAN project to investigate the interaction between hydrogen isotopes and liquid LiPb. Solubility of hydrogen in liquid LiPb was measured under a static condition. Kyoto University provided the first experimental apparatus shipped to Idaho, and Kyushu University succeeded the experiment and further improved. Obtained solubility generally agreed with some previous reports, but varied orders of magnitudes suggesting influence of impurity or other chemical processes.

I. INTRODUCTION

In order to clarify the behavior of tritium in liquid blanket systems, interaction with breeder needs more understanding. Both solubility and diffusivity of tritium in liquid LiPb have been studied in the past, however approximately 4 orders of magnitude difference were found in previous reports. In the TITAN project that investigated overall phenomena of material-tritium interaction in the blanket systems, Task 1-2 on the Solubility Measurement with tritium was planned to be conducted in the STAR Facility in the Idaho National Laboratory. In the first half of the 6 years project,Kyoto University developed a pot experimental apparatus for the static measurement of solubility and diffusivity, shipped to the INL, for the tritium experiment. Kyushu University has further continued the experiment and expand it to kinetic measurement based on it. This research report describes this initial part of the study.

II. DEVELOPMENT OF EXPERIMENTAL APPARATUS

The basic concept of the measurement is very simple. Known amount of hydrogen gas is repeatedly loaded on to the liquid LiPb by exposing and equilibrated in the static container for some extended period of time. When the pressure of the hydrogen is determined to be steady and equilibrated, another known amount of gas is loaded. The repeated procedure provides a Pressure-Composition Isotherm. Figure 1 shows the configuration of this isotherm measurement. Sample is contained in the test section 1, and reservoirs of measured volumes are 8,9 and 10.

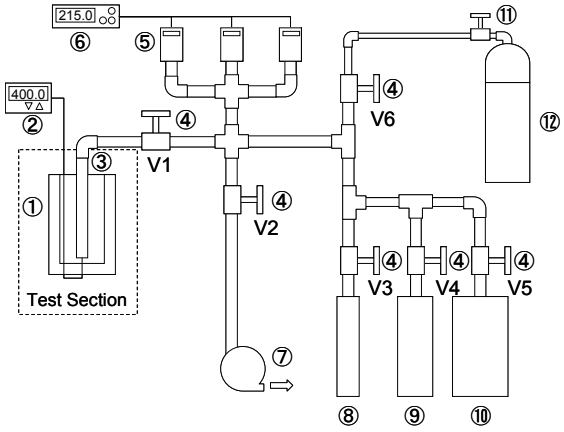

The apparatus was designed to be compatible with the glovebox in INL for the tritium experiment to be finally conducted. For this purpose, all the fittings and valves were made of metals and no organic material was used.

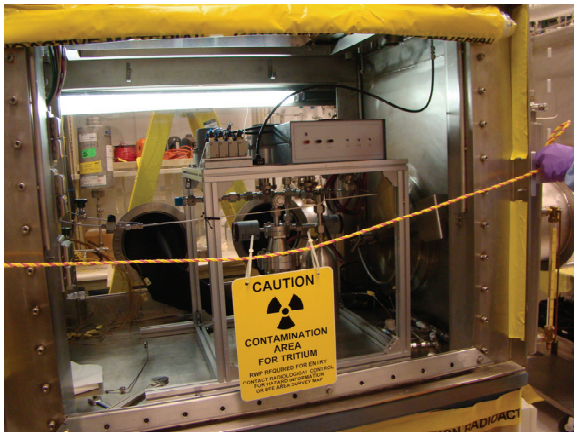

Fig.2 Apparatus for the LiPb-hydrogen isotherm measurement installed in the glovebox of STAR in INL.

Vacuum pump was turbo-molecular pump with magnetic bearing.

Figure 2 shows the apparatus installed in the glovebox of the STAR facility in INL. Effluent processing for tritiated exhaust from the vacuum pumping from the experiment was interfaced with the STAR facility.

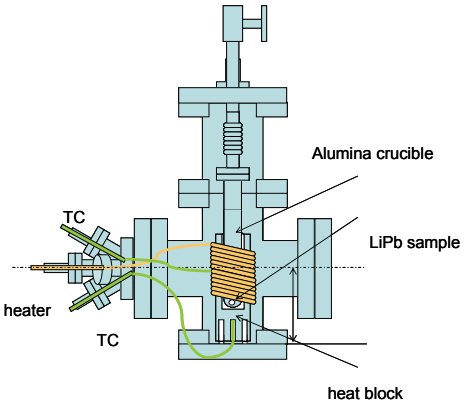

Detail of the sample holder is shown in the fig.3. Sample container is heated with heater wire wound on the cupper heat block surrounding the crucible and contained in a vacuum chamber so that tritium permeation and heat load to the glovebox would be minimal. Material for the LiPb sample was alumina for early experiments and replaced with Mo later. Silica was also tried and found to react with LiPb. Alumina was also suspected to affect the result, and in a related experiment, formation of lithium aluminate was found, probably due to the reaction between oxide impurities in LiPb. Entire experimental apparatus was first heated and evacuated, and hydrogen isotopes gas was repeatedly equilibrated with the melt LiPb sample at a prescribed temperature. Apparent solubility of hydrogen, i.e. pressure drop contains dissolution into the materials consisting the apparatus such as sample container, and thus the result of blank measurement subtracted. Tested temperature was 300 to 650 degree C, and the pressure was 1~100kPa.

III.RESULTS AND DISCUSSION

An experimental result of the isotherm did not show any plateaus suggesting the formation of hydrides. When the amount of hydrogen isotope gas is proportional to the square root of the pressure, solubility can be determined as the Sievert's constant. Figure 4 shows the result of the solubility of deuterium measured in the experiments performed in 2009~2009 fiscal year. Solubility was considerably small, however the obtained result clearly showed the dependence with the square root of the pressure. No formation of stable hydrides were observed, however the error in the absolute value of the solubility should be considered, because the subtracted blank solubility (amount of gas absorbed by the apparatus) was 15~30 % of recovered gas.

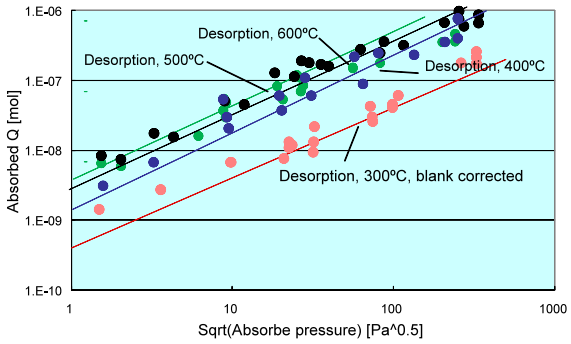

Fig.4 Pressure dependence of the solubility of deuterium.

Temperature dependence of the solubility is shown in the figure 5. Observed enthalpy from the slope of the linear relation is rather small, and the absolute value is also small. Comparison with other reported data is also shown. In the wide range of the values previously published, this result was close to the Reiter's[1], and two orders of magnitude lower than Aiello's[2].

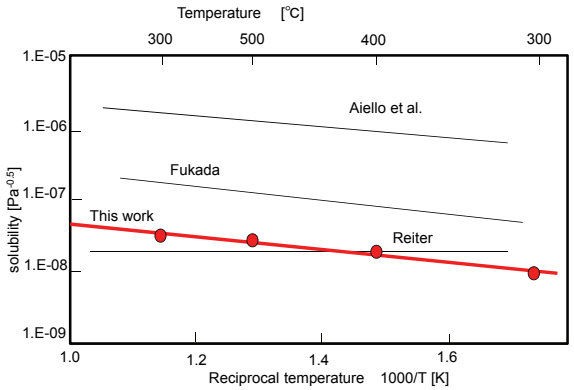

Fig.5 Temperature dependence of the solubility of Deuterium in LiPb.

It agreed well with the previous measurement conducted in Kyoto university with the similar experiment that was tested to higher temperature range (~900 degree C). It is also noted that the measurement by Fukada and Kyushu university team given a higher solubility value in the later experiments.

IV. CONCLUSION

As the cold test of the static measurement of hydrogen solubility in LiPb, the preparation and operation of the experiment in STAR facility of INL provided a sound basis for the subsequent experiments with tritium. The value of solubility obtained with deuterium was small, and proportional to the square root of pressure. Temperature dependence was small and slightly endothermic, indicating very week chemical affinity between them. Absolute value of solubility was lowest level among the previous reports or subsequent measurements by Kyushu University. One of the possible explanation is an effect of oxide impurity to be slowly formed even in a controlled environment of the glovebox. The result also suggests an insignificant impact on the total tritium inventory in fusion fuel cycle.

ACKNOWLEDGEMENT

This research was supported by the TITAN project conducted by the collaborative program between the USDOE and MEXT, Japan. The authors thank INL staffs and Japanese supporting collaborators.

REFERENCES

[1] F. Reiter, Fus. Eng., Des.,14.207(1991).
[2] A.Aiello et al., Fus. Eng., Des.,81, 639(2006).

4-3 Task 1-3(1)Electrical insulation test of alumina coating fabricated by sol-gel method inmolten PbLi pool

Yoshitaka Ueki[a], Tomoaki Kunugi[a], Neil B. Morley[b], Mohamed A. Abdou[b]

[a]*Department of Nuclear Engineering, Kyoto University, Yoshida, Sakyo, Kyoto 606-8501, Japan*
[b] *Mechanical and Aerospace Engineering Department, University of California, Los Angeles, 420 Westwood Plaza, 44-114 Engineering IV, Los Angeles, CA 90095, USA*

ABSTRACT

Development of electrical insulation coatings, which insulate an induced electric current from electricalconducting walls, is a key technology for the research and development of self-cooled liquid metal blanketincluding lead-lithium (PbLi) fusion blankets. As for magnetohydrodynamic (MHD) thermofluid study, anelectrical insulation coating is extremely important from the viewpoint of the secure electrical insulatingwall condition. The present study employs a sol-gel (SG) method to fabricate an Al_2O_3 coating, anddiscusses the feasibility of the SG coating as an electrical insulation coating for the PbLi through theelectrical insulation test in the molten PbLi pool and theSEMwithEDSanalysis on theSGcoating structure.The present study shows that the SG coating will be a potential electrical insulation coating for PbLi withboth the operation time and the temperature limitation.

1. Introduction

Aliquid metal flow in a strong magnetic field $\boldsymbol{B}$ induces an electriccurrent J, and then interacts with $\boldsymbol{B}$. As a result, the Lorentzforce, $\boldsymbol{J}\times\boldsymbol{B}$ dominates the liquid metal flow under the strong magneticfield. The heat and mass transfers of the liquid metal flowunder the strong magnetic field are also significantly affected by theLorentz force,knownas amagnetohydrodynamic (MHD) effect. TheMHD thermofluid regime is determined by not only hydrodynamicand thermal conditions but also electric boundary conditions. AMHDduct flow confined by electrical conducting walls experiencesa significant increase in pressure drop, known as MHD pressuredrop.

Development of electrical insulation coatings, which insulatean induced electric current from electrical conducting walls, is akey technology for the research and development of self-cooledliquid metal blanket including lead-lithium (PbLi) fusion blankets[1]. As for MHD thermofluid study, an electrical insulation coatingis extremely important from the viewpoint of the secure electricalinsulating wall condition.

The dual-functional lead–lithium (DFLL) concept adopts twooptional concepts of PbLi blankets including the reduced activationferritic/martensitic (RAFM) steel-structured Helium-cooledquasi-static PbLi tritium breeder (SLL) blanket and the RAFMsteel-structured Helium-gas/PbLi dual-cooled (DLL) blanket. DFLLconcept considers an alumina (Al_2O_3) as a candidate for the electricalinsulation coating against PbLi flows for the DLL blanket. TheDFLL blanket concept employs a hot dip aluminizing (HDA) process,chemical vapor deposition (CVD) [2], or atmospheric plasma spray(APS) [3] to fabricate Al_2O_3 coatings on the RAFM steels. There areother purposes of coatings in fusion reactor blankets, dependingon fusion blanket concepts. The water-cooled PbLi breeder (WCLL)concept with ferritic steel structures [4] adopts an Al2O3 coatingas tritium permeation barrier (TPB) in order to reduce the tritiumpermeation into the water coolant caused by relatively high tritiumpartial pressure produced in the PbLi breeder to an acceptable level.In addition to the TPB, Al_2O_3 coatings have been studied as PbLi corrosionbarrier because the PbLi solubility of Fe, Cr and particularlyNi are much higher than molten Li, resulting in greater dissolutionthan Li [5,6].

Most efforts of the Al_2O_3 coating development focus on fabricatingan Al_2O_3 coating on ferritic/martensitic steels by means ofHDA process [7], CVD [8], vacuum plasma spray (VPS) [9], low pressureplasma spray (LPPS) and APS [10]. The above investigations areoriginally not oriented for the Al2O3 electrical insulation coatingagainst PbLi flows, but for the coating as TPB and corrosion barrier.Nevertheless, they are informative for the Al_2O_3 coating as electricalinsulation coating in terms of the Al_2O_3 coating compatibilitywith the molten PbLi [11,12].

There are considerable requirements that must be satisfied inthe coating for the fusion application. General requirements of coatingsused for all fusion system are summarized as follows [1]:

(1) Potential for coating large complex geometry or configuration,
(2) potential for in situ self-healing of defects that might occur,
(3) processing parameters should be compatible with material andcapabilities, e.g. temperatures and processing durations,
(4) bonding/thermal expansion should match with substrate,
(5) acceptable neutronic properties,
(6) material availability/cost,
(7) safety/environmental characteristics, and
(8) radiation damage resistance.

In addition, electrical insulation coatings are required to havesufficient insulation efficiency. An electrical insulation efficiency ofcoatings is generally evaluated by

the product of coating electricresistivity ρ_i and coating thickness δ_i, called as coating resistance$\rho_i\delta_i$. A previous study has estimated 10μm thickness of an Al_2O_3,which has an electric resistivity $\rho_i \sim 10^{10}\Omega$m at 400°C, yields thealmost perfect electrical insulation with $\rho_i\delta_i=10^5\Omega m^2$ [13]. Forthe MHD thermofluid studies, some coating requirements may beeased because the thermofluid studies require a secure electricalinsulation wall condition without neutron irradiation just for theexperiment time period, which is much shorter compared to a timeperiod of the fusion reactor operation.

The Al_2O_3 coatings fabricated on RAFM steels by HDA processand VPS have the favorable adhesion to its substrate even afterbeing exposed in molten PbLi. However, the fabrication techniquesare, in general, high cost and it is hard to fabricate the coatings on alarge complex configuration. The present study employs a sol-gel(SG) method to fabricate an Al_2O_3 coating. The SG method is a wet-chemicaltechnique used for fabricating ceramic materials, and ithas the following advantages:

(1) Easy material availability,
(2) easy process to fabricate the Al_2O_3 coating on a substrate,
(3) applicable to large complex configurations, and
(4) low cost fabricating process.

On the other hand, the SG coating has poor adhesion to its substratecompared to the other processes such as HDA process.

The present study focuses on the Al_2O_3 coatings fabricated bySG method and discusses the feasibility that the SG coating worksas electrical insulation coating for the purpose of PbLi MHD flowexperiments, where the PbLi operation temperature is relativelylower, the PbLi exposure time is shorter compared to the fusionblanket operation, and the neutron irradiation is not applied.

2. Al_2O_3 coating by sol-gel method

The present study employs a commercial SG coating material:Ceramacoat™ 503-VFG-C (The Armco Products, Inc.).The Ceramacoat™ is a single-component, Al_2O_3-filled, hightemperature(maximum durable temperature: 1650 °C), andelectrical insulation coating material. The Ceramacoat™ containsAl$_2$O$_3$ and mono aluminum phosphate ($AlPO_4$) suspended in aninorganic binder system. The cured Al_2O_3 coating is $10^7\Omega$m atroom temperature in volume resistivity.

The SG coating hardly gets enough adhesion to a smoothsurfacesubstrate after curing. Substrate surfaces are roughenedand cleaned using a surface cleaner in order to remove mechanicaloil leftovers before applying the Al_2O_3 coating material. Then, the Al_2O_3 coating material is applied to the surface-prepared substratesin a thin coat using a brush to maintain a uniform material thickness.The coating applied substrates are dried in the air for about 4 hat room temperature, then cured at 95 °C, 260 °C and 370 °C for 2 hat each temperature sing electric furnace. In the curing process, arapid increase temperature of the coatings may cause a rapid evaporationof the coating binder. As results, some coating cracks andpeelings might occur. Therefore we employed the step curing toavoid the effect by following the coating company instructions.

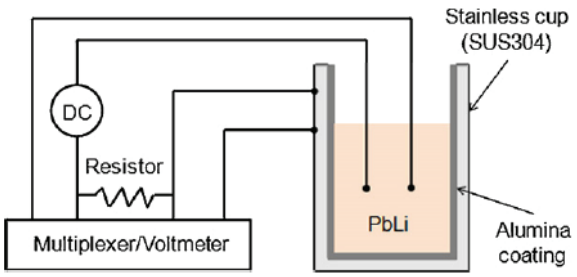

Fig. 1 Electrical insulation test stand

3. Electrical insulating test of the Al_2O_3 coating in a PbLipool

There are considerable studies performed on coating issues.However, attentions have been paid mainly to coating fabricationtechniques, the tritium permeation and corrosion behaviorsthrough morphology of the corrosion layers and discussions onchemical reactions between the liquid metal and wall material[11,12,14].
There is no research on electric insulation performance of thecoatings in contact with liquid metal. The SG coating is expectedto be less durable against thermal expansion differences becausethe SG coating has poor adhesion. An electrical insulation test ofthe SG coating in a PbLi pool was carried out to discuss the electricalinsulation performance in contact with the molten PbLi, andthen discuss the feasibility of the SG coating as electrical insulationcoating for MHD thermofluid research.

3.1. Experimental setup

Electrical insulating tests in amolten PbLi pool were performedto examine an electrical insulating performance of the Al_2O_3 coatingfabricated by the SG method. The SG coatings were fabricatedon SUS304 cups used in the test by going through the abovementionedprocedure. Fig. 1 shows the setup of the electricalinsulating test. The Al_2O_3-coated cups were filled with the moltenPbLi in an electric furnace. One side of electrodes was attached tothe cup substrate, and the other side of electrodes was immersedin the molten PbLi. The electrodes were connected to a power supplyto apply a few volts on them. They were also connected to amultiplexer to measure an electric current passing through the SGcoating with time variation. The PbLi temperature, the air temperaturein the electric furnace and the electric current passing throughthe SG coating were measured every 10 min by the multiplexer. Thefollowing two kinds of test runs were conducted;

Run #1: molten PbLi temperature was at 300 °C for around 170 h.(Isothermal)

Run #2: molten PbLi temperature was increased from 300 °C upto 500 °C. (Heating-up test)

In a design of PbLi blanket, it is proposed to operate at highertemperature. However, the present study is primarily oriented forthe PbLi MHD thermofluid. The experiment temperatures weredetermined from a viewpoint of keeping the PbLi melt duringexperiments. The PbLi melting temperature is 235 °C. The presenttemperature range (around 300-500 °C) is high enough for the PbLiMHDthermofluid because similarity laws exist in heat transfer andflows, and eliminates some problems related to a high-temperatureoperation, such as an enhancement of the PbLi corrosion.

The PbLi eutectic alloy was prepared by the Atlantic Metals &Alloys, Inc. The chemical composition of the PbLi alloy was 81 at%in Pb and 19 at% in Li with some impurities (Cu, Zn, Fe, Ag, Biand Si).

3.2. Results and discussion

The results of electrical insulation test are shown in Figs. 2 and 3.Fig. 2 shows the results of Run #1, indicating that the SG coatinginsulated the electric current between the molten PbLi at 300 °Cand its substrate for around 170 h. Fig. 3 shows the results of Run#2, indicating that the electrical insulation coating was broken toallow the electric current at around 430 °C. Another similar testwas conducted, and showed the electrical insulation was brokenat around 410 °C. These results indicate the SG coating cured up toaround 370 °C have a threshold for the electrical insulation breaksabove 400 °C of the molten PbLi temperature.

4. SEM observation with EDS analysis

4.1. Results and discussion

Scanning electron microscopy (SEM) observations together withenergy-dispersive X-ray spectroscopy (EDS) were conducted toexamine the cured SG coating surface, structure and thickness. TheSG coating structure is significant for the coating compatibility withthe molten PbLi. Fig. 4 shows the SEM images of the SG coatingsurface. The SEM images revealed that the SG coating consisted ofintegrated network of around 5μm particles.

In order to observe cross-sections of the SG coating after theelectrical insulation test, theSGcoated cupwascut intosomepiecesbefore a resin impregnation, and consecutively a surface polishingprocess. Figs. 5 and 6 show the SEM images of SG coating cross-sectionsexposed and unexposed to the molten PbLi in Run #1 ofthe electrical insulation test, respectively.

In Fig. 5, a coarser area in between the bulk SG coating and substratewas the roughened substrate surface. It depicted that the SGcoating was combined to its roughened substrates not chemicallybut physically. That is why the SG coating adhesion is weaker thanthe other processes such as the HDA process. The SEM observation

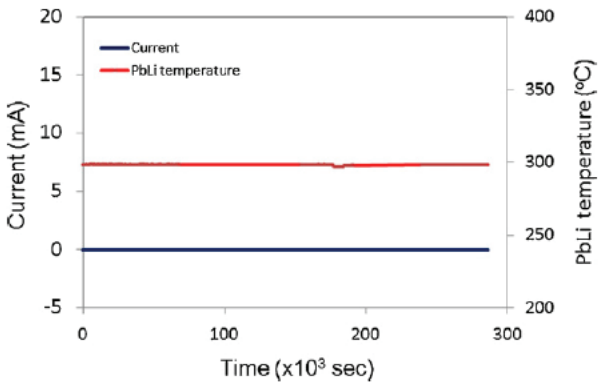

Fig. 2 Electrical insulation test (Run #1)

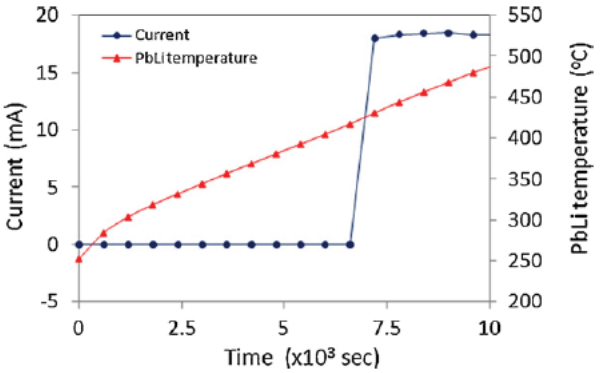

Fig. 3 Electrical insulation test (Run #2)

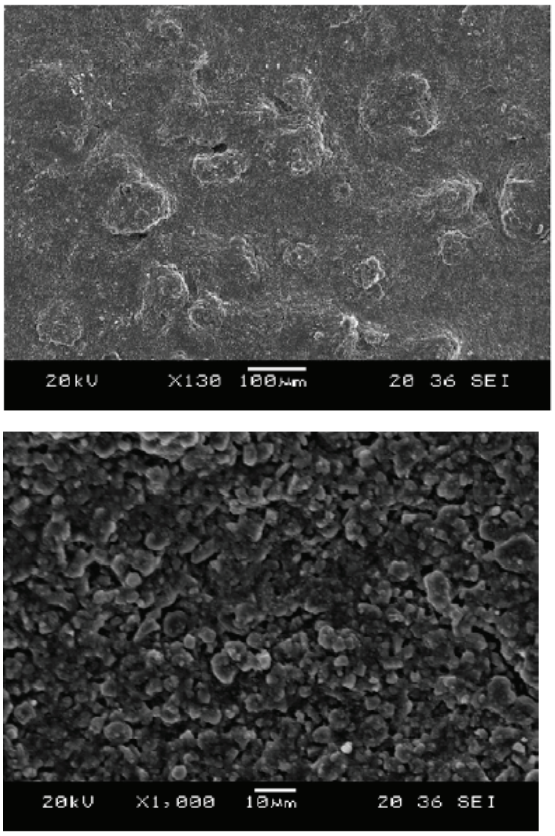

Fig. 4SEM images of the Al_2O_3 coating surface (top: ×130, bottom: ×1000)

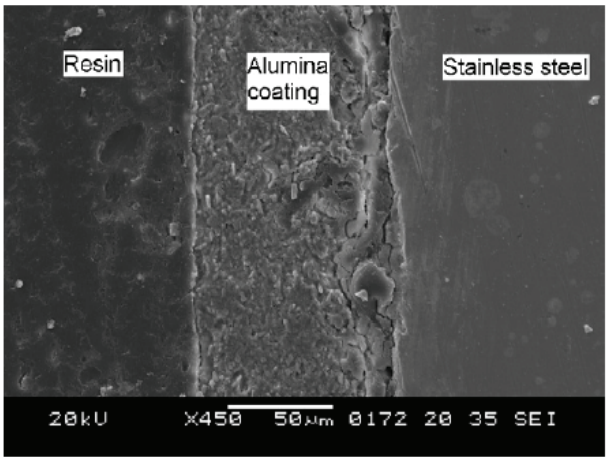

Fig. 5 SEM image of the Al_2O_3 coating cross-section without experience of moltenPbLi exposure during the electrical insulating test

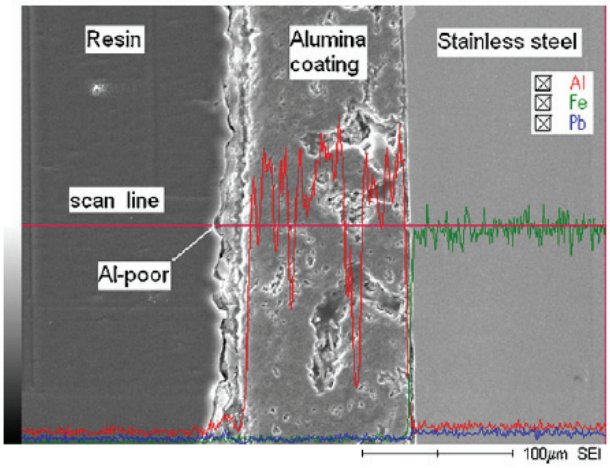

Fig. 6 SEM image of the Al_2O_3 coating cross-section with experience of molten PbLiexposure during the electrical insulating test

also showed the SG coatings were around 100μmof average thicknesswith concave–convex surfaces. Based on these results, it wasfound that the SG coating was approximately 10 times more effective in the coating resistance than the almost electrical insulationvalue: $\rho_i\delta_i=10^5\Omega m^2$, assuming that the SG coating has same electricalresistivity as employed in the coating resistivity estimation[13].

Figure 6 showed the SG coating surface was corroded by the moltenPbLi by the depth of around 15-25μm, and Al in the corroded SGcoating layer decreased after the 170 h exposure in the molten PbLi,however Pb in the Al-poor layer was still small. Therefore, it wasconcluded that Al in the SG coating was transferred into the moltenPbLi, but the SG layer did not allow the molten PbLi to permeateinto itself in the present study. If the SG coating is exposed in themolten PbLi flows, the PbLi corrosion will be more serious thanin the present study. More experiments on the corrosion behaviorin the PbLi flows are necessary to examine whether or not thecorrosion rate is within an acceptable level.Fig. 6 also depicted that there were large pores in the SG coatingnear its substrate. The large pore will increase the entire electricalresistivity of the SG coating. On the other hand, they may enhance the coating peelings or cracks.

4.2. Discussion on the electrical insulation break

A mismatch of thermal expansion is a dominant parameter forcoating adhesion durability. In the present study, a thermal expansionmismatch between the Al_2O_3 coating and its substrate causedthe coating detachment or the crack with the PbLi temperatureabove the curing temperature, resulting in the electrical insulationbreaks. A previous study [15] showed that an undercoatingbetween a stainless steel and an Al_2O_3 coating with the coefficientof thermal expansion close to Al_2O_3 could overcome the coatingcracks or peelings. In addition to the mismatch of thermal expansions,poor adhesion of the Al_2O_3 coating caused coating cracks orpeelings more easily. The SEM together with EDS analysis showedthat the PbLi corrosion did not reach the substrate, only in the surfaceregion of the SG coating. Therefore, all the results indicate thatthe mismatch of the thermal expansions is the primary contributorto the electrical insulation break.

The curing processes and conditions are also dominant parametersfor the SG method to determine the coating structure. Curingthe SG coatings at higher temperature may improve the SG coatingperformance to be durable up to the higher curing temperature.More experiments on the curing temperature issue are necessaryfor the detailed discussion.

5. Conclusions

The present study discusses the feasibility of the Al_2O_3 coatingfabricated by the SG method as an electrical insulation coatingfor molten PbLi through the electrical insulation test in the moltenPbLi pool and the SEM together with EDS analysis on the SG coatingstructure. The present study conclusions are summarized asfollows:

(1) The SG coatings worked as an electrical insulating coating for170 h in a molten PbLi pool at 300 °C in the present study.The SG coating performance in longer operation still remainsto be evaluated. Nevertheless, the SG coating fabricated willhave a potential electrical insulation for PbLi MHD thermofluidstudies with both the operation time and the temperaturelimitation.

(2) The present results indicate the SG coating cured up to around370°C have a threshold for the electrical insulation break above400 °C. More experiments on the curing temperature issue arenecessary for the detailed discussion.

(3) The SEM with EDS analysis revealed the structural characteristicsof the SG coating, and the PbLi corrosion occurred duringthe electrical insulation test, indicating that the primary contributionto the electrical insulation break was not from

thePbLicorrosion, but was due to the mismatch of the thermalexpansions between the SG coating and the substrate.

Further investigations on material interactions and chemistrycontrol issues associated with the fabrication process, the stabilityand the performance of the SG coating are necessary even for theusage in PbLi MHD thermofluid study.

Acknowledgements

The authors are grateful for great help and fruitfuldiscussion on the SEM/EDS analyses with Dr. Masatoshi Kondo andProf. Akio Sagara at National Institute for Fusion Science (NIFS),Japan.

References

[1] D.L. Smith, J.-H. Park, I. Lyublinski, V. Evtikhin, A. Perujo, H. Glassbrenner, etal., Progress in coating development for fusion systems, Fusion Eng. Des. 61–62(2002) 629–641.

[2] Y. Wu, F.D.S. Team, Conceptual design activities of FDS series fusion powerplants in China, Fusion Eng. Des. 81 (2006) 2713–2718.

[3] Z. Guo, Q. Huang, Z. Yan, Y. Song, Z. Zhu, S. Gao et al., Compatibilities of atmosphericplasma sprayed Al2O3 coatings on CLAM with liquid LiPb, Fusion Eng.Des., (2010), doi:10.1016/j.fusengdes.2010.04.007.

[4] L. Giancarli, L. Baraer, B. Bielak, M. Eid, M. Futterer, E. Proust, et al., Europeanreference design of the water-cooled lithium–lead blanket for a demonstrationreactor, Fusion Technol. 26 (1994) 1079–1085.

[5] P.F. Tortorelli, Dissolution kinetics of steels exposed in lead–lithium and lithiumenvironment, J. Nucl. Mater. 191–194 (1992) 965–969.

[6] B.A. Pint, K.L. More, Transformation of Al_2O_3 to $LiAlO_2$ in Pb–17Li at 800 ^oC, J.Nucl. Mater. 376 (2008) 108–113.

[7] H. Glasbrenner, K. Stein-Feechner, J. Konys, Scale structure of aluminized Manetsteel after HIP treatment, J. Nucl. Mater. 283–287 (2000) 1302–1305.

[8] C. Chabrol, E. Rigal, F. Schuster, Report CEA, No. 73/97, CEA Grenoble,1997.

[9] A. Perujo, T. Sample, E. Serra, H. Kolbe, Low aluminum content permeationbarrier coatings for din 1.4914 martensitic steel (Manet), Fusion Technol. 28(1995) 1256–1261.

[10] G. Benamati, C. Chabrol, A. Perujo, E. Rigal, H. Glassbrenner, Development oftritium permeation barriers on Al base in Europe, J. Nucl. Mater. 271–272 (1999)391–395.

[11] J. Konyz, W. Krauss, Z. Voss, O. Wedemeyer, Comparison of corrosion behaviorof bare and hot-dip coated EUROFER steel in flowing Pb–17Li, J. Nucl. Mater.367–370 (2007) 1144–1149.

[12] H. Glasbrenner, J. Konys, Z. Voss, O. Wedemeyer, Corrosion behavior of Albased permeation barriers in flowing Pb-17Li, J. Nucl. Mater. 307–311 (2002)1360–1363.

[13] L. Buhler, S. Molokov, Magnetohydrodynamic flow in ducts with insulatingcoatings, Report KfK 5103, Forschungzentrum Karlsruhe, 1993.

[14] D.L. Smith, J. Koneys, T. Muroga, V. Evitkhin, Development of coatings for fusionpower applications, J. Nucl. Mater. 307–311 (2002) 1314–1322.

[15] M. Nakamichi, H. Kawamura, Out-of-pile characterization of Al_2O_3 coating aselectrical insulator, Fusion Eng. Des. 58–59 (2001) 719–723.

Task 1-3(2)Acoustic Propertiesof Pb-17Li Alloy for Ultrasonic DopplerVelocimetry

Y. Ueki[a], M. Hirabayashi[b], T. Kunugi[a], T. Yokomine[a], K. Ara[b]

[a]*Department of Nuclear Engineering, Kyoto University, Yoshida, Sakyo, Kyoto 606-8501, Japan*
[b]*Japan Atomic Energy Agency, 4002 Narita, Oarai, Ibaraki, 311-1393, Japan*

ABSTRACT

In a lead-lithium (Pb-17Li) liquid metal blanketconcept, Pb-17Li eutectic alloy circulates both as breederand coolant under a strong plasma-confining magneticfield, experiencing magnetohydrodynamic (MHD) force:Lorentz force. An important aspect of the bilateralUS/Japan collaboration on Tritium, Irradiations, andThermofluid for America and Nippon (TITAN) is toinvestigate tritium behavior and thermal control in thePb-17Li eutectic alloy, flow and heat transfercharacterizations, and mitigation of MHD effects. Thepresent paper focuses on Ultrasonic Doppler Velocimetry(UDV) as an effective diagnostic to measure the Pb-17Liflow in the presence of the strong magnetic field. Thispaper firstly describes a favorable wetting material forhigh-temperature transducer. Next, the acoustic propertydatabase of Pb-17Li eutectic alloy is presented. Finally,material analyses after high-temperature measurementsare performed to discuss the durability of titaniumtransducer.

1. Introduction

In some liquid metal fusion blanket concepts, leadlithiumeutectic alloy (Pb-17Li) circulates as a breeder(e.g. helium-cooled lead-lithium (HCLL) blanket concept[1]), or both as a breeder and a coolant (e.g. dual-coolantlead-lithium (DCLL) blanket concept [2]). The liquidmetal motion in a strong magnetic field $\boldsymbol{B}$ induces anelectric current $\boldsymbol{J}$, and then interacts with the strongmagnetic field. As a result, the Lorentz force, $\boldsymbol{J}\times\boldsymbol{B}$dominates the liquid metal flow under the strong magneticfield. The heat and mass transfer of the liquid metal flowunder a strong magnetic field are also significantlyaffected by the Lorentz force, known as magnetohydrodynamic(MHD) effects.

In a nuclear fusion blanket, MHD phenomena arecombined with a volumetric heating due to high neutronflux loading, and eventually provoke buoyancy flows.

Especially in the DCLL blanket, full turbulenceclosure modeling for MHD flows combined withbuoyancy effects is very difficult [3]. Therefore, thepredictions of tritium behavior are even more difficult. Atpresent, understandings of MHD flows in fusion-relevantconditions are limited at a qualitative level. Prototypicphysical experiments have been required to study themajor multiple effects, but have not been conducted yet inspite of their own significance.

In order to comprehend the liquid Pb-17Li flowcombined with buoyancy force in a strong magnetic field,Ultrasonic Doppler Velocimetry (UDV) was expected asan appropriate diagnostic. The UDV is based on a pulsedultrasonic echography together with detection of theinstantaneous Doppler shift frequency [4]. A pulsedultrasonic travelling time between its emission andreception provides the spatial information, and theDoppler shift frequency provides the velocity information.Since liquid metals are opaque fluids,all optical methodsused to measure velocities, such as a Particle ImageVelocimetry (PIV), cannot be applied to any liquid metalflows. The UDV needs no optical windows, and is a noninvasiveflow measuring technique applicable to liquidmetals.

Until now, the UDV has been applied to various liquidmetals, such as mercury [4], gallium [5] using normaltransducer, and lead-bismuth (PbBi) using acoustic waveguide[6]. Nevertheless, the UDV technique has not beenapplied to any liquid Pb-17Li flows. Pb-17Li has highmelting point (235 ^{o}C). An ultrasonic transducer requiresheat resistance, and also favorable ultrasonic transmissionat the material interface between liquid Pb-17Li and thesurface material of the high-temperature transducer. TheUDV requires a sound speed of the target fluid to evaluatethe time of flight (TOF) of a pulsed ultrasonic. In addition,the acoustic impedances, i.e., the product of the densityand the sound speed, characterize the ultrasonicbehaviors at the material interface: acoustic transmission,reflection and refraction.

In the present paper, a favorable material of hightemperaturetransducer is firstly presented, and then thetwo acoustic properties of liquid Pb-17Li are reported.Next, material analyses are performed to discuss thedurability of the high-temperature transducer.

2. Ultrasonic transmission test

Firstly, the ultrasonic transmission test was conducted.The ultrasound reflects at a material interface dependingon the acoustic impedance. Large difference of acousticimpedances between liquid Pb-17Li and a surfacematerial of a high-temperature transducer degradesultrasonic transmission at the interface. In addition, theinsufficient wetting of the transducer surface materialagainst liquid Pb-17Li prevents the ultrasound fromtransmitting efficiently at the material interface. Theymight lead to insufficient signal/noise(S/N) ratio whenevaluating the sound speed in liquid Pb-17Li fromtransmission signal through itself, and applying the

UDVfor liquid Pb-17Li flow.

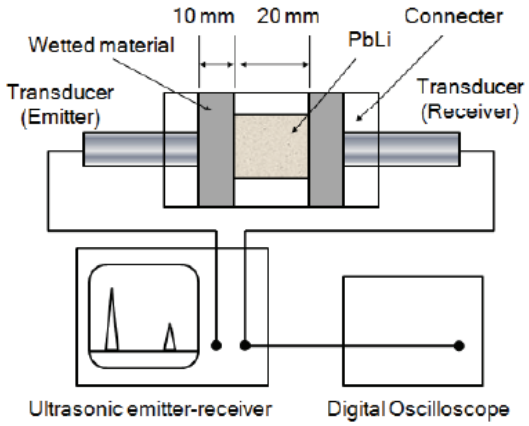

Fig.1 Liquid Pb-17Li ultrasonic transmission test

In order to clarify the transmission characteristics atthe interface between liquid Pb-17Li and the surfacematerial of high-temperature transducer, the ultrasonictransmission test was performed.

2-1. Experimental Setup and Conditions

Figure 1 shows the ultrasonic transmission testapparatus. The wetted materials were assembled at eachside of the horseshoe-shaped holder whose thickness was20 mm. The material of horseshoe-shaped holder wasSUS304. The Pb-17Li wetted material was 40 mm squareand 10 mm in thickness.

The test apparatus let the liquid Pb-17Li exposed tothe surrounding gas, so that the Pb-17Li handling in anArgon-filled glove box was unavoidable because of theserious oxidation of liquid Pb-17Li. Tests were conductedunder strictly humidity-controlled and oxygen-controlledatmosphere of the glove box (under 1ppm). The wettedsurfaces were mirror-finished to improve ultrasonictransmission at the liquid-wall interface because the roughsurfaces hold gas in their own surface gaps to degradeultrasonic transmission at the interface. Titanium (Ti) wasused as the transducer surface material. Titanium has thefavorable compatibility with the piezoelectric element athigh-temperature because the thermal expansioncoefficient of Ti is comparable with the piezoelectricelement material ($LiNbO_3$).

The holder was filled with the liquid Pb-17Li beforethe holder and the transducers were preheated. Thetransducers were connected to the ultrasonic emitterreceiver,and the pulsed ultrasonic waves were emittedinto the liquid Pb-17Li through the test material. Ti platewas wetted at 420 ^{o}C for around 10 hours. At every onehour, the ultrasonic transmission was tested.

The high-temperature transducers were fixed on thetest materials by the connectors. Figure 2 shows thetransducer geometry (JAEA-type transducer). Thetransducer was endurable up to at 500 ^{o}C. The mainemission frequency was 4 MHz, and the pulse repetitioninterval was 2 msec.

2-2. Results and Discussion

At the beginning of the liquid Pb-17Li wetting, theultrasonic transmission at the interface was sufficient forevaluating the signals through the liquid Pb-17Li. Figure3 shows the ultrasonic transmission signal through thestagnant liquid Pb-17Li.

The ultrasonic transmission improved with time, i.e.the wetting condition improved with time. It meant theliquid Pb-17Li corrosion effects could manifest. Theliquid Pb-17Li corrosion effects on the ultrasonictransmission will be discussed in the following section.

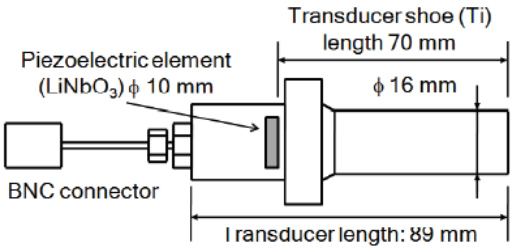

Fig.2 High-temperature transducer

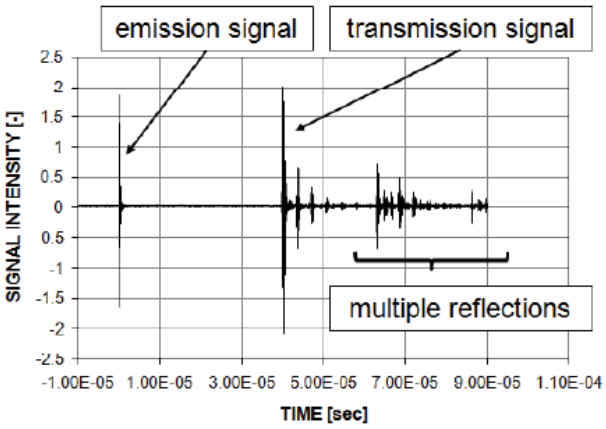

Fig.3 Ultrasonic transmission signal (Liquid Pb-17Li at 420 ^{o}C)

3. Acoustic properties of liquid Pb-17Li

The sound speed in liquid Pb-17Li was evaluated bythe pulsed ultrasonic transmission path-length betweenthe emitter and the receiver divided by the TOF of pulsedultrasonic waves.

3-1. Experimental Setup and Conditions

Figure 4 shows the apparatus to evaluate the soundspeed in liquid Pb-17Li. The apparatus consisted of ahorizontal conduit for the transmission path, two verticalholes as the Pb-17Li inlet/outlet, the gas vents, and thethermocouple port measuring the liquid Pb-17Litemperature. The material of the apparatus was SUS304.The Ti high-temperature transducers were attached to theapparatus, so that the distance between the

twotransducers was precisely 100.0 mm. The four electricheaters were horizontally inserted into the apparatus. Theapparatus was preheated up to 300 °C before filled withthe liquid Pb-17Li. The temperature of the liquid Pb-17Liwas measured by the thermocouple inserted into thevertical hole and was adjusted by a temperature controller.The test apparatus let the liquid Pb-17Li exposed to thesurrounding gas, so that the measurement was performedin the Argon-filled glove box.

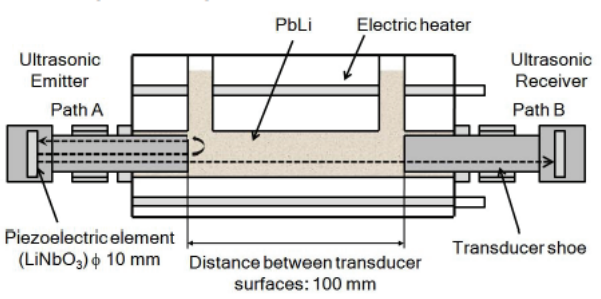

Fig. 4 Sound speed measurement test apparatus

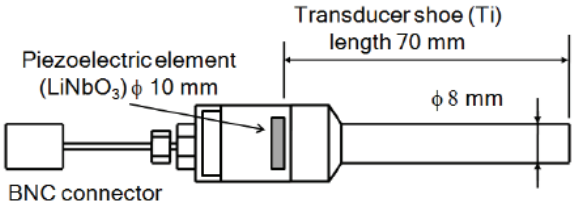

Fig. 5 High-temperature transducer

Figure 5 shows the transducer geometry (JAEA-typetransducer). The piezoelectric element of the transducerwas the lithium niobate (LiNbO3) and attached to thetransducer shoe by high-temperature brazing. Thepiezoelectric element was 10 mm in diameter, and themain emitting frequency was 4 MHz. The transducer shoewas 70 mm in length, made of Ti. The transducer wasendurable up to around 500 oC. The transducers wereconnected to the ultrasonic emitter/receiver. Theultrasonic waves were emitted into the liquid Pb-17Li,travelling through it and received by the other transducer.The received signals were recorded by a digitaloscilloscope. The sampling frequency was 1.25 GHz. Themeasurement temperature ranged from 240 up to 510 °C.Before the measurement of the liquid Pb-17Li, apreliminary check was performed using an ethanol atroom temperature. The measured sound speed in theethanol was within 1% error compared to the referencevalue.

3-2. Results and Discussions

Figure 4 also shows the schematic view of the soundspeed measurement. The transmission time in liquid Pb-17Li was evaluated by the time difference between thetransmission paths A and B, since the shoe lengths of twotransducers were equal. Figure 6 shows an example of themeasured signals. The signals transmitting the paths Aand B shown in Figure 6 were overlapped with referenceto the input signals. The first large peak was the reflectionsignal at the shoe-(Pb-17Li) interface (Path A), and thesecond large peak was the transmission signal through theshoes and the liquid Pb-17Li (Path B). Since two shoelengths were equal, the time difference between twopeaks corresponded to the transmission time throughliquid Pb-17Li.

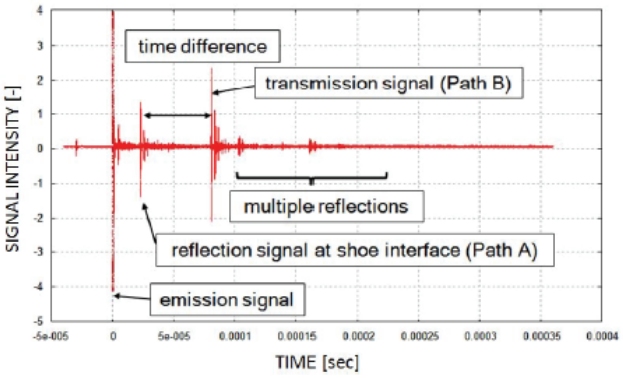

Fig. 6 Measured signal (liquid Pb-17Li at 500 °C)

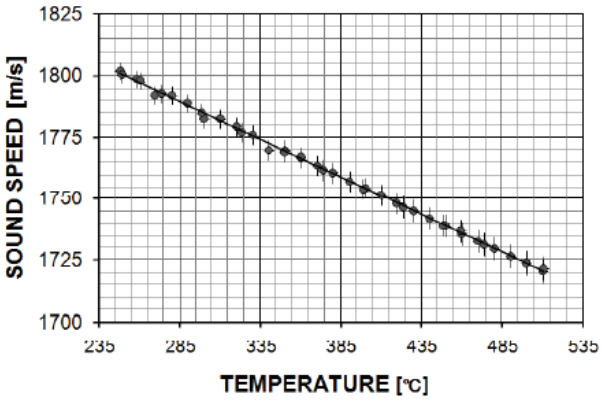

Fig. 7 Temperature dependency of sound speed in liquidPb-17Li

Figure 7 shows the dependency of the sound speed inliquid Pb-17Li on temperature. As well as sodium [7] andlead-bismuth [8], the sound speed in liquid Pb-17Li haslinearity to temperature, and thus the sound speed wasevaluated by the linear approximation method. Theexperimental correlation equation relating the soundspeed in liquid Pb-17Li, CPbLi, to the liquid temperature, T[°C], is given as follows;

$$C_{PbLi}[m/s] = 1876 - 0.316T \quad (240 \le T[^{\circ}\mathrm{C}] \le 510) \qquad (1)$$

Using liquid Pb-17Li density [9], the acoustic impedanceof liquid Pb-17Li, $Z_{PbLi}=\rho_{PbLi}C_{PbLi}$, is given as follows;

$$Z_{PbLi}\left[kg/m^2 s\right] = 1.87\times10^7 - 6.20\times10^3 T + 0.513T^2 \quad (240 \le T\left[^{\circ}\mathrm{C}\right] \le 450) \quad (2)$$

In measuring sound speed in liquid Pb-17Li, errors arecaused by the measurement error of the transmission pathlength, a reading error of the signal peak values and ameasurement error of the liquid Pb-17Li temperature. Themeasurement error of the transmission path length wasfound to be the largest among them, because the distancebetween two transducer surfaces was displaced from thelength measured at room temperature due to the thermalexpansion. As the error of the transmission path lengthderived from thermal linear expansion coefficients wasestimated within ± 1mm, the error of the sound speed inliquid Pb-17Li was within ± 3 m/s. The reading error ofthe signal peak values and the temperature measurementerror sums up to be ± 7 m/s as the total measurement error.The horizontal error bar shows the temperature measuringerror by the thermocouple. The vertical error bar showsthe sound speed measuring error.

4. Effects of surface structureat liquid-wall interface

In application of the ultrasonic technique to liquid Pb-17Li flow velocity measurement, the wetted materialagainst liquid Pb-17Li, i.e. the shoe material, is requiredto withstand the corrosion and the dissolution into theliquid Pb-17Li. In the ultrasonic transmission test, Ti testplate was employed as the liquid Pb-17Li wetted material,resulting in the transmission was improved with thewetting time. It meant the Ti test plate was corroded bythe liquid Pb-17Li to be better wetted, resulting in theimprovement of the ultrasonic transmission at the materialinterface. Two material analyses were conducted toclarify the surface characteristics effects on the ultrasonictransmission. One was the surface roughnessmeasurement using an atomic force microscope (AFM).The other analysis was a scanning electron microscopic(SEM) observation with an energy dispersivespectrometer (EDX).

4-1. Surface Roughness Measurement

After the transmission test, the Pb-17Li was adherentto the Ti test plate. The Pb-17Li adherents were removedchemically using the mixture solution of an acetic acid, anethanol and a hydrogen peroxide (1:1:1) until the testplate weight kept constant. Firstly, the wetted surface wasobserved by an optical microscope, and the surfaceroughness and the submicron structure were measuredusing the AFM (Keyence VN-8000). Arithmetic averagedroughness, *Ra*, Maximum depth, *Ry*, and 10-pointaveraged roughness, *Rz*, were employed to evaluate thesurface characteristics. The surface roughness definitionsemployed were JIS standard (1994).

Figure 8 shows the optical images. The left image isthe picture of the Ti plate surface before the liquid Pb-17Li, and the right is the picture of the Ti plate surfaceafter the Pb-17Li wetting at 420 oC for around 10 hours.The color change of the Ti surface was found. Table1 shows the surface roughness measurement result. Thearithmetic roughness of the wetted surface increasedaround 700% compared to the original surface.

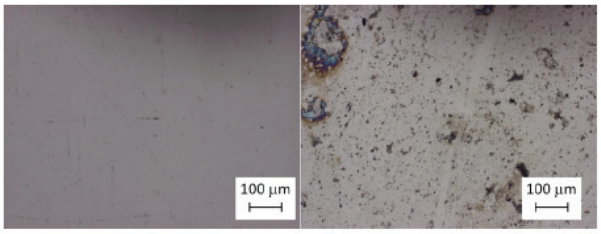

Fig. 8 Optical observation (left: Ti plate before Pb-17Liwetting, right: Ti plate after Pb-17Li wetting)

Table 1. Measurement result

Titanium surface	Ra [nm]	Ry [nm]	Rz [nm]
Before PbLi wetting	14.84	326.0	184.1
After PbLi wetting	100.8	2944	2046

4-2. SEM Observation with EDX Analysis

The other Ti test plate after the ultrasonictransmission test was set in an epoxy resin and cut itbefore polishing the cutting surface. A cross-section ofresin-(Pb-17Li)-substrate interface was observed usingthe SEM with the EDX (JEOL JED-2140). Figure 9shows the SEM images of the cross-sectional Ti plate, Pbelement mapping, and Ti element mapping. It showed thePb-17Li was adherent to the Ti surface, but nomicrometer scale corrosion was observed.

4.3. Discussion

Taking the two results into consideration, the liquidPb-17Li corrosion effects were limited to the submicronscale in the time scale for achieving sufficient ultrasonictransmission for the UDV measurement. That is becausethe liquid Pb-17Li exposure time in the transmission testwas too short for the micrometer scale corrosion tomanifest. The time scale of ordinary corrosionexperiments is order of 103 hours. From the point of viewof transducer durability, it is favorable to achieve thesufficient transmission at the beginning of the liquid Pb-17Li exposure, and for the high-temperature transducernot to have serious damages in time scale for achievementof the sufficient transmission.

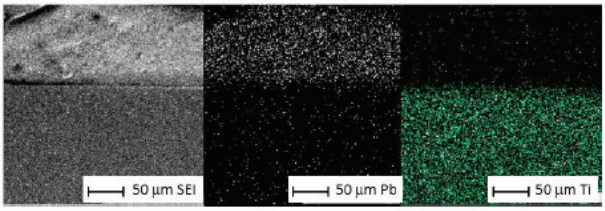

Fig. 9 SEM image of cross-sectional Ti plate (left),

Pbelement mapping (center), Ti element mapping (right)

5. Conclusions

The conclusions of the present research regarding thedevelopment of liquid Pb-17Li flow speed measurementusing high-temperature UDV technique are as follows:

(1) Titanium has favorable sound characteristic to liquidPb-17Li eutectic alloy, and is a promising materialas surface of high-temperature transducer to achieveultrasonic emission into liquid Pb-17Li sufficient forUDV measurement. It is confirmed that Titaniumhigh-temperature transducer is suitable for UDVmeasurement of liquid Pb-17Li flow.
(2) The sound speeds in liquid Pb-17Li were measuredin the temperature range from 240 up to 510 ^{o}C. Thesound speed in liquid Pb-17Li shows the linearity intemperature, as well as other liquid metals. Theexperimental correlations of the two acousticproperties were obtained.
(3) Liquid Pb-17Li corrosion thickness of Titanium waslimited to submicron meter after the ultrasonictransmission test. The durability of titanium high-temperaturetransducer was confirmed in the rangeof the present experimental conditions.

The remaining issue in applying UDV for liquid Pb-17Li flow is to find appropriate tracer particles reflectingemitted ultrasonic pulses in liquid Pb-17Li to the high-temperaturetransducer in its listening mode. Since theexcessive or deficient tracer particles such as liquid metaloxides particles prevent us from appropriate UDVmeasurement, an evaluation of appropriate amount andsize of tracer particles is necessary for achieving liquidPb-17Li flow measurement by UDV technique.

Acknowledgements

This work was partly supported by “Energy Science inthe Age of Global Warming” of Global Center ofExcellence (G-COE) program (J-051) of the Ministry ofEducation, Culture, Sports, Science and Technology ofJapan.This research was partly performed under thecollaboration program of the Laboratory for ComplexEnergy Processes, Institute of Advanced Energy,KyotoUniversity.

References

[1] G. Rampal et al. “HCLL TBM for ITER-DesignStudies, Fusion Eng. Des., 75-79, 917-922, (2005)
[2] C. P. C. Wong et al., “An Overview of DualCoolant Pb-17Li Breeder First Wall and BlanketConcept Development for the US ITER-TBMDesign”, Fusion Eng. Des., 81, 461-467, (2006)
[3] S. Smolentsev et al., “Characterization of KeyMagnetohydrodynamic Phenomena in PbLi Flow forthe US DCLL Blanket”, Fusion. Eng. Des, 83, 771-783, (2008)
[4] Y. Takeda, “Velocity Profile Measurement byUltrasonic Doppler Method”, Experimental Thermaland Fluid Science, 10, 444-453, (1995)
[5] D. Brito et al., “Ultrasonic Doppler Velocimetryin Liquid Gallium”, Experiments in Fluids, 31, 653-663, (2001)
[6] S. Eckert et al., “Velocity Measurements at HighTemperatures by Ultrasonic Doppler Velocimetryusing Acoustic Wave Guide”, Experiments in Fluids,35, 381-388, (2003)
[7] H. Hayashiba et al., Proc. of 8th Int. Conferenceon Nuclear Engineering (ICONE8), 8409, (2000)
[8] M. Hirabayashi et al., “Development ofUltrasonic Flow Meter for Liquid Lead-BismuthFlow”, Proc. of 13th Int. Conference on NuclearEngineering (ICONE13), Beijing, China, May 16-20,2005, 50346, (2005)
[9] B. Shultz, “Thermophysical Properties of thePb(83)Li(17) Alloy” Fusion Eng. and Des., 14, 199-205, (1991)

Task 1-3(3)Velocity Profile Measurementof Lead-Lithium Flows by High-Temperature Ultrasonic DopplerVelocimetry

Y. Ueki[a], M. Hirabayashi[b], T. Kunugi[a], K. Nagai[b], J. Saito[b], K. Ara[b], N. B. Morley[c]

[a]*Department of Nuclear Engineering, Kyoto University, Yoshida, Sakyo, Kyoto 606-8501, Japan*
[b]*Japan Atomic Energy Agency, 4002 Narita, Oarai, Ibaraki, 311-1393, Japan*
[c]*Mechanical and Aerospace Engineering Department, University of California, Los Angeles, 420 Westwood Plaza, 44-114 Engineering IV, Los Angeles, CA 90095, USA*

ABSTRACT

This paper describes a high-temperature ultrasonicDoppler Velocimetry (HT-UDV) technique that has beensuccessfully applied to measure velocity profiles of thelead-lithium eutectic alloy (PbLi) flows. The impact oftracer particles is investigated to determine requirementsfor HT-UDV measurement of PbLi flows. The HT-UDVsystem is tested on a PbLi flow driven by a rotating-disk inan inert atmosphere. We find that a sufficient amount ofparticles contained in the molten PbLi are required tosuccessfully measure PbLi velocity profiles by HT-UDV.An X-ray diffraction analysis is performed to identify thoseparticles in PbLi, and indicates that those particles weremade of the lead mono-oxide (PbO). Since the specificdensities of PbLi and PbO are close to each other, the PbOparticles are expected to be well-dispersed in the bulk ofmolten PbLi. We conclude that the excellent dispersion ofPbO particles enables the HT-UDV to obtain reliablevelocity profiles for operation times of around 12 hours.

1. Introduction

The heat and mass transfer in a liquid metal flow underthe influence of a plasma-confining magnetic field issignificantly affected by magnetohydrodynamic (MHD)effects arising from the interaction between the appliedfield and electrical currents induced inside the movingliquid metal (such as lead-lithium eutectic alloy: PbLi).However, the understanding of MHD flows in fusion-relevantconditions is limited since the MHD flow regimesare determined by multiple effects such as a strongmagnetic field, buoyancy forces, an interfacial phenomenarelated to the liquid metal wettability, and the complexflow passage geometry[1]. A technique to measure localvelocity inside these opaque liquid metal flows is necessaryto study such effects. Therefore, we have been developinghigh-temperature, ultrasonic Doppler velocimetry (HTUDV)as a PbLi flow diagnostic.

UDV is based on pulsed ultrasonic echographytogether with the detection of the instantaneous Dopplershift frequency[2,3]. The travelling time between the emissionand reception of a pulsed ultrasound provides spatialinformation, and the Doppler shift frequency provides thevelocity.

UDV has the following advantages:

(1) Acquisition of spatial-temporal velocity informationalong the beam line of ultrasound,
(2) A non-intrusive method, and
(3) Applicability to opaque fluids, such as liquid metals.

UDV requires the following prerequisites:

(1) Ultrasonic transmission at the interface of the UDVprobe material and the target fluid,
(2) Acoustic properties of the target fluid, and
(3) Ultrasonic reflecting particles (in other words: tracerparticles).

In addition, UDV can potentially work in hightemperature conditions, and therefore requires high-temperatureUDV probes or waveguide sensors [4,5].

In thisstudy, we employ high-temperature UDV probes since theyare more compact than waveguide sensors, and thereforecan fit in a narrow gap between electromagnets to measurePbLi flows in a magnetic field.In the past, UDV has been applied to various liquidmetals, such as mercury (Hg) [2,3], gallium (Ga) [6,7], and gallium-indium-tin eutectic ally (GaInSn) byusing the normal transducer,8 and sodium (Na) [4],lead-bismuth (PbBi), and bronze (CuSn) by using theacoustic waveguide [5]. Nevertheless, UDV has not beenapplied to PbLi flows. As a prerequisite, the authors havemeasured PbLi acoustic properties, the results of whichindicate that the acoustic coupling between PbLi and thewetting material of the HT-UDV titanium (Ti) tipped probeis good enough for the HT-UDV measurement [9].

The UDV technique requires the presence of ultrasonicreflecting particles inside a target fluid. Artificial or naturalparticles, gas bubbles, or fluctuations in density can workfor this purpose [10]. The UDV signal quality depends onparameters such as the concentration and size of theparticles, as well as the ultrasonic reflection characteristicsof the particles. Usually the liquid metals contain somenatural impurities such as oxide particles etc. It is favorableto utilize these natural impurities suspended in the liquidmetals to work as tracer particles instead of seeding anyartificial tracer particles in the liquid metals. Since mercurycontains a higher concentration of natural oxides,introducing small bubbles are necessary to reflect

emittedultrasound [3]. Additionally, Ga is easily oxidized,contributing to an excess amount of oxide particles thatcauses the multi-scattering of ultrasound. Therefore,artificial particles, which are made of ZrB_2, are added intoGa as tracer particles for the UDV [6,7]. According to the pastreferences, it is important, but not easy, to choose suitabletracer particles for each liquid metal.

A goal of this study is to determine suitable tracerparticles for the HT-UDV measurement of PbLi flows. Weapplied the HT-UDV to a PbLi flow driven by a rotatingdiskin an inert atmosphere glovebox in order to determineif the natural particles contained in PbLi work as tracerparticles. A chemical analysis was also carried out toexamine the chemical composition of the natural particles.

2. Velocity profilemeasurementofPbLi flows

2-1. Experimental setup

The HT-UDV measurement was performed in an argon-filledglovebox, where the oxygen and the moisture werecontrolled to stay under 1 ppm in concentration. PbLiingots (from Atlantic Metals & Alloys, Inc.) were melted ina melt pot inside the glovebox. An oxide layer, floating onthe liquid surface, was removed by using a metallic mesh tomanually scrape the surface. After this treatment, themolten PbLi was transferred to a test cylinder, shown inFig.1. The test cylinder and the disk were made of anaustenitic stainless steel. The test cylinder was 90 mm indiameter, and 120 mm in height, and heated by an electricheater underneath it. Serious PbLi corrosion occurs againstthe stainless steel at temperatures higher than around 400°C.

Based on this limitation, the PbLi temperature wascontrolled to stay at around 320°C, in order to mitigate thePbLi corrosion effect. The physical properties of the moltenPbLi at 320°C are shown in Table 1. The PbLi flow wasdriven by the rotating disk which was spinning in thevicinity of the cylinder bottom. The disk-rotating frequencywas about 500 rpm, either in clockwise and counterclockwisedirections.

Even though the PbLi was melted in the inert glovebox,we observed that the free surface of the molten PbLi wascovered with fine particles after tens of minutes. Still, wewere not sure if the fine particles came from the PbLioxidation or the separation of the particles by the differenceof the specific gravities. Because of our concern about thePbLi oxidation, we carried out second run of the HT-UDVmeasurement approximately 12 hours after the first run.

After the first measurement, the molten PbLi wascontrolled to stay at around 320oC for approximately 12hours.

Table1. Physical properties of molten PbLi (at 320 °C) [9,11]

Melting point	235°C
Density: ρ	9.45 x 10^3 kg/m^3
Kinetic viscosity: ν	2.10 x 10^{-7} m^2/s
Sound velocity: C	1780 m/s

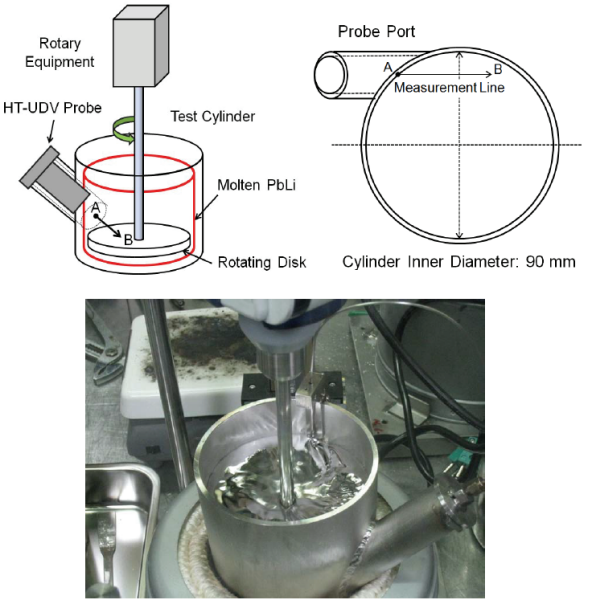

Fig.1. Schematic view and photograph of the HT-UDVmeasurement of the PbLi flow.

In this study, we employed a HT-UDV probe (JAEAtypetransducer) shown in Fig.2. The HT-UDV probe wasloosely inserted into the probe port of the test cylinder. TheHT-UDV probe was connected to a UDV system (UVPMonitor model X-1, by Met-Flow SA). The HT-UDVprobe has a thin Ti membrane at the tip of the probe. Ahigh-temperature piezoelectric element is attached to theinner side of the membrane. The thin membrane is around0.5 mm in thickness. The piezoelectric element is made oflithium-niobate ($LiNbO_3$), and 10 mm in diameter. Ti ischosen as membrane material, since the thermal expansioncoefficient of Ti is comparable with that of piezoelectricelement material. The authors have showed that theacoustic coupling between molten PbLi and Ti tipped probewas satisfactory for the HT-UDV measurement [9]. The HTUDVprobe is 56 mm in length, and 20 mm in diameter.

A set of the UDV measurement parameters is shown inTable 2. The ultrasonic frequency is the basic frequency ofthe emitted ultrasonic waves. The ultrasonic emissionvoltage is the voltage applied to the probes by the UDVsystem in order to emit ultrasonic waves. The number ofemitted cycles is the wavenumber per one pulse. TheDoppler angle is the angle at which the tracer particles aremoving, with respect to the axis of the ultrasonic beam.The pulse repetition rate (f_{PRF}) is a repetition frequency ofthe pulses. The maximum depth (D_{max}) is the maximummeasurable length of the measuring line, and is determinedby $D_{max}=c/2f_{PRF}$. The spatial resolution in molten PbLi inthe longitudinal direction (δ) corresponds to the length ofthe emitted pulse, and is determined by nc/f_0. The spatialresolution in the radial direction is mainly determined bythe diameter of the ultrasonic beam, and is

10 mm in thisstudy.

Table2. Set of system parameters adjusted in thisexperiment

Ultrasonic frequency	4 MHz
Ultrasonic emission voltage	160 V
Number of emitted cycles: n	4
Doppler angle	45°
Pulse repetition rate: f_{PRF}	7812 Hz
Maximum depth: D_{max}	114 mm
Spatial resolution in the longitudinal direction: δ	1.78 mm
Temporal resolution (single profile)	37.2 ms
Number of profiles for averaging	1024

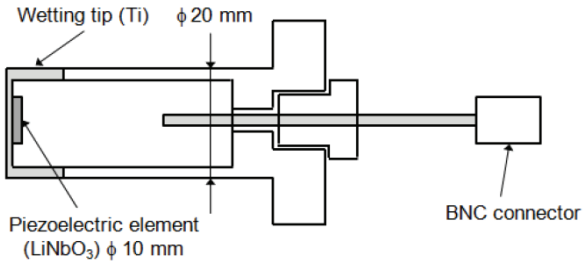

Fig.2. Schematic view and photograph of the HT-UDVprobe

2-2. Chemical composition of PbLi

The PbLi eutectic alloy was fabricated by the AtlanticMetals & Alloys, Inc. in the USA. The chemicalcomposition of the PbLi alloy was examined by aninductively coupled plasma–mass spectrometry (ICP-MS).The chemical composition was 84.2 at% Pb and 15.8at %Li, and at almost the Pb-Li eutectic point (84.3 at% Pband 15.7 at% Li, revised by Okamoto12). The percentage ofimpurities in the alloy was less than the detection limit ofan inductively coupled plasma–Auger electronspectrometry (ICP-AES).

2-3. Measuredvelocity profiles

Mean velocity profiles were determined by averaging1024 single profiles, and shown in Fig.3. The horizontalaxis shows the distance from the cylinder surface, and thevertical axis shows the mean velocity profiles.In this study, we found that the measured velocityprofiles were continuous. When the molten PbLi does notcontain any suitable type or sufficient amount of tracerparticles, we cannot acquire any velocity profiles due to theinsufficient signal reception of the probe. Plus, whenserious oxidation of the PbLi results in too many tracerparticles, this causes a multi-scattering of the emittedultrasounds and the velocity profile is deformed like thecase of Ga. Based on this, we infer that the HT-UDVtechnique was successfully applied to the molten PbLiflows, and that the amount of the tracer particles, whichwere naturally contained in the molten PbLi, was sufficientfor the HT-UDV measurement.

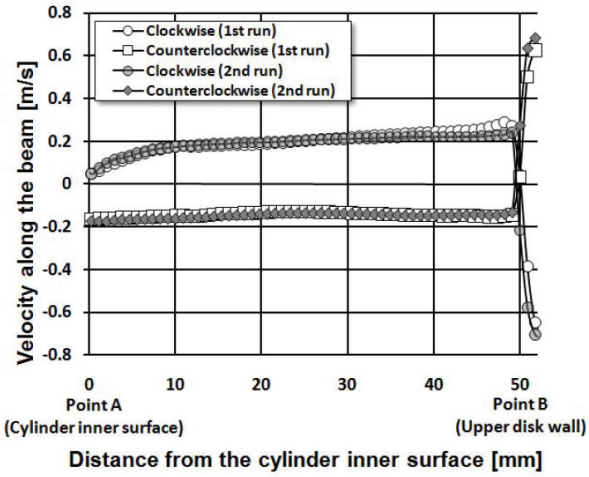

Fig.3. Average velocity profiles along the ultrasonic beam

The local velocities went reversed at the position ofaround 50 mm apart from the cylinder inner surface (PointA hereafter), which indicated that the upper wall of therotating-disk (Point B hereafter) was located at around 50mm away from the Point A. The results agreed with thetesting geometry.

Even after approximately 12 hours, the second run ofthe HT-UDV measurement showed good agreement withthe first run. We infer that the natural particles wereuniformly dispersed in the molten PbLi and worked well asthe ultrasonic reflector, resulting in the sufficient quality ofthe ultrasound signals.

The probe port was installed to the test cylinder with adegree of asymmetry, as shown in Fig.1. Thus, the velocityprofiles were not symmetric especially near the probe port.

3. TracerparticlesforPbLiflows

An X-ray diffraction (XRD) technique was employed toidentify the chemical composition of the natural particledispersed in molten PbLi. The specimen was prepared inthe inert glovebox by maintaining the molten PbLi at 300°Cfor approximately 16 hours before cooling it down, andseparating lighter particles from the bulk of the moltenPbLi. After this treatment, the specimen was packed in theglovebox and transferred to the inert XRD analyzer in orderto avoid the surface oxidation, which happens even at roomtemperature.

Our analysis shows that the bulk of the solidified PbLicontains some amount of a lead monoxide (PbO), despitethe presence of many Li atoms in the molten PbLi. Thespecific density of PbO at room temperature is around9.53 [13], and is close to the 9.45 of PbLi (at 320°C). Becauseof this, we infer that PbO exists uniformly in the bulk, andsmall quantities of PbO exist on the liquid surface due tothe difference in the specific density. Since the meltingpoint of PbO is around 886oC,14 the PbO particles areexpected to be still in solid state at around 320°C, anddispersed in the molten PbLi.

Based on our results, we conclude that the PbO particles,which are naturally contained in molten PbLi, areuniformly dispersed in the molten PbLi to work as HTUDVtracer particles. This is a fortunate conclusionindicating that PbLi does not require any artificial tracerparticles for HT-UDV.

4. Velocityprofilemeasurement of waterflows

We measured a water laminar flow by using the HTUDVin order to characterize the HT-UDV measurementwith respect to the case of the PbLi flows.

4-1. Experimental setup

A simple loop was used in this measurement. A circularpipe made of acrylic was used as the test channel, and was40 mm in diameter. The loop consisted of the test section, apump, and the connecting pipes. The length of the pipe was1000 mm, and the probe was installed at 850 mm from theentrance of the test channel. A water flow was driven byusing the pump, and the flow got developed through thetest section. Artificial reflecting particles were seeded inthe water, in order to give enough scattering signals of theultrasound.

The fully-developed flows were measured by the HTUDVprobe and the UDV system. The set of ultrasonicparameters was the same as the PbLi case. The Reynoldsnumber of the water flow was about 1800, and therefore theflow was a laminar.

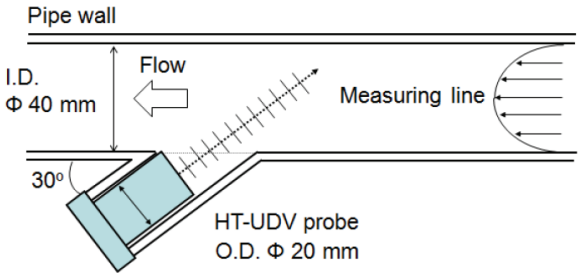

Fig.4. Experimental setup of the velocity measurement ofwater flows.

4-2. Measurement results

The measured velocity was normalized and comparedwith a theoretical solution. Theoretical velocity profile in alaminar regime in a pipe channel is expressed as:

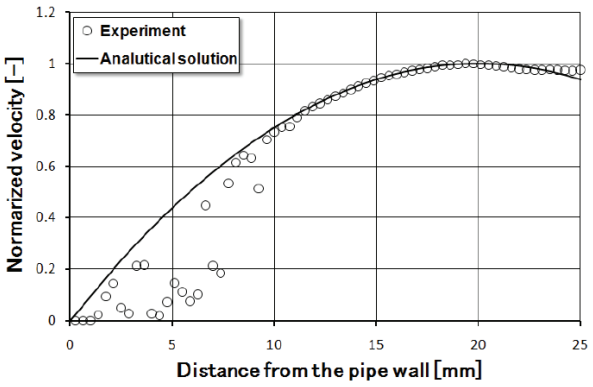

Fig.5. Non-dimensional velocity profile of water

$$\frac{v}{v_{\max}} = 1-(R-r)^2 \qquad (1)$$

where$v$: local velocity, v_{max}: maximum velocity, R: thepipe radius, and r: the distance from the pipe surface.

The normalized velocity profile is shown in Fig.5, withrespect to the analytical solution. The results showed thegood agreement in the range between about 10-20 mmfrom the pipe wall as shown in Fig.5. Plus, Fig.5 showedthat the measured velocity profile had defective region inthe vicinity of the pipe wall (less than about 10 mm fromthe pipe wall).

We conclude that the measurement defect was causedmainly by the effect of the probe port region on the flow,since the probe port was not so small compared to the mainchannel. Compared to room-temperature piezoelectricelements, the piezoelectric element, which is made of$LiNbO_3$, poorly damps the remaining oscillation even whenthe HT-UDV probe was in listening mode of the reflectedechoes. However, the effect of the unstable sound field wasexpected to be less, compared to the effect of the probe portregion.

Plus, Fig.5 showed that the measurement reliability wasnot good beyond around 20 mm from the pipe wall, sincethe ultrasound beam radically spread when it traveled inlongitudinal direction.

5. Conclusions

This study has demonstrated that the HT-UDV has beensuccessfully applied to measure the velocity profiles ofmolten PbLi flows. We have showed that the PbO particles,which are naturally contained in the molten PbLi, havecapability to work as the HT-UDV tracer particles in thetime range of approximately 12 hours.

In order to understand more detailed characteristics ofthe HT-UDV measurement, we are planning to apply theHT-UDV to the PbLi flows in a simple flow passage, suchas a circular or rectangular duct. After this characterization,we will test the HT-UDV under strong

magnetic field, inorder to examine if the HT-UDV is an effective diagnosticof the PbLi MHD flows. The concern is that the HT-UDVprobe, which is electrical conducting, may give anelectrical disturbance to MHD flows which are sensitive toelectrical boundary conditions.

If the HT-UDV has capability to acquire the PbLivelocity profiles under strong magnetic field, the HT-UDVis expected to open new prospects for investigating PbLiMHD flows and heat/mass transfers in the fusion-relevantconditions.

Acknowledgements

This work was supported by Grand-in-Aid for theJapan Society for the promotion of Science (JSPS) researchfellows.

References

[1] S. Smolentsev, R. Moreau, L. Buhler, C.Mistrangelo, "MHD thermofluid issues of liquidmetalblankets: Phenomena and advances", FusionEngineering and Design, 85, 1196-1205 (2010).

[2] Y. Takeda, "Development of an ultrasound velocityprofile monitor", Nuclear Engineering and Design,126, 277-284 (1991).

[3] Y. Takeda, H. Kikura, "Flow mapping of themercury flow", Experiments in Fluids, 32, 161-169(2002).

[4] S. Eckert, G. Gerbeth, "Velocity measurements inliquid sodium by means of ultrasonic Dopplervelocimetry", Experiments in Fluids, 32, 542–546(2002).

[5] S. Eckert, G. Gerbeth, V. I. Melnikov, "Velocitymeasurements at high temperatures by ultrasoundDoppler velocimetry using an acoustic wave guide" ,Experiments in Fluids, 35, 381–388 (2003).

[6] D. Brito et al., "Ultrasonic Doppler velocimetry inliquid gallium", Experiments in Fluids, 31, 653-663(2001).

[7] Y. Tasaka, Y. Takeda, T. Yanagisawa,"Ultrasonic visualization of thermal convective motionin a liquid gallium layer" Flow Measurement andInstrumentation, 19, 131–137 (2008).

[8] A. Cramer, C. Zhang, S. Eckert, "Local flowstructures in liquid metals measured by ultrasonicDoppler velocimetry", Flow Measurement andInstrumentation, 15, 145-153 (2004).

[9] Y. Ueki, M. Hirabayashi, T. Kunugi, T.Yokomine, K. Ara, "Acoustic properties of Pb-17Li Alloy for ultrasonic Doppler Velocimetry",Fusion Science and Technology, 56, 846-850 (2009).

[10] S. Eckert, A. Cramer, G. Gerbeth, "VelocityMeasurement Techniques for Liquid Metal Flows",Magnetohydrodynamics – Historical Evolution andTrends, 275-294, S. Molokov et al. Ed., Springer,(2007).

[11] E. Mas De LesValls, L.A. Sadano, L. Batet,I. Ricapito, A. Alello, O. Gastaldi, F.Gabriel, Lead-lithium eutectic material database fornuclear fusion technology, J. Nuclear Mater. 376,353-357 (2008).

[12] H. Okamoto, "Li-Pb (lithium-lead)", Journal ofPhase Equilibria, 14, 770(1993).

[13] CRC Handbook of Chemistry and Physics, W. M.Haynes (Ed. in chief), the 91st Edition, InternetVersion 2011, CRC press, 2010.

[14] D. Risold, J.-I. Nagata, R.O. Suzuki,"Thermodynamic Description of the Pb-O system",Journal of Phase Equilibria, 19, 213-233 (1998).

Task 1-3(4)Construction and initial operation of MHD PbLi facility at UCLA

T.Kunugi[a], S.Smolentsev[b], T.Yokomie[a], F.-C. Li[b],
Y.Ueki[a], K.Yuki[c], T.Sketchley[b], M. A. Abdou[b]

[a]*Department of Nuclear Engineering, Kyoto University, Yoshida, Sakyo, Kyoto 606-8501, Japan*
[b]*Mechanical and Aerospace Engineering Department, University of California, Los Angeles, 420 Westwood Plaza, 44-114 Engineering IV, Los Angeles, CA 90095, USA*
[c]*Department of Mechanical Engineering, Tokyo University of Science-Yamaguchi, Yamaguchi 756-0884, Japan*

ABSTRACT

We review current accomplishments in Task 1-3 "Flow Control and Thermofluid Modeling" of the Japan-US "TITAN" collaboration program. Our task focuses on experimental activities and also computer modeling of magnetohydrodynamic flows and heat and mass transfer of electrically conducting fluids under conditions relevant to fusion blankets. Since our task started, major efforts were taken to design, construct and test a new magnetohydrodynamic lead-lithium (PbLi) loop at UCLA, to accumulate the PbLi handling technology, and to develop a high-temperature ultrasonic Doppler velocimetry and a differential-pressure measurement system for PbLi flows. In the present paper, the loop construction, the electromagnetic pump performance test, our on-going experiments with the constructed loop are described.

1. Introduction

Because of its lower chemical reactivity with air, water andconcrete compared to pure lithium, eutectic alloy lead-lithiumPbLi (originally Pb17Li, and more recently Pb16Li) has been proposedas a tritium breeder and coolant fluid in several liquidmetal blanket concepts for future fusion power plants, includingself-cooled lead-lithium (SCLL) [1], dual-coolant lead–lithium(DCLL) [2], helium-cooled lead–lithium (HCLL) [3], and water-cooledlead–lithium (WCLL) [4] blankets. Starting from the 1980s,various studies, both experimental and theoretical, were performedfocusing on various aspects of PbLi flows and associated heat andmass transfer phenomena with and without a magnetic field. Forthe last two decades of the 20th century, many experimentalfacilities utilizing PbLi as a working fluid were constructed and successfullyoperated all over the world, some of which are still in use.

Among them are purely hydrodynamic loops (no magnetic field):PICOLO at KIT (former FZK) in Germany [5], ANAPURNA at CEA,France [6], a loop at the ENEA Research Center in Brasimone, Italy[7], and a loop at the Institute of Advanced Energy, Kyoto University,Japan [8]. There are only a few magnetohydrodynamic (MHD) PbLifacilities currently in operation: a loop at the Institute of Physicsin Latvia [9], several MHD PbLi loops DRAGON I–IV at the Instituteof Plasma Physics of the Chinese Academy of Sciences [10–12], andthe ELLI loop at the Korea Atomic Energy Research Institute [13,14].

Using these facilities, many studies were conducted over thelast two decades, focusing on various aspects of PbLi flows withand without a magnetic field, alloy manufacturing, its handling andinteraction of PbLi with structural and functional materials. Amongthem are: compatibility and corrosion behavior of candidate steelsfor fusion reactor blankets [4,9,10,15–25], mechanical properties ofstructural materials exposed to PbLi flows [26], physical–chemicalprocesses associated with the extended use of PbLi in blanket-relevantconditions [27], chemical interaction between liquidPbLi with oxygen-containing gases and water [28–30], onlinemonitoring of liquid PbLi composition [31,32], PbLi impuritycontrol and removal [33], and compatibility of silicon carbide (SiC)with high-temperature alloy [34]. Although a good understandingof PbLi behavior in blanket relevant conditions has been achieved,many practical problems vital to liquid metal blankets still remainopen; thus, further studies are required.

In particular, many unresolved issues still remain in regardsto potential use of SiC (either composite or foam) as a functionalblanket material for electrical and thermal insulation or even as astructural material in some innovative blanket concepts. For example,in the DCLL blanket, which is currently the main US choice forfurther utilization in FNSF and DEMO reactors, a SiC flow channelinsert (FCI) is proposed to decouple high-temperature PbLi from theferritic steel wall, both thermally and electrically [35,36]. Althoughmany blanket design studies [35–37] rely on good insulating propertiesof the SiC FCI, its effectiveness as electrical and thermalinsulator in the flowing PbLi conditions has not been demonstratedyet. Another concern, which needs to be resolved, is corrosionbehavior of reduced activation ferritic/martensitic (RAFM) steelsexposed to a molten PbLi flow in the presence of a strong magneticfield followed by transport and deposition of corrosion products inthe "cold" leg of the loop. The effect of a magnetic field

on the corrosionrate seems to be strong, resulting in some cases in doublingof the mass loss [17,38], but the physical

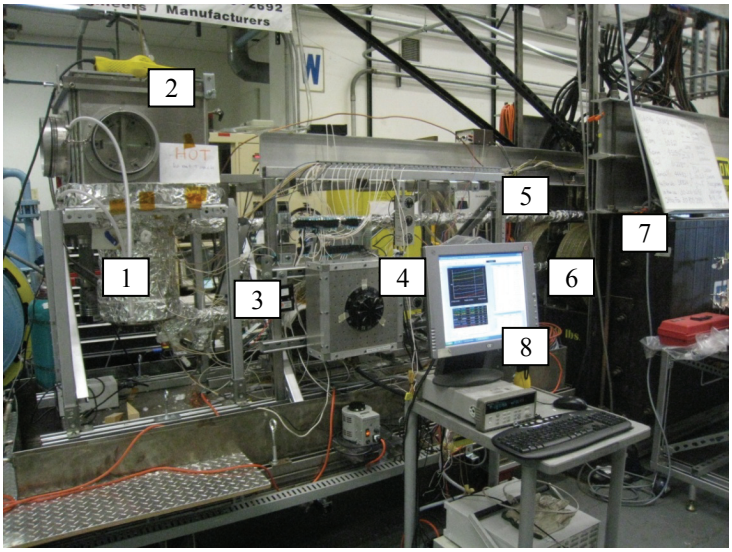

Fig.1. MHD PbLi Loop at UCLA; 1) PbLi Melting Tank with Heaters; 2) Glovebox; 3) EMP; 4) EMF; 5) Pipes with Heaters & Thermal Insulators; 6) Circular-Pipe Test-Section 7) Electromagnet; 8) Data Acquisition System

mechanisms associatedwith such a process are not well understood yet. Moreover, theexisting experimental databases on corrosion are not full enoughto extrapolate to blanket conditions. Also, further experimentalprogress in the case of PbLi flows can be seriously limited by lackof flow diagnostics tools, which need to be developed and tested totake into account special effects not pertinent to ordinary fluids orroom-temperature liquid metals, due to high-temperature effects,presence of a magnetic field and high PbLi chemical reactivity.

The prime objective of the newly constructed (2011) MHD PbLiflow loop at University of California, Los Angeles (UCLA) calledMaPLE (MagnetohydrodynamicPbLi Experiment) is to address theabovementioned issues via a series of experiments, first of all totake into account the effect of a magnetic field. Some results of thefirst runs of the loop were briefly reported in a conference paper[39] to highlight research progress achieved in the course of the so-calledTITAN project between the US and Japan (see Ref. [39]). Thepresent article introduces more details about the facility, its operationand flow diagnostics and also introduces details of currentexperiments and near-term experimental plans.

In the present paper, the loop construction, the EMP performance test, our on-going experiments with the constructed loop are described.

2. PbLi loop construction and performance test

The MHD PbLi loop is shown in Fig. 1. There are a glovebox with attached cylindrical melting tank at its bottom, the EMP, the EMF, a vacuum pump and a gas purification system. All parts of the loop including pipes were heated by electric heaters and thermally insulated to prevent the molten PbLi from solidification. At the start of the loop operation, approximately 100 kg of PbLi ingots (from Atlantic Metals & Alloys, USA) are loaded into the melting tank, the air was evaluated and then melting started. After the melting was done, the loop was filled with an ultrahigh purity argon gas.

The EMP (Style V from Creative Engineers, USA) was chosen for the loop since EMPs have a simple pump structure, which is suitable for the corrosive PbLi. The EMP performance with the PbLi was tested and characterized. The circular-pipe test-section was mounted onto the constructedPbLi loop as shown in Fig. 1. The transverse magnetic field was applied to the test-section by using the electromagnet. An MHD pressure drop was non-invasively imposed on the test-section by applying a transverse magnetic field. The MHD pressure load was controlled by changing the magnetic field intensity.

The test-section was identical to the rest of the loop pipe, which was made of SUS304, 25 mm in outer diameter, and 22 mm in interior diameter. The whole loop was installed on the wheeled platform, and was able to move in and out of the electromagnet gap. The bellows made of a stainless steel were mounted to the loop pipes to relax the longitudinal stress due to the thermal expansion of the loop pipes.

The EMF measured the PbLi flow-rate downstream from the EMP. The total pressure loss of the loop Δp was theoretically estimated as follows:

$$\Delta p = \Delta p_{\mathrm{HD}} + \Delta p_{\mathrm{EMF}} + \Delta p_{MHD} \qquad (1)$$

here, the hydrodynamic flow resistance is Δp_{HD}; the flow resistance at the EMF Δp_{EMF}; and the MHD pressure drop induced by the electromagnet Δp_{MHD}.

The pressure loss at the EMP was not considered. Thus,

the hydrodynamic flow resistance Δp_{HD} is expressed by:

$$\Delta p_{HD} = \frac{\rho_f U_0^2}{2}\left\{ f\frac{L}{d_{ID}} + \sum \zeta_{\text{bend}} + \zeta_{\text{melting tank}} \right\},$$
$$= \frac{\rho_f U_0^2}{2}\left\{ f\frac{L}{d_{ID}} + 4\times 0.5 + 1.0 \right\}, \quad (2)$$

here, $\rho_f$is the fluid density; U_0 the mean flow velocity; f the friction factor of pipe; L the total length of the piping;d_{ID} the pipe inner diameter; ζ a factor of hydrodynamic pressure drop due to pipe bends or the melting tank. The friction factor of pipe f was evaluated by the BlasiusLaw ($f=0.316Re^{-1/4}$). The present estimation employed that ζ_{bend} was 0.5; $\zeta_{\text{melting tank}}$ was 1.0. The total length of the piping L was 7.9 m (except for lengths of the EMF and the EMP).

A theoretical relation of an MHD pressure drop in a circular pipe with an electrical conducting wall [40] is given by:

$$-\frac{dp}{dx} = \left(\frac{c_w}{1+c_w}\right)\sigma_f U_0 B_0^2$$
$$c_w = \frac{\sigma_w (R-r)}{\sigma_f R} \quad (3)$$

here, $R$is the outer radius of the pipe (25 mm); r the interior radius of the pipe (22 mm); B_0 the magnetic induction perpendicular to the flow; c_w the wall conductance ratio; σ_w the electrical conductivity of the pipe; σ_f the electrical conductivity of the fluid. The mean flow velocity was calculated from the flow-rate measured by the EMF.

The fringing magnetic field produces the additional MHD pressure drop Δp_{fringe} is expressed by [41]:

$$\Delta p_{fringe} = \frac{1}{2}\eta N \rho_f U_0^2 \quad (4)$$

here, $\eta$is the empirical coefficient (the present estimation employed that η =0.2 based on the reference [41]); N the Interaction parameter.

The pressure dropsΔp_{EMF}andΔp_{MHD} were calculated from Eqs. (3) and (4), respectively. Figure 2 plots the total pressure drop Δp versus the flow-rate Q measured by the EMF, with the magnetic field of different intensity of from 0.4 to 1.8 T. The corresponding Hartmann number Ha was from 86 to 391. From the figure, it was found that the full EMP performance with the molten PbLi was close to the estimation calculated from the performance with the sodium-potassium (as shown in the solid line). It was confirmed by the test that the constructedloop was capable of working for MHD experiments.

With weak intensity of the magnetic field, the total pressure drop Δp was proportional to the squared mean velocity U_0^2. On the other hand, with high intensity of the magnetic field of more than 1.2 T, Δp was linearlyproportional to the mean velocity U_0. Since the MHD pressure drop is proportional to U_0 as expressed by Eq. (3) and the hydrodynamic pressure drop is proportional to the squared mean velocity U_0^2 as expressed by Eq. (2), with high intensity of the magnetic field of more than 1.2 T, the MHD pressure drop was dominant over the hydrodynamic pressure drop in the total pressure drop.

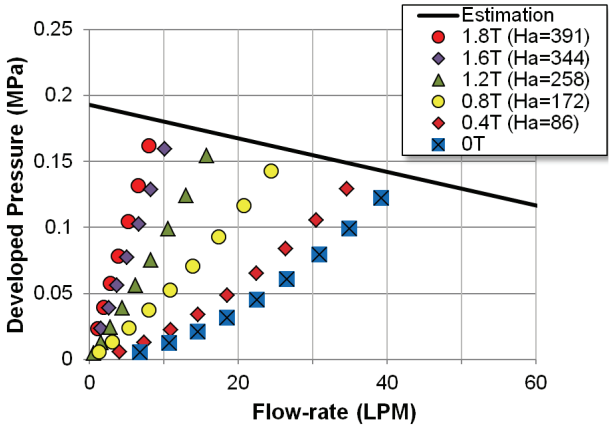

Fig. 2.EMP Characteristics

3. On-Going Experiments

The main purposes of the experiment with the 3SML channel are to experimentally validate that the 3SML channel mitigates the MHD pressure drop; and to verify the MHD flow simulation code. The channel consists of a thin metal layer and a ceramic insulating layer on three of the four channel wall inner surfaces, as shown in Fig. 3. Corn-shaped connectors were mounted at the ends of the test channel to connect the loop pipes and the 3SML channel.

Figure 4plots the measured pressure drops in the downstream region of the 3SML channel in the magnetic field of 1.5 T with respect to the mean velocity, as well as the computational results.The figure shows that the measured pressure drops in the 3SML channel were mitigated by one-tenth,with respect to the computational predictions ofthose in the conducting channel; the measured values were close to the computational prediction of those in the 3SML channel.As results, it was demonstrated that the 3SML channel mitigated MHD pressure drops.

The main purposes of the experiment with the 3SML channel are to experimentally validate that the 3SML channel mitigates the MHD pressure drop; and to verify the MHD flow simulation code. The channel consists of a thin metal layer and a ceramic insulating layer on three of the four channel wall inner surfaces, as shown in Fig. 3. Corn-shaped connectors were mounted at the ends of the

test channel to connect the loop pipes and the 3SML channel.

Figure 4plots the measured pressure drops in the downstream region of the 3SML channel in the magnetic

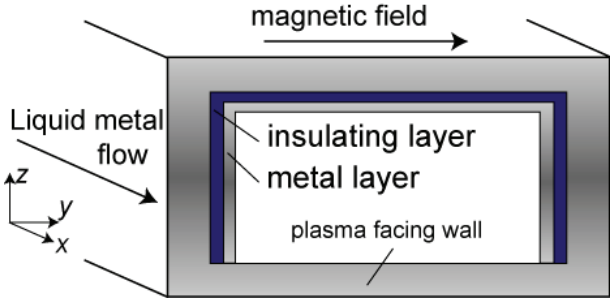

Fig. 3. Schematic Drawing of 3SML Channel

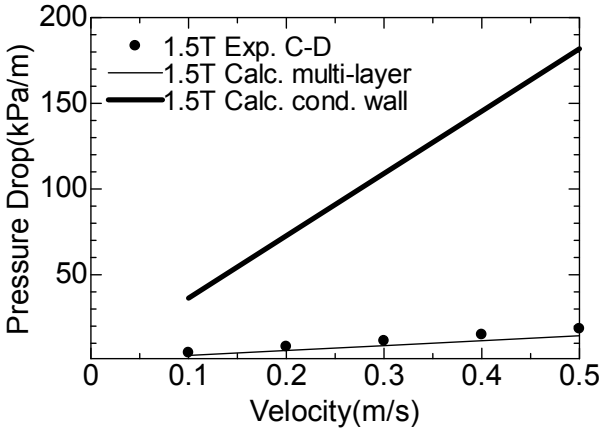

Fig. 4. Comparison of MHD Pressure Drops (Measurement: Dot Plots; Calculation of 3SML Channel: Thin Line; Calculation of Conducting Channel: Thick Line).

field of 1.5 T with respect to the mean velocity, as well as the computational results.The figure shows that the measured pressure drops in the 3SML channel were mitigated by one-tenth,with respect to the computational predictions ofthose in the conducting channel; the measured values were close to the computational prediction of those in the 3SML channel.As results, it was demonstrated that the 3SML channel mitigated MHD pressure drops.

4. Summary

In the task under the TITAN project, we had constructed the MHD PbLi loop, tested the loop components, and then confirmed that the loop was capable of working for MHD experiments. The 3SML channel was mounted on the constructed PbLi loop, and it was experimentally demonstrated that the 3SML channel mitigated MHD pressure drops. The SiC foam-based FCI will be tested after the 3SML channel.These experimental results will be dedicated to verify and develop MHD numerical simulations. In the task under the TITAN project, we had constructed the MHD PbLi loop, tested the loop components, and then confirmed that the loop was capable of working for MHD experiments. The 3SML channel was mounted on the constructed PbLi loop, and it was experimentally demonstrated that the 3SML channel mitigated MHD pressure drops. The SiC foam-based FCI will be tested after the 3SML channel.These experimental results will be dedicated to verify and develop MHD numerical simulations.

References

[1] S. Malang, R. Mattas, Comparison of lithium and the eutectic lead–lithium alloy,two candidates liquid metal breeder materials for self-cooled blankets, FusionEngineering and Design 27 (1995) 399–406.

[2] S. Malang, M. Tillack, C.P.C. Wong, N. Morley, S. Smolentsev, Development of thelead lithium (DCLL) blanket concept, Fusion Science and Technology 60 (2011)249–256.

[3] G. Rampal, A. Li Puma, Y. Poitevin, E. Rigal, J. Szczepanski, C. Boudot, HCLL TBMfor ITER-design studies, Fusion Engineering and Design 75–79 (2005) 917–922.

[4] L. Giancarli, L. Baraer, P. Leroy, J. Mercier, E. Proust, Y. Severi, et al., Water-cooledlithium–lead blanket design studies for DEMO reactor: definition andrecent developments of the box-shaped concept, Fusion Technology 21 (1992)2081–2088.

[5] W. Krauss, J. Konys, H. Steiner, J. Novotny, Z. Voss, O. Wedemeyer, Developmentof modeling tools to describe the corrosion behavior of uncoated EUROFER inflowing Pb–17Li and their validation by performing of corrosion tests at T upto 550 ◦C, Forschungszentrum Karlsruhe, FZKA 7295, 2007.

[6] F. Barbier, Continuous monitoring and adjustment of the lithium content in liquidPb–Li alloys: assessment of an electrical resistivity meter in a loop system,Fusion Engineering and Design 36 (1997) 299–308.

[7] Main Facilities in ENEA, http://web.brasimone.enea.it/mat/matindfa.htm.

[8] K. Noborio, Y. Yamanoto, C. Park, Y. Takeuchi, S. Konishi, High temperatureoperation of LiPb loop, Fusion Science and Technology 60 (2011) 298–302.

[9] I. Bucenieks, R. Krishbergs, E. Platacis, G. Lipsbergs, A. Shishko, A. Zik, et al.,Investigation of corrosion phenomena in EUROFER steel in Pb–17Li stationaryflow exposed to a magnetic field, Magnetohydrodynamics 42 (2006) 237–251.

[10] Q.-Y. Huang, M.-L. Zhang, Z.-Q. Zhu, S. Gao, Y.-C. Wu, Y.-F. Li, Y. Song, et al., Corrosionexperiment in the first liquid metal LiPb loop of China, Fusion Engineeringand Design 82 (2007) 2655–2659.

[11] Q.-Y. Huang, FDS series fusion reactor conceptual designs and R&D activitiesin China, in: US/Japan Workshop on Power Plant Studies and Advanced Technologieswith EU participation, 16–18 March 2009, University of Tokyo, Japan,2009.

[12] R.-J. Lu, H.-L. Chen, T. Zhou, Z.-Y. Yang, F.D.S Team, Magnetohydrodynamicexperimental design and analysis for Chinese liquid metal LiPb experimentalloop DRAGON-IV, Chinese Journal of Nuclear Science and Engineering 29(2009) 76–80 (in Chinese).
[13] J.S. Yoon, D.W. Lee, Y.D. Bae, S.K. Kim, K.S. Jung, S. Cho, Development of an experimentalfacility for a liquid breeder in Korea, Fusion Engineering and Design 86(2011) 2212–2215.
[14] J.S. Yoon, Y.D. Bae, S.K. Kim, S. Cho, D.W. Lee, Performance test of the electromagneticpump in an experimental liquid breeder loop for developing a KO testblanket module, Fusion Science and Technology 60 (2011) 139–143.
[15] J. Konys, W. Krauss, J. Novotny, H. Steiner, Z. Voss, O. Wedemeyer, Compatibilitybehavior of EUROFER steel in flowing Pb–17Li, Journal of Nuclear Materials386–388 (2009) 678–681.
[16] Q.-Y. Huang, S. Gao, Z.-Q. Zhu, M.-L. Zhang, Y. Song, C.-J. Li, et al., Progress incompatibility experiments on lithium–lead with candidate structural materialsfor fusion in China, Fusion Engineering and Design 84 (2009) 242–246.
[17] R. Krishbergs, E. Ligere, F. Muktepavela, E. Platacis, A. Shishko, A. Zik, Experimentalstudies of the strong magnetic field action on the corrosion of RAFMsteels in Pb17Li melt flows, Magnetohydrodynamics 45 (2009) 289–296.
[18] J. Konys, W. Krauss, H. Steiner, J. Novotny, A. Skrypnik, Flow rate dependentcorrosion behavior of Eurofer Steel in Pb–15.7Li, Journal of Nuclear Materials417 (2011) 1191–1194.
[19] G. Benamati, C. Fazio, I. Ricapito, Mechanical and corrosion behaviour of EUROFER97 steel exposed to Pb–17Li, Journal of Nuclear Materials 307–311 (307)(2002) 1391–1400.
[20] H.U. Borgstedt, G. Drechsler, G. Frees, Z. Peric, Corrosion testing of steel X 18CrMoVNb 121 (1.4914) in a Pb–17Li pumped loop, Journal of Nuclear Materials155–157 (1988) 728–731.
[21] H.U. Borgstedt, H.D. Rijhrig, Recent results on corrosion behaviour of MANETstructural steel in flowing Pb47Li eutectic, Journal of Nuclear Materials179–181 (1991) 596–598.
[22] H. Glasbrenner, J. Konys, Z. Voss, Corrosion behaviour of low activation steelsin flowing Pb–17Li, Journal of Nuclear Materials 281 (2000) 225–230.
[23] J. Konys, W. Krauss, Z. Voss, O. Wedemeyer, Corrosion behavior of EUROFERsteel in flowing eutectic Pb–17Li alloy, Journal of Nuclear Materials 329–333(2004) 1379–1383.
[24] J. Konys, W. Krauss, Z. Voss, O. Wedemeyer, Comparison of corrosion behaviorof bare and hot-dip coated EUROFER steel in flowing Pb–17Li, Journal of NuclearMaterials 367–370 (2007) 1144–1149.
[25] Y.-P. Chen, Q.-Y. Huang, S. Gao, Z.-Q. Zhu, X.-Z. Ling, Y. Song, et al., Corrosionanalysis of CLAM steel in flowing liquid LiPb at 480◦C, Fusion Engineering andDesign 85 (2010) 1909–1912.
[26] A. Aliello, M. Agostini, G. Benamati, B. Long, G. Scaddozzo, Mechanical propertiesof martensitic steels after exposure to flowing liquid metals, Journal ofNuclear Materials 335 (2004) 217–221.
[27] P. Magaud, F.L. Vagueres, Annual Report of the Association CEA/EURATOM,1998, 171–174.
[28] P. Hubberstey, T. Sample, Thermodynamic and experimental evaluation of thesensitivity of Pb–17Li breeder blankets to atmospheric contamination, Journalof Nuclear Materials 191–194 (1992) 277–282.
[29] I. Ricapito, A. Ciampichetti, G. Benamati, Pb–17Li/water interaction in DEMOWCLL blanket: water micro-leaks, Fusion Engineering and Design 65 (2003)577–587.
[30] A. Ciampichetti, I. Ricapito, A. Aiello, G. Benamati, Water large leaks into liquidPb–17Li: first experimental results on LIFUS 5 facility, Fusion Engineering andDesign 69 (2003) 563–567.
[31] P. Hubberstey, M.G. Barker, T. Sample, An electrical resistivity monitor for thedetection of composition changes in Pb–17Li, Fusion Engineering and Design14 (1991) 227–233.
[32] F. Barbier, Continuous monitoring of lithium in dynamic Pb–17Li systems,Fusion Engineering and Design 46 (1999) 77–88.
[33] M.G. Barker, D.J. Siddons, F. Barbier, The removal of nickel dissolved in Pb–17Liby the formation of a less soluble nickel–manganese alloy, Journal of NuclearMaterials 233–237 (1996) 1436–1440.
[34] X.-Z. Ling, Q.-Y. Huang, S. Gao, Z.-Q. Zhu, Y.-P. Chen, Y. Song, et al., Compatibilityof SiC with static liquid LiPb at 800 ◦C, Fusion Engineering and Design 86 (2011)2655–2657.
[35] A.R.I.E.S Team, M.S. Tillack, X.R. Wang, J. Pulsifer, S. Malang, D.K. Sze, ARIESSTbreeding blanket design and analysis, Fusion Engineering and Design 49/50(49) (2000) 689–690.
[36] M. Abdou, D. Sze, C. Wong, M. Sawan, A. Ying, N.B. Morley, et al., U.S. plansand strategy for ITER blanket testing, Fusion Science and Technology 47 (2005)475–487.
[37] S. Smolentsev, R. Moreau, M. Abdou, Characterization of key magnetohydrodynamicphenomena in PbLi flows for the US DCLL blanket, Fusion Engineeringand Design 83 (2008) 771–783.
[38] S. Smolentsev, S. Saedi, S. Malang, M. Abdou, Numerical study of corrosion offerritic/martensitic steels in the flowing PbLi with and without a magnetic field,Journal of Nuclear Materials 432 (2013) 294–304.
[39] S. Smolentsev, T. Kunugi, K. Messadek, T. Yokomine, J. Young, K. Yuki, et al.,Status of TITAN Task 1–3 flow control and thermofluid modeling, Fusion Engineeringand Design 87 (2012) 777–781.
[40] K. Miyazaki, S. Kotake, N. Yamaoka, Y. Fujii-e, MHD Pressure Drop of NaK Flow in Stainless Steel Pipe. Nuclear Technology/Fusion, 4 (1983) 447-452.

[41] S. Smolentsev, C. Wong, S. Malang, M. Dagher, M.A. Abdou, MHD Considerations for the DCLL Inboard Blanket and Access Duct. Fusion Eng. Des., 85 (2010) 1007-1011.

Task 1-3(5)Verification Test of Three-Surface-Multi-Layered Channel for MHD Pressure Drop Reduction

M.Aoyagi[a], Y.Inage[a], S.Ito[a], S.Ebara[a], Y.Ueki[b], K.Yuki[c], F.-C. Li[d], S.Smolentsev[d],
T.Yokomine[b], T.Kunugi[b], T. Sketchley[d], M.Abdou[d],H.Hashizume[a]

[a]*Tohoku University6-6-01-2, Aramaki Aza Aoba, Aoba-ku, Sendai, Miyagi 980-8579, Japan*
[b]*Department of Nuclear Engineering, Kyoto University, Yoshida, Sakyo, Kyoto 606-8501, Japan*
[c]*Department of Mechanical Engineering, Tokyo University of Science-Yamaguchi, Yamaguchi 756-0884, Japan*
[d]*Mechanical and Aerospace Engineering Department, University of California, Los Angeles, 420 Westwood Plaza, 44-114 Engineering IV, Los Angeles, CA 90095, USA*

ABSTRACT

A three-surface-multi-layered channel is one of the possible methods for reducing the magnetohydrodynamic (MHD) pressure drop in the liquid metal blanket of a fusion reactor. An MHD flow experiment was conducted to verify the MHD pressure drop reduction by using the three-surface-multi-layered channel with ceramic insulator in this study. We used a PbLi flow loop and a magnet generating a magnetic field of up to 1.8 T. The experimental results were compared with numerical predictions. The pressure drop obtained by the experiment was one-tenth of the numerical one for a conducting channel. Though the measured pressure drop shifted slightly, the result was reasonable since it showed good agreement with numerical predictions as the result of modifying the shift. In this study, it was verified that the three-surface-multi-layered channel works as it had been supposed and the MHD pressure drop was reduced by using this channel.

1. Introduction

MHD pressure drop reduction is one of the most important R&D issues in liquid metalfusion blankets. A three-surface-multi-layered (3SML) channel shown in Fig. 1, which consists of a thin metal layer and a ceramic insulating layer on three of the four channel wall's inner surfaces, is an advanced concept to reduce the MHD pressure drop[1]. In order to validate this concept, a liquid metal flow experiment has been conducted by means of an open annular channel where one surface of the channel had the multi-layered structure with a thin metal layer and Teflon insulating one [2]. Since the channel was axial symmetrical, the flow should have been two dimensional. The experimental result showed that the MHD pressure drop was reduced more by using thinner metal layer as was predicted in the 2D MHD numerical analysis. This result means that the MHD pressure drop is reduced by an ideal three-surface-multi-layered channel which is completely insulated between the metal layer and structural wall. However at the actual fusion blanket channel, the insulator must be ceramic which is much more fragile than Teflon and besides 3D MHD effect such as the current flowing in the streamwise direction could affect the pressure drop. In this study, therefore, we verify the MHD pressure drop reduction experimentally by means of a closed straight channel with 3SML structure and ceramic insulating.

2. Experimental method

2.1 Experimental apparatus

This MHD flow experiment is conducted using an MHD experimental loop at UCLA[3,4]. Layout of the loop is sketched at the Fig. 2. The loop system consists of a melting tank, an electromagnetic (EM) pump, an EM flow meter, a test channel and circular pipes with outer diameter of 25.4 mm to connect the foregoing components. A sub loop sketched at Fig. 3 is connected to the test channel in order to measure the pressure differences. Thermocouples are installed in the melting tank and attached on the pipe and buffer tanks as shown in Figs. 2 and 3. The working fluid is the PbLi eutectic alloy. A uniform magnetic field up to 1.8 T is applied transversely against the flow for 1 m in the streamwise direction. The test channel's structural wall is made of 316 grade of austenite stainless steel (SUS 316). As a ceramic insulating layer, silica is painted on the inner surface of the structural wall. The coating thickness is 0.05 – 0.15 mm. The metal layer of a 0.1 mm thick SUS 316 is installed in the channel. The dimensions of the test channel are 0.8 m in the streamwise direction, 20 mm in the inner width and 8 mm in the inner height. The wall

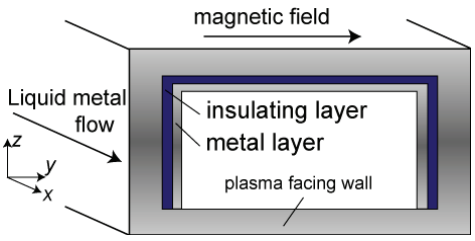

Fig. 1 Schematic view of the Three-surface-multi-layered channel

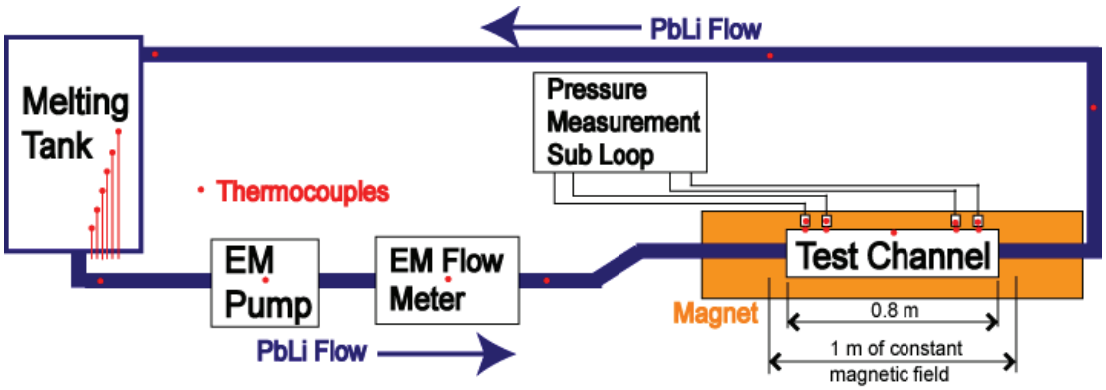

Fig. 2 Schematic view of the PbLi loop system

thicknesses are 3 mm in the non-layered wall and 5 mm in the three layered walls, respectively. These channel dimensions were optimized for a blanket cooling channel [5]. The space between the metal layer and the structural wall are closed by welding at the both ends of the channel in order to prevent the fluid invading into the space. Corn-shaped connectors are mounted at the both ends of the test channel to connect the circular pipe of the experimental loop and the rectangular test channel. These connectors are not insulated.

The experimental parameters are the magnetic field intensity (0~1.8 T), the flow velocity (0.1~2.0 m/s) and the operating temperature (270 ~ 350 °C). Maximum flow velocity is limited by the EM pump capacity and is 1.5 m/s for 1 T, 1.0 m/s for 1.5 T and 0.5 m/s for 1.8 T, respectively.Non-dimensional parameters are, in the cases of 270, 300 and 350 °C,Ha < 3.2×10^2, 3.5×10^2 and 3.8×10^2 and Re <7.8×10^4, 8.8×10^4 and 1.1×10^5, respectively, where Ha andRe are a Hartmann numberand a Reynolds numberrespectively and they are defined by Eqs.(1) and (2):

$$Ha = BL\left(\frac{\sigma}{\mu}\right)^{0.5} \quad (1)$$

$$Re = \frac{\rho u L}{\mu} \quad (2)$$

The nomenclatures are described at the end of paper. Half width of the channel of 0.01 mm is used as characteristic length L in the foregoing Ha and Re. Reynolds number based on the hydraulic equivalent diameter is Re< 2.0×10^5 for 300 °C.

2.2Measurement principle

2.2.1 Flow rate

Flow rate is measured by the EM flow meter installed downstream of the pump. The EM flow meter consists of electrodes at the top and bottom of the pipe and a pair of permanent magnets existing at the both side of the pipe. The flow rate can be calculated from the voltage between the electrodes and the magnetic field.

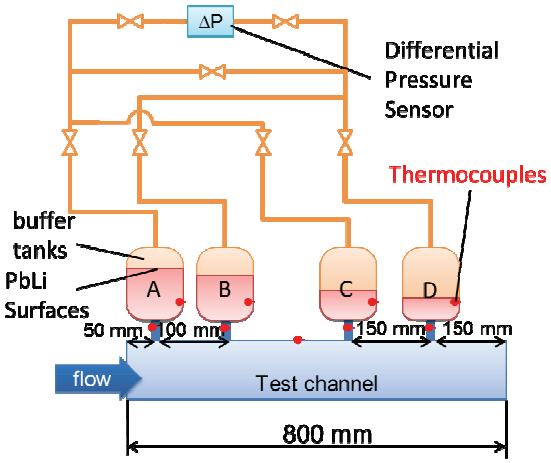

Fig. 3 Schematic view of the sub loop for differential pressure measurement

2.2.2Pressure difference

Since it is difficult to measure directly the pressure of the high temperature PbLi, we used an indirect measurement system [4] as shown in Fig. 3. Four buffer tanks are connected to the test channel and contain the liquid PbLi and Ar gas with fluid surface in the tanks. Then the pressure difference of the gas Ar is measured by a differential pressure sensor. Four valves connecting the tanks and the sub loop enable us to measure three different sections; upstream region (A-B), downstream region (C-D) and entire the test section (A-D). Since the pressure difference measured in this experiment is up to 14 kPa and is relatively small compared with the absolute pressure of about 100 kPa, the measured pressure drop is susceptible to error caused by even slight initial pressure difference due to small temperature change or something. Then the experimental results are modified to make the pressure drop zero at the zero velocity. It is assumed that the amounts of the shift are the same among the data obtained in the same magnetic field and temperature and do not depend on the velocity.

3. Numerical prediction

In order to analyze whether the 3SMLchannel works

as it has been supposed or not in the experiment, numerical simulation is conducted with two-dimensional fully-developed MHDlaminar flow assumption.The governing equations are a two-dimensional steady Navier-Stokes equation and a Poisson equation in terms of the electrostatic potential given by Eq. (3) and (4) respectively:

$$\frac{\partial}{\partial y}\left(\mu\frac{\partial u}{\partial y}\right)+\frac{\partial}{\partial z}\left(\mu\frac{\partial u}{\partial z}\right)+\sigma\left(\frac{\partial \phi}{\partial z}-uB\right)B=0 \qquad (3)$$

$$\frac{\partial}{\partial y}\left(\sigma\frac{\partial \phi}{\partial y}\right)+\frac{\partial}{\partial z}\left(\sigma\frac{\partial \phi}{\partial z}\right)-\frac{\partial}{\partial z}(\sigma uB)=0 \qquad (4)$$

The *x*-, *y*- and *z*-directions are described in Fig. 1. These equations are discretized by a finite volume method and solved iteratively.

Two different models are calculated. One is the three-surface-multi-layered channel as shown in Fig. 1, and the other is simple conducting wall without insulator. If the insulating coating is perfect and there is no 3D effect in the experiment, the experimental result should correspond to the calculation for the 3SML channel. On the other hand, if the coating has defections and the thin metallic layer has a lot of electrical contact with the structural wall, the experimental result could be close to the conducting wall one.

The calculation is conducted for the same parameters of the velocity, magnetic field and temperature as those tested in the experiment. Table 1 shows the physical properties of the PbLi and SUS 316 used in the calculation.

Table 1 Physical properties

Temperature (^{o}C)	PbLiconductivity (S/m)	PbLi viscosity (Pa·s)	SUS316 conductivity (S/m)
270	7.97×10^{5}	2.46×10^{-3}	1.08×10^{6}
300	7.89×10^{5}	2.15×10^{-3}	1.05×10^{6}
350	7.76×10^{5}	1.77×10^{-3}	1.00×10^{6}

4. Results and discussions

4.1. Pressure drop for low magnetic field

Figures 4 and 5 show the pressure drop in the downstream region (C-D) obtained by the experiment and the calculations in the case of 300 °C and 0.5 and 1.0 T, respectively. Although the experimental data is much smaller than the calculation ones for the conducting channel without insulating coating indicated by thick lines, there are comparatively large differences between the experimental results and the numerical ones for the three-surface-multi-layered channel indicated by thin lines in the case of high velocity. Turbulence is considered to increase the pressure drop in the experiment. It is well known that the MHD flow transit from the laminar flow to

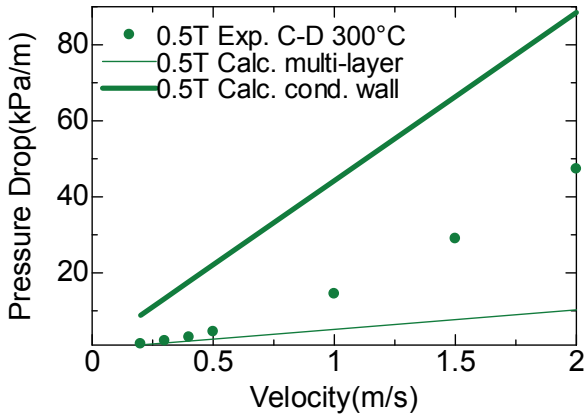

Fig. 4Pressure drop in the region C-D at 0.5 T, 300°C

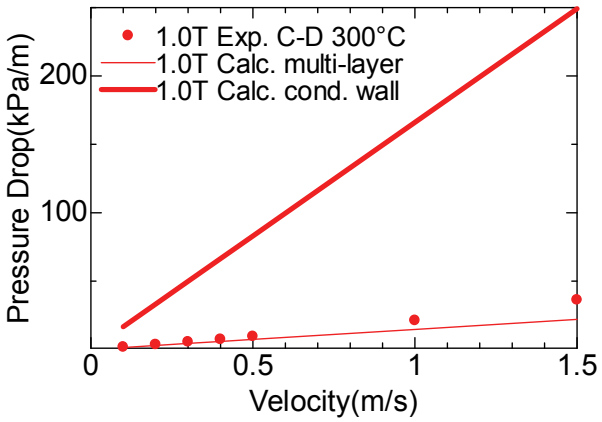

Fig. 5Pressure drop in the region C-D at 1.0 T, 300°C

theturbulent one in the case of *Ha*/*Re*< 1/200 [6]. The value of *Ha*/*Re* becomes smaller than 1/200 in the cases of *u*> 0.44 m/s at *B*=0.5 T or *u*> 0.88 m/s at *B*=1.0 T. Therefore, in such cases of low *Ha*/*Re*, large pressure drop is obtained in the experiment.

4.2Pressure drop for high magnetic field

Figure 6 shows the pressure drop in the downstream region (C-D) obtained by the experiment and the calculations in the case of 300 °C and 1.8 T. In the case of 1.8 T, the experimental result is almost corresponding to the calculation for the three-surface-multi-layered channel indicated by a thin line and is one-tenth the value of the calculation for the conducting channel without insulating coating indicated by a thick line. This result represents the MHD pressure drop is reduced drastically by the three-surface-multi-layered channel.

4.3Velocity dependency

Figures 7 and 8 show the change in the pressure drop against the mean flow velocity in the upstream (A-B) and downstream (C-D) regions, respectively. Dashed lines are linear approximation expressions for the experimental data

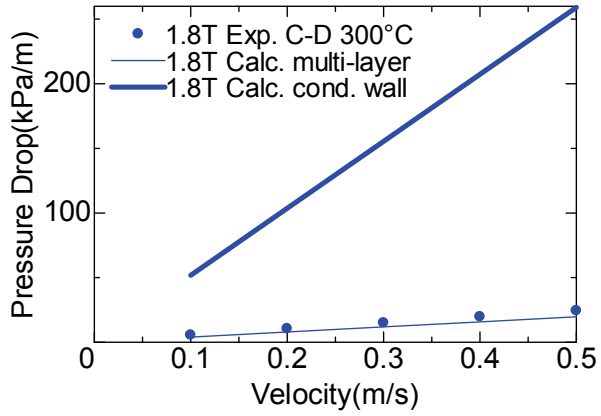

Fig. 6Pressure drop in the region C-D at 1.8 T, 300°C

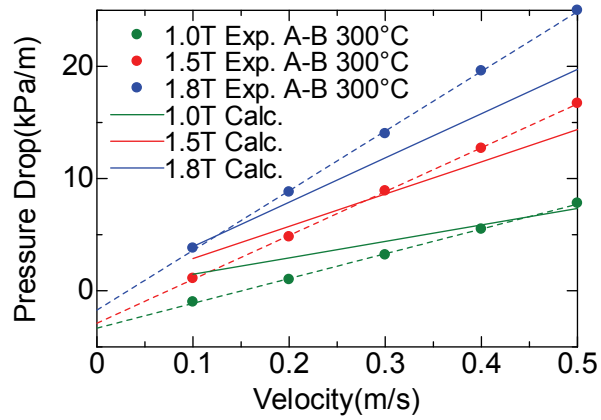

Fig. 7Pressure drop change against the velocity in the region A-B at 300°C

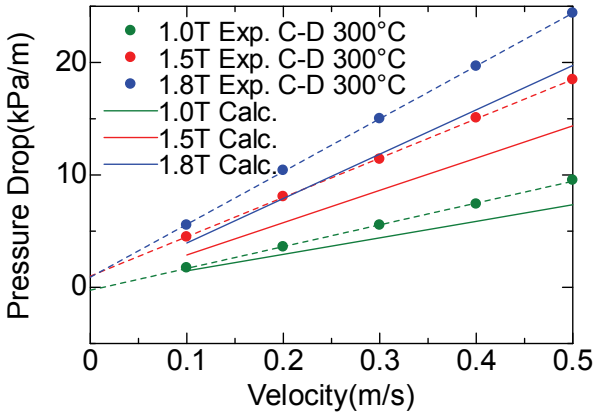

Fig. 8Pressure drop change against the velocity in the region C-D at 300°C

by the least squares method. The solid lines are the numerical data for the three-surface-multi-layered channel.Negative pressure drop is measured in the case of 1 T and 0.1 m/s. The extrapolated values are not zero at the zero velocity for almost all cases. This can be inferred that the initial pressure difference between the buffer tanks due to different level of the liquid PbLi in the tank.

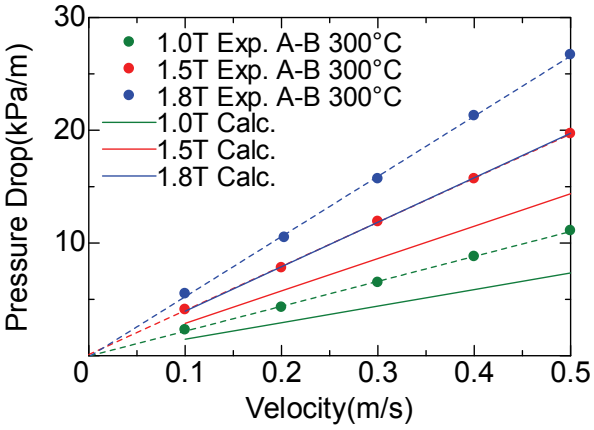

Fig. 9Modified pressure drop change against the velocity in the region A-B at 300°C

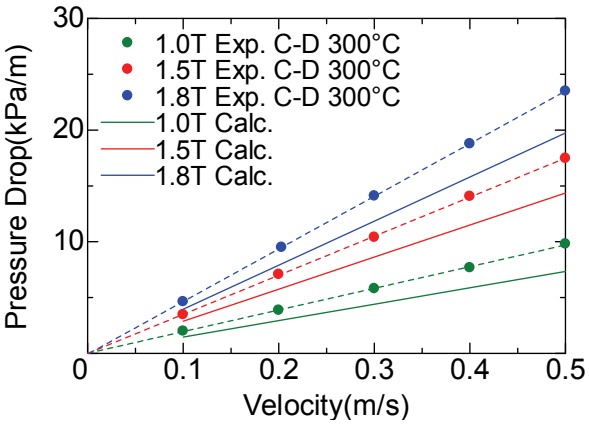

Fig. 10Modified pressure drop change against the velocity in the region C-D at 300°C

Figures 9 and 10 show the modified pressure drop with respect to the mean flow velocity. The pressure drop changes almost linearly against the velocity in all of the cases as is predicted by the numerical result. The experimental results are close to the numerical ones but there exists some gap between them. The differences are about 30 % in the region A-B and about 20 % in the region C-D, respectively.

4.4Temperature dependency

As shown in Table 1, there are temperature dependencies in the physical properties especially in viscosity. In order to examine whether the pressure drop shows characteristic changes depending on the physical properties change, we have tested for three different temperatures.Figures 11 and 12 show the pressure drop change depending on the temperature. The pressure drop changes slightly depending on the temperature. Since the viscosity and the electric conductivities decrease with the temperature, both

the Lorenz force and the friction force decrease and hence the pressure drop is reduced. The differences depending on the temperature are well corresponding to those obtained by the numerical simulation.

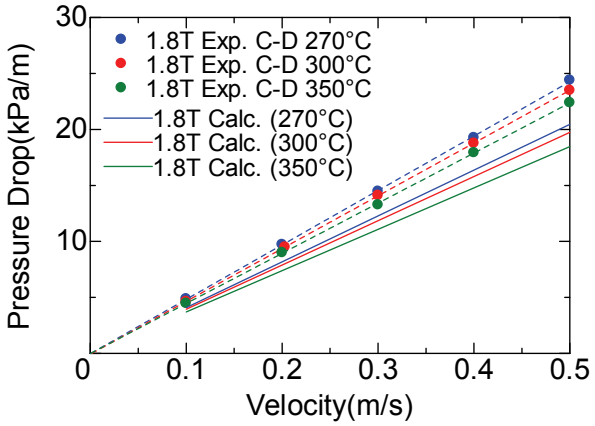

Fig. 11Modified pressure drop change depending on the temperature in the region A-B at 1.8 T

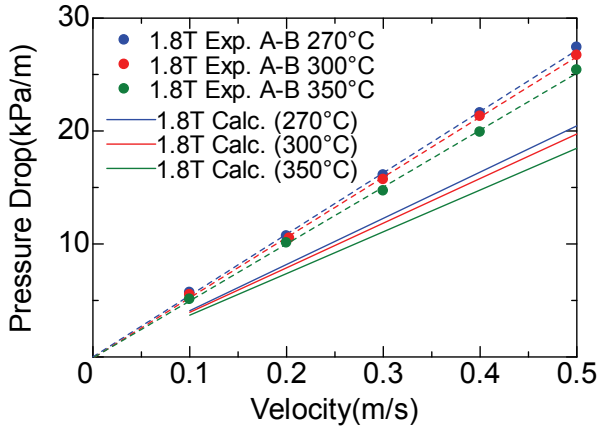

Fig. 12Modified pressure drop change depending on the temperature in the region C-D at 1.8 T

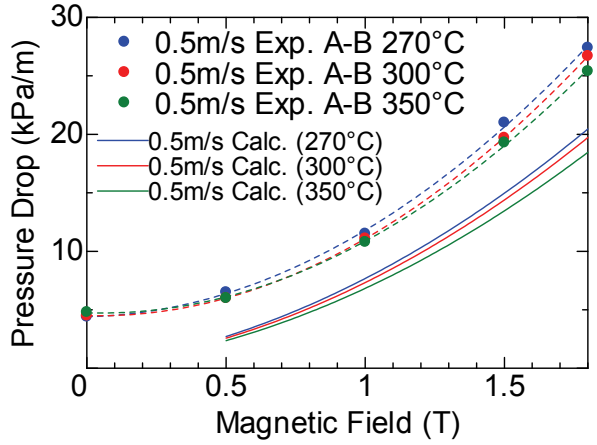

Fig. 13Modified pressure drop change against the magnetic field in the region A-B at 0.5 m/s

4.5Magnetic field dependency

Figures 13 and 14 show the changes in the pressure drop against the magnetic field in the upstream (A-B) and downstream (C-D) regions, respectively. Dashed lines are quadric approximation expressions for the experimental data by the least squares method. The pressure drop shows thequadric change against the magnetic field as given by the basic MHD theory in all the temperature conditions.

Figures 15 and 16 show the differences between the modified experimental data and the numerical ones. Solid and dash lines are the net Lorentz force and friction force per unit volume acting on the fluid, respectively, obtained numerically. In the case of the magnetic field larger than 1 T, the differences change almost linearly against the magnetic field. This means that the difference between the experimental results and calculated ones is possibly caused by the friction force which changes linearly against the magnetic field. If the Lorentz force affected the difference, the difference should have changed nonlinearly like the change in the Lorentz force described in Fig. 15 and 16. Therefore there is no more Lorentz force in the experiment than those in the calculation. It means that the insulating coating works well.

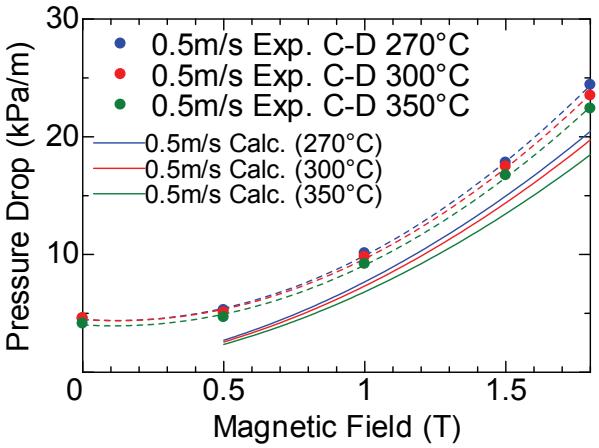

Fig. 14Modified pressure drop change against the magnetic field in the region C-D at 0.5 m/s

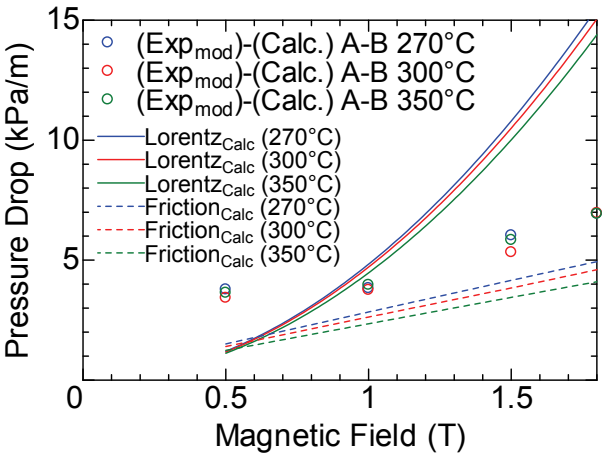

Fig. 15Difference between the modified experimental data and the numerical ones in the region A-B at 0.5 m/s

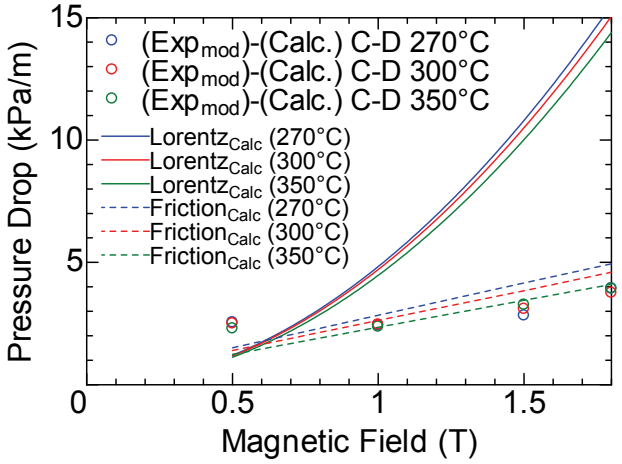

Fig. 16Difference between the modified experimental data and the numerical ones in the region C-D at 0.5 m/s

5. Conclusions

We conducted the MHD flow experiment with the three-surface-multi-layered channel and the PbLi as working fluid. The results are summarized as follows:

(1) It was verified that the MHD pressure drop was reduced by using the three-surface-multi-layered channel under the high magnetic field of up to 1.8 T.

(2) As the result of modifying zero shifts, the experimentalresults showed qualitatively good agreement with the numerical results against changes in the velocity, the temperature and the magnetic field.

(3) The experimental results were slightly larger than those by the numerical simulation. The amounts of the increase were about 30 % in the upstream region and about 20 % in the downstream region, respectively.

(4) Since the differences between the modified experimental data and the numerical ones changed linearly against the magnetic field, no more Lorentz force acted in the experiment as compared to that in the calculation. Therefore the insulating coating works well as it had been supposed.

Acknowledgements

This work was partially supported byJNIFS Collaboration Research program (NIFS11KEMF016) and Grant-in-Aid for JSPS fellows.

References

[1] H. Hashizume,“Numerical and experimental research to solve MHD problem in liquid blanket system,” Fusion Engineering and Design, 81, 8-14, 1431-1438(2006).

[2] M. Aoyagi,et al.,“MHD pressure drop characteristics in a three-surface-multi-layered channelunder a strong magnetic field,”Fusion Engineering and Design, 85, 1181-1184(2010).

[3] S. Smolentsev, et al. "Status of “TITAN” Task 1–3 “Flow Control and Thermofluid Modeling,” Fusion Engineering and Design, In Press

[4] Li, F. -C. et al.“Construction and initial operation of MHD PbLi facility at UCLA,” Fusion Engineering and Design, In Press

[5] M. Aoyagi,et al.,“Thermo-Fluid Simulation in a Liquid Metal Blanket with Three-Surface-Multi-Layered Channel,” Fusion Science and Technology, American Nuclear Society, 60,283-28(2011).

[6] D. S. Krasnov, et al. “Numericalstudy of the instability of the Hartmann layer,”J. Fluid Mech., 504, 183(2004).

4-4 Task 2-1(1) DESIGN AND CONSTRUCTION OF THERMAL DESORPTION MEASUREMENT SYSTEM FOR TRITIUM CONTAINED MATERIALS

M. Hara[1], Y. Hatano[1], P. Calderoni[2], M. Shimada[2]

[1]*Hydrogen Isotope Research Center, University of Toyama, 3190 Gofuku, Toyama, Toyama, 930-8555 JAPAN,*

masahara@ctg.u-toyama.ac.jp, hatano@ctg.u-toyama.ac.jp

[2]*Fusion Safety Program, Idaho National Laboratory, Idaho Falls, ID, USA,*

pattrick.calderoni@inl.gov, Masashi.Shimada@inl.gov

The dual-mode thermal desorption analysis system was designed and built in Idaho National Laboratory (INL) to examine the evolution of the hydrogen isotope gas from materials. The system is equipped with a mass spectrometer for stable hydrogen isotopes and an ionization chamber for tritium components. The performance of the system built was tested with using tritium contained materials. The evolution of tritiated gas species from contaminated materials was measured successfully by using the system.

I. INTRODUCTION

Hydrogen isotope atoms penetrating from plasma into plasma-facing materials (PFMs) are captured by the trap sites in the materials. The physicochemical properties of the trap sites play important roles for the thermodynamics and kinetics of the interactions between hydrogen isotopes and PFMs [1-6].

The trapping energy of hydrogen atom in materials is evaluated by the various methods. The thermal desorption measurement is one of valuable techniques for the evaluation of the trapping energy, the activation energy of hydrogen desorption and the amount of hydrogen atoms trapped. In the thermal desorption measurement, the gaseous hydrogen species evolved from the sample is commonly measured by a mass spectrometer. The thermal desorption spectra from samples containing hydrogen and deuterium gives the information of the isotope effects in hydrogen-trap interactions. The thermal desorption measurements of PFMs are used by many researchers [3-6]. However, a measurement of tritium with a mass spectrometer is difficult because of impairment of a multiplier by β-rays from tritium [7]. Handling of large radioactivity is necessary due to high specific activity of tritium. For these reasons, tritium is commonly measured with higher sensitivity using an ionization chamber, a proportional counter and a liquid scintillation counter.

A thermal desorption measurement system equipped with a mass spectrometer and an ionization chamber (or a proportional counter) is suitable to measure the evolution of tritium-containing hydrogen isotope gases from the materials. A mass spectrometer works in vacuum conditions, whereas an ionization chamber requires the working gas. In other words, an ionization chamber cannot work in vacuum conditions. Therefore, the measurement system needs to be newly designed for simultaneous measurement of the hydrogen isotope gases containing tritium.

In Japan-US joint research project TITAN, the measurement system equipped with a mass spectrometer and an ionization chamber was designed and constructed in Safety and Tritium Applied Research (STAR) facility of Idaho National Laboratory (INL). The designed system was denoted the dual-mode thermal desorption analysis system (hereafter DM-TDS). The performance of DM-TDS was evaluated by the thermal desorption spectrum of the stainless steel containing tritium. This subsection describes the technical side of DM-TDS in detail.

II. CONCEPT OF THE DUAL-MODE THERMAL DESORPTION ANALYSIS SYSTEM

DM-TDS was designed to measure the hydrogen isotopes evolved from the materials. The system should detect the main stable hydrogen isotopes by a mass spectrometer and tritium in a trace amount by an ionization chamber. Since ionization chambers require a working gas to obtain ionization current, a gas-flow system should be installed in DM-TDS. The system consists of a mass flow controller, an infrared furnace, a mass spectrometer, an ionization chamber and water bubblers as shown in Fig. 1. Argon gas is selected as the carrier gas.

The sample is placed on the sample stage made from the molybdenum sheet. The thickness and purity of the molybdenum sheet are 0.005 inch and 99.97%, respectively. To make the stage, the sheet was folded by the pliers as shown in Figs. 2 and 3. The stage is directly fixed to the thermocouple (1/8 inch sheath thermocouple with unground junction) and inserted into the quartz tube.

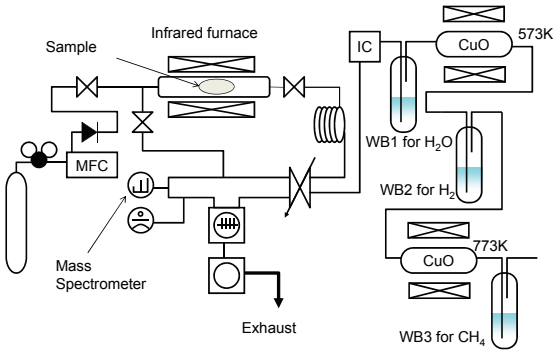

Fig. 1. Schematic diagram of dual-mode thermal desorption analysis system constrcucted. MFC and IC mean a mass flow controller and an ionization chamber, respectively. WB1 to 3 are water bubblers.

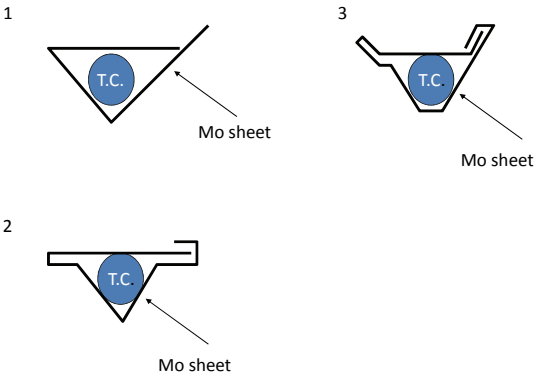

Fig. 2. Preparation of sample stage. The stage is made from a molybdenum sheet. T.C. means the sheath thermocouple.

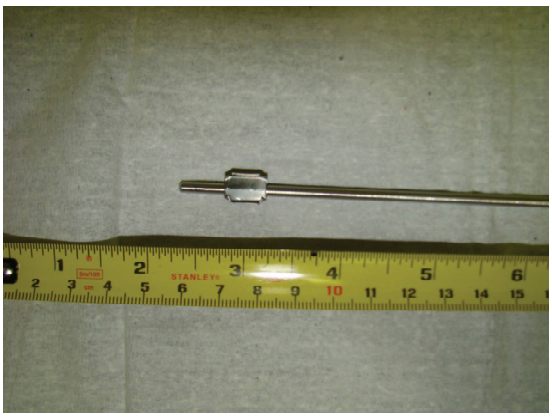

Fig. 3. Photograph of sample stage. The size of stage is around 10 mm × 8 mm. The sheath thermocouple is inserted into the opening of the stage.

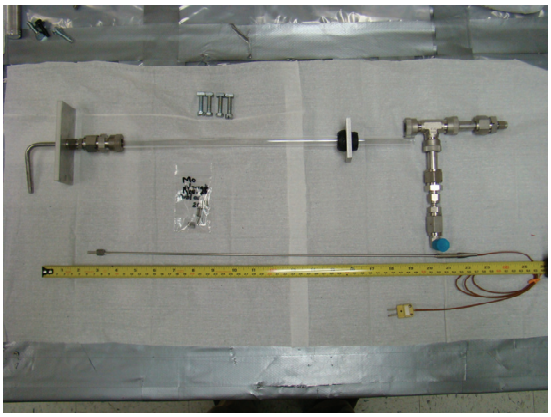

Fig. 4. Photograph of sample stage and unions for quartz tube fixing.

The sample on the stage is heated under argon gas flow by an infrared furnace. The quartz tube is connected by Ultra-Torr connections, because the quartz tube will be contaminated by the tritium evolved from samples and need to be replaced easily. The photograph of the sample holder and the unions for the quartz tube fixing is shown in Fig. 4.

The hydrogen isotope gases evolved from the sample are transported by the carrier gas. A portion of the gas evolved is introduced into the mass spectrometer through the leak valve. A single port leak valve is suitable for a vacuum thermal desorption measurement system but not for a gas-flow thermal desorption measurement system. Since a gas flow can be stuck in a single port leak valve, real-time measurement of the change in the gas composition is difficult. Hence, we needed to modify the port of the leak valve to be used in DM-TDS. Fig. 5 shows the schematic diagram of the modified leak valve. The modified leak valve is hereafter denoted the dual-port leak valve. The dual-port leak valve is designed to reduce the stuck time of flowing gas. The 1/8 inch tube is inserted into the inside of the single port leak valve through the 1/4 inch bored through type T-shape connection. Since the dual-port leak valve has the inlet and the outlet ports, the carrier gas readily passes through the inner volume of the valve. Fig. 6 shows the dual-port leak valve installed in DM-TDS.

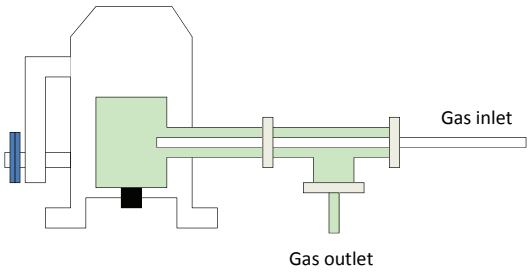

Fig. 5. Schematic diagram of dual-port leak valve.

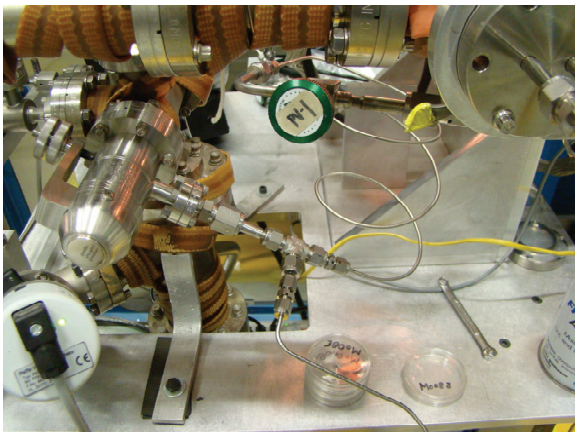

Fig. 6. Photograph of dual-port leak valve installed into DM-TDS.

Three water bubblers connected in series via two CuO beds were installed into DM-TDS as shown in Fig. 1 to determine the amount of released tritium. The first water bubbler captures HTO from the carrier gas. Subsequently, the gas passes through the CuO bed maintained at 573 K to convert HT to HTO, and the second water bubbler captures HTO. The second CuO bed maintained at 773 K oxidizes residual tritiated hydrocarbons into HTO being captured by the third water bubbler. The tritium concentrations in water in the bubblers were determined by a liquid scintillation counting to evaluate the tritium retention in the sample.

Since the ionization chamber is usually calibrated for air, the concentration of tritium in the flowing gas was evaluated from the ionization current by taking account of difference in the W value [8] between argon and air.

The mass spectrometer is evacuated by a turbo-molecular pump backed with an oil-sealed rotary pump. The pressure of residual gases was less than 10^{-7} Torr.

III. PERFORMANCE TEST OF THE DUAL-MODE THERMAL DESORPTION ANALYSIS SYSTEM

DM-TDS was built at STAR facility, INL. The 200 cm^3 ionization chamber was used for the test to detect tritium components. On the other hand, the water bubblers and the CuO beds were not installed in the test. The argon flow rate was set to 26 sccm by the calibrated mass flow controller. Two samples containing tritium were obtained from 1/4 inch stainless steel tubes used in Tritium Plasma Experiment (TPE). The length of sample 1 and 2 were 5 mm and 15 mm, respectively. The carrier gas was fed into the mass spectrometer up to around 10^{-6} Torr via the dual-port leak valve.

IV. RESULTS AND DISCUSSION

The thermal desorption spectra are shown in Fig. 7. The samples were 1/4 inch stainless steel pipes used in TPE and consequently contaminated with tritium. In Fig. 7, the abscissa gives the time and the ordinate gives the temperature, the ionization chamber output and the ion current of mass 18 (H_2O), respectively. The thin line indicates temperature. The black dot means the ion current of mass 18. The bold line is the ionization chamber output. The signal of mass 18 contained much noise, because the mass spectrometer was used before the baking treatment. However, the signal of mass 18 gave the water evolution behavior from the sample with heating. The intensity of mass 18 for sample 1 (5 mm length) increased with increasing temperature and the signal of mass 18 formed a peak at 1150 s. On the other hand, the ionization chamber output formed a peak at 1900 s. This difference was ascribed to the volume of ionization chamber. The relatively large volume causes the resident time of the carrier gas extended in the ionization chamber. In this case, the resident time of the carrier gas in the ionization chamber was calculated to be about 10 min. This result indicates that the relationship between the volume of the ionization chamber and the flow rate is one of the important issues to improve thermal desorption spectra obtained. The intensity of mass 18 increased again when the temperature descended. Subsequently the ionization chamber output also increased.

The intensity of mass 18 and ionization chamber output showed also two peaks for sample 2. We could not have clear explanation for the second peak.

The dual-mode thermal desorption analysis system could simultaneously detect the evolution of the H_2O vapor and the tritium components. Such capability should

be used for understanding the physicochemical properties

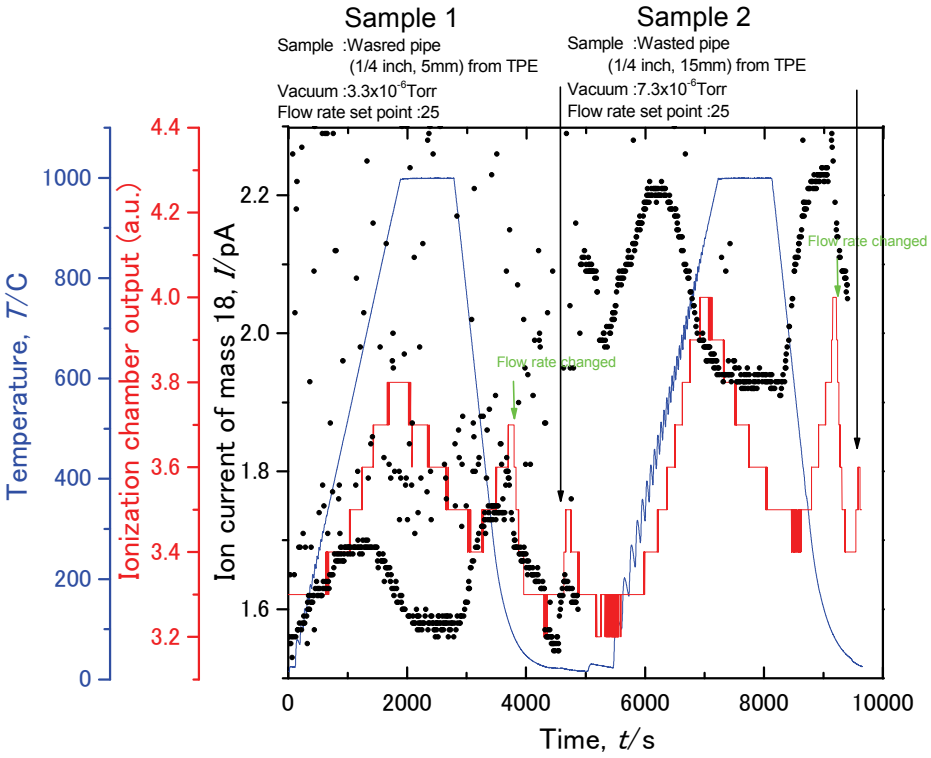

Fig. 7. Thermal desorption spectra for the stainless steel tube containing tritium. The samples were taken from the pipe wastes from TPE. The dots mean the ion current of mass 18 of the mass spectrometer. The bold line is the ionization chamber output.

of the trap sites.

V. CONCLUSIONS

To understand the physicochemical properties of the hydrogen trap sites, the dual-mode thermal desorption analysis system was designed and built in INL. Using this system, the evolution behavior of the stable hydrogen isotope gases and tritium components can be simultaneously measured. Therefore, the system will give various information on hydrogen isotope retention and release of plasma-facing materials.

ACKNOWLEDGMENTS

This study was supported by the Japanese Ministry of Education, Culture, Sports, Science and Technology via TITAN collaboration.

REFERENCES

[1] R. A. CAUSEY, "Hydrogen Isotope Retention and Recycling in Fusion Reactor Plasma-Facing Components," *J. Nucl. Mater.*, **300**, 91, (2002).

[2] T. VENHAUS, R. CAUSEY, R. DOERNER and T. ABELN, "Behavior of Tungsten Exposed to High Fluences of Low Energy Hydrogen Isotopes," *J. Nucl. Mater.*, **290-293**, 505, (2001).

[3] N. YOSHIDA, "Review of Recent Works in Development and Evaluation of High-Z Plasma Facing Materials," *J. Nucl. Mater.*, **266-269**, 197, (1999).

[4] Y. OYA, M. SHIMADA, M. KOBAYASHI, T. ODA, M. HARA, H. WATANABE, Y. HATANO, P. CALDERONI and K. OKUNO, "Comparison of Deuterium Retention for Ion-Irradiated and Neutron-Irradiated Tungsten," *Phys. scr.*, **T145**, 014050, (2011).

[5] M. SHIMADA, G. CAO, Y. HATANO, T. ODA, Y. OYA, M. HARA and P. CALDERONI, "The Deuterium Depth Profile in Neutron-Irradiated

Tungsten Exposed to Plasma," *Phys. scr.* **T145**, 014051, (2011).

[6] Y. HATANO, M. SHIMADA, T. OTSUKA, Y. OYA, V. Kh. ALIMOV, M. HARA, J. SHI, M. KOBAYASHI, T. ODA, G. CAO, K. OKUNO, T. TANAKA, K. SUGIYAMA, J. ROTH, B. TYBURSKA-PUSCHEL, J. DORNER, N. YOSHIDA, N. FUTAGAMI, H. WATANABE, M. HATAKEYAMA, H. KURISHITA, M. SOKOLOV and Y. KATOH, "Deuterium Trapping at Defects Created with Neutron and Ion Irradiations in Tungsten," *Nucl. Fusion*, **53**, 073006, (2013).

[7] K. WATANABE, K. ICHIMURA and M. MATSUYAMA, *Ann. Rep. Tritium Res. Ctr., Toyama U.*, **5**, 1, (1985). (in Japanese)

[8] G. F. KNOLL, *Radiation Detection and Measurement*, 4th Ed., John Wiley & Sons, Inc., New Jersey, (2010).

Task 2-1(2) MEASUREMENT OF TRITIUM RETAINED IN NEUTRON-IRRADIATED MOLYBDENUM USING IMAGING PLATE AND BETA-RAY INDUCED X-RAY SPECTROMETRY

Kun Zhang[1], Masashi Shimada[2], Yasuhisa Oya[3], Masao Matsuyama[1], Yuji Hatano[1]

[1]*University of Toyama, Gofuku 3190, Toyama 930-8555, Japan,*
zhangkun__2000@163.com, matsu3h@ctg.u-toyama.ac.jp, hatano@ctg.u-toyama.ac.jp
[2]*Idaho National Laboratory, Idaho Falls, ID, USA, Masashi.Shimada@inl.gov*
[3]*Shizuoka University, Shizuoka 422-8529, Japan, syoya@ipc.shiuoka.ac.jp*

The radiations from Mo samples irradiated with neutrons to 7.2 × 10^{-4}, 7.2 × 10^{-3}, 0.072 and 0.28 dpa were measured using imaging plates (IPs) with and without protection coating, and low energy, high resolution Ge detector used for β-ray induced X-ray spectrometry (BIXS). A non-irradiated reference Mo sample was exposed to DT plasma at 200 ℃ and tritium concentration of 0.5%, and the intensity of β-rays and β-ray induced X-rays were measured for comparison. The β-rays from tritium at the surface and in the subsurface layer of the sample was detected using IP without protection coating (BAS-TR, Fujifilm Co., Japan) with sufficiently high sensitivity compared with radiations induced in the Mo samples by neutron irradiation. In other words, surface tritium contamination was able to be measured with sufficiently low interference of neutron-induced radiations. On the other hand, the measurement of β-ray induced X-rays using IP with protection coating (BAS-MS, Fujifilm Co., Japan) was difficult due to interference of the neutron-induced radiations. Nevertheless, the intensity of neutron-induced radiation in a low energy region (< 20 keV) was relatively low, and the energy spectra of X-rays measured using the Ge detector clearly showed Ar Kα characteristic X-rays and bremsstrahlung X-rays induced by β-rays from tritium. It was concluded that β-ray induced X-ray spectrometry has a potential for non-destructive evaluation of depth profiles of tritium in neutron-irradiated PFMs.

I. INTRODUCTION

Measurements of tritium retention in plasma-facing materials (PFMs) are important issues from the viewpoints of control of tritium inventory in a vacuum vessel, waste management and tritium accountancy. Imaging plate (IP) [1,2] and β-ray induced X-ray spectrometry (BIXS) [3,4] are widely used for those purposes. However, in future fusion reactors, radioactivity is induced in PFMs by irradiation of 14 MeV neutrons, and those radiations may interfere with tritium measurements by IP and BIXS. Matsuyama et al. [4] measured tritium retained in carbon tiles used in DT campaign in JET under the presence of ^{60}Co and ^{137}Cs γ-sources. They reported that the presence of the γ-fields has no influence in the shape of the β-ray-induced X-ray spectra, although the whole intensity in the observed energy region was dependent on radioactivity of the γ-emitters. However, the effects of radiations from neutron-irradiated high-Z materials have not been investigated.

In this study, radiations from neutron-irradiated Mo samples were measured with IPs and a low energy, high resolution semiconductor detector used in BIXS measurements. A non-irradiated reference Mo sample was exposed to DT plasma, and the measurements of β-rays and β-ray induced X-rays were also performed. Applicability of IPs and BIXS are discussed by comparing the results of those measurements.

II. EXPERIMENTAL

Specimens used were neutron irradiated Mo samples and reference non-irradiated one (>99.95%) provided by Oak Ridge National Laboratory (ORNL) [5]. Those specimens were irradiated with neutrons in High Flux Isotope Reactor (HFIR) at ORNL to fluences in the range of 2 × 10^{21} to 8 × 10^{24} n m^{-2} (E > 0.1 MeV) corresponding to 7.2 × 10^{-4}, 7.2 × 10^{-3}, 0.072 and 0.28 displacement per atom (dpa) at ~80 ℃.

From the viewpoint of tritium measurements, IPs can be separated into two types by the absence or presence of protection layers for hygroscopic Eu-doped BaFX (X = Cl, Ba and I) phosphor. BAS-TR and BAS-MS produced by Fujifilm Co., Japan belong to the former and the latter, respectively. The IPs without coatings are sensitive to low-energy β-rays from tritium, and hence they have been widely used to measure surface tritium contamination of solids. The escape depth of β-rays from tritium is several micrometers or less in solids, and tritium in a deeper region cannot be measured by detecting β-rays. The IPs with protection coatings (9 μm-thick polyethylene terephthalate film in the case of BAS-MS [6]) cannot

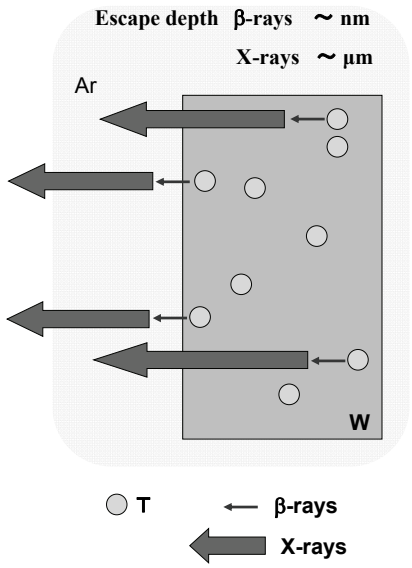

Fig. 1. Schematic drawing of principle of β-ray induced X-ray spectrometry.

detect low energy β-rays due to attenuation in the coating layers. Nevertheless, they are sensitive to X-rays induced by β-rays and, in principle, suitable for analysis of tritium in deeper regions. BAS-TR also detects X-rays but sensitivity to X-rays (and γ-rays) is far less than that of BAS-MS due to smaller thickness of phosphor layer [6]. Hence, BAS-TR is commonly used for β-ray detection. In this study, both β-ray measurement with BAS-TR and X-ray detection with BAS-MS were attempted. The samples were placed on IPs in air in the dark for several hours. Then, 2-dimensional distributions of photo-stimulated luminescence (PSL) were observed using laser scanner (FLA-7000, Fujifilm Co., Japan).

A semiconductor detector equipped with a high purity Ge crystal was used for measurements of β-ray induced X-rays. Energy resolution of the present X-ray detector was determined to be 129 eV at 5.9 keV [4]. The radiation entrance window of the X-ray detector was made of a specially designed thin Be plate (8 μm in thickness) to gain an effective transmittance of low energy X-rays. Fig. 1 shows the principle of BIXS measurements. A sample was placed in Ar atmosphere (~0.1 MPa). β-rays emitted by tritium on the surface and in the subsurface layer within the range of the β-rays mainly excite characteristic X-rays of Ar, whereas those from tritium in the bulk of sample induce characteristic X-rays of constituent elements of sample and bremsstrahlung X-rays.

The non-irradiated reference Mo sample was exposed to DT plasma at 200 °C in a linear plasma machine called TPE at Idaho National Laboratory. Flux and fluence of D were 7×10^{21} D $m^{-2}s^{-1}$ and 5×10^{25} D m^{-2}, respectively. Concentration of T was 0.5%. Hence, flux and fluence of T should be 3.5×10^{19} T $m^{-2}s^{-1}$ and 2.5×10^{23} D m^{-2}.

III.RESULTS AND DISCUSSION

III.A. IP measurements

Fig. 2 shows IP images of neutron-irradiated Mo samples [(a)–(d) and (f)–(i)] and those of non-irradiated reference sample exposed to DT plasma [(e) and (j)]. In this figure, variation in color from blue to red indicates increase in PSL intensity. Rectangular contrasts in blue, green and red colors indicate samples. In the case of neutron-irradiated samples, the PSL intensity from both BAS-MS and BAS-TR increased with damage level, indicating increase in intensity of radiations from the samples. In Fig. 3, the PSL intensity is plotted against damage level. A linear correlation was observed between damage level and PSL intensity. The PSL intensity from BAS-MS was higher than that from BAS-TR by a factor of 3. This observation indicates that major radiations from neutron-irradiated Mo samples are γ- and X-rays. As described previously, BAS-MS has higher sensitivity to γ- and X-rays than BAS-TR. Consequently, PSL intensity induced by γ- and X-rays should be higher for BAS-MS than for BAS-TR.

In contrast to the neutron-irradiated samples, the PSL intensity from BAS-TR after contact with the tritium-exposed sample [(j) in Fig. 2] was far higher than that from BAS-MS [(e) in Fig. 2]; the former was higher than the latter by a factor of 800. This is, at least in part, due to low conversion factors ($10^{-4} \sim 10^{-3}$ [7]) from β-rays to X-rays. Another possible reason is a depth profile of tritium. The spectrum of β-ray induced X-rays given later showed that tritium was localized at the surface and/or in the subsurface layer of the sample. As previously mentioned, IP measurements were performed in air. Because the energies of Kα X-rays of nitrogen and oxygen are low (N: 0.392 keV, O: 0.525 keV [8]), the contributions of X-rays from air in PSL excitation is negligible. Hence, PSL intensity from BAS-MS should be low if tritium is localized at the surface and/or in the subsurface layer of a material. On the contrary, if tritium penetrates into deep in the bulk of a material, the intensity of bremsstrahlung X-rays and characteristic X-rays of constituent elements become high, and hence contribution of X-rays to PSL excitation can be larger.

The PSL intensity from BAS-TR after contact with tritium-exposed sample [(j) in Fig. 2] was significantly higher than that after contact with neutron-irradiated samples [(f)–(i) in Fig. 2]. Hence, it was concluded that measurements of β-rays using IP is applicable for the evaluation of tritium retention on the surface and in the subsurface of moderately neutron-irradiated PFMs. On the

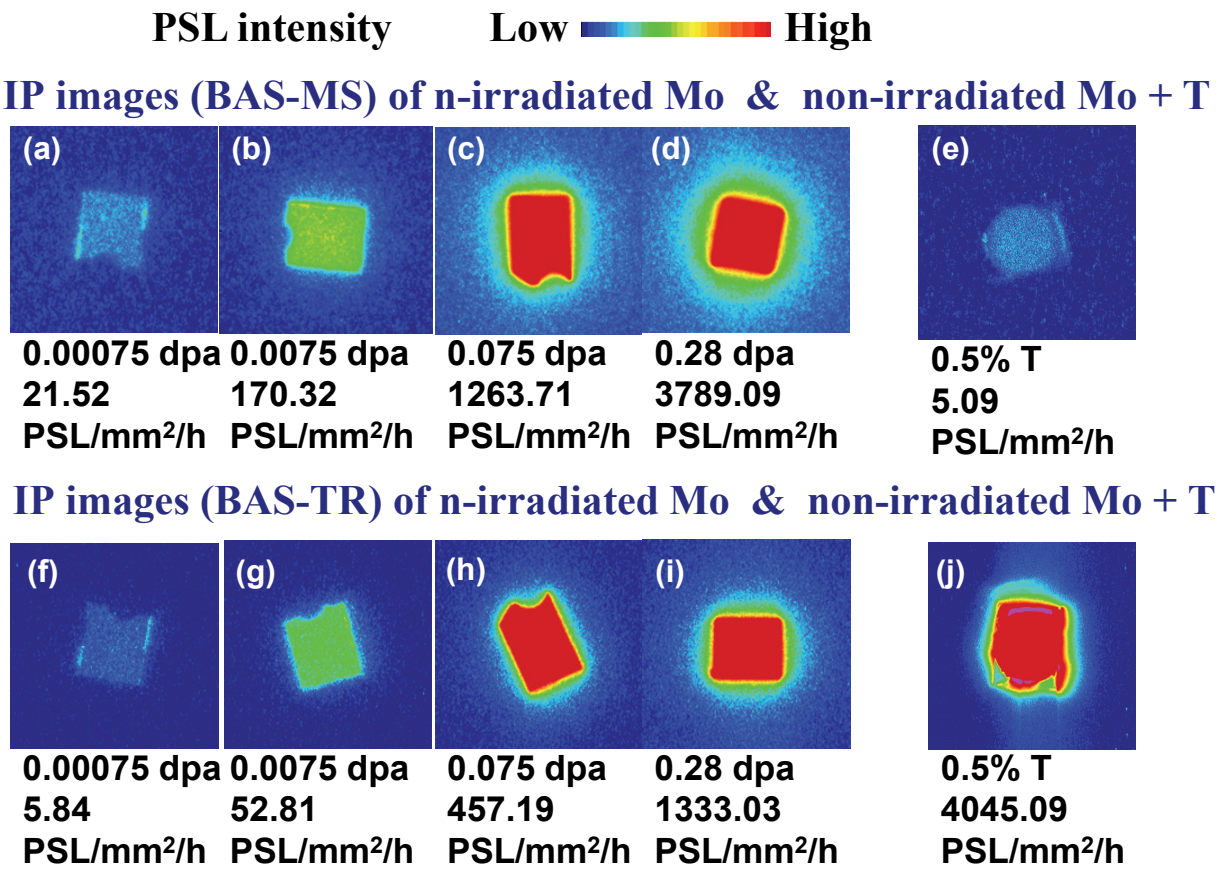

Fig. 2. Images obtained using BAS-MS [(a)–(e)] and BAS-TR [(f)–(j)] for neutron-irradiated Mo samples [(a)–(d) and (f)–(i)] and tritium-exposed reference sample [(e) and (j)].

other hand, the PSL intensity from BAS-MS after contact with tritium-exposed sample [(e) in Fig. 2] was far lower than that after contact with neutron-irradiated samples [(a)–(d) in Fig. 2]. These observations indicate that measurements of β-ray induced X-rays using IP for neutron-irradiated PFMs is much more difficult than β-ray detection. In this study, the non-irradiated reference sample was exposed to DT plasma at tritium concentration of 0.5%. However, neutron irradiation induces defects such as vacancy and voids. In TITAN project, the authors revealed that those radiation-induced defects act as trapping sites against hydrogen isotopes and increase tritium retention [9-16]. In addition, tritium concentration in fusion plasma should be higher than 0.5%. Hence, the detection of β-ray induced X-rays may be easier than the present case. Further investigation, however, is necessary to derive final conclusion on this point.

III.B. BIXS measurements

Range of X-ray energy examined with the low energy, high resolution Ge detector was 1–165 keV. The most intense radiation observed in this energy range was Mo Kα and Kβ X-rays (17.4 and 19.6 keV [8]). Fig. 4 shows X-ray spectra of samples irradiated with neutrons to 0.0075, 0.075 and 0.28 dpa together with one of tritium-exposed reference sample. The spectrum of the specimen irradiated to 7.2×10^{-4} dpa is omitted because intensity of X-rays was too low to compare in the same scale. Because the maximum energy of β-rays emitted by tritium is 18.6 keV [7], spectra in the range of energy higher than 20 keV are also omitted. Intensities of characteristic X-rays of Mo and other impurity elements increased with increase in damage level. This observation agrees with the results of IP measurements.

It should be emphasized that the most intense Ar Kα X-rays was observed for tritium-exposed reference sample. This is due to the excitation by β-rays emitted by tritium on the surface and in the subsurface layer of the sample. In addition, a broad peak of bremsstrahlung X-rays induced in Mo by β-rays from tritium was clearly observed in the range of energy from 1 to 10 keV. These observations indicate that tritium in neutron-irradiated PFMs can be detected by measuring energy spectrum of

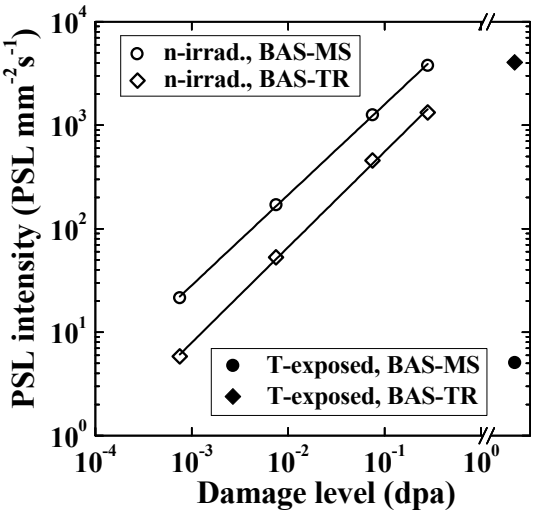

Fig. 3. Correlation between PSL intensity and damage level of neutron-irradiated Mo samples. PSL intensities after contacting with tritium-exposed reference sample are also given in this figure for comparison.

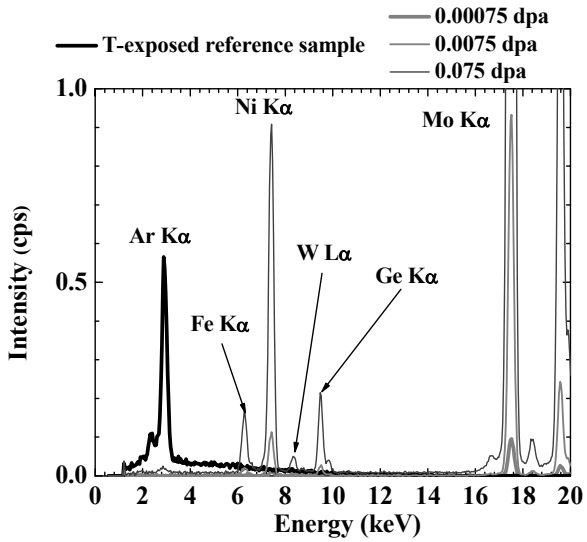

Fig. 4. Spectra of neutron-induced radiations and β-ray induced X-rays measured using low energy, high resolution Ge detector.

X-rays using a low energy, high resolution semiconductor detector.

In the range of energy higher than 3 keV, the intensity of bremsstrahlung X-rays monotonously decreased with increase in energy. This observation suggests that tritium was concentrated at the surface and/or in the subsurface layer. X-rays induced by tritium in the bulk of material reach a detector after attenuation in a material, whereas that induced by T on the surface experiences no attenuation. Attenuation becomes stronger with increase in a depth where T had been present. The X-ray absorption coefficient of Mo monotonously decreases with increase in energy in the range from 2.5 to 20 keV (L-and K-absorption edges). Hence, the peak of bremsstrahlung X-rays shifts to high energy side with increase in penetration depth of tritium. Matsuyama et al. [3] evaluated the correlation between the peak position of bremsstrahlung X-rays and penetration depth of tritium in ZrNi. They reported that the peak position shifts from 4.5 to 6.5 keV if penetration depth of tritium changes from 5 to 135 μm. Because bremsstrahlung X-ray peak was clearly observed, it was concluded that BIXS has a potential for non-destructive evaluation of depth profiles of tritium in neutron-irradiated PFMs.

IV. CONCLUSIONS

β-rays from tritium at the surface and in the subsurface layer of Mo sample was able to be detected using IP without protection coating (BAS-TR) with sufficiently low interference of radiations induced by neutron irradiations up to 0.28 dpa. On the other hand, the measurement of β-ray induced X-rays using IP with protection coating (BAS-MS) was difficult due to interference of neutron-induced γ- and X-rays. Nevertheless, the intensity of neutron-induced radiations in the low energy region (< 20 keV) was relatively low, and the energy spectra of X-rays measured using the Ge detector clearly showed Ar Kα characteristic X-rays and bremsstrahlung X-rays induced by β-rays from tritium. This observation indicated that β-ray induced X-ray spectrometry has a potential for non-destructive evaluation of depth profiles of tritium in neutron-irradiated PFMs.

ACKNOWLEDGMENTS

This study was supported by the Japanese Ministry of Education, Culture, Sports, Science and Technology via TITAN collaboration. Authors would like to express their sincere thanks to Dr. M. Li of ORNL for providing Mo samples.

REFERENCES

[1] H. SAITOH, T. HISHI, T. MISAWA, T. OHNISHI, Y. NOYA, T. MATSUZAKI and T. WATANABE, "Quantitative Visualization of Tritium Distribution in Vanadium by Tritium Radioluminography," *J. Nucl. Mater.*, **258–263**, 1404, (1998).

[2] T. TANABE and V. PHILIPPS, “Tritium Detection in Plasma Facing Component by Imaging Plate Technique,” *Fusion Eng. Des.*, **54**, 147, (2001).
[3] M. MATSUYAMA, K. WATANABE and K. HASEGAWA, “Tritium Assay in Materials by the Bremsstrahlung Counting Method,” *Fusion Eng. Design*, **39–40**, 929, (1998).
[4] M. MATSUYAMA,Y. TORIKAI, N. BEKRIS, M. GLUGLA, A. ERBE, W. NAEGELE, N. NODA, V. PHILLIPS, P. COAD and K. WATANABE, “Applicability of β-Ray-Induced X-ray Spectrometry to In-Situ Measurements of Tritium Retention in Plasma-Facing Materials in ITER,” *Fusion Eng. Des.*, **81**, 163, (2006).
[5] M. LI, N. HASHIMOTO, T. S. BYUN, L. L. SNEAD and S. J. ZINKLE, "Defect Cluster Formation and Radiation Hardening in Molybdenum Neutron-Irradiated at 80 ºC”, *J. Nucl. Mater.*, 367-370, 817 (2007).
[6] THE JAPAN RADIOISOTOPE ASSOCIATION, *Radioisotope Pocket Data Book*, 10th Ed., Maruzen, Tokyo, Japan, (2001). (in Japanese)
[7] P. CLARK SOUERS, *Hydrogen Properties for Fusion Energy*, University of California Press, Berkeley and Los Angeles, (1986).
[8] J. A. BEARDEN, “X-ray Wavelength,” *Rev. Mod. Phys.*, **39**, 78, (1967).
[9] M. SHIMADA et al., “First Result of Deuterium Retention in Neutron-Irradiated Tungsten Exposed to High Flux Plasma in TPE”, *J. Nucl. Mater.*, **415**, S667, (2011).
[10] Y. OYA et al., “Comparison of Deuterium Retention for Ion-Irradiated and Neutron-Irradiated Tungsten”, *Phys. Scr.*, **T145,** 014050, (2011).
[11] M. SHIMADA et al., “Deuterium Depth Profile in Neutron-Irradiated Tungsten Exposed to Plasma”, *Phys. Scr.*, **T145**, 014051, (2011).
[12] M. SHIMADA et al., “Overview of the US-Japan Collaborative Investigation on Hydrogen Isotope Retention in Neutron-Irradiated and Ion-Damaged Tungsten, *Fusion Eng. Des.*, **87**, 1166, (2012).
[13] Y. HATANO et al., Retention of Hydrogen Isotopes in Neutron-Irradiated Tungsten (Overview), *Mater. Trans.*, **54**, 437, (2013).
[14] M. KOBAYASHI et al., Deuterium Trapping by Irradiation Damage in Tungsten Induced by Different Displacement Processes, *Fusion Eng. Des*., **88**, 1749, (2013).
[15] Y. HATANO et al., Deuterium Trapping at Defects Created with Neutron and Ion Irradiations in Tungsten, *Nucl. Fusion*, **53**, 073006, (2013).
[16] Y. HATANO et al., Trapping of Hydrogen Isotopes in Radiation Defects Formed in Tungsten by Neutron and Ion Irradiations, *J. Nucl. Mater.*, **438**, S114, (2013).
[17] http://www.nist.gov/pml/data/xraycoef/.

Task 2-1(3) COMPARISON OF DEUTERIUM RETENTION FOR ION-IRRADIATED AND NEUTRON-IRRADIATED TUNGSTEN

Yasuhisa Oya[1], Masashi Shimada[2], Makoto Kobayashi[1], Takuji Oda[3], Masanori Hara[4], Hideo Watanabe[5], Yuji Hatano[4], Pattrick Calderoni[2] and Kenji Okuno[1]

[1]*Graduate School of Science, Shizuoka University, 836 Ohya, Suruga-ku, Shizuoka, 422-8529, Japan, syoya@ipc.shizuoka.ac.jp, f5144008@ipc.shizuoka.ac.jp, srkokun@ipc.shizuoka.ac.jp*
[2] *Fusion Safety Program, Idaho National Laboratory, Idaho Falls, 83415, USA, masashi.shimada@inl.gov, pattrick.calderoni@inl.gov*
[3]*Department of Nuclear Engineering and Management, Graduate School of Engineering, The University of Tokyo, Tokyo, 113-8656, Japan, oda@flanker@q.t.u-tokyo.ac.jp*
[4]*Hydrogen Isotope Research Center, University of Toyama, Toyama, 930-8555, Japan, masahara@ctg.u-toyama.ac.jp, hatano@ctg.u-toyama.ac.jp*
[5]*Institute for Applied Mechanics, Kyushu University, Kasuga, Fukuoka 816-8580, Japan, watanabe@riam.kyushu-u.ac.jp*

The behavior of D retentions for Fe^{2+} irradiated tungsten with the damage of 0.025-3 dpa was compared with that for neutron irradiated tungsten with 0.025 dpa. The D_2 TDS spectra for Fe^{2+} irradiated tungsten consisted of two desorption stages at 450 K and 550 K although that for neutron irradiated tungsten was composed of three stages and addition desorption stage was found around 750 K. The desorption rate of major desorption stage at 550 K increased as the number of dpa by Fe^{2+} irradiation increased. In addition, the first desorption stage at 450 K was only found for the damaged samples, indicating that the second stage would be based on intrinsic defects or vacancy produced by Fe^{2+} irradiation and the first stage should be the accumulation of D in mono vacancy leading to the lower activation energy, where the dislocation loop and vacancy was produced. The third one was only found for the neutron irradiation, showing the D trapping by void or vacancy cluster and the diffusion effect is also contributed due to high FWHM of TDS spectrum. It can be said that the D_2 TDS spectra for Fe^{2+}-irradiated tungsten could not represent that for neutron-irradiated one, showing that the deuterium trapping and desorption mechanism for neutron-irradiated tungsten has a difference from that for ion-irradiated one.

I. INTRODUCTION

Plasma facing components research for fusion applications has recently focused on tungsten materials due to low sputtering yield and low tritium retention [1-4]. One of the key issues under performance evaluation of plasma facing materials is tritium retention and recycling under fusion relevant conditions. To predict hydrogen isotope recycling, including tritium, it is important to elucidate the effects of radiation damages especially the impact of neutron irradiation for tungsten. It is thought that the neutron irradiation would produce additional trapping sites and tritium retention would dramatically enhance. Recently, energetic ion irradiation experiment was performed on tungsten to demonstrate neutron irradiation effect on tritium retention [5-9]. However, the neutron irradiation may introduce some other effects and comparison of D retentions for ion-irradiated tungsten and neutron-irradiated tungsten with the same plasma device and TDS system is quite meaningful.

In our previous research, it was found by TDS (Thermal Desorption Spectroscopy) that the deuterium retention for the 0.025 dpa neutron-irradiated tungsten was about three times as large as that for un-irradiated one [10]. The TDS spectrum was extended toward higher temperature side, indicating that deuterium was stably trapped in radiation damages. The behavior of hydrogen isotopes implanted into tungsten with vacancies was simulated by Monte Carlo technique and correlation between hydrogen isotope distribution and trap density and distribution were evaluated [11]. In order to elucidate hydrogen isotope trapping mechanisms for damaged tungsten, comparison of deuterium retention for ion-irradiated and neutron-irradiated tungsten is quite important.

II. EXPERIMENTAL

The disk-type samples with 6 mm diameter and ~ 0.2 mm thickness were prepared from a rod of tungsten under stress-relieved conditions supplied by Allied Tungsten Co. Ltd, whose grains were normal to the surface. The samples were polished mechanically to mirror finish

surfaces and cleaned by an ultra-sonic bath with, acetone, ethanol and de-ionized water for 5 minutes each.

2.8 MeV Fe^{2+} was implanted into all the surface area of W specimens at room temperature by Tandetron Accelerator System, RAPID (Rutherford Backscattering Spectroscopic Analyzer with Particle Induced X-ray Emission and Ion Implantation Devices), at The University of Tokyo. The implantation depth of Fe^{2+} was 0.5 □m by TRIM estimation. Three different damaged samples were prepared by changing the ion fluences of 2.7×10^{17}, 3.3×10^{18} and 3.3×10^{19} Fe^{2+} m^{-2}, corresponding to the damages of 0.025 dpa, 0.3 dpa and 3 dpa, respectively.

Thereafter, the samples were transferred to Idaho National Laboratory and exposed to the deuterium plasma by TPE [12,13]. The tungsten mask was used to mount the tungsten sample with the clearance hole of □ 8 mm. The sample temperature was monitored by the thermocouple touched on the backside of the sample. The plasma diagnostics, namely electron temperature and density profiles, were evaluated by a pneumatically actuated Langmuir probe. The un-irradiated tungsten sample was also used to compare the D retention in tungsten with the same deuterium plasma exposure condition. The primarily species was D^+ [10]. The ion flux and energy were $\sim 1.0 \times 10^{22}$ D^+ m^{-2} s^{-1} and 100 eV. The sample temperature was set to be almost constant to be 473 K and the deuterium plasma fluence was within the order of $\sim 6 \times 10^{25}$ D^+ m^{-2}. After the ion implantation, the sample was cooled down to room temperature within 30 minutes by contacting the Cu plate with cooling water. The oxidized sample without ion irradiation was also prepared to evaluate the surface effect for the D retention. The sample was oxidized at 673 K for 2 hours in air atmosphere after the sample pretreatment including polishing and rinsing. Thereafter, the D plasma exposure was performed at 473 K with the same experimental condition.

The deuterium retention and desorption behaviors were analyzed by TDS which was located near the TPE device. So, the sample was quickly replaced to the TDS chamber with several minutes' air exposure. TDS was applied with heating rate of 10 K min^{-1} from room temperature to 1273 K. The sample heating was continued to keep 1273 K for 30 minutes to confirm the total deuterium desorption from the sample. Only the peaks associated with D_2^+ and HD^+ were considered for the estimation of D retention because no other desorption species like water form or hydrocarbon form was observed. The TDS calibration was done by three standard leaks [10]. The surface morphology was observed by SEM (Scanning Electron Microscope, VE-9800, KEYENCE Inc.). For the observation of ion implantation effect on the surface morphology, 2.4 MeV Cu^{2+} was irradiated into tungsten samples with 0.03, 0.3 and 3 dpa at the Institute of Applied Mechanics, Kyushu University and the TEM (Transmission Electron Microscope, JEM 2000EX, JASCO Inc.) observation was performed. The thickness of the sample was less than 0.1 μm and electrical polishing was performed before the irradiation.

III. RESULTS AND DISCUSSION

Figure 1 shows the D_2 TDS spectra for tungsten with the damage of 0.025 – 3 dpa by Fe^{2+} irradiation. The major desorption stage was located at the temperature of 550 K. Some reports for plasma exposure showed the D desorption was initiated at the lower desorption temperature than plasma exposure temperature [13]. Most of deuterium would be desorbed just after the plasma exposure and some of deuterium would be stabilized during the desorption process by the trapping site with lower activation energy. For the Fe^{2+} irradiated tungsten, an additional desorption stage was found at lower temperature side. Both of these peak intensities were increased as the number of dpa increased. Comparing the TDS spectra with that for the neutron-irradiated tungsten, it was clear the shape of TDS spectra was quite different and another large desorption peak was found at around 750 K for the neutron-irradiated tungsten. The D_2 desorption spectra were extended toward lower temperature side and the D_2 desorption rate was increased as the amount of irradiation damages increased for ion irradiated tungsten. However, it was found that the D_2 TDS spectra for Fe^{2+}-irradiated tungsten could not represent that for neutron-irradiated one, indicating that the deuterium trapping mechanism for neutron-irradiated tungsten has a difference from that for ion-irradiated one. Total D retention for 0.025 dpa Fe^{2+} irradiated tungsten was 1.5 times as large as that for un-irradiated tungsten, which was almost a half compared to that for 0.025 dpa neutron irradiated tungsten. For the dpa dependence by Fe^{2+} irradiation, the D retention increased almost twice as the dpa increased one order between 0.025 dpa and 3 dpa ranges. The D desorption stages were assumed to consist of three stages at around 450 K, 550 K and 750 K, namely Peaks 1, 2 and 3, and peak separation was performed.

Fig. 2 shows the result of D retentions for Peaks 1, 2 and 3, and total D retention as a function of dpa by Fe^{2+} irradiation. Large D desorption was found for second stage for 3 dpa Fe^{2+} irradiated tungsten. The D desorption stage of Peak 3 was observed only for 0.025 dpa neutron irradiated tungsten as mentioned above. Fig. 3 shows SEM images for (a) 0.025 dpa Fe^{2+} irradiated tungsten and (b) 0.3 dpa Fe^{2+} irradiated one after D plasma exposure and TDS. The surface morphology for the sample before experiment is rather smooth (not shown in this paper) and only the grain boundary was found. Some impurities with white color in the picture were adsorbed on the surface especially for the 0.025 dpa sample and small pores (black dots) were introduced which would be

formed on the surface by Fe^{2+} irradiation or D plasma exposure. In the case of 0.3 dpa Fe^{2+} irradiation, the morphology was quite different as shown in Fig. 3 (b). The fracture around the grain boundary was found for the D plasma exposure area. Many cavities and fractures existed in grains, which would induce the peel. To reveal microstructure change by ion irradiation, TEM observation for 2.4 MeV Cu^{2+} irradiated tungsten was performed and shown in Fig. 4. In the un-irradiated sample, almost all the dislocations which would be introduced during the fabrication process for rod type sample were removed, but all the defects should not be completely removed from the sample due to stress-relieved condition A large number of dislocation loops with the size less than 10 nm was dispersedly observed for 0.03 dpa sample. The density of dislocation loops was enhanced as the number of dpa (irradiation fluence) was increased and the nucleation of dislocation loop was found.

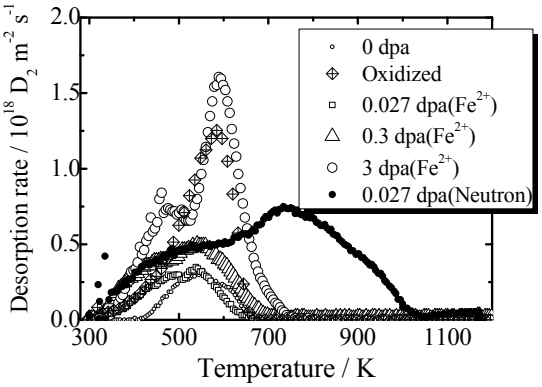

Fig. 1 D_2 TDS spectra for Fe^{2+} irradiated tungsten samples after plasma exposure at TPE. The TDS spectra for neutron irradiated tungsten and oxidized tungsten were also shown.

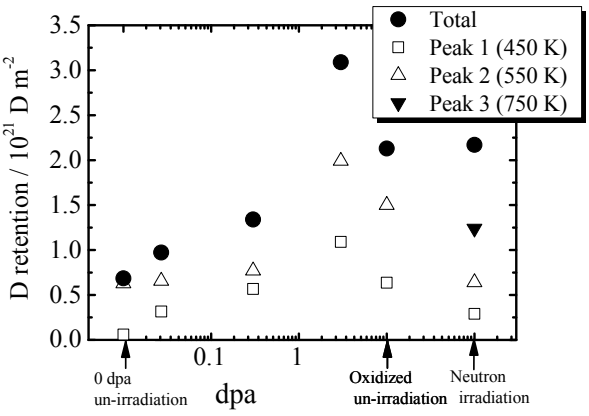

Fig. 2 The D retentions for tungsten as a function of damage density [dpa]. The D retentions for oxidized sample with un-irradiation and neutron irradiated sample were also shown.

Based on these experimental results, D retention behaviors for ion-irradiated tungsten and neutron-irradiated tungsten are discussed. The D retention was clearly changed by the number of damages introduced in tungsten. By the introduction of damages, D desorption stage in lower temperature side namely 450 K was emerged, which was not observed for un-irradiated sample, indicating that accumulation of damages in ion-irradiated area would enhance D trapping with different activation energy. The activation energy for D desorption at Peak 1 should be less than 1.48 eV, which corresponded to that at Peak 2 estimated by low energy (1.5 keV) ion implantation experiment and was almost consistent with the reported value of 1.45 eV [8]. Recently, hydrogen-vacancy binding energies have been reported and multiple hydrogen trapping in a vacancy reduces the binding energy [14,15], which would produce additional desorption stage at lower temperature side. However, most of D was retained in a vacancy with one atom or two atoms due to H atoms also stabilize vacancies as reported in [15]. However, the TDS spectrum for neutron-irradiated one had one more additional desorption stage, which was not observed for ion-irradiated sample and the desorption temperature extended to higher temperature side more than 900 K. This difference should be caused by D trapping in deeper regions, because the neutron irradiation produces the irradiation damages throughout the sample, although the ion irradiation limits within the depth less than one micro meter. The D depth profiling by NRA as reported in Ref. [16] indicate the enhancement of D retention within the depth of 3 □m compared to that for un-irradiation case. At this time, the D depth profile for the2.8 MeV Fe^{2+} irradiated sample was not evaluated but the TRIM estimation showed the damage was introduced within the depth of 0.5 □m, indicating that the effect of D diffusion toward the depth by neutron irradiation would make a large contribution on high activation energy for D desorption although the D accumulation for ion-irradiated sample would be limited within the shallow surface region. The FWHM for Peak 3 was large of about 250 K compared to that for Peaks 1 and 2 of 130 K 115 K, which is also support the different desorption and / or trapping mechanism. In the present study, the oxidized sample was also prepared and performed with the same D plasma exposure condition to observe the surface effect on D trapping and desorption. As seen in Fig. 1, only the one desorption stage located at 660 K was found, indicating that the surface trapping effect does not largely impact on the desorption temperature and only the D retention enhancement with the same trapping state as the un-irradiated sample was contributed, which would interfere the diffusion toward the surface. The retention enhancement factor, namely the ratio of D retention for neutron or ion irradiated sample to that for un-irradiated sample, was also evaluated to be 1.5 to 5 in the preent study, which was almost consistent with

that reported by G. M. Wright [5,6] and W. R. Wampler [9] as shown in Fig.5.

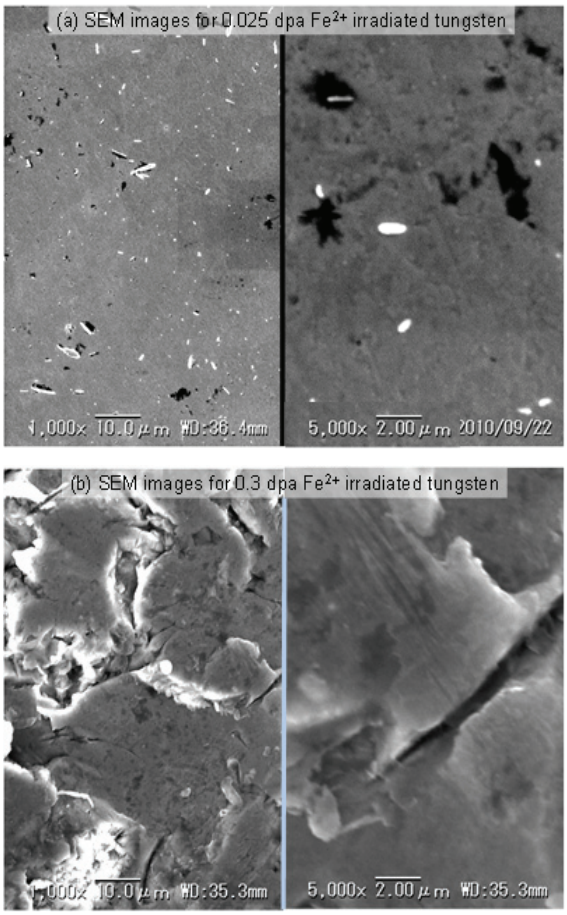

Fig. 3 SEM micrographs for Fe^{2+} irradiated tungsten with 0.025 dpa and 0.3 dpa after D plasma exposure and TDS.

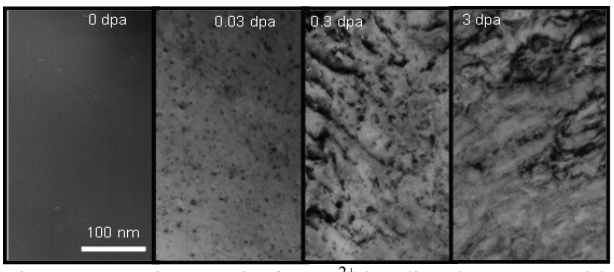

Fig. 4 TEM micrographs for Cu^{2+} irradiated tungsten with 0-3 dpa without D plasma exposure.

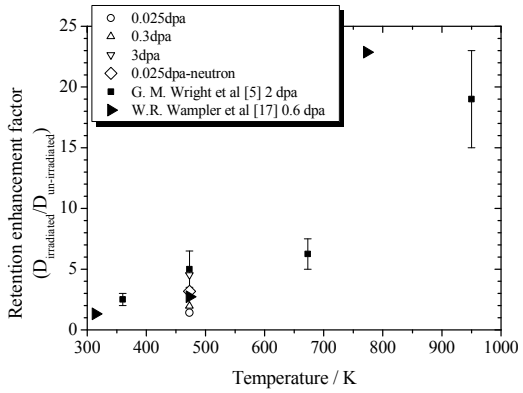

Fig. 5 Deuterium retention enhancement factor as a function of irradiation temperature.

IV. CONCLUSIONS

The behavior of D retentions for Fe^{2+} irradiated tungsten with the damage of 0.025-3 dpa was compared with that for neutron irradiated tungsten with 0.025 dpa. The D_2 TDS spectra for Fe^{2+} irradiated tungsten consisted of two desorption stages at 450 K and 550 K although that for neutron irradiated tungsten was composed of three stages, showing that an additional desorption stage was found around 750 K. The desorption rate of major desorption stage at 550 K increased as the number of dpa. The first desorption stage at 450 K was only found for the damaged samples. The second stage would be based on existence of intrinsic defects or vacancy produced by Fe^{2+} irradiation and the first stage should be the accumulation of D in mono vacancy leading to the lower activation energy, where the dislocation loop and vacancy were produced. The third one was only found for the neutron irradiation, showing the D trapping by void or vacancy cluster and the diffusion effect is also contributed due to high FWHM. Therefore, D_2 TDS spectra for Fe^{2+}-irradiated tungsten could not represent that for neutron-irradiated one, indicating that the deuterium trapping and desorption mechanism for neutron-irradiated tungsten has a difference from that for ion-irradiated one.

ACKNOWLEDGMENTS

This study was supported by JSPS Kakenhi No. 22360389 and 19055002 from MEXT, Japan, and Japan-US collaboration program (TITAN). The TEM observation was performed under the collaboration program at the Institute of Applied Mechanics, Kyushu University.

REFERENCES

[1] J. ROTH, E. TSITRONE, A. LOARTE et al., "Recent analysis of key plasma wall interactions issues for ITER", *J. Nucl. Mater.,* 390-391, 1 (2009).

[2] T. LOARER, "Fuel retention in tokamaks", *J. Nucl. Mater.*, 390-391 20 (2009).

[3] Y. UEDA, N. OHNO, S. KAJITA et al., "Development of tungsten materials for plasma facing components in Japan", *Fusion Sci. Technol.*, 52, 513 (2007).

[4] V. PHILIPPS, "Tungsten as material for plasma-facing components in fusion devices", *J. Nucl. Mater.*, 415, S2 (2011).

[5] G. M. WRIGHT, M. MAYER, K. ERTL et al., "Hydrogenic retention in irradiated tungsten exposed to high-flux plasma", *Nucl. Fusion* 50, 075006 (2010).

[6] G. M. WRIGHT, M. MAYER, K. ERTL et al., "TMAP7 simulations of deuterium trapping in pre-irradiated tungsten exposed to high-flux plasma", *J. Nucl. Mater.*, 415, S636 (2011).

[7] B. TYBURSKA, V.KH. ALIMOV, O.V. OGORODNIKOVA, et al., "Deuterium retention in self-damaged tungsten", *J. Nucl. Mater.*, 395, 150 (2009).

[8] O.V. OGORODNIKOVA, B. TYBURSKA, V. KH. ALIMOV, et al., "The influence of radiation damage on the plasma-induced deuterium retention in self-implanted tungsten", *J. Nucl. Mater.*, 415, S661 (2011).

[9] W. R. WAMPLER AND R. P. DOERNER, "Deuterium retention in tungsten from exposure to plasma" *Phys Scr.* T138 014037 (2009).

[10] M. SHIMADA, Y. HATANO, P. CALDERONI, et al., " First result of deuterium retention in neutron-irradiated tungsten exposed to high flux plasma in TPE", *J. Nucl. Mater.*, 415, S667 (2011).

[11] T. ODA, M. SHIMADA, K. ZHANG, et al., "Development of monte carlo simulation code to model behavior of hydrogen isotopes loaded into tungsten containing vacancies", *Fusion Sci. Tech.*, 60, 1455 (2011).

[12] P. CALDERONI, J. SHARPE, M. SHIMADA, et al., "An overview of research activities on materials for nuclear applications at the INL Safety Tritium and Applied Research facility", *J. Nucl. Mater.*, 417, 1336 (2011).

[13] J. P. SHARPE, R.D. KOLASINSKI, M. SHIMADA et al., "Retention behavior in tungsten and molybdenum exposed to high fluences of deuterium ions in TPE", *J. Nucl. Mater.*, 390-391 709 (2009).

Task 2-1(4) INFLUENCE OF DISPLACEMENT PROCESSES ON THE FORMATION OF IRRADIATION DEFECTS AND DEUTERIUM RETENTION IN TUNGSTEN

Makoto Kobayashi[1], Masashi Shimada[2], Yuji Hatano[3], Takuji Oda[4],
Brad Merrill[2], Yasuhisa Oya[1] and Kenji Okuno[1]

[1]*Radioscience Research Laboratory, Faculty of Science, Shizuoka University, Shizuoka, Japan*
f5144008@ipc.shizuoka.ac.jp, syoya@ipc.shizuoka.ac.jp, srkokun@ipc.shizuoka.ac.jp
[2]*Fusion Safety Program, Idaho National Laboratory, Idaho Falls, ID, U.S.A.*
Masashi.Shimada@inl.gov, Brad.Merrill@inl.gov
[3]*Hydrogen Isotope Research Center, University of Toyama, Toyama, Japan*
hatano@ctg.u-toyama.ac.jp
[4]*Department of Nuclear Engineering and Management, The University of Tokyo, Tokyo, Japan*
oda@snu.ac.kr

The deuterium trapping behaviors in tungsten was examined by means of TDS in this study. Tungsten samples were damaged by light ions with lower energy (10 keV C^+ and 3 keV He^+) or a heavy ion with higher energy (2.8 MeV Fe^{2+}) prior to deuterium injection to understand the effects of cascade collisions on deuterium retention in tungsten. By light ion irradiation, most of deuterium was trapped by vacancies, whose retention was almost saturated at around 0.2 dpa. For the heavy ion irradiation, the deuterium trapping by voids was found, indicating that cascade collisions by the heavy ion irradiation would create the voids in tungsten. Most of deuterium trapped by the voids was desorbed in higher temperature region compared to that trapped by vacancies. It was also found that deuterium could accumulate in the voids, resulting in the formation of blisters in tungsten.

I. INTRODUCTION

Tungsten (W) is a candidate for plasma facing material of fusion reactors due to relatively low solubility for hydrogen isotopes. However, it has been reported that irradiation damage in tungsten will be trapping sites for hydrogen isotope and therefore, enhance the hydrogen isotope retention [1,2]. The hydrogen trappings by irradiation damages have been simulated by higher energy ion irradiation technique to introduce the defects, such as dislocation loops, vacancies and voids and so on. In TDS (Thermal Desorption Spectroscopy) spectra, the characteristic hydrogen desorption peak was observed in the temperature above 800 K for tungsten damaged by higher energy ion irradiation [2].

The irradiation damage would be introduced by a displacement of lattice atom of tungsten by energetic particles. As the energy transfer from incident particle to lattice atom increases, the displaced lattice atom (primary knock-on atom, PKA) can induce displacements of other lattice atoms (cascade collision), resulting in the larger size defects like voids and vacancy clusters. These differences in displacement processes would induce the different concentration of these defects, resulting in the differences of hydrogen retention behaviors in tungsten since the concentration of hydrogen trapped by each type of defects are different as reported by Roth and Schmid [3]. The influences of neutron irradiation on hydrogen retention behaviors were also investigated in the framework of US-Japan joint research project TITAN (Tritium, Irradiation, and Thermofluids for America and Nippon). The TDS experiments for tungsten damaged by neutron showed deuterium desorption peak in the temperature region around 800 K, similar to that observed for tungsten damaged with higher energy ion irradiation [4]. In TITAN project, Shimada has examined deuterium retention in tungsten damaged up to about 0.3 -3 dpa (displacement per atom) by different types of impact ions, such as 2.8 MeV Fe^{2+}, 20 MeV W^{2+} and 0.7 MeV H^- [2]. The deuterium TDS spectra for these specimens showed different deuterium desorption behaviors even in the comparable damage level. For example, the deuterium desorption in higher temperature region around 800 K was observed for tungsten damaged by 20 MeV W^{2+} irradiation but not appeared in the case of 2.8 MeV Fe^{2+}. The difference was also found in deuterium retentions in each desorption peak. In tungsten damaged by 2.8 MeV Fe^{2+} or 0.7 MeV H^-, deuterium TDS spectra were concentrated in lower temperature region below 700 K. The deuterium retentions in higher temperature region and lower temperature region were almost equivalent in the case of 20 MeV W^{2+} irradiation. These facts indicate that the concentration and type of trapping sites for deuterium are changed by the energy and/or species of impact ions, showing that the deuterium retention behaviors cannot be estimated only by the parameter of dpa level.

As the energy transfer rate is controlled by mass of impact ion as well as its energy, we have categorized the impact ions into two groups in the present study to clarify

the effect of impact ions on formation of irradiation damage and consequent hydrogen retention behaviors in tungsten. The first is named as light ion with lower energy, namely 10 keV C^+ and 3 keV He^+ in this work. The second group is heavy ion with higher energy which is 2.8 MeV Fe^{2+}. Deuterium was injected into tungsten after these ion irradiations mentioned above. The deuterium retention and desorption behaviors were evaluated by means of TDS measurement. The surface morphology was also observed by Scanning Electron Microscope (SEM) for tungsten after TDS measurements.

II. EXPERIMENTAL

The tungsten samples (6 mm^{ϕ} x 0.2 mm^{t}) were prepared by cutting polycrystalline tungsten rod (99.99 at. % purity, from A.L.M.T. Corp.) annealed under stress relieved condition. The samples were mechanically polished with abrasive papers and diamond powders (9 and 3μm). Then, these samples were annealed at 1173 K for 0.5 hour in ultra-high vacuum (~10^{-6} Pa) to remove the impurity and stress introduced by polishing processes.

The 10 keV C^+ and 3 keV He^+ were implanted into tungsten at room temperature by triple ion implantation system at Shizuoka University [5]. The flux of each ion was set to be 1.0 x 10^{17} m^{-2} s^{-1}. Several samples with different ion fluences were prepared to introduce various dpa levels in tungsten. The C^+ fluence was ranged in 1.0 × 10^{19} – 1.0 × 10^{21} C^+ m^{-2}. The corresponding dpa levels are ranged in 0.78 to 78 dpa. The He^+ fluence was changed in similar range, and dpa levels were around 0.03 to 3 dpa. The damage by 10 keV C^+ and 3 keV He^+ was distributed up to about 25 nm from surface. The dpa levels and distributions of damaged regions were estimated by SRIM (Stopping Range of Ions in Matter) code calculation assuming the displacement energy of tungsten atom as 90 eV [6].

The 2.8 MeV Fe^{2+} were irradiated into tungsten at room temperature by the Tandetron Accelerator, RAPID (Rutherford backscattering spectroscopic Analyzer with Particle induced X-ray Emission and Ion implantation Devices), at the University of Tokyo. The ion fluence was 3.3 × 10^{19} Fe^{2+} m^{-2}, corresponding to 3.0 dpa. The damage was distributed up to ~ 1000 nm beneath the surface.

Thereafter, the deuterium ion (D_3^+) implantation and deuterium plasma exposure were carried out in TRIIX (Tritium Ion Implantation Experiment) and TPE (Tritium Plasma Experiment) systems at Idaho National Laboratory (INL), US. The energy of D_3^+ was set to be 900 eV to prevent damage creation in tungsten during the deuterium ion implantation. The D^+ flux and fluence were set to be 1.6 × 10^{19} D^+ m^{-2} s^{-1} and 3.2 × 10^{23} D^+ m^{-2}, respectively. The implantation temperature was controlled at 473 K. The D_3^+ implantation for the non-damaged tungsten was also carried out at 473 K and room temperature. D^+ flux and D^+ fluence for deuterium plasma exposure were 6 × 10^{21} D^+ m^{-2} s^{-1} and 5.5 × 10^{25} D^+ m^{-2}, respectively. The energy of D^+ and the sample temperature were set as 100 eV and 473 K in this plasma exposure experiment, respectively. Details of deuterium plasma exposure can be found in Ref. [3]. Thermal desorption experiments were carried out at INL after the D_3^+ implantation. The samples were heated in ultra-high vacuum and by infrared furnace up to the temperature of 1173 K with the heating rate of 10 K min^{-1}. Heating at the maximum temperature of 1173 K was continued for 30 min and then sample temperature was decreased at the rate of 20 K min^{-1}. The mass species of 3 and 4, which corresponded to HD and D_2, respectively, were measured in TDS experiments for the estimation of deuterium retention. SEM observations were also conducted for these tungsten samples after TDS experiments.

III. RESULTS and DISCUSSION

Fig. 1(a) shows deuterium TDS spectra for non-damaged tungsten samples implanted with D_3^+ at room temperature and 473 K. The desorption temperature of deuterium for the sample implanted at room temperature was ranged in 300 - 700 K, which could be divided into three peaks located at 440 K, 530 K, 630 K, namely Peaks 1, 2 and 3, respectively. It was found that most of deuterium was desorbed as Peaks 1 and 2 under the D_3^+ implantation at room temperature. The deuterium TDS spectrum for tungsten implanted with D_3^+ at 473 K consists of almost single desorption stage as Peak 3. Because the desorption

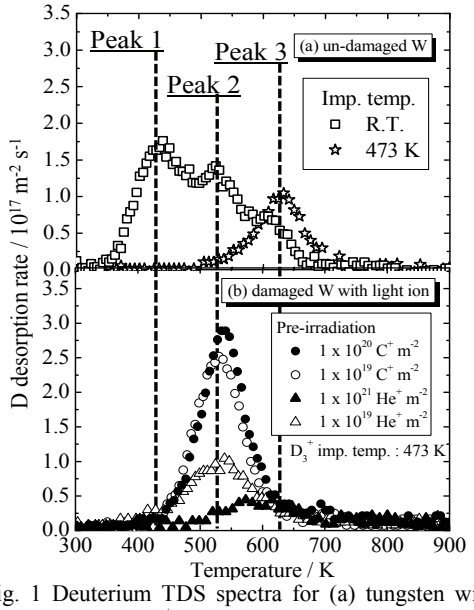

Fig. 1 Deuterium TDS spectra for (a) tungsten with different D_3^+ implantation temperatures and (b) tungsten damaged with light ion irradiation prior to D_3^+ implantation at 473 K

temperatures for Peaks 1 and 2 are located close to or lower than the implantation temperature of 473 K, almost all deuterium trapped as Peaks 1 and 2 would be desorbed during D_3^+ implantation. The deuterium TDS spectra for tungsten damaged by lower energy light ion subsequently irradiated with D_3^+ at 473 K showed clear differences compared to those for the non-damaged sample as found in Fig. 1(b). The enhancement of deuterium retention as Peak 2 suggests that the irradiation damages induced by light ion irradiation would act as deuterium trapping sites. The SRIM calculations indicate that 10 keV C^+ and 3 keV He^+ can introduce 6 vacancies and 1 vacancy in tungsten for each impact ion, respectively, expecting that point defects would be mainly formed. Actually, the formation of vacancies and dislocation loops via aggregation of interstitial atoms in tungsten were found in our previous micro-structure observation [5]. In general, vacancies can trap hydrogen strongly compared to that by dislocation loops due to the stabilization of hydrogen in vacancy [7]. These facts suggest that deuterium trapping site as Peak 2 should be vacancies created by light ion impact, and that as Peak 1 would be weaker trapping site such as dislocations, surface and self-interstitial sites of tungsten. The other difference was observed in tungsten damaged by He. The deuterium retention as Peak 2 increased in lower He^+ fluence such as 1.0×10^{19} He^+ m^{-2}, which subsequently decreased with higher He^+ fluence at 1.0×10^{21} He^+ m^{-2}. The deuterium retention as Peak 3 clearly decreased by light ion irradiation, indicating that irradiation damages introduced by light ion irradiation would disturb deuterium trapping as Peak 3, which should not relate to so-called 'ion induced defects' [2]. The intrinsic defects in bulk region such as intrinsic cavity, grain boundary and oxygen impurity would be candidates as the trapping site for deuterium as Peak 3 [8].

The deuterium retentions as Peak 2 in tungsten damaged by light ions as a function of dpa value were summarized in Fig. 2. In lower dpa region less than 0.2 dpa, the enhancement of deuterium retention was observed. In both ion irradiations, the deuterium retention as Peak 2 was saturated at the same deuterium retention of 2×10^{20} D m^{-2} at the defect density above 0.2 dpa, which is consistent with the other report [2]. As mentioned above, the deuterium retention in tungsten damaged by He^+ irradiation decreased in higher He^+ fluence. These deuterium retention behaviors were quite different in the case of C^+ irradiation. The reduction of deuterium retention in tungsten with higher He^+ fluence can be explained by the formation of He bubbles, which is easily formed in tungsten with higher He^+ fluence[9]. In this formation process, vacancies would be filled with He atoms for bubble nucleation, preventing deuterium trapping in vacancies consequently. The He bubbles would also act as the diffusion barrier of deuterium into bulk as well as the by-pass for deuterium molecule to surface [9]. Iwakiri et al., have observed microstructure of tungsten by Transmission Electron Microscope (TEM) with increasing He^+ fluence [10]. The formation of He bubble was observed at the He^+ fluence above 6×10^{19} He^+ m^{-2}. In the present study, the decrease of deuterium retention was observed in the He^+ fluence above 5×10^{19} He^+ m^{-2}, corresponding to 1.6 dpa as shown in Fig. 2. This comparison would support our hypothesis that He bubbles prevent deuterium trapping in vacancies.

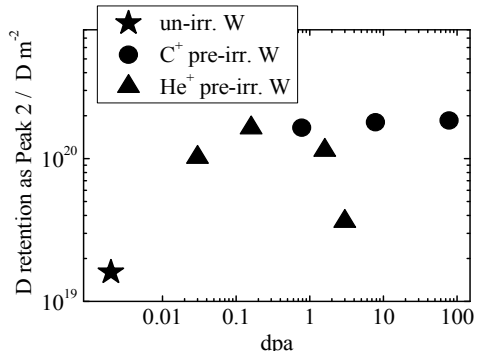

Fig. 2 Deuterium retention as Peak 2 for tungsten damaged with light ion irradiation

Fig. 3 depicts the deuterium TDS spectrum for tungsten damaged by heavy ion irradiation and subsequently implanted with D_3^+. Two peaks were appeared at around 460 K and 700 K with larger FWHM compared to the case of tungsten irradiated with light ions. The deuterium retention was three times as large as that for tungsten damaged by 10 keV C^+ irradiation at the same dpa level. These results, which are the broader deuterium desorption peaks and the deuterium retention enhancement, would be caused by the extension of damage zone toward the depth by 2.8 MeV Fe^{2+} compared to that by light ions. The predominant deuterium desorption above 700 K was attributed to the desorption of deuterium molecules chemi-sorbed on the inner surface of voids [4]. In tungsten, the maximum energy of primary knock-on tungsten atom (PKA-W) by 2.8 MeV Fe^{2+} was estimated to be about 200 eV by SRIM, although those by 10 keV

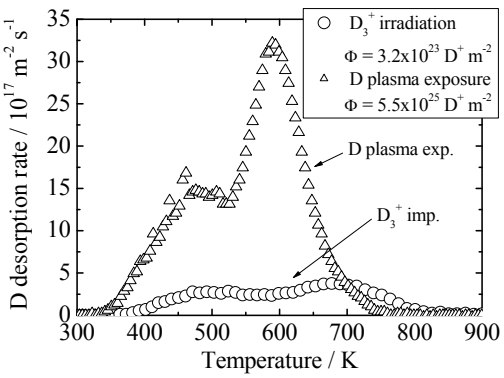

Fig. 3 Deuterium TDS spectra for tungsten irradiated with D_3^+ or exposed to deuterium plasma (Φ indicates D^+ fluence, both of the temperatures for D_3^+ implantation and deuterium plasma exposure were 473 K)

C^+ and 3 keV He^+ were around 20 eV and 1 eV, respectively, showing that the PKA-W energy by heavy ion irradiation was much higher than those by light ion irradiation, and also higher than displacement energy of tungsten atom of 90 eV. It was considered that voids were also formed in tungsten in addition to dislocation loops and vacancies by heavy ion irradiation through the cascade collisions by PKA-W. As the trap energy for deuterium in voids would be higher than that in vacancies, deuterium was easily trapped by voids than vacancies [4]. However, it is still unclear that desorption of deuterium trapped by voids was not obviously appeared in tungsten damaged by 2.8 MeV Fe^{2+} and subsequently exposed to deuterium plasma, reported previously as displayed in Fig. 3. The energy of D^+ and the sample temperature were set as 100 eV and 473 K in this plasma exposure experiment, respectively. TDS spectrum showed larger deuterium retention, compared to that with D_3^+ irradiation, with the predominant deuterium desorption peak at 600 K. These differences would result from higher D^+ flux and/or fluence in plasma exposure condition. The SEM images were taken after TDS experiments for Fe^{2+} pre-irradiated tungsten samples with different dpa levels as shown in Fig. 4. The SEM images for Fe^{2+} pre-irradiated tungsten, which was subsequently implanted with D_3^+, showed little change on surface morphology compared to non-irradiated sample. Almost the same results were obtained for light ion pre-irradiated tungsten samples implanted with D_3^+ (not shown in this paper). These facts indicate that the surface morphology of tungsten is hardly changed by D_3^+ implantation in the present experimental condition. On the other hand, the blister formation was clearly observed on damaged tungsten exposed to deuterium plasma. The cracks were also introduced on the surface of blister in Fig. 4 (d), indicating that deuterium was desorbed by blister-bursting during TDS experiment. In addition, the size of blisters was increased with increasing dpa value by the comparison of Figs. 4(c) and (d). It was considered that higher deuterium flux was one of key parameters for blister formation. Under higher flux deuterium irradiation circumstance, the concentration (chemical potential) of deuterium in tungsten increases. A part of deuterium would accumulate into cavity and/or void. Hence, blisters are formed by exposure to high flux plasma. In these processes, voids would act as accumulation site for deuterium. The larger voids would result in the larger blisters. Consequently, desorption of deuterium chemi-sorbed on the inner surface of void would be disappeared in TDS spectra for the samples exposed to deuterium plasma. Instead, the deuterium desorptions at 460 K and 600 K named as Peaks A and B was increased. Peak A was located in lower temperature than the temperature of deuterium plasma exposure. The deuterium desorption behavior as Peak A showed sharp desorption peaks around 450 K. These sharp desorption peaks were derived from blister-bursting as reported by

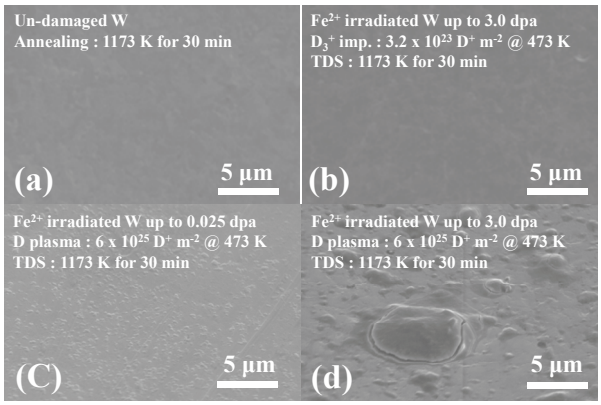

Fig. 4 SEM images for tungsten (a) after polishing, (b) damaged by 2.8 MeV Fe^{2+} at 3 dpa and subsequently irradiated with D_3^+ at 473 K, (c) damaged by 2.8 MeV Fe^{2+} at 0.025 dpa and subsequently exposed to deuterium plasma at 473 K, (d) damaged by 2.8 MeV Fe^{2+} at 3 dpa and subsequently exposed to deuterium plasma at 473 K. All samples were heated at 1173 K for 30 min before SEM observations.

Shu [11]. Peak B was attributed to deuterium trapped in vacancy from the comparison of Peak 2 in Fig. 1 (b). The temperature for Peak B was clearly higher than that for Peak 2 due to the deeper deuterium distribution in the case of 2.8 MeV Fe^{2+} irradiation, indicating that the Peak B is including the contribution of deuterium diffusion process to the surface. Vacancy has the highest trap energy for deuterium in this tungsten sample because void has been changed to blisters. Therefore, large portion of deuterium was trapped in vacancies for tungsten exposed to deuterium plasma because voids have been changed to blisters.

It was found that the voids were hardly formed by lower energy light ion irradiation even in higher dpa level around 80 dpa, where the concentration of vacancies were already saturated, although voids were existed in tungsten damaged by high energy heavy ion at 3 dpa. These facts indicate that the formation of irradiation damage clearly depends on cascade collision processes. This result suggests that self-ion (tungsten ion) irradiations have the highest formation rate for void in tungsten due to the highest energy transfer rate, leading to the high deuterium retention ratio in higher temperature stage above 700 K as found in Ref [2]. However, the energy transfer from neutral particle (neutrons) should be different that from charged particles (ions). The evaluation of the actual energy transfer rate from neutrons to tungsten atoms and the subsequent cascade collisions are necessary. In addition, the interaction of hydrogen with defects such as the trap concentration and the trapping preference are individual for each type of defect as found in this study. These basic parameters should be precisely revealed to estimate the hydrogen retention behavior in actual first wall.

IV. CONCLUSIONS

In the present work, deuterium trapping behaviors in tungsten damaged by light ions with lower energy (10 keV C^+ and 3 keV He^+) or a heavy ion with higher energy (2.8 MeV Fe^{2+}) were compared by means of TDS to understand effects of cascade collisions on deuterium retention in tungsten. For the light ion irradiation, the dislocation loops and the vacancies were formed in tungsten. Most of deuterium was mainly trapped by vacancy and deuterium retention was almost saturated at the damage level of 0.2 dpa. For the heavy ion irradiation, the deuterium trapping by the void was found, indicating that cascade collision induced by the heavy ion irradiation created the void in tungsten. Deuterium trapped by the void was desorbed in higher temperature region than that trapped in the vacancy. It was also found that deuterium can accumulate in the void, resulting in the blisters in tungsten.

ACKNOWLEDGMENTS

Authors are grateful for the financial support from the Japan–US collaboration research program, TITAN, JSPS Kakenhi No. 22360389 from MEXT, Japan, and the Center for Instrumental Analysis at Shizuoka University.

REFERENCES

[1] OGORODNIKOVA, B. TYBURSKA, V.Kh. ALIMOV *et al.,* "The influence of radiation damage on the plasma-induced deuterium retention in self-implanted tungsten", *J. Nucl. Mater*. **415,** S661 (2011)

[2] M. H. HOEN, B. TYBURSKA, K. ERTL, *et al.,* "Saturation of deuterium retention in self-damaged tungsten exposed to high-flux plasmas", *Nucl. Fusion* **52** 023008 (2012)

[3] J. ROTH and K. SCHMID, "Hydrogen in tungsten as plasma-facing material" *Phys. Scr.* **T145,** 014031 (2011).

[4] M. SHIMADA, Y. HATANO, Y. OYA *et al*., "Overview of the US–Japan collaborative investigation on hydrogen isotope retention in neutron-irradiated and ion-damaged tungsten", *Fusion Eng. Des*., **87** (2012) 1166-1170.

[5] Y. OYA, S. SUZUKI, W.WANG *et al*., "Correlation between deuterium retention and microstructure change for tungsten under triple ion implantation", *Phys. Scr*. **T138,** 014051 (2009)

[6] J.F.ZIEGLER "SRIM code" (2006)

[7] M. POON, A.A. HAASZ, J.W.DAVIS, "Modelling deuterium release during thermal desorption of D^+-irradiated tungsten", *J. Nucl. Mater*. **374,** 390 (2008).

[8] T. AHLGREN, K. HEINOLA, K. VORTLER *et al*., "Simulation of irradiation induced deuterium trapping in tungsten", *J. Nucl. Mater*. **427,** 152 (2012).

[9] Y. UEDA, M. FKUMOTO, J. YOSHIDA *et al*., "Simultaneous irradiation effects of hydrogen and helium ions on tungsten", *J. Nucl. Mater*. **386,** 725 (2009).

[10] H. IWAKIRI, K. YASUNAGA, K. MORISHITA, *et al.,* "Microstructure evolution in tungsten during low-energy helium ion irradiation", *J. Nucl. Mater*. **283,** 1134 (2000)

[11] W. SHU, E. WAKAI, T. YAMANISHI *et al*., "Blister bursting and deuterium bursting release from tungsten exposed to high fluences of high flux and low energy deuterium plasma", *Nucl. Fusion* **47**, 201 (2007)

Task 2-1(5) DOSE DEPENDENCE OF DEUTRIUM RETENTION IN NEUTRON-IRRADIATED TUNGSTEN

T. Otsuka[1], M. Shimada[2], Y. Hatano[3], Y. Oya[4], M. Hara[3], M. Kobayashi[4], G. Cao[5], K. Okuno[4], T. Tanaka[6], M. A. Sokolov[7], Y. Katoh[7]

[1]*Interdisciplinary Graduate School of Engineering Sciences, Kyushu University, Kasuga 816-8580, Japan, t-otsuka@nucl.kyushu-u.ac.jp*
[2]*Fusion Safety Program, Idaho National Laboratory, Idaho Falls, ID, USA, Masashi.Shimada@inl.gov*
[3]*Hydrogen Isotope Research Center, University of Toyama, Toyama 930-8555, Japan, hatano@ctg.u-toyama.ac.jp, masahara@ctg.u-toyama.ac.jp*
[4]*Faculty of Science, Shizuoka University, Shizuoka 422-8529, Japan, syoya@ipc.shizuoka.ac.jp*
[5]*Department of Engineering Physics, The University of Wisconsin, Madison, WI, USA, gcao@wisc.edu*
[6]*National Institute of Fusion Science, Toki, Japan, teru@nifs.ac.jp*
[7]*Oak Ridge National Laboratory, Oak Ridge, TN, USA, sokolovm@ornl.gov, katohy@ornl.gov*

The dose dependence of deuterium (D) retention in neutron-irradiated tungsten (W) was investigated. Specimens of pure W were irradiated with neutrons to 0.025 and 0.3 dpa at around 323 K and then exposed to high flux D plasma at 473 and 773 K. The concentration of D in W significantly increased by neutron irradiation and reached 0.8 at.% at 473 K and 0.3 at.% at 773 K after irradiation to 0.3 dpa. On the other hand, those at 0.025 dpa were 0.3–0.4 at.% at 473 K and 0.2 at.% at 773 K. In other words, the concentration of D increased with increase in damage level due to trapping effects of radiation-induced defects. However, the concentrations of D at 0.3 dpa were only higher by a factor of 2 than those at 0.025 dpa, whereas the damage level increased by an order of magnitude. These observations indicated that the trap density observed after irradiation to 0.3 dpa is close to the saturation level. The exposure of neutron-irradiated specimen to plasma at 773 K resulted in deep penetration of D into the bulk (50–100 μm) and consequently large D retention. Thermal desorption spectrum of D showed that release of D from neutron-irradiated specimen was controlled by long-range diffusion process under strong trapping effects.

I. INTRODUCTION

Tritium inventory in plasma-facing materials (PFMs) is an important issue to assess the safety margins of fusion reactors. Tungsten (W) is believed to be most promising candidate PFM with respect to very low hydrogen solubility as well as a low erosion yield though a potential increase in tritium retention by neutron irradiations will be great concern. Although many studies have been devoted to understand retention behavior of hydrogen isotopes in W after ion irradiations as reviewed in [1], effects of neutron irradiation on the retention behavior of hydrogen isotopes had been scarcely examined before the Japan-US joint research project TITAN. From these viewpoints, the Task 2–1 of the TITAN project aimed to understand neutron irradiation effects on retention behavior of hydrogen isotopes in W.

As described in 4-4(3), in the first half of TITAN project, the authors irradiated W to 0.025 dpa (displacement per atom) with neutrons in a fission reactor at the coolant temperature of the reactor (around 323 K). Depth profiles of deuterium (D) were measured by nuclear reaction analysis (NRA) after exposure to high-flux D plasma at 373, 473 and 773 K [2]. Thermal desorption spectra of D from the specimen exposed to the plasma at 473 K were also examined [3-5]. A significant increase in D retention with neutron irradiation was observed even at a damage level as low as 0.025 dpa, and the D concentration in neutron-irradiated W reached values of 0.1–0.2 at.% at all temperatures examined [2]. The desorption of D from neutron-irradiated specimens exposed to the plasma at 473 K continued up to temperatures above 1173 K, while that from non-irradiated specimen was completed at ≈700 K [3,4]. These observations suggested strong trapping effects against hydrogen isotopes by defects induced by neutron irradiation. However, thermal desorption spectrum after exposure to plasma at 773 K was not measured in the first half of the project. The retention of hydrogen isotopes at a higher damage level was not examined, either.

In this subsection, the results for W specimens irradiated with neutrons to 0.3 dpa prepared in the latter half of the project [6-8] are reported. The neutron-irradiated W specimens were loaded with D from D plasma at 473 K and 773 K. The concentrations of D in the near surface regions were examined by NRA [6]. The result of thermal desorption measurements after plasma exposure at 773 K [6-8] is also reported. In addition, the results of radioactivity measurements for neutron-irradiated W by γ-spectrometry [6] are also described,

because this type of information would be helpful for detailed planning of specimen handling in future programs on plasma-surface interaction studies with neutron-irradiated specimens (for example, Ref. [9]).

II. EXPERIMENTAL

II.A. Neutron Irradiation

Specimens used were disks (ϕ6 × 0.2 mm) of pure W (99.99 mass%) supplied by A. L. M. T. Co., Japan. All the specimens were mirror-finished and annealed in vacuum (10^{-6} Pa) at 1173 K for 30 min to relieve the stress induced by mechanical polishing and remove impurity hydrogen (H) in W.

The specimens were sealed in molybdenum (Mo) envelopes and irradiated with neutrons in the High Flux Isotope Reactor (HFIR) at Oak Ridge National Laboratory (ORNL) for 391 h at the coolant temperatures of the reactor (around 323 K). The damage level reached 0.3 dpa. The specimens examined in the first half of the project were irradiated for 33 h corresponding to 0.025 dpa, as described in [2-4]. Radioactivity induced in the specimens was evaluated using the FISPACT-2001 computer code. The specimens irradiated to 0.025 and 0.3 dpa were shipped to Idaho National Laboratory (INL) after storage in a water pool and hot cell for around 300 and 800 days, respectively. The radioactivity in the specimens was examined by γ-ray spectroscopy.

After the neutron irradiation, the surfaces of the specimens were covered by thin oxide layers formed during the neutron irradiation and/or the storage in the water pool. They were gently removed with a lapping film (3M, aluminium oxide, 0.3 μm) before D loading at INL.

II.B. Deuterium Loading and Measurements

D was loaded to the specimens from high-flux D plasma in a linear plasma machine (Tritium Plasma Experiment, TPE) located at INL. The details of TPE have been described elsewhere [10]. The primary species in the plasma was D^+, and the ion energy and flux were 100 eV and (5–7) × 10^{21} D^+ m^{-2} s^{-1}, respectively. The D loading was conducted up to a fluence of (5–7) × 10^{25} D m^{-2} at 473 ± 10 and 773 ± 10 K in the present study. The specimen temperature was monitored using the thermocouple attached on the back of the sample. After the D loading, the depth profiles of loaded D were measured by NRA with 3.5 MeV ^{3}He ions at the University of Wisconsin. The total retention was measured by means of thermal desorption spectroscopy at temperature ramp rate of 10 K min^{-1}. Details of both analyses are described elsewhere [2,3].

III. RESULTS AND DISCUSSION

III.A. Radioactivity in Neutron-Irradiated Specimens [6]

Measurements of γ-ray spectra performed for the neutron-irradiated specimens showed the presence of ^{188}W and ^{188}Re. The latter is the daughter of the former, and the half-life of the latter (17 h) is far shorter than that of the former (69.4 days). Hence, the radioactivity of these two nuclides was almost equal (secular equilibrium). The values of radioactivity of ^{188}W and ^{188}Re in the specimens irradiated to 0.025 and 0.3 dpa were 50 and 4 MBq g^{-1} at 353 and 926 days after completion of irradiation, respectively. The lower radioactivity for the higher neutron dose was due to the longer period of time between completion of irradiation and measurement. Fig. 1 shows the radioactivity of major radionuclides evaluated with the FISPACT-2001 code as a function of elapsed time after completion of irradiation. In this evaluation, the duration of neutron irradiation was set to 30 days (720 h). The half-filled circles in this figure indicate the values of radioactivity of ^{188}W and ^{188}Re calculated from the measured values for the specimens irradiated to 0.025 and 0.3 dpa by assuming that the radioactivity immediately after the completion of irradiation is proportional to the

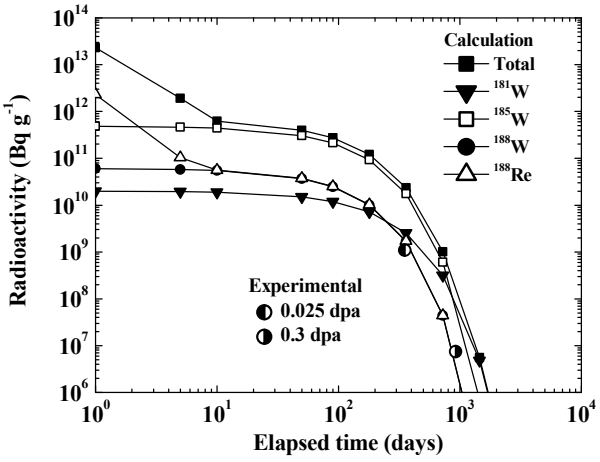

Fig. 1 Radioactivity in W irradiated with neutrons in HFIR for 30 full power days evaluated using the FISPACT-2001 code. Half-filled circles indicate the radioactivity of ^{188}W and ^{188}Re calculated from the measured values for W specimens irradiated to 0.025 and 0.3 dpa by assuming that the radioactivity immediately after completion of neutron irradiation is proportional to the duration of irradiation.

irradiation duration. The values evaluated with the FISPACT-2001 code and those calculated from the measured values agreed with each other within a factor of 2. Both ^{188}W and ^{188}Re emit high-energy β-rays, while the probabilities of γ-ray emission are relatively low. The maximum energies of β-rays from ^{188}W and ^{188}Re are 0.349 and 2.12 MeV, respectively [11]. Hence, β-rays from ^{188}Re were the most important radiation from the viewpoint of safe handling of the neutron-irradiated W specimens.

Although the FISPACT-2001 code predicted the presence of ^{181}W and ^{185}W, these nuclides were not detected by γ-ray spectroscopy. The absence of a γ-ray peak from ^{185}W can be explained by low probability of γ-ray emission of ^{185}W (0.019%). No detection of ^{181}W was attributed to the fact that the cut-off energy in the measurement (50 keV) was comparable to the energy of the most intense X-rays from ^{181}W (57.5 keV) [11].

III.B. Depth Profiles and Thermal Desorption of D in Neutron-Irradiated Specimens [6-8]

Fig. 2 (a) and (b) shows the depth profiles of D in the neutron-irradiated specimens measured by NRA after exposure to plasma at 473 and 773 K, respectively, together with those in the non-irradiated specimens for comparisons. In the case of the specimen loaded with D at 473 K, D penetrated to a depth of around 3 μm, and the D concentration in the penetration zone increased with increase in the neutron dose. D concentration in the penetration zone reached 0.8 at.% at 0.3 dpa, 0.3–0.4 at.% at 0.025 dpa, and 0.1 at.% in the non-irradiated specimen. In the case of the specimen loaded with D at 773 K, D penetrated beyond the detection range of NRA (~5 μm). D concentrations in the penetration zone reached 0.4 at.% at 0.3 dpa and 0.2 at.% at 0.025 dpa. Although the D concentrations increased clearly with increase in the neutron dose, the former was not in proportion to the latter. The concentrations of D after neutron-irradiation to 0.3 dpa were only higher by a factor of 2 than those at 0.025 dpa at both 473 and 773 K, while the damage level increased by an order of magnitude. According to Roth and Schmid [1] who summarized the correlation between damage level and trap density in W irradiated with high-energy ions at room temperature, the density of traps sharply rises at dpa values <0.1 and ceases to increase at around 0.7 dpa and a D concentration of 1.0–1.4 at.%. It is plausible that saturation with traps also takes place with neutron irradiation, and the trap density after irradiation to 0.3 dpa was close to the saturation level. However, measurements of D concentration after neutron irradiation to higher damage levels are necessary to draw a final conclusion.

Fig. 3 shows TDS spectra of D for the neutron-irradiated specimens (0.025 dpa) loaded with D at 473 K

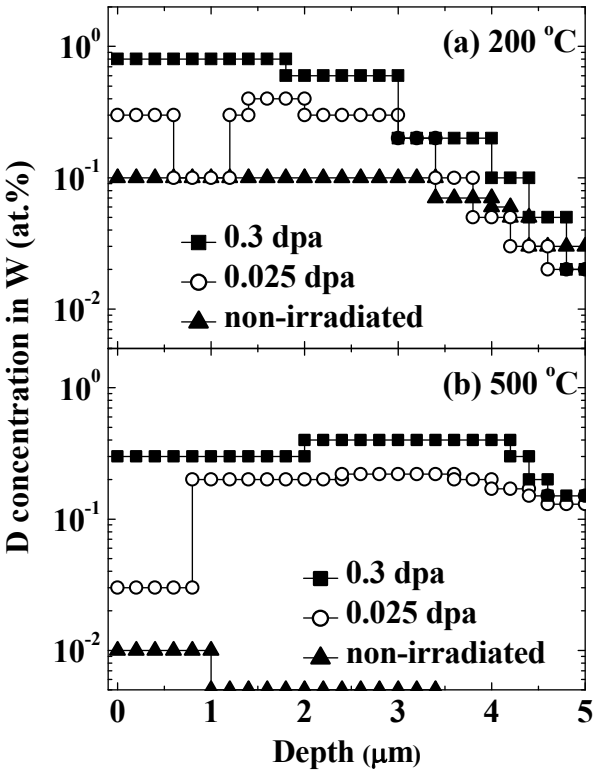

Fig. 2 Depth profiles of D in non-irradiated and neutron-irradiated W specimens (0.025 and 0.3 dpa) after D loading at 473 K (a) and 773 K (b).

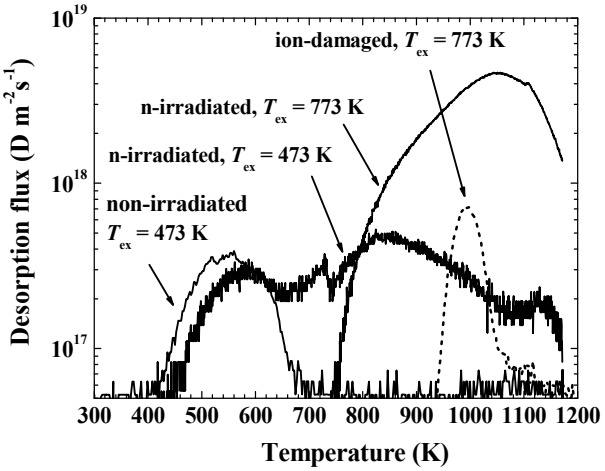

Fig. 3 Thermal desorption spectra of D from non-irradiated, neutron-irradiated (0.025 dpa) and ion-damaged W (0.5 dpa); T_{ex} indicates temperature of exposure to D plasma and D_2 gas.

and 773 K together with those for the non-irradiated specimens. The spectrum for the specimen irradiated with 20 MeV W ions at room temperature to 0.5 dpa and exposed to D_2 gas at 673 K and 0.1 MPa is also shown for comparison [6]. D release from the neutron-irradiated specimens continued to high temperatures above 1173 K, as described above. The broad desorption peak for the specimen loaded with D at 473 K indicates the presence of various types of traps with different activation energies for detapping E_{det} [2,3,11]. As for the specimen loaded with at 773 K, traps with large trapping energy contribute to D retention. The value of E_{det} for such strong traps was evaluated to be ≈1.8 eV by simulation using the TMAP4 program in previous studies [7,8]. The retention of D in the neutron-irradiated specimen loaded at 773 K was 6.4×10^{21} D m^{-2}, while that after D loading at 473 K was 2.4×10^{21} D m^{-2}. In other words, the retention after plasma exposure at 773 K was significantly greater than that at 473 K despite lower D concentration in Fig. 2. The larger D retention at 773 K can be explained by the deeper penetration of D. Assuming uniform D concentration throughout the penetration depth, the penetration depth of D was calculated to be 50–100 μm as the quotient of the amount of retained D (6.4×10^{21} D m^{-2}) and D concentration (0.1–0.2 at.% = $6.3–12.6 \times 10^{25}$ D m^{-3}).

The ion-irradiated specimen also showed D desorption in the high-temperature region, i.e. 930–1150 K. This temperature range of D desorption agreed with that for the neutron-irradiated specimen loaded at 773 K, although the desorption peak observed for the ion-irradiated specimen was much narrower and smaller than that for the neutron-irradiated specimen. Therefore, it is reasonable to consider that the types of defects which play a dominant role in the trapping effects in these two different specimens were similar. Ion-irradiation creates defects only in a shallow region behind the surface, while neutron irradiation forms defects uniformly throughout the bulk of the material. The thickness of the damaged zone formed by irradiation of 20 MeV W ions was ≈2 μm, as described in [6]. Hence, the number of traps in the ion-damaged specimen was significantly smaller than that in the neutron-irradiated specimens. This is the cause of the smaller D retention in the ion-irradiated specimen than in the neutron-irradiated one. The narrower desorption peak observed for the former can also be attributed, at least in part, to the shallow depth of D penetration in comparison with the latter (50–100 μm, as described above). In other words, the penetration and desorption of D into/from neutron-irradiated specimens were controlled by the long-range diffusion process under strong trapping effects.

IV. CONCLUSIONS

Neutron-irradiation of W resulted in a significant increase in D retention owing to the formation of defects that act as traps. The D concentrations in the specimens irradiated with neutrons to 0.3 dpa were 0.8 at.% at 473 K and 0.4 at.% at 773 K, while those in the specimens irradiated to 0.025 dpa were 0.3–0.4 at.% at 473 K and 0.2 at.% at 773 K. In other words, clear increase in trap density with increase in damage level was observed. However, the concentrations of D after neutron-irradiation to 0.3 dpa were only higher by a factor of 2 than those at 0.025 dpa at 473 and 773 K, whereas the damage level increased by an order of magnitude. These observations indicated that the trap density observed after irradiation to 0.3 dpa is close to the saturation level. Thermal desorption spectrum of D from neutron-irradiated specimen exposed to plasma at 773 K showed that release of hydrogen isotope from neutron-irradiated specimen was controlled by long-range diffusion process under strong trapping effects.

ACKNOWLEDGMENTS

This study was supported by the Japanese Ministry of Education, Culture, Sports, Science and Technology via TITAN collaboration.

REFERENCES

[1] J. ROTH and K. SCHMID, "Hydrogen in Tungsten as Plasma-Facing Material," *Phys. Scr.,* **T145**, 0014031, (2011).

[2] M. SHIMADA et al., "Deuterium Depth Profile in Neutron-Irradiated Tungsten Exposed to Plasma", *Phys. Scr.,* **T145**, 0014051, (2011).

[3] M. SHIMADA et al., "First result of deuterium retention in neutron-irradiated tungsten exposed to high flux plasma in TPE", *J. Nucl. Mater.,* **415**, S667, (2011).

[4] Y. OYA et al., "Comparison of Deuterium Retention for Ion-Irradiated and Neutron-Irradiated Tungsten", *Phys. Scr.,* **T145**, 0014050, (2011).

[5] M. SHIMADA et al., "Overview of The US-Japan Collaborative Investigation on Hydrogen Isotope Retention in Neutron-Irradiated and Ion-Damaged Tungsten", *Fusion Eng. Des.,* **87**, 1166, (2012).

[6] Y. HATANO et al., "Deuterium Trapping at Defects Created with Neutron- and Ion-Irradiation in Tungsten", *Nucl. Fusion.,* **53**, 073006, (2013).

[7] Y. HATANO et al., "Trapping of Hydrogen Isotopes in Radiation Defects Formed in W by Neutron ind Ion Irradiations", *J. Nucl. Mater.,* **438**, S114, (2013).

[8] Y. HATANO et al., "Retention of Hydrogen Isotopes in Neutron Irradiated Tungsten (Overview)", *Mater. Trans.*, **54**, 437, (2013).

[9] B. UNTERBERG et al., "New Linear Plasma Devices in the Trilateral Euregio Cluster for an Integrated Approach to Plasma Surface

Interactions in Fusion Reactors, *Fusion Eng. Des.,* **86**, 1797, (2011).
[10] M. SHIMADA et al., "Tritium Plasma Experiment: Parameters and Potentials for Fusion Plasma-Wall Interaction Studies", *Rev. Sci. Instrum.*, **82**, 083503, (2011).
[11] E. BROWNE and R.B. FIRESTONE, "*Table of Radioactive Isotopes*", Shirley V.S. (Ed.), John Wiley & Sons, New York, 1986.
[12] B. J. MERRILL et al., "Simulating Tritium Retention in Tungsten with a Multiple Trap Model in the TMAP Code", *J. Plasma Fusion Res. SERIES*, **10**, 71, (2011).

4-5 Task2-2(1) Hardness distribution and tensile properties in an electron-beam-welded F82H irradiated in HFIR

N. Hashimoto[1*], H. Oka[1], T. Muroga[2], A. Kimura[3], M.A. Sokolov[4] and T. Yamamoto[5]

[1] *Hokkaido University, Sapporo, Hokkaido, Japan*
[2] *National Institute for Fusion Science, Toki, Gifu, Japan*
[3] *Kyoto University, Uji, Kyoto, Japan*
[4] *Oak Ridge National Laboratory, Oak Ridge, Tennessee, USA*
[5] *University of California Santa Barbara, Santa Barbara, CA, USA*

F82H-IEA and its EB-weld joint were irradiated at 573 and 773 K up to 9.6 dpa in the HFIR and the irradiation effect on its mechanical properties and microstructure were investigated. A hardness profile across the weld joint before irradiation showed the hardness in transformed region (TR) was high and especially that in the edge of TR was the highest (high hardness region: HHR) compared to base metal. This hardness distribution corresponds to grain size distribution. After irradiation, hardening in HHR was small compared to other region in the sample. In tensile test, the amount of hardening in yield strength and ultimate tensile strength of F82H EB-weld joint was almost similar to that of F82H-IEA but the fracture position of EB-weld joint was at the boundary of TR and BM. Therefore, the TR/BM boundary is the structural weak point in F82H EB-weld joint after irradiation. As the plastic instability was observed, the dislocation channeling deformation can be expected though the dislocation channel was not observed in this study.

I. INTRODUCTION

In the fusion reactor, there will be a lot of joint part of a reduced activation ferritic/martensitic steel F82H, which is a promising structural material for first wall and blanket components of fusion reactor [1]. An electron beam (EB) welding is one of a competitive method because the volume which is affected by heating is small compared with the other welding method such as a tungsten inert gas welding [2]. However, the effect of neutron irradiation on microstructure evolution and mechanical property change in EB welded F82H has not been revealed yet. In this study, neutron-irradiated F82H-IEA and its EB-weld joint were compared to investigate the irradiation effect in F82H EB-weld joint through conducting a hardness profile across joint, tensile test and transmission electron microscopy (TEM).

II. EXPERIMENTAL

F82H-IEA and F82H EB-weld joint were irradiated up to 9.6 dpa at 573 and 773 K in the rabbit capsule of the High Flux Isotope Reactor at Oak Ridge National Laboratory. The chemical composition of F82H-IEA and F82H EB-weld were found elsewhere [3]. A small sheet-type tensile specimen with the gauge section of 5 mm long, 1.2 mm wide and 0.5mm thick was machined from the joint center so as to coincide with the specimen center for F82H EB-weld joint. Post-irradiation hardness test was performed along the gauge section to obtain the profile of irradiation hardening using Mitutoyo AAV-500 with the load of 9.8 N. The strain-controlled tensile test with the strain rate of 1×10^{-3} s^{-1} was conducted by loading on the shoulders of the specimen in MTS test machines in hot cells. The fracture surface observation was performed on a scanning electron microscopy. The samples for microstructural observation were prepared by a focused ion beam facility, and then observed in TEM.

III.RESULTS AND DISCUSSIONS

III.A. Hardness distribution

Figure 1 shows the distribution of hardness in an unirradiated F82H EB-weld joint used in this study. Horizontal axis of Fig. 1 represents the distance from the edge of the tensile specimen. The center region of the specimen with the length of 5 mm was very hard compared to the shoulder of the tensile specimen. In the following, the 5 mm-length region is called transformed region (TR). Notably, both ends in the TR showed the highest hardness in the specimen, so called the high hardness region (HHR). Figure 2 shows the microstructure of BM, the center of TR and HHR in F82H EB-weld joint. In the center of TR, the grains with enormously high-aspect ratio (0.2-1.0 μm width and 5-10 μm length) were observed, which is in contrast with the microstructure observed in BM; a typical

ferritic/martensitic microstructure (Fig. 2a). On the other hand, HHR contains very fine grains (less than 0.5 μm) and needle-like grains (width of 0.3-0.5 μm). These structures may include over-tempered martensite and freshly formed martensite produced due to be heated above Ac1 temperature during the EB welding. Obviously, the distribution of these microstructures was responsible for the distribution of hardness (Fig. 1).

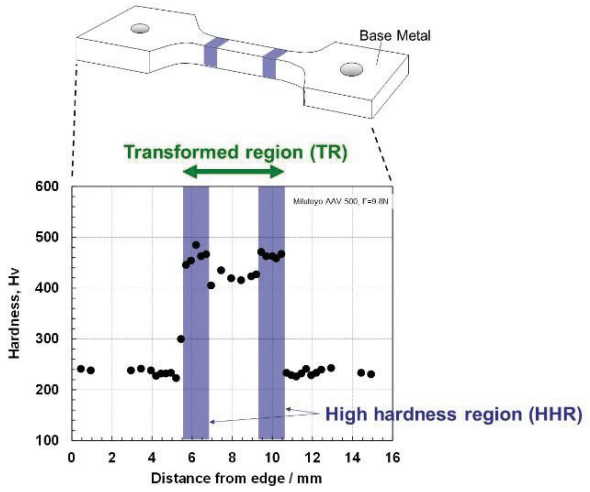

Fig. 1 The distribution of hardness in an unirradiated F82H EB-weld joint. The configuration of tensile specimen and the range of transformed region (TR) and high hardness region (HHR) are also shown.

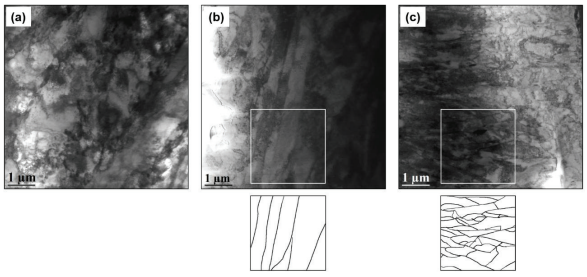

Fig. 2 Microstructure of (a) base metal (BM), (b) the center of transformed region (TR) and (c) high hardness region (HHR) in unirradiated F82H EB-weld joint.

Irradiation at 573 K resulted in hardening of about 100 in Hv for F82H EB-weld joint, as shown in Fig. 3a. HHR showed less irradiation hardening compared with BM. It must be pointed out that the profile of the irradiation hardening shown in Fig 3 was obtained based on the difference between before and after irradiation where the raw data was smoothed. The irradiation hardening was attributable to the dislocation loops induced by irradiation [4]. The less irradiation hardening in HHR can be interpreted that the high density of grain boundaries attributed to the fine-grained structure act as sink sites for irradiation-induced defects and suppress the formation of dislocation loops. In contrast to the irradiation at 573 K, irradiation softening of about 200 in Hv was detected in the TR after irradiation at 773 K (Fig. 3b). Note that the distance of 9-16 mm from the specimen edge was excluded from hardness measurement due to the inappropriate surface condition.

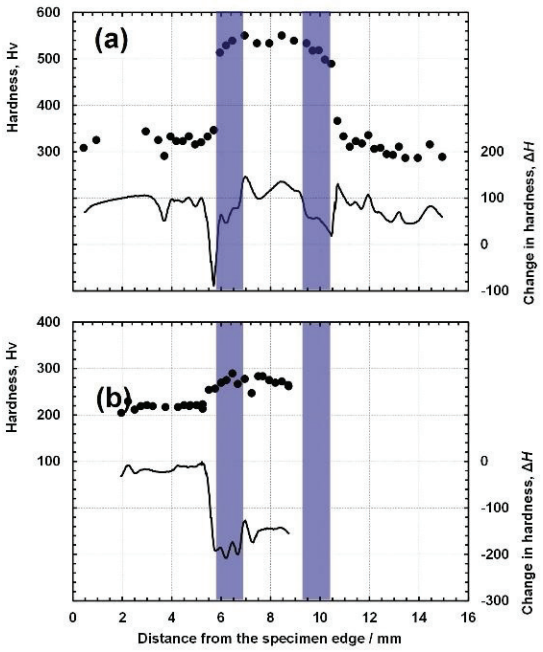

Fig. 3 The distribution of the hardness and the irradiation hardening in F82H EB-weld joint irradiated at (a) 573 K up to 9.6 dpa and (b) 773 K up to 5.5 dpa. Axis for the irradiation hardening is provided in right hand side.

III.B. Tensile Properties

Stress-strain curve of F82H-IEA and F82H EB-weld joint before and after irradiation were shown in Fig. 4a-d. In each graph, the curves in the left hand side represent F82H-IEA, and that in right hand side represent F82H EB-weld joint. Materials, irradiation conditions and the results of the tensile test were summarized in Table 1. The results of unirradiated F82H-IEA tested at 573 and 773 K were quoted from the reference [4]. Before irradiation (0 dpa), F82H EB-weld joint had slightly higher ultimate tensile strength and less total elongation compared with F82H-IEA at room temperature. This tendency was also exhibited in 573 or 773 K testing as well. Additionally, the work hardening capability of F82H EB-weld joint was small compared to that of F82H-IEA. The elongation after achieving ultimate tensile strength, namely the elongation in inhomogeneous deformation, was small in F82H EB-

Table 1 Summary of the tensile properties of all the materials used in this study

Material	Irradiation temperature / K	Capsule ID	Irradiation dose / dpa	Specimen ID	Test temperature / K	Yield strength / MPa	Ultimate tensile strength / MPa	Uniform elongation / %	Total elongation / %
F82H-IEA	573	T9G1	1.2	1	298	727	731	5.5	13.7
				4	298	996	1000	5.1	13.1
				5	573	895	911	5.4	11
				OWAQ	573	744	744	3.8	6.9
		T9G2	9.6	H02	298	982	988	5.8	11.7
				G02	298	829	836	5.9	12.1
				H03	573	995	997	5.4	11.1
				G03	573	943	946	5.2	10.7
	773	T9C1	5.5	3	298	486	594	9.4	21.2
				6	298	498	608	10.1	23.3
				2	773	454	473	5.4	14.2
				7	773	446	487	5.8	15.6
		T9C2	9.6	W6	298	450	546	8.8	20
				8	298	474	587	10.3	25.6
				W5	773	496	519	4.9	14.5
				9	773	430	453	5.7	15.8
F82H/F82H EB-weld	573	T9G1	1.2	HA01	298	760	766	4.3	8.4
				HA03	573	789	789	4	7.7
		T9G2	9.6	HA31	298	973	973	4.8	7.6
				HA33	573	930	930	4.4	6.8
	773	T9C1	5.5	HA18	298	526	623	5.9	10.5
				HA16	773	451	465	5	9.8
				HA17	773	426	441	4	9.3
		T9C2	9.6	HA46	298	479	574	6.7	12.3
				HA47	773	412	459	4.2	9.3
				HA48	773	451	467	4.4	11
F82H-IEA	-	-	-	F04	298	540	635	9.6	22.2
F82H/F82H EB-weld	-	-	-	HA57	298	591	655	6.6	10.4
	-	-	-	HA04	573	530	574	4.8	9.3
	-	-	-	HA55	773	528	555	4.5	8.8

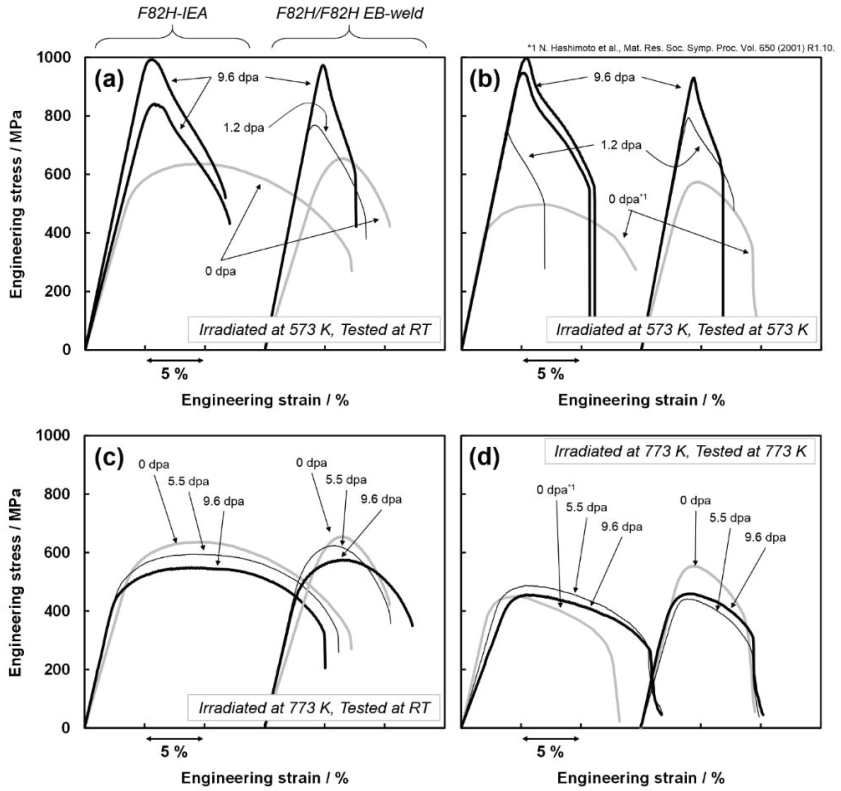

Fig. 4 The stress-strain curve of F82H-IEA and F82H EB-weld joint irradiated up to 9.6 dpa at 573 K tested at (a) room temperature and (b) 573 K, and irradiated at 773 K tested at (c) room temperature and at (d) 773 K. In each graph, the curves in the left and right hand side represent F82H-IEA and F82H EB-weld joint, respectively.

weld joint, as well. The significant hardening resulting from the irradiation at 573 K was observed and it increased with increasing irradiation dose in both F82H-IEA and F82H EB-weld joint. The yield strength increased almost 80-100% after irradiation to 9.6 dpa. Moreover, the degradation of total elongation was exhibited after the irradiation. Notably in room temperature test, the reduction in total elongation of about 50 % was observed in F82H-IEA. However, unlike the F82H-IEA, the reduction in total elongation in F82H EB-weld joint was small, about 30%. Although F82H-IEAand F82H EB-weld joint were different in the reduction of total elongation, plastic instability was exhibited for both material tested at room temperature and 573 K after irradiation, shown in Fig. 4a and b. The detail of the plastic instability was discussed later in section 3.4. In contrast to the irradiation at 573 K, the irradiation at 773 K exhibited almost no difference for both materials compared with un-irradiated condition, as seen in Fig. 4c and d.

III.C. Fracture surface and fracture position

The fracture surface of F82H EB-weld joint after 573 K irradiation exhibited that dimple with the size of 20-30 μm and a very fine (1 μm) dimple distribution were observed, indicating that the fracture mode was a ductile fracture, as seen in Fig. 5. Focusing on the broken point on the tensile specimen, it appeared to break at the boundary between TR and BM (Fig. 5c and g) though the size of TR and BM were too small to evaluate the break position. Therefore, technically, the boundary between TR and BM is a structural weak point of F82H EB-weld joint after irradiation. This result seems to be valid because the distribution of hardness in TR/BM boundary drastically change even after irradiation; the hardness of TR and BM is 500 and 250, respectively. Inhomogeneous distribution of hardness in a structural material produced the structural weakness in itself.

III.D. Microstructure

Post irradiation TEM observation was carried out for the tensile tested F82H EB-weld joint in order to know its deformation mechanism. Fig. 6a shows the configuration indicating lift-out position of FIB specimen. Position A corresponds to BM, meaning that microstructure of position A is as-irradiated condition. Position B is corresponding to the center of TR. Simultaneously, it is a uniformly-deformed region. Position C, which is the necked region during tensile test, corresponds to the HHR. The observed microstructure are shown in Figs. Fig. 5 6b-g, and the direction of tension are also shown by white arrow. Note that the ion beam tracks (diagonal in the fig. 6) were produced during FIB preparation. As-irradiated microstructure (1.2 dpa for Fig. 6b and 9.6 dpa for Fig. 6e) exhibited the irradiation-induced defect cluster but the grain size and/or precipitation distribution seemed to remain after irradiation. The microstructure in the center of TR including the grains with high-aspect ratio was also retained after irradiation (see fig.6c). In the same manner, the very fine grain structure in position C was also retained (fig.6d and g) after irradiation at 573 K up to 9.6 dpa. The irradiation hardening observed in this study might be attributable to the dislocation loops induced by irradiation.

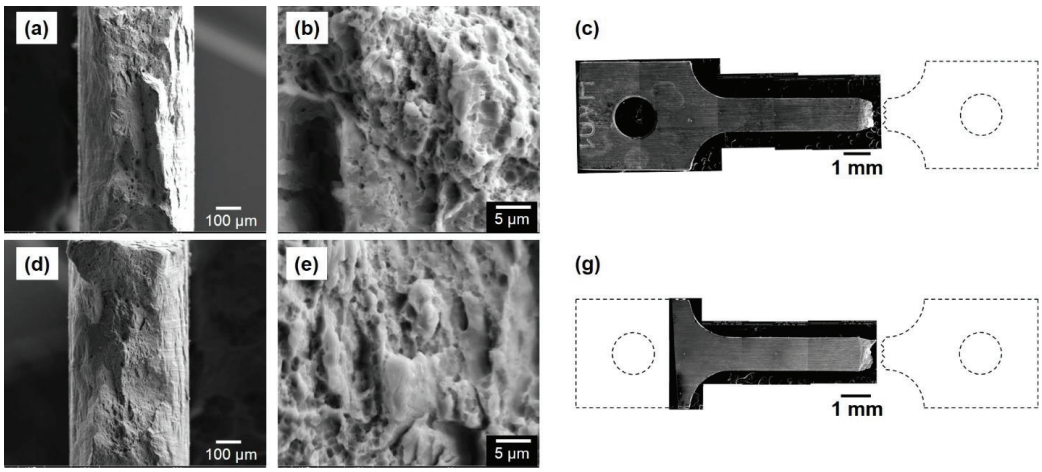

Fig. 5 The fracture surface and the overview of the broken tensile specimen of F82H EB-weld joint irradiated at 573 K up to (a-c) 1.2 dpa and (d-f) 9.6 dpa.

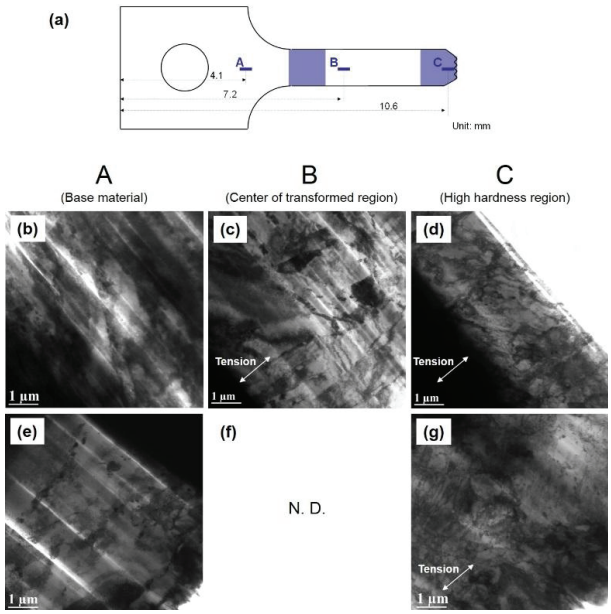

Fig. 6 Microstructure of F82H EB-weld joint irradiated at 573 K up to (b-d) 1.2 dpa and (e-g) 9.6 dpa. FIB/TEM sample lifted out from position A: (b) and (e), position B: (c) and position C: (d) and (g).

Hashimoto et al. [5] found the dislocation channeling deformation in the deformed region of F82H irradiated up to 5 dpa at 573 K, which is due to the existence of the dislocation loops with high density, leading to the plastic instability. Although the dislocation channel was not observed microstructurally in this study, the dislocation channeling deformation can be expected for F82H EB weld joint because the plastic instability was observed in its stress-strain curve. The further investigation to assess the density of dislocation loops need to be done because the dislocation channeling deformation is strongly related to the density of dislocation loops. Furthermore, the microstructure of the necked region in the shoulder side of tensile (the other half of tensile) sample also need to be investigated. Since that region is the deformed BM, the dislocation channel structure can be expected.

IV. CONCLUSIONS

F82H-IEA and its EB-weld joint irradiated at 573 and 773 K up to 9.6 dpa in the HFIR were investigated. F82H EB-weld joint had a hardness distribution in accordance with microstructural distribution. Although HHR exhibited much less irradiation hardening in Fig. 6 hardness compared with BM in F82H EB-weld joint, the boundary between TR and BM is a structural weak point after irradiation. As both F82H-IEA and its EB-weld joint exhibited a plastic instability in tensile test, it can be considered that the dislocation channeling deformation was dominant.

ACKNOWLEDGMENTS

Authors are grateful to Janet Robertson, Pat Bishop and the 3025E operators, Daniel Lewis, Keith Leonard, Kiran, Marie Williams, Kiyohiro Yabuuchi, Takashi Nozawa and Dai Hamaguchi for helping this research. This work was sponsored by Japan-US.

REFERENCES

[1] K. Shiba, M. Suzuki and A. Hishinuma: J. Nucl. Mater. 233–237 (1996) 309–312.
[2] H. Tanigawa et al., Fusion Eng. Des. 83 (2008) 1471–1476.
[3] K. Shiba, R.L. Klueh, Y. Miwa, N. Igawa, J.P. Robertson, Fusion Materials Semiannual Progress Report, DOE/ER-0313/28 (2000) p. 131.
[4] N. Hashimoto, S.J. Zinkle, R.L. Klueh, A.F. Rowcliffe, K. Shiba, Mat. Res. Soc. Symp. Proc. Vol. 650 (2001) R1.10.
[5] N. Hashimoto, R.L. Klueh, M. Ando, H. Tanigawa, T. Sawai, K. Shiba, Fusion Sci. Technol. 44 (2003) 490–494.

Task2-2(2) EFFECTS OF NEUTRON IRRADIATION ON VPS-W COATED ODS FERRITIC STEELS

Sanghoon Noh[1], Ryuta Kasada[1], Takuya Nagasaka[2], Akihiko Kimura[1], M.A. Sokolov[3] and T. Yamamoto[4]

[1]*Kyoto University, Gokasho, Uji, Kyoto 611-0011, Japan, sanghoon.noh@iae.kyoto-u.ac.jp*
[2]*National Institute of Fusion Science, 322-6 Oroshi-cho, Toki-city, Gifu 509-5292, Japan, nagasaka@nifs.ac.jp*
[3] *Oak Ridge National Laboratory, Oak Ridge, Tennessee, USA*
[4] *University of California Santa Barbara, Santa Barbara, CA, USA*

In present study, the effects of neutron irradiation on the hardness of W-coated ODS steels were investigated. Vacuum plasma spraying (VPS) technique was employed to fabricate W layer on the surface of substrates. Substrate materials were K1-, K4-ODS ferritic steels and F82H steel, which are 3mm thick plates. Tungsten powder of 99.9% high purity was used for VPS process. The powders were sprayed by the plasma jet of argon and hydrogen mixture to the surface of substrates pre-annealed at 773K. VPS-W coated specimens were irradiated at 723K to 4.5, 9.6 dpa in the High Flux Isotope Reactor (HFIR), respectively. To investigate the effect of neutron irradiation on joint area, the hardness distributions were evaluated on the cross section using a micro Vickers hardness tester. Microstructure analysis revealed that W was successfully coated on each substrate by VPS process, in spite of mismatch of the CTE between these materials. The hardness of W was significantly varied from 260 to 480Hv because inhomogeneous cooling rate during the process. After irradiations, irradiation hardening was occurred in the VPS-W, while substrate materials did not.

I. INTRODUCTION

Tungsten (W) is currently considered as a candidate of plasma-facing material (PFM) of blanket and diverter in fusion systems, because it is superior to the other candidates in high melting point, sputtering rate and low tritium inventory[1]. Recently, International Thermonuclear Experimental Reactor (ITER) design was also settled on full W version for diverter[2]. As for the PFM of blanket, W coating has been considered to be adequate to protect blanket from spattering.

Among several methods to coat structural material, for example, vacuum plasma spraying (VPS), physical vapor deposition (PVD), chemical vapor deposition (CVD), and hot isostatic pressing (HIP), VPS has the following features: 1) the substrate material receive no thermal effect during process. 2) a variety of spray materials can be selected. 3) more dense coat is available than plasma spraying in air. 4) it is possible to make thicker coating on large substrates.

Oxide dispersion strengthened steels (ODSS) were considered to be one of candidates of high-temperature structural materials for fusion application. The service temperature can be elevated to 1023K that is in the temperature range showing upper shelf energy for W. It is also well known that the elevation of spraying temperature is effective to produce dense W-coat. The microstructure of substrate metal, however, can be influenced when the spraying temperature is too high. Application of ODS steels as a substrate of W plasma spray coat may increase the spraying temperature with maintaining microstructure of substrate. The objective of this work is to investigate mechanical properties of the VPS-W produced on F82H and an ODS steel, and to evaluate the bonding strength between the VPS-W coat and the substrate metals by means of small specimen 3-point bending test technique.

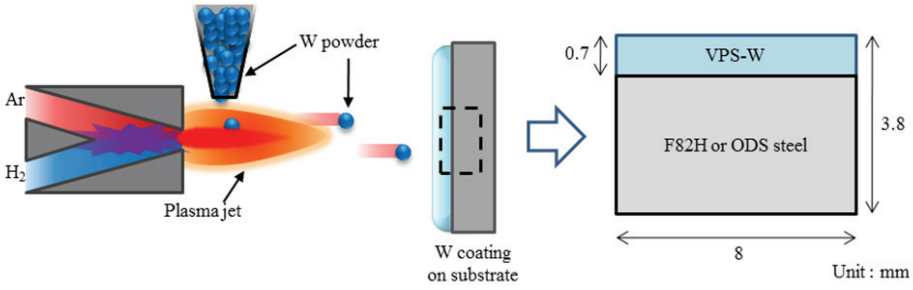

Fig. 1 Schematic of VPS process

Table 1 Chemical composition and process description

	Materials	Dimension	Capsule ID	History	Irr. Cond.
KFW4	W-F82H(Fe-8Cr-2W-0.1C)				
K1C4	W-K1(Fe-19Cr-0.3W-0.35Y_2O_3)		-		As received
K4S4	W-K4(Fe-19Cr-4Al-2W-0.35 Y_2O_3)				
KFW1	W-F82H(Fe-8Cr-2W-0.1C)		T9C1		4.5dpa@773K
KFW2	W-F82H(Fe-8Cr-2W-0.1C)	4x8x0.5t (mm^3)	T9C2	VPS at 773K	9.6dpa@773K
K1C1	W-K1(Fe-19Cr-0.3W-0.35 Y_2O_3)		T9C1		4.5dpa@773K
K1C2	W-K1(Fe-19Cr-0.3W-0.35 Y_2O_3)		T9C2		9.6dpa@773K
K4S1	W-K4(Fe-19Cr-4Al-2W-0.35 Y_2O_3)		T9C1		4.5dpa@773K
K4S2	W-K4(Fe-19Cr-4Al-2W-0.35 Y_2O_3)		T9C2		9.6dpa@773K

The effects of neutron irradiation on various ODS steel joints were investigated. Materials were some VPS-W coated ODS steels. To investigate the neutron irradiation behavior in the joint area, the hardness measurements as post irradiation experiment (PIE) were carried out on the cross section using a micro Vickers hardness tester.

II. EXPERIMENTAL

The substrate materials were F82H (IAE HEAT) steel, two kinds of oxide dispersion strengthened (ODS) ferritic steels. The thickness of the substrates were 3-8 mm. W powder was temporarily melted and sprayed on the substrate by a plasma jet of argon and hydrogen mixture in a vacuum chamber. The substrate temperature was annealed at around 773K during the process. The resulting thickness of the W coatings was about 0.1 mm or 0.7 mm. Schematics of VPS process are illustrated in Fig. 1. Microstructure was observed by field-emission type scanning electron microscope (FE-SEM). VPS process is described in previous study[1]. W coated substrates for the neutron irradiation were machined with a dimension of 8(L)×3.8(H)×0.5(t) mm, so coated interface is located on the cross section.

Neutron irradiation was conducted in the high flux isotope reactor (HFIR) at 723K to 4.5 and 9.6 dpa in the capsule ID T9C1 and T9C2, respectively. After irradiation, hardness measurement across the coated interface was carried out using a micro Vickers hardness tester with 100gf for 10s at room temperature in a regular interval of 200 μm in the hot cell. Chemical composition and specimen description are summarized in Table 1.

III. RESULTS

1. Neutron irradiation effects on VPS-W

The hardness profiles for VPS-W coated specimens as received are shown in Fig. 2. VPS-W has hardness values from 260 to 480HV. It is due to inhomogeneous solidification and cooling rate resulting closed pores during VPS process as shown in Fig. 3. Nagasaka et al. reported the VPS-W had lower measured density than that

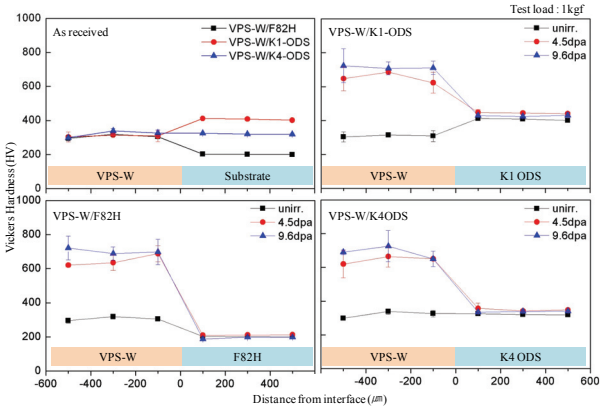

Fig. 2 Hardness distributions of VPS-W coated steels before and after HFIR irradiation

of bulk tungsten fabricated by powder sintering and hot rolling[1]. Hardness of substrates shows different distributions due to their different chemical composition. K1 ODS steel has highest hardness about 400HV and hardness of K4 ODS steel was lowered to 320HV because of Al addition, finally F82H steel showed lowest, about 220HV. However, each substrate showed uniform hardness distribution. In substrates, irradiation hardening is not occurred in increase of dose rate. Neutron irradiation defects of steels are easily diffused because annealing rate is faster than defect forming rate on irradiation at 500 °C. After neutron irradiation, degrees of hardening of VPS-W are also not so higher even with increase of dose rate. This is because dose rate which

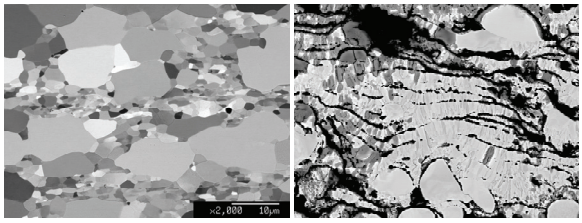

Fig. 3 Microstructures of bulk W (Left) and VPS-W (Right)

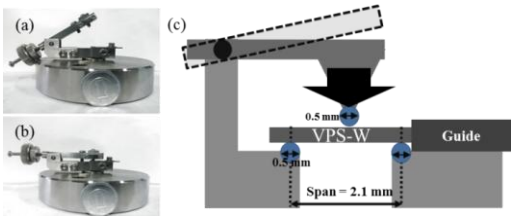

Fig. 4 Miniaturized 3-point bending test tool.

effects on hardening of pure W may be saturated on 4.5 dpa and it is reported that hardening rate is experimentally saturating between 1 and 10 dpa in HFIR[2]. It is known that hardening mechanism of pure W is mainly caused by void formation, and the saturation of the hardening effect was probably due to void lattice formation[3]. The relation between irradiation hardening and dose rate is shown in Fig. 1-4. While bulk W fabricated powder-sintering method shows significant hardening rate about 530HV, VPS-W was not so high, about 360HV.

2. Miniaturized 3-point bending test

Bending strength of VPS-W coating was measured by using miniaturized 3-point bending tester as shown in Fig. 4. Fig. 5(a, b) show the stress-strain behavior of VPS-W specimens sampled from the coating of the vacuum plasma sprayed substrates. Two different VPS methods were adopted. Old method is sprayed without masking and new method is with masking. All the specimens break down in the elastic region. The average value of the fracture stresses of the VPS-W(new) sprayed on ODSS was 470 MPa, and the fracture stresses of VPS-W(old) was 390 MPa, indicating 20% higher strength was achieved by masking. On the contrary, the fracture stresses of VPS-W(M) and VPS-W (old) sprayed on F82H was 420 MPa and 400 MPa, respectively which is only 5 % of increase in strength. The results indicate that VPS-W(new) have been improved in mechanical properties more effectively for the ODSS substrate. We considered that the reduction of pores in VPS-W(new) was interpreted in terms of temperature maintainability of the particles, which was due to 1) masking, 2) large powder size and 3) high substrate temperature. The powder with a low flight speed and away from the center of the spray jet was masked so that the powder was unable to arrive on the substrate. Larger powders arrived on the substrate can maintain higher temperature because of a larger heat capacity. High substrate temperature gives an opportunity to the powders be melted and joined to the other melted powders.

Fig. 5(c, d) show the stress-strain behavior of the joint of VPS-W and substrate metal (ODSS, F82H) measured by using miniaturized 3-point bending tester. The fracture stress of VPS-W (old)/ODSS joints was 60 MPa, and that of VPS-W (M)/ODSS joints was 130 MPa, indicating more than twice of increase in the strength by

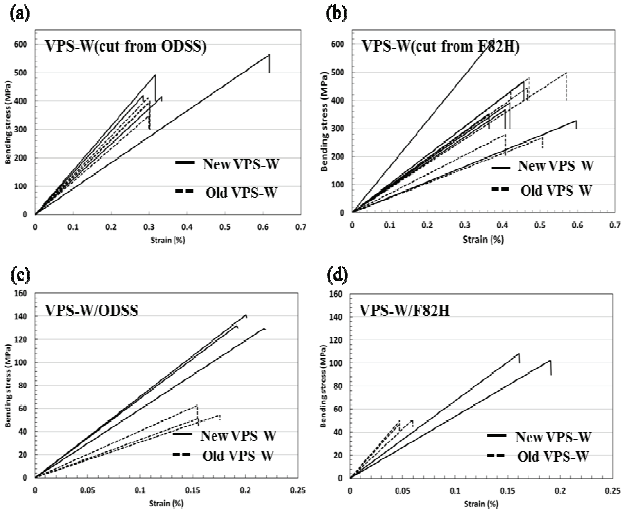

Fig. 5 (a) and (b) :bending strength of VPS-W alone. (c) and (d) bending strength of bonding specimens.

masking. This is similar in the case of F82H substrate, where the fracture stress of VPS-W (old)/F82H joints was 50 MPa, while that of VPS-W (new) one was 110 MPa.

IV. CONCLUSIONS

Neutron irradiation hardening is observed for VPS-W irradiated at 500 °C that is the temperature iron and steels generally show softening. The hardening is increasing with increasing the dose from 1 to 3 dpa.

The VPS-W produced with masking during spraying shows a bending strength higher than 500 MPa measured without the substrate, while that is 140 MPa with the substrate. This indicates that the residual stress control is critical for the VPS-W on the substrate and cracking between the layers is a result of stress relief which occurs cooling after spraying.

ACKNOWLEDGMENTS

Authors are grateful for the financial support from the U.S. D.O.E., Grant No. DE-FG03-86ER52123, and the Japanese Ministry of Education, Culture, Sports, Science and Technology via JUPITER-II collaboration.

REFERENCES

[1] T. Nagasaka, R. Kasada, A. Kimura, Y. Ueda, T. Muroga, Fusion Science and Technology, 56, p.1053-1057 (2009)

[2] A. Hasegawa, T. Tanno, S. Nogami, M. Satou, Journal of Nuclear Materials, In Press (2010)

[3] T. Tanno, A. Hasegawa, J. C. He, M. Fujiwara, S. Nogami, M. Satou, T. Shishido and K. Abe: Material Transection. 48, p. 2399–2402 (2007)

Task2-2(3) HARDNESS DISTRIBUTION AND EFFECT OF IRRADIATION IN FSW-ODS FERRITIC STEELS

Sanghoon Noh[1], Ryuta Kasada[1], Takuya Nagasaka[2], Akihiko Kimura[1], M.A. Sokolov[3] and T. Yamamoto[4]

[1]*Kyoto University, Gokasho, Uji, Kyoto 611-0011, Japan, sanghoon.noh@iae.kyoto-u.ac.jp*
[2]*National Institute of Fusion Science, 322-6 Oroshi-cho, Toki-city, Gifu 509-5292, Japan, nagasaka@nifs.ac.jp*
[3] *Oak Ridge National Laboratory, Oak Ridge, Tennessee, USA*
[4] *University of California Santa Barbara, Santa Barbara, CA, USA*

Oxide dispersion strengthened ferritic steels (ODS-FS) have been considered as one of the most promising structural materials for advanced nuclear systems such as fusion reactors and next generation fission reactors, because of its excellent elevated temperature strength, corrosion and radiation resistance. Especially, irradiation resistance is a critical issue for the high performance of ODS-FS. In this study, effects of the irradiation on hardness properties of friction stir processed (FSP) ODS-FS were investigated. FSP technique was employed on ODS-FS. A plate specimen was cut out from the cross section and irradiated to 1.2 dpa at 573K in the High Flux Isotope Reactor (HFIR). To investigate the effect of neutron irradiation on processed area, the hardness distributions were evaluated on the cross section. Hardness of FSP ODS-FS was various with each microstructure after irradiation to 1.2 dpa at 573K. The increase of Vickers hardness was significant in the stirred zone and heat affected zone. Base material exhibited the lowest hardening about 38HV. Since nano-oxide particles in stirred zone showed identical mean diameter and number density, it is considered that hardening differences between stirred zone and base material is due to differences in initial dislocation density.

I. INTRODUCTION

Oxide dispersion strengthened ferritic steel (ODS-FS) has been considered one of the most promising structural materials for advanced nuclear systems such as fusion reactors and next generation fission reactors because of its excellent elevated temperature strength, corrosion and radiation resistance. These good performance comes from favorable microstructures consisting of fine grains and nano oxide particles dispersed in high number density[1-3]. For more applications of the ODS-FS to fusion systems with a huge and complex structure, its weldability is one of the key technologies to be solved. However, it is well known that welding of ODS-FS with conventional melting-solidification process is not adequate to reserve nano-oxide particles in the matrix homogeneously[4,5]. Friction stir welding (FSW) is a solid-state process developed by The Welding Institute (TWI), which is processed by scanning the rotating friction-tool at a very high speed along the joining boundary. The tool is plunged into workpiece and moved in the welding direction[6,7]. Some preliminary practices have been already shown to check the reliability of FSW on ODS-FS, because FSW is expected to keep the well-featured microstructures of ODS-FS[8-10].

In this study, the effects of friction stir processing (FSP) on the microstructure and mechanical properties of hot extruded ODS-FS were investigated to apply FSW process to ODS-FS. To investigate the neutron irradiation behavior in the joint area, the hardness measurements as post irradiation experiment (PIE) were carried out on the cross section using a micro Vickers hardness tester.

II. EXPERIMENTAL

ODS-FS used in this study is Fe-15Cr-4Al-0.7Y2O3 ODS ferritic steel. Chemical compositions are shown in Table 1. The ODS-FS were fabricated by mechanical alloying and hot-extrusion process. An ODS-FS rod was machined to the dimension of 115 mm length × 20 mm width × 8 mm thickness, of which the longitudinal direction (L-direction) was parallel to the extruded direction, was friction stir processed in the air at room temperature. The material of the rotating tool used in this study is a polycrystalline cubic boron nitride (PCBN). The rotating tool is plunged into the plate and moved along bonding direction. The ODS-FS was friction stir

Table 1 Chemical compositions of ODS ferritic steel (wt.%)

Fe	C	Si	Mn	P	Cr	W	Al	Ti	Y_2O_3
Bal.	0.018	0.02	0.02	<0.005	15.39	0.28	3.78	0.1	0.7

Fig. 1 Cross sectional optical micrograph of friction stir processed ODS-FS

processed at a tool traveling speed of 50mm/min and tool rotating speed of 800rpm. Consequently, the process was done parallel to the extruded direction. Detailed fabrication and processing condition are described in previous paper[11]. A plate specimen was cut out from the cross section and irradiated to 1.2 dpa at 573K in the High Flux Isotope Reactor (HFIR). To investigate the effect of neutron irradiation on processed area, the hardness distributions were evaluated on the cross section using a micro Vickers hardness tester with 200gf for 10s at room temperature in a regular interval of 0.5 mm.

III. RESULTS

1. Neutron irradiation effects on FSP-ODS steel

Optical micrograph of friction stir processed ODS-FS on transverse cross section is shown in Fig. 1. Two distinct zones can be clearly identified as base material (BM) and stirred zone (SZ). The SZ exhibits a symmetric basin-shape with about 3mm depth at bottom and significantly spreading toward the upper surface. In Fig.2, the hardness distribution on the transverse cross section is illustrated as a color level map. Each cross line indicates the measured point of hardness and its color shows the hardness level. The variable colored distribution area is well corresponding with the changes in the microstructure developed during friction stir process, that is, changing colored area matches with the geometries of rotating pin and shoulder. As seen in Fig. 2(b), boundary area between SZ and BM is limited to very narrow area that can be defined as a heat affected zone (HAZ). SZ around the weld center shows lower hardness of 210 ± 12 HV than that of 316 ± 6 HV of base material.

The hardness distribution of tool advancing side after neutron irradiation in HFIR to 1.2 dpa at 573K is illustrated in Fig. 2(c, d). After irradiation, hardness distribution changed randomly from 310 to 420 HV, but degrees of irradiation hardening was clearly occurred in each microstructure. In Fig. 3, irradiation hardening of each microstructure SZ, HAZ and BM is illustrated. The irradiation hardening in BM is not so high about 38HV, compared with those in SZ showed about 120HV. This means that microstructural difference results different irradiation hardening at 572K.

S. Noh et al. reported that nano-oxide particles in SZ were uniformly distributed and reserved with same mean particle size and number density with BM[11]. More detailed microstructural observation is essentially required, however, it can be assumed that this is because of dislocation density difference between BM and SZ developed during the friction stir process.

Meanwhile, the dislocation density of metal is closely related to the thermal history during the processing. The maximum temperature of the work piece by frictional heat can be examined with some FSW parameters by Arbegast and Hartley[12]. They measured the average maximum

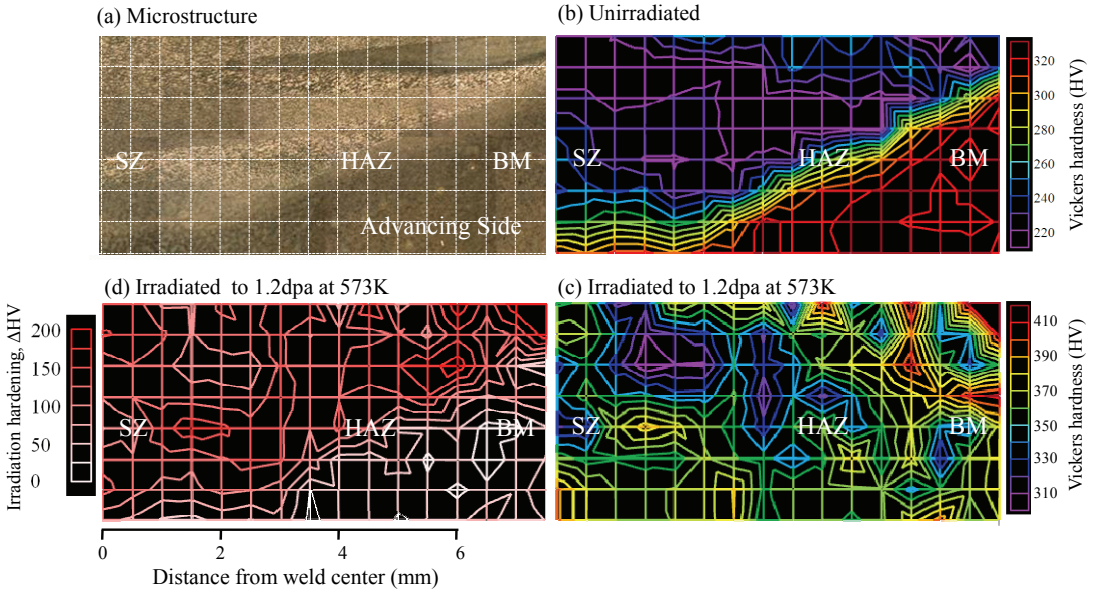

Fig. 2 Irradiation hardening of friction stir processed ODS ferritic steel

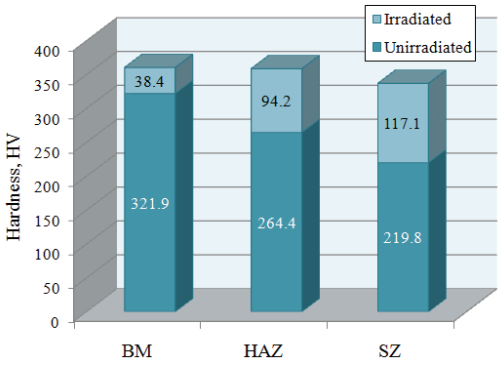

Fig. 3 Irradiation hardening of each region

temperature for a relationship between maximum welding temperature (T, °C) and FSW parameters (ω, ν; tool rotation speed (rpm), traveling speed (mm/min)) and it can be expressed by,

$$\frac{T}{T_m} = K\left(\frac{\omega^2}{\nu \times 10^4}\right)^{\alpha} \qquad (1)$$

where, the exponent α was reported to be in the 0.06 in steels, the constant K is 0.65 in steels, and Tm is the melting point, 1513°C of this ODS-FS. Thus, the maximum temperature of the ODS-FS estimated during the process is estimated to be about 1305°C. Compared with tool traveling speed of Al alloy, 50mm/min on ODS-FS is very slow in this study, so the workpiece could be heated up to high temperature, 1305°C in several minutes. Consequently, it is considered that dislocation recovery occurred in the SZ and dislocation density was reduced during friction stir process. This could explain the result of irradiation hardening difference between SZ and BM after HFIR irradiation.

2. Neutron irradiation effects on FSP-ODS steel

Alinger at el. reported that MA957 fabricated by hot extrusion process showed a strong anisotropy in tensile properties and fracture toughness due to elongated grain with alumina stringers[6]. This isotropic tensile property in friction stir processed ODS-FS is entirely consistent with its microstructural analysis which is coarsened equiaxed grains and uniformly distributed Y-Al oxides and Ti carbides in the grains of both directions. This fact is also supported in fracture surface observation after tensile test. Fracture surface of base material in L-direction shows typical ductile fracture with the micro-void coalescence, as shown in Fig. 4 (a). While, the fracture surface in T-direction showed a line-shape cracking without sufficient area reduction. These behavior is normal in hot extruded ODS steel that the crack propagation along the extrusion direction is more favorable which fracture strain of the specimen elongated in perpendicular to the direction of hot extrusion was smaller than that of the specimens elongated in parallel to the direction of hot extrusion. On the other hand, the specimens both in L, T-direction of stirred zone fractured in ductile mode, as shown in Fig. 4 (b). This anisotropic deformation behavior is arisen from fiber texture, coarsened brittle phases along the elongated grain such as Y-Al oxide and Ti carbide. EBSD analysis showed clearly evolution of the texture in friction stir processed ODS-FS. Base material has a strong <110> texture parallel to extrusion direction. However, random texture which is difficult to define the dominant orientation is developed in the stirred zone. Also, WDS analysis that longitudinally elongated brittle phase of Y-Al oxide and Ti carbide was uniformly distributed in grains of stirred zone is well corresponded to the result of tensile test which show isotropic behavior after the process. In this sense, it is expected that friction stir welding of ODS-FS likely suppresses the anisotropy on mechanical properties effectively.

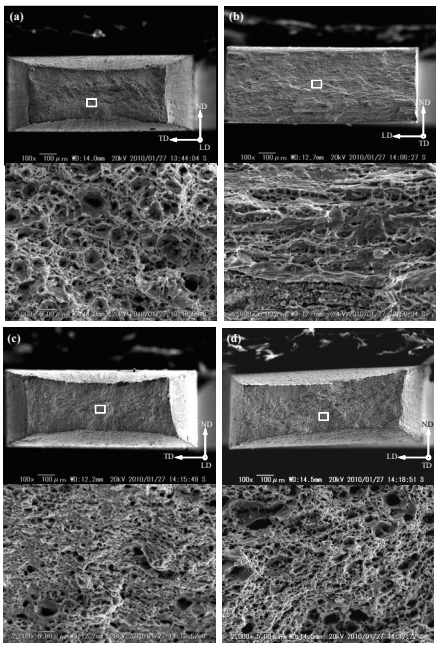

Fig. 4 Fracture surfaces of friction stir processed ODS-FS deformed at RT in L-direction (a), T-direction (b) in base material, and in L-direction (c), T- direction (d) in stirred zone

The tensile test results of the friction stir processed ODS-FS deformed at elevated temperatures are shown in Fig. 5. The tensile specimens were sampled, so that the gage plate is parallel to the T-direction cross section. As

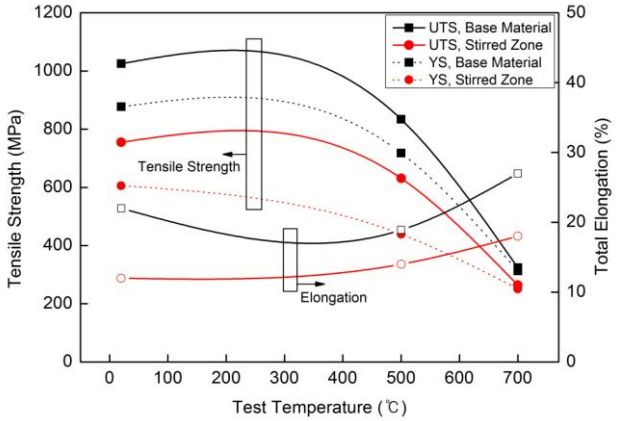

Fig. 5 Tensile test results of the friction stir processed ODS-FS deformed at elevated temperature

can be clearly seen, tensile strengths of stirred zone at 500 °C are about 40% lower than that of the strength of base material. This difference in the yield stress at 500°C, however, is remarkably reduced at 700 °C, showing that the yield strength of stirred zone decreased to 15% compared to that of base material. Furthermore, it should be noted that friction stir process could increase the ductility in stirred zone at elevated temperatures.

Strength difference between stirred zone and base material at room temperature can be correlated with the differences in grain size and dislocation density caused by dynamic recovery and recrystallization during friction stir process. However, the strength difference is reduced at 700 °C because at high-temperatures finely dispersed nano-oxide dispersion mainly controls the motion of dislocations, what can be called as the interaction between dislocations and dispersed nano-oxide particles, as reported by Kasada et al.[13]. Therefore, it is expected that friction stir welding is an attractive welding technique for ODS steels not only to suppress the anisotropy but also to minimize the change of dispersion morphologies of nano-oxide particles not to degrade the elevated temperature strength in welding region.

IV. CONCLUSIONS

The increase of Vickers hardness was significant in the stirred zone and heat affected zone. Base material exhibited the lowest hardening about 38HV. Since nano-oxide particles in stirred zone showed identical mean diameter and number density, it is considered that hardening differences between stirred zone and base material is due to differences in initial dislocation density.

The microstructure of friction stir processed ODS-FS was consisted of a stirred zone and base material. The stirred zone had equiaxed and coarsened grains caused by dynamic recrystallization and grain growth during friction stir processing. The hardness profile of friction stir processed ODS-FS shows an asymmetric characteristic as the hardness in retreating side is higher than that in advancing side. Although friction stir processing resulted in the reduction of hardness and tensile strength, it is attractive to suppress the anisotropy with minimizing the change in the dispersion morphologies of fine nano-oxide particles on ODS-FS. Therefore, friction stir welding is a potential welding method to preserve fine nano-oxide distribution effectively.

ACKNOWLEDGMENTS

Authors are grateful for the financial support from the U.S. D.O.E., Grant No. DE-FG03-86ER52123, and the Japanese Ministry of Education, Culture, Sports, Science and Technology via JUPITER-II collaboration.

REFERENCES

[1] A. Kimura, R. Kasada, A. Kohyama, H. Tanigawa, T. Hirose, K. Shiba, S. Jitsukawa, S. Ohtsuka, S. Ukai, M.A. Sokolov, R.L. Klueh, T. Yamamoto, G.R. Odette, J. Nucl. Mater. 367-370 (2007) 60

[2] A. Kimura, H.S. Cho, N. Toda, R. Kasada, K. Yutani, H. Kishimoto, N. Iwata, S. Ukai, M. Fujiwara, J. Nucl. Sci. Technol. 44 (3) (2007) 323

[3] S. Yamashita, N. Akasaka, S. Ukai, S. Ohnuki, J. Nucl. Mater., 367-370 (2007) 202

[4] R. Lindau, A. Möslang, et al., Fusion Eng. Design, 989-996 (2005) 75

[5] N. Baluc, D.S. Gelles, S. Jitsukawa, A. Kimura, R.L. Klueh, G.R. Odette, B. van der Schaaf, Jinnan Yu, J. Nucl. Mater. 367-370 (2007) 33

[6] Thomas WM, Nicholas ED, Needham JC, Murch MG, Temple-Smith P, Dawes CJ., International Patent Application No. PCT/GB92/02203; 1991

[7] Thomas WM, Dolby RE. Friction stir welding developments, Proc. of the sixth international trends in welding research, ASTM International 203-211 (2003)

[8] F. Legendre, S. Poissonnet, P. Bonnaillie, L. Boulanger, J. Nucl. Mater. 386-388 (2009) 537

[9] M.H. Mathon, V. Klosek, Y. de Carlan, L. Forest, J. Nucl. Mater. 386-388 (2009) 475

[10] P. Miao, G.R. Odette, J. Gould, J. Bernath, R. Miller, M. Alinger, J. Nucl. Mater. 367-370 (2007) 1197

[11] S. Noh, R. Kasada, A. Kimura, S. H. C. Park, S. Hirano, J. of Nucl. Mater., in press (2011)

[12] W.J. Arbegast, P.J. Hartley, in: Proceedings of the 5th Int. Conf. on Trends in Welding Research 541 (1998)

[13]R. Kasada, N. Toda, K. Yutani, H.S. Cho, H. Kishimoto, A. Kimura, J. Nucl. Mater., 367–370 (2007) 222–228

Task2-2(4) DEVELOPMENT OF SOLID STATE DIFFUSION BONDING OF ODS FERRITIC STEELS

Sanghoon Noh[1], Ryuta Kasada[1], Takuya Nagasaka[2], Akihiko Kimura[1]

[1]*Kyoto University, Gokasho, Uji, Kyoto 611-0011, Japan, sanghoon.noh@iae.kyoto-u.ac.jp*
[2]*National Institute of Fusion Science, 322-6 Oroshi-cho, Toki-city, Gifu 509-5292, Japan, nagasaka@nifs.ac.jp*

Solid-state diffusion bonding (SSDB) was employed to join high-Cr oxide dispersion strengthened (ODS) ferritic steel (Fe-15Cr-2W-0.2Ti-0.35Y_2O_3) blocks under uniaxial hydrostatic pressure using a high vacuum hot press, and the microstructure and mechanical properties of the joints were investigated. High-Cr ODS ferritic steels were successfully diffusion bonded at 1200 °C for 1 h, without precipitates and micro-voids at the bonding interface or degradation in the base materials. TEM observation revealed that the nano-oxide particles near the bonding interface were uniformly distributed in the matrix and that the chemical composition across the bonding interface was virtually constant. At room temperature, the joint had nearly the same tensile properties and exhibited anisotropic behavior similar to that of the base material. The tensile strength of the joint region at elevated temperatures is nearly the same as that of the base material, with necking behavior at several μm from the bonding interface. The total elongation of the joint region slightly decreased at 700 °C, with an exfoliation fracture surface at the bonding interface. Although a small ductile-brittle transition temperature (DBTT) shift was observed in the joints, the upper shelf energy (USE) was fully reserved in the case of joints with the L-R bonding orientation, for which cracks did not propagate on the bonding interface. Therefore, it is concluded that SSDB can be potentially employed as a joining method for high-Cr ODS ferritic steel owing to the excellent mechanical properties of the joints.

I. INTRODUCTION

For applications of the ODS-FS to advanced nuclear systems such as next generation IV fission system and DEMO fusion system with a huge and complex structure, reliable bonding and welding techniques need to be developed with such a process that the microstructures with very fine grain and homogeneous distribution of nano-scaled oxide particles are not remarkably changed by the joining processing[1]. However, the application of conventional melting-solidification welding technique such as tungsten inert-gas (TIG) welding, electron beam welding and laser welding for joining ODS steels may result in the disruption of fine-scaled microstructures, especially nano-oxide particle, and consequently a loss of the high-temperature strength because of the agglomeration or growth of the featured microstructures. Solid state diffusion bonding (SSDB) does not create the molten zone at the bonding interface, so that degradation of featured microstructures may be avoided or minimized. Therefore, this process is expected that can be used to bond large areas as well as pre-machined components, complex shapes and interfaces. Because no bulk plastic deformation occurs, SSDB can be used to fabricate blanket structure for tokamak fusion reactor. For this reason, especially in the fusion reactor systems, hot isostatic pressing (HIP) technique has been studied to fabricate the fusion blanket components with reduced activation ferritic/martensitic steels[2-6].

In this study, SSDB was employed to join high-Cr ferritic ODS steel blocks with high vacuum hot press. The microstructures and mechanical properties of the joint were investigated to evaluate the applicability of SSDB to ODS steel joining.

II. EXPERIMENTAL

The ODS FS used as the base material in this study is Fe(bal.)-15Cr-2W-0.2Ti-0.35Y_2O_3. The ODS FS was fabricated via mechanical alloying and hot extrusion.

The samples were cut into 20 × 12 × 12 mm^3 test pieces for bonding, and the surfaces to be bonded were wet-ground with SiC emery papers; finally, they were buff-polished such that they had an average roughness of 0.25 μm. After surface polishing, the samples were stored in acetone for cleaning and for preventing surface contamination. A hydrostatic vacuum hot press furnace was used for diffusion bonding in this study. Two ODS FS blocks were placed vertically between the pressing punches, and they were linearly heated up to the bonding temperature at a rate of 10 °C/min. The bonding temperature was maintained for various durations in a high-vacuum atmosphere (5× 10^{-4} Pa), under a hydrostatic pressure of 25 MPa in a uniaxial compressive loading mode. After the bonding process, the hydrostatic pressure was reduced, and the samples were cooled in the furnace.

The grain morphology was observed using a field-emission scanning electron microscope (FE-SEM). The nano-oxide particle morphology and bonding interface were observed via TEM at an acceleration voltage of 200

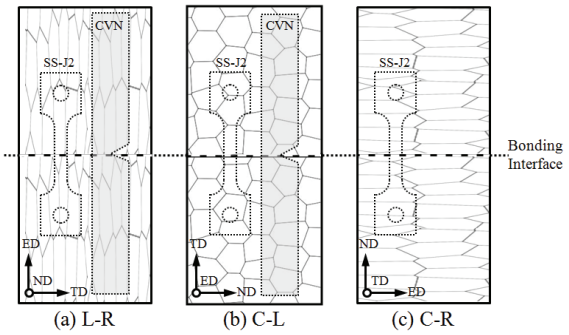

Fig. 1 The bonding orientation relationships for SS-J2 tensile and Charpy V-notched (CVN) specimens; each specimen has each orientation relationship in extrusion direction (ED), transverse direction (TD), normal direction (ND)

kV. Energy dispersive X-ray spectroscopy (EDS) analysis of the bonding interface was also carried out.

To evaluate the joint strength, tensile and impact tests were carried out on the base material and joint for each bonding orientation relationship. In this study, two ODS FS samples were bonded such that the joint interface is perpendicular to the extrusion direction parallel to the loading direction; this is termed as the L-R bonding orientation. In addition, samples whose joint interfaces are parallel to the extrusion direction are categorized under C-R and C-L bonding orientations. The bonding orientation relationships of the tensile and impact test specimens used in this study are shown in Fig. 1. Each specimen was electro-discharge machined such that the joint interface was located at the center of the gage length and V-notch.

Tensile tests were performed in the temperature range from room temperature to 700 °C at a strain rate of 6.67×10^{-4} s^{-1}, in a high-vacuum atmosphere. The impact tests were carried out in the temperature range of 130 K to 453 K with a load of 500 N using a drop-tower-type impact test instrument at a loading speed of 5 m/s. The ductile-brittle transition temperature (DBTT) and upper shelf energy (USE) were determined by fitting the plots of the relationship between the absorbed energy and temperature to the following hyperbolic functions:

$$R(T) = a+b \tanh\{(T-T_0)/c\},$$

where T is the test temperature and a, b, c, and T0 are the regression coefficients. The DBTT and USE are defined as T_0 and (a+b), respectively.

III. RESULTS

1. Optimization of bonding conditions

In order to investigate the optimum condition, SSDB on ODS-FS blocks were carried out in various bonding temperature and it is considered that available temperature range is 950~1200 ºC which is not detrimental on Vickers hardness after annealing for 1h of base material. The microstructures on bonding interface with various bonding temperature for 1h are shown in Fig. 2. In an interface bonded at 950 ºC presented in Fig. 2(a), although voids do not exist, there are many inclusions can be observed at the bonding interface. Wavelength dispersive X-ray spectroscopy (WDS) analysis revealed much of coarsened inclusion at the interface is Cr carbide, $Cr_{23}C_6$, which are agglomerated and resided in bonding process at 950 ºC. Residual creep deformed layer by high temperature and compressive load is observed at the bonding interface in bonding process of 1050 ºC for 1h, while there is no Cr carbide inclusions as seen in Fig. 2(b). SSDB joints at 1150 ºC and 1200 ºC shows the fairy good

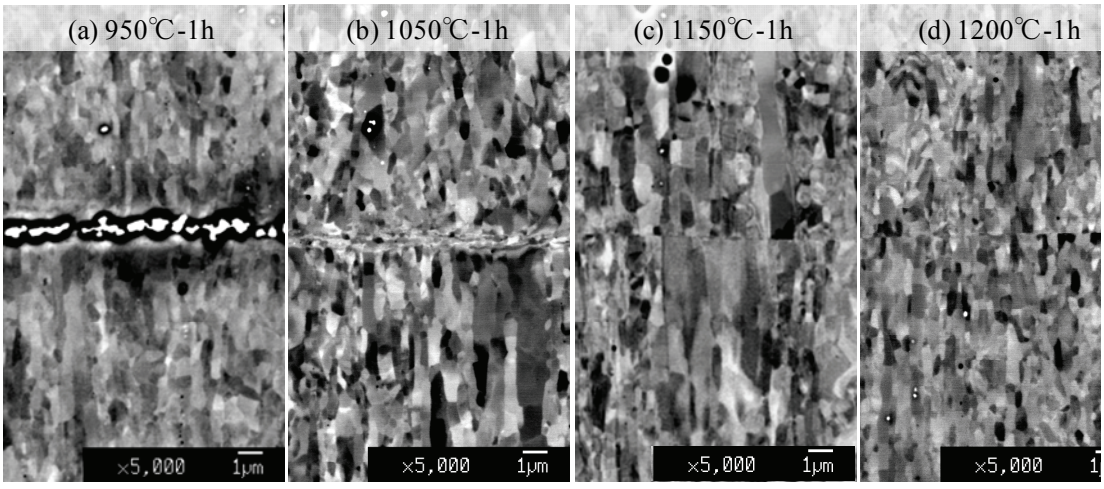

Fig. 2 Microstructural changes with the bonding temperature in SSDB of 15Cr ODS ferritic steel

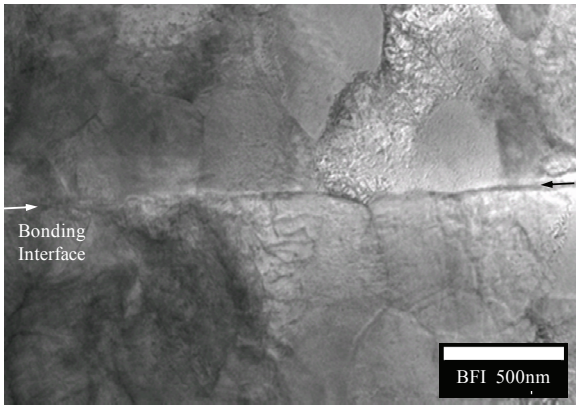

Fig. 3 TEM image at solid-state diffusion bonding interface of 15Cr ODS FS.

interface without any of voids and deformed layer and bonds at 1200 ºC is more difficult to distinguish the bonding interface than 1150 ºC one. Therefore, higher bonding temperature is essentially required for satisfactorily fine interface, in consideration of annealing temperature limitation not to deteriorate the mechanical property of 15Cr ODS ferritic steel, optimum bonding temperature is determined as 1200 ºC.narrow area that can be defined as a heat affected zone (HAZ). SZ around the weld center shows lower hardness of 210 ± 12 HV than that of 316 ± 6 HV of base material.

All ODS ferritic steel blocks were successfully diffusion bonded at 1200 ºC for 1h. The surfaces of the bonded sample showed no trace of macroscopic deformation under the hydrostatic pressure of 25 MPa, which is in agreement with the report that the threshold stress for the surface deformation of commercial ODS alloy, Inconel MA956, is about 60MPa[7].

In Fig. 3, low magnification bright field TEM image at bonding interface is presented. The bonding interface is located horizontally in the center of a micrograph. It is too hard to observe the any voids and inclusions at bonding interface. In more detailed observation shown in Fig. 4, 2 or 3 nm oxide particles which are $Y_2Ti_2O_7$ complex oxides, are observed in uniformly distributed in the matrix. Kasada et al. reported nano-oxide particles in K1-ODS steel are $Y_2Ti_2O_7$[8], which has similar compositions and fabrication process with the ODS ferritic steel used in this study. As for this Y-Ti-O complex, Miller et al. showed that they were thermally stable during annealing even at 1300 ºC for several hours[9]. Thus, it is confirmed that the bonding process, 1200 ºC for 1h, does not affect the nano-oxide particles morphology of base material. EDS profiles across the bonding interface shows that element distributions in Fe, Cr, W, Ti, O and C is significantly constant and no oxides and carbides exist at SSDB joint interface.

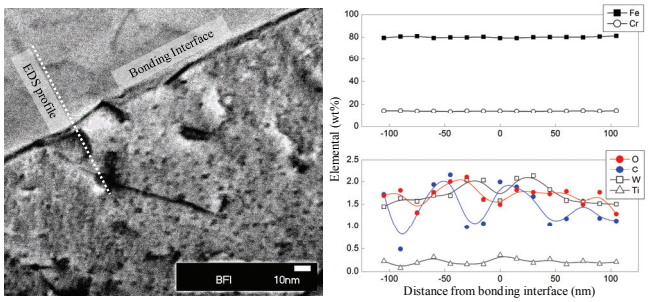

Fig. 4 TEM image at SSDB interface of 15Cr ODS FS and a result of EDS profile across the bonding interface.

Consequently, these results suggest that solid-state diffusion bonding technique is promising way for the joining of the high Cr ODS ferritic steel without microstructual degradations in both base material and bonding interface.

2. Mechanical properties of SSDB-ODS ferritic steel

1) Tensile properties

Microstructure observation revealed that the SSDB joint had a good bonding interface without voids and inclusions. To compare the bonding strength with that of base material, tensile tests were carried out at room temperature for base material and SSDB joint with each bonding orientation relationship. The obtained stress-strain curves of base material and SSDB joints are presented in Fig. 5. Base material shows typical anisotropic behavior that the base material with L-R orientation can be more strained than the others, which is general behavior for hot extruded ODS ferritic steel which has elongated grains in parallel to the loading direction. Surprisingly, nearly the same anisotropic tensile behavior with base material was obtained in SSDB joints. All SSDB joint specimens tested at room temperature were fractured in a ductile mode showing the necking even at a hundred μm far from the joint interface.

Bonded component is expected to be operated in the temperature range of about 500~700 ºC, so that it is important to investigate the mechanical property at elevated temperatures. Tensile test result of base material and SSDB joint in L-R orientation at elevated temperatures is shown in Fig. 6. Ultimate tensile strength (UTS) of both materials show almost same tendency and is clearly decreased from 1250 MPa to about 410 MPa with increasing test temperature to 700 ºC. In base material, total elongation (TE) appears to increase with increasing test temperature to 700 ºC, and above 700 ºC necking was not observed in spite of sufficient TE. This is because the grain boundary sliding mechanism was occurred at elevated temperature, the TE reached as much

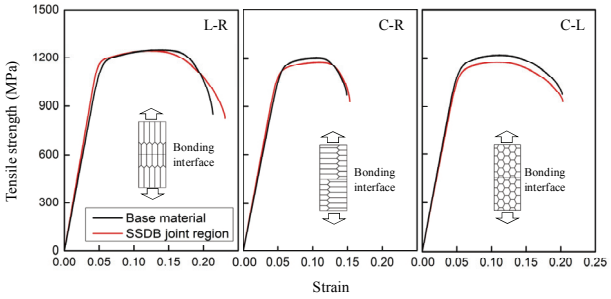

Fig. 5 Stress-strain curves of base material and SSDB joints with each orientation relationship tensile tested at room temperature

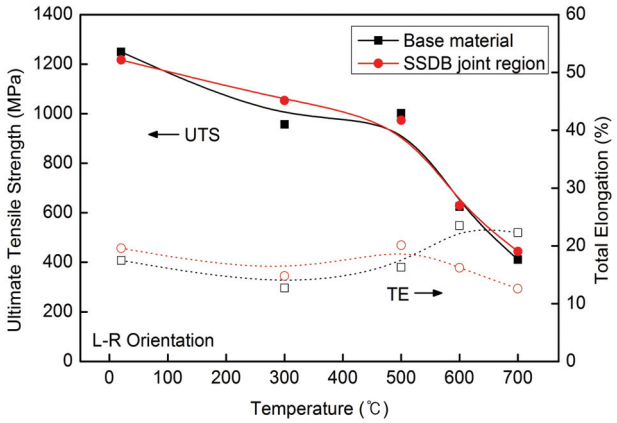

Fig. 6 Tensile test results of base material and SSDB joint region with L-R orientation relationship at elevated temperatures.

as 22%. SSDB joint also shows same behavior of TE in the temperature range from room temperature to 500 ºC. Above 600 ºC, however, it is shown that the TE of SSDB joint region is a little lower than that of base material, and it is slightly decreased as increasing the temperature to 700 ºC. In this, all SSDB joint regions tested under 500 ºC were fractured in the base material with necking behavior at a hundred μm far from the bonding interface. At 700 ºC, on the other hand, the failure was occurred at the bonding interface with an exfoliation fracture surface. Since its sufficient TE reached to 13% with the comparable elevated temperature strength, this fact suggests that grain boundary sliding at elevated temperature is partially occurred when it is compared with TE of base material.

Tensile test results obtained at elevated temperatures revealed that SSDB joints have an satisfactory and comparable joint strength not to fracture at bonding interface. Although good bonding interface with free of defects, the TE above 600 ºC becomes less than base material.

2) Impact properties

The Charpy V-notched impact test results of base material and SSDB joints are shown in Fig. 7. It is estimated that upper shelf energy (USE) of base material is about 0.7J, and DBTT is 250K in C-L bonding orientation relationships. Despite the data scatter, the USE of SSDB joint region with C-L orientation relationship is estimated to be about 0.6J, which is 15% lower than that of base material, as seen in Fig.7(a). The DBTT is also slightly shifted to 270K. On the contrary, SSDB joint region with L-R orientation relationship shows high USE of about 0.9J which is completely reserved for base material in L-R, while DBTT shift is occurred from 225K to 265K, as seen in Fig. 7(b).

Macro fracture appearance of the Charpy impact test specimens in L-R orientation relationship indicates that in lower shelf energy (LSE) range, both the base material and SSDB joint region exhibited delaminated cracking propagation, where the cracks branched parallel to the longitudinal direction of the impact test specimen. This delaminated cracking is well observed in high-strength low alloy bcc steel which has ultrafine elongated ferritic grain structure with a strong <110> deformation texture that was parallel to RD (RD, rolling direction//<110>) [10]. Because this 15Cr ODS ferritic steel also have <110>strong deformation texture in parallel with extrusion direction (ED//<110>)[11], base material and SSDB joint shows the same behavior.

An interesting thing, although SSDB joint specimen has a bonding interface that be aligned parallel to impact striking direction at the center of V-notch tip, cracks were not propagated along the bonding interface and this means bonding interface induced by SSDB is much stronger and tougher than fiber grain structure. Typical blunted crack propagation is shown in the USE region in both materials. Hence, in the macro fracture observation after impact test, there is no significant difference.

Fracture surfaces observations revealed that at 173K, typical cleavages are clearly seen in both materials. However, some delaminated cracking patterns are observed in SSDB joint region as mentioned in macro fracture appearance. At 353K, typical ductile fracture

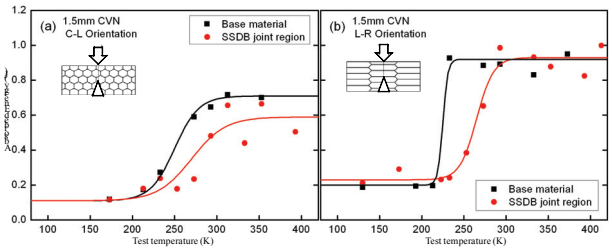

Fig. 7 Ductile-brittle transition curves of base material and SSDB joint with (a) C-L and (b) L-R orientation.

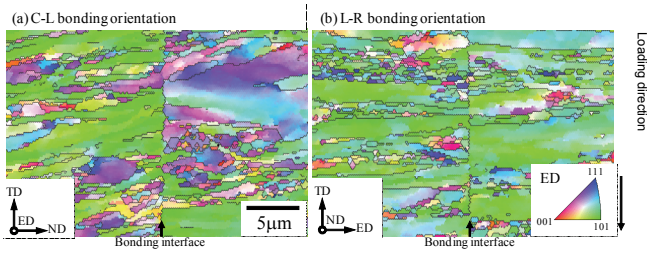

Fig. 8 IPF maps of SSDB joint region with (a) C-L and (b) L-R bonding orientation relationships taken by EBSD analysis

surface with many dimples were shown in both base material and SSDB joint. These fracture behavior means that SSDB is very effective way to have similar impact properties with sufficient bonding strength.

Meanwhile, in spite of same impact behavior of base materials with two different orientations, significantly different anisotropic behavior of impact property in both USE and ΔDBTT on SSDB joint regions was clearly seen in accordance to different bonding orientation relationships, C-L and L-R. The anisotropic behavior in SSDB joint region is considered to be due to grain misorientation at bonding interface. Inverse pole figure (IPF) maps, which were taken by electron backscattering diffraction pattern (EBSD) analyzer, are shown in Fig. 8. Each colors of the grains and black lines between the grains correspond respectively to grain orientation and high angle grain boundaries (HAGB) with misorientation above 15º. It is observed that bonding interface of C-L orientation relationship consists with the contacts of many different grain orientations each other. Contrary to this, however, bonding interface of L-R orientation relationship is partially discontinued and adjoining grains in the interface have same grain orientation each other with almost green as [101] orientation. Since deformation texture of hot extruded ODS ferritic steel has a strong <110> texture parallel to extruded direction axis[12], it seems that L-R bonding orientation relationship is more preferable to diffuse the atoms than bonding with the other orientations.

Consequently, the Charpy impact test revealed that SSDB joint with L-R orientation relationship is very promising way to reserve the absorbed energy of base material for the preferable crystallographic texture.

IV. CONCLUSIONS

High Cr ODS ferritic steels were bonded by solid-state diffusion bonding in high vacuum under uni-axial hydrostatic pressure at 1200 ºC for 1h. The high Cr ODS ferritic steel was successfully bonded by SSDB technique without microstructual degradation. It was practicable to have free of defects at the bonding interface with a reservation of either fine grain size and nano-oxide particle distribution in the base material by optimum bonding condition at 1200 ºC for 1h under 25MPa. SSDB joints showed nearly the same anisotropic tensile behavior with base material at room temperature not to fracture at bonding interface because optimized microstructures in joint region. At elevated temperatures, tensile strength of SSDB joint is equal to that of base material and the elongation is also fairly good. Although a little DBTT shift was occurred, upper shelf energy was reserved in SSDB joint with L-R orientation relationship.

In conclusion, SSDB is an adequate joining method of ODS steels which are strengthened by dispersion of nano-scaled oxide particles without coarsening of the particles. The next step to practical construction of blanket is to develop bonding technology of dissimilar joint of ODS steel with reduced activation ferritic steel.

ACKNOWLEDGMENTS

Authors are grateful for the financial support from the U.S. D.O.E., Grant No. DE-FG03-86ER52123, and the Japanese Ministry of Education, Culture, Sports, Science and Technology via JUPITER-II collaboration.

REFERENCES

[1] R. Lindau, A. Möslang, M. Rieth, et al., Fusion Eng. Design 75-79 (2005) 989-996
[2] S. Ukai, T. Kaito, M. Seki, A. A. Mayorshin, O. V. Shishalov, J. Nucl. Sci. Technol. 42 (2005) 109–122
[3] K. Furuya, E. Wakai, M. Ando, T. Sawai, A. Iwabuchi, K. Nakamura, H. Takeuchi, Fusion Eng. Design 69 (2003) 385-389
[4] C. Li, Q. Huang, Q. Wu, S. Liu, Y. Lei, T. Muroga, T. Nagasaka, J. Zhang, J. Li, Fusion Eng. Design 84 (2009) 1184-1187
[5] F. Adcock, J Iron Steel Inst. 124 (1931) 99-139
[6] Y. Kohno, A. Kohyama, M. L. Hamilton, T. Hirose, Y. Katoh, F. A. Garner, J. Nucl. Mater. 283-287 (2000) 1014-1017
[7] R. F. SINGER, E. ARZT, Proc. of High Temperature Alloys for Gas Turbines and Other Applications, p. 97, D. Reidel, Dordrecht, Holland (1986)
[8] R. Kasada, N. Toda, K. Yutani, H.S. Cho, H. Kishimoto, A. Kimura, J. Nucl. Mater., 367-370, 222-228 (2007)
[9] M.K. Miller, D.T. Hoelzer, E.A. Kenik, K.F. Russell, Intermetallics, 13, 387-392 (2005)
[10] Y. Kimura, T. Inoue, F. Yin, K. Tsuzaki, Science 320 (2008) 1057-1060
[11] H. Okuda, S. Ukai, M. Inoue, J. Nucl. Sci. Technol., 33, 936-943 (1996)
[12] S. Ukai, T. Okuda, M. Fujiwara, T. Kobayashi, S. Mizuta, H. Nakashima, J. Nucl. Sci. Technol. 39, 872-879 (2002)

Task2-2(5) Effect of hydrogen and helium on swelling in electron-irradiated pure iron

N. Hashimoto[1], T. Kimura[1], T. Muroga[2], A. Kimura[3], M.A. Sokolov[4] and T. Yamamoto[5]

[1] *Hokkaido University, Sapporo, Hokkaido, Japan*
[2] *National Institute for Fusion Science, Toki, Gifu, Japan*
[3] *Kyoto University, Uji, Kyoto, Japan*
[4] *Oak Ridge National Laboratory, Oak Ridge, Tennessee, USA*
[5] *University of California Santa Barbara, Santa Barbara, CA, USA*

Ion irradiation of Fe^{3+} and H^+ at 400°C for pure iron resulted in the formation of relatively large voids in matrix. While, voids observed in both base metal (BM) and a heat affected zone (HAZ) of EB-welded F82H indicated smaller than that in pure iron. This behavior of void formation seemed a similar tendency to that of dislocation loop formation. The ion-irradiated F82H indicated the formation of smaller voids with higher number density compared to that in pure iron. In addition, voids observed in the HAZ appeared to be smaller and the number density was higher than that in the BM of F82H. The synergistic effects of hydrogen and helium on swelling for pure iron under electron irradiation have been investigated. The dual beam irradiation of H^+ and electron was performed at 623 K to 5 dpa after He^+ pre-injection of 100 appm at room temperature. In the pure iron pre-doped with 100 appmHe, the electron irradiation exhibited the formation of cavities with high number density. In addition, the presence of H^+ enhanced swelling about 30% at a maximum. Dislocation densities were increasing with increasing H^+ concentration at the same dose. From those results, it is suggested that the existence of H^+ would lead to the reduction of dislocation bias.

I. INTRODUCTION

In order to clarify the effect of transmuted helium and hydrogen on cavity formation, ion and/or electron irradiation experiments were carried out for pure iron, Fe-based alloy, and one of reduced activation ferritic/martensitic steels: F82H, including EB-welded F82H. Ion irradiation and in-situ electron irradiation experiments were carried out using the TIARA facility of JAEA and the multi-beam high voltage electron microscope (HVEM) of Hokkaido University. It is well-known that helium has a strong interaction with vacancy [1]. It has been confirmed the enhancement of the cavity nucleation in F82H when helium exists in matrix [2]. Thus, helium has been considered as an important factor for swelling. The synergistic effects of H^+ and He^+ for swelling was reported in the Fe-9Cr and Fe-12Cr alloys irradiated to 50 dpa at 783 K [3], which indicated that swelling was increasing by the effect of H^+ when H^+ and He^+ coexist. Experiments in this study were expected to provide information on behavior of transmuted gas atom on secondary defect formation and growth, especially void (cavity) in Reduced Activation Ferritic/Martensitic (RAFM) steels. This study aimed to investigate the mechanism of the synergistic effects of hydrogen and helium for swelling, especially the effects of H^+ for growth of cavities, nucleation of cavities and dislocation bias when H^+ and He^+ coexist.

II. EXPERIMENTAL

Materials used in this study were pure iron and EB-welded F82H (Base Metal and Heat Affected Zone). The chemical compositions of the pure iron are given in Table 1. the pure iron was rolled and punched out to 3mm disks, followed by annealing at 873 K for 30 minutes, followed by mechanically and electrochemically polished for transmission electron microscopy (TEM). The ion irradiation experiments using TIARA were carried out at 673K up to 10 dpa with 10.5MeV-Fe^{3+} and 380keV-H^+, followed by TEM observation for cross section of the irradiated specimens fabricated using a Focused Ion Beam (FIB) facility. In-situ electron irradiation experiments for ion-pre-injected specimens were carried out at 673K up to 10 dpa using a HVEM at 1.25 MeV. The total amount of pre-injected helium and hydrogen were 1000 appm and 2000 appm, respectively. The accelerating voltages of He^+ pre-injection were 30, 70 and 100 keV to implant He^+ over the depth range from 0 to 400 nm in the specimen. The accelerating voltages of H^+ and electron beams were 100 and 1250 keV, respectively. The temperature of He^+ pre-injection and dual beam irradiation were RT and 623 K. The helium concentration was 100 appm. The injection rate of H^+ was 20 and 100 appm/dpa. The damage rate of electron irradiation was 0.5×10^{-3} dpa/s.

Table 1 The chemical compositions of pure iron used in this study (wt%).

C	Pb	S	Si	Mn	Cu	As	Sn	Bi	Ni	O
6	1	1	<5	1	2	1	1	1	5	20
H	Al	Bi	Cd	Co	Cr	Ni	Pb	Sb	Zn	
1	1	1	1	1	1	1	1	1	1	

III.RESULTS AND DISCUSSIONS

III.A. The effect of hydrogen on microsturucture in EB-welded F82H and pure iron

Figure 1 shows a typical microstructure in EB-welded F82H (BM and HAZ) and pure iron after Fe^{3+} irradiation with 1000appmH^+ at 673K to 10 dpa. Dual beam irradiation of Fe^{3+} and H^+ at 673K up to 10dpa for pure iron resulted in the formation of voids with 40-50 nm in size in matrix. While, voids observed in both base metal (BM) and a heat affected zone (HAZ) of EB-welded F82H irradiated in the same condition as pure iron indicated several nanometer in size.

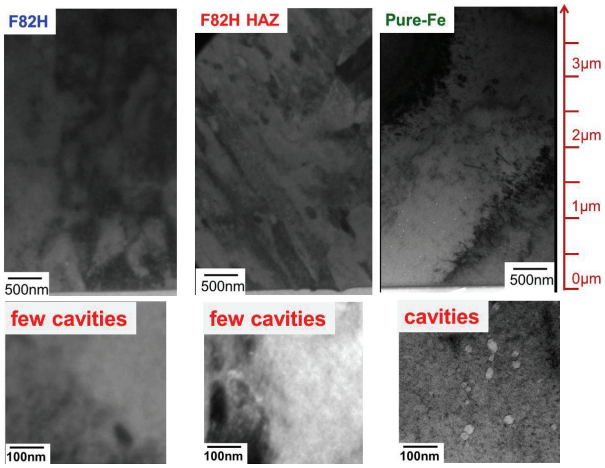

Fig. 1 Distribution of void in EB-welded F82H (BM and HAZ) and pure iron after Fe^{3+} irradiation with 1000appmH^+ at 673K to 10 dpa.

This behavior of void formation in this irradiation condition seemed similar to that of dislocation loop formation. Figure 2 shows a typical image of dislocation loops in EB-welded F82H (BM and HAZ) and pure iron after Fe^{3+} irradiation with 1000appmH^+ at 673K to 10 dpa. The ion-irradiated F82H indicated the formation of smaller voids with higher number density compared to that in pure iron. In addition, voids observed in the HAZ appeared to be smaller and the number density was higher than that in the BM of F82H.

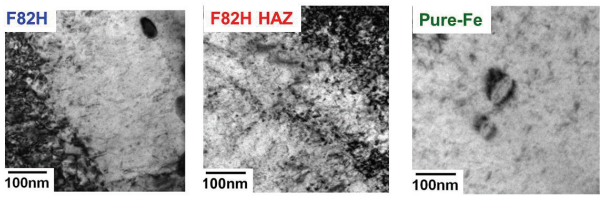

Fig. 2 Dislocation loops in EB-welded F82H (BM and HAZ) and pure iron after Fe^{3+} irradiation with 1000appmH^+ at 673K to 10 dpa.

Figure 3 indicates comparison of volume fraction of carbide (mainly $M_{23}C_6$) between EB-welded F82H BM and HAZ. Considering volume fraction of carbide in BM and HAZ, HAZ seemed to include much more carbon in matrix compared with BM. From this result, it is suggested that the difference of secondary defects formation between BM and HAZ in EB-welded F82H seemed to be affected by carbon concentration in matrix.

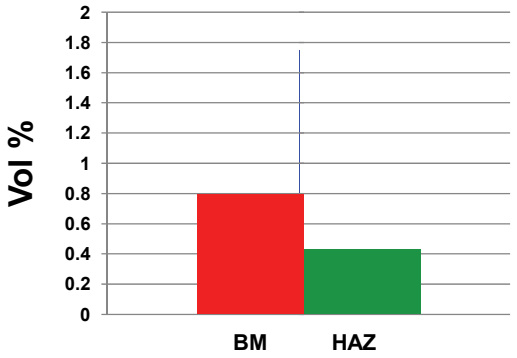

Fig. 3 Comparison of volume fraction of carbide (mainly $M_{23}C_6$) between EB-welded F82H BM and HAZ.

III.B. The effect of hydrogen on nucleation of cavities when helium and hydrogen coexist Tensile Properties

Void formation in pure iron during in-situ experiments was summarized in Table2. Electron beam irradiation to pure iron resulted in none of void formation, while, the pre-injection of He^+ (1000appm) indicated formation of voids (average diameter: 2.3nm, number density: $2.2x10^{21}$ m^{-3}) in pure iron during electron irradiation. Furthermore, in the case of pre-injection of He^+ (1000appm) and H^+ (2000appm), a much higher number density of voids were observed as shown in Fig. 4, indicating the synergetic effect of helium and hydrogen on void formation.

Table 2 Summary of void formation after electron irradiation for ion-pre-injected pure iron.

	Pure iron	1000appmHe	2000appmH+1000He
Average Diameter (nm)	0	2.3	2.4
Number Density (m^{-3})	0	2.2×10^{21}	1.3×10^{22}
Swelling (%)	0	2.3×10^{-3}	1.7×10^{-2}

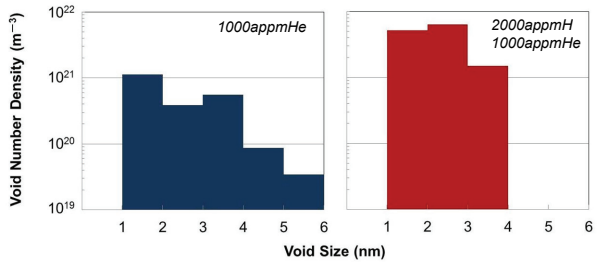

Fig. 4 Size distribution of void formed in He and/or H-doped pure iron after electron irradiation at 673K to 10 dpa.

Figures 5 and 6 show cavity formation in the He^+ pre-injected pure iron irradiated by electron beam up to 5 dpa and the cavity number density as a function of hydrogen injection rate in pure iron, respectively. It exhibited little change of cavity number density up to 5 dpa, meaning that hydrogen effect on cavity formation might be very small. This is in good agreement with the result of F82H irradiated to 50 dpa at temperatures between 743 and 873 K by Wakai et al.[4].

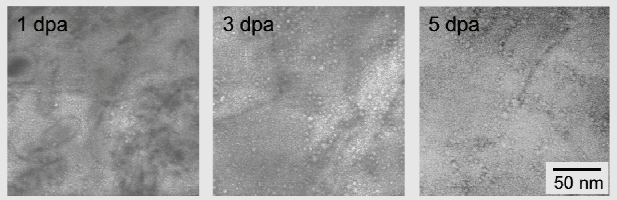

Fig. 5 Cavity formation in the He^+ pre-injected pure iron irradiated by electron beam up to 1, 3 and 5 dpa.

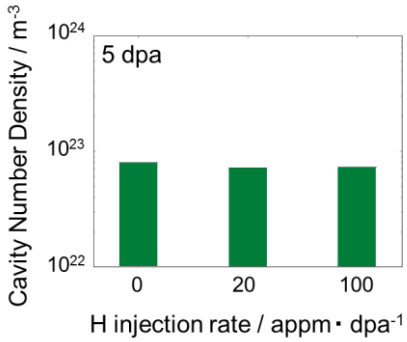

Fig. 6 Cavity number density as a function of hydrogen injection rate in pure iron at a dose of 5 dpa.

III.C. The effect of hydrogen on growth of cavities when helium and hydrogen coexist

Figure 7 shows the dose dependence of cavity size in He-pre-injected pure iron irradiated by electron and hydrogen with the injection rate of 0, 20 and 100 appmH/dpa. The cavity size increased with increasing dose, however no relationship with the injection rates was observed. Figure 8 shows cavity size distributions of each irradiation condition. The distribution peak shifted from 1-2 nm to 2-3 nm with increasing dose from 1 dpa to 5 dpa in all the irradiation conditions. In particular, bimodal distribution: 1-5 nm (Peak 1) and 6-9 nm (Peak 2), was observed at 5 dpa in the H^+ irradiated samples, meaning that H^+ would enhance growth of cavities.

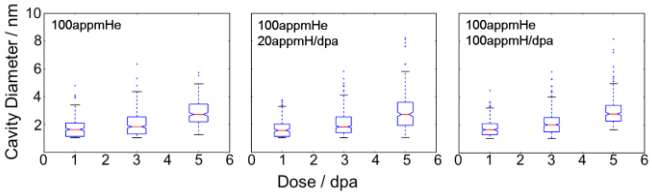

Fig. 7 Dose dependence of cavity size in He pre-injected pure iron irradiated at an indicated conditions

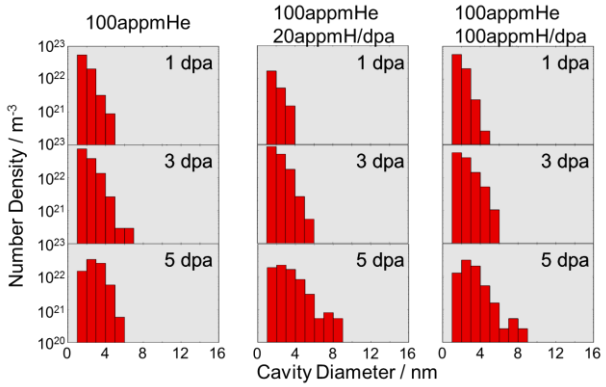

Fig. 8 Cavity size distributions in pure iron irradiated at several conditions at 1, 3 and 5 dpa

Figure 9 shows the comparison of swelling at 5 dpa in each irradiation condition. The swelling in H^+ irradiated samples was larger than that without hydrogen. The increment of swelling was mainly derived from the cavities in Peak 2. However, as explained above, difference in average cavity size between with and without H^+ was very small. It means that H^+ might affect only growth of some cavities appeared as Peak 2.

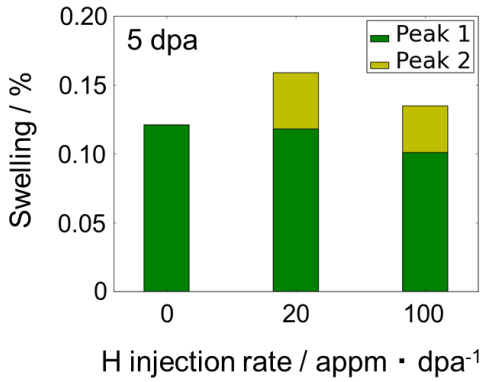

Fig. 9 Swelling of pure Fe irradiated at 5 dpa with various H injection rate

III.D. The effect of hydrogen on dislocation bias when helium and hydrogen coexist

Figure 10 shows the residual dislocation structure experimentally observed after irradiation up to 5 dpa. Dislocation densities were increasing with increasing H concentration. Dislocation densities in single electron beam irradiation were lower than that in dual beam irradiation with electrons/H^+ at 5 dpa. It seems that dislocation bias would be small due to H^+. In addition, H^+ effect on dislocation bias seemed to be depending on H^+ concentration. From the view point of H^+ effect on dislocation bias, it is suggested that H^+ would suppress the swelling. Figure 11 shows dose dependence of swelling at each irradiation condition. Swelling increased with increasing dose in all the hydrogen concentration, meaning that there seemed no hydrogen concentration dependence on swelling rate. On the other hand, the electron irradiation at 20 appmH/dpa resulted in the highest swelling. It indicates that there might be a peak of swelling value as a function of H^+ concentration. As described in section 3-1 and 3-2, H^+ would not affect the cavity nucleation but cavity growth.

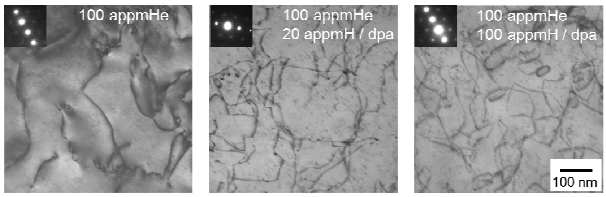

Fig. 10 Dislocation structures in pure iron irradiated at several conditions at 5dpa.

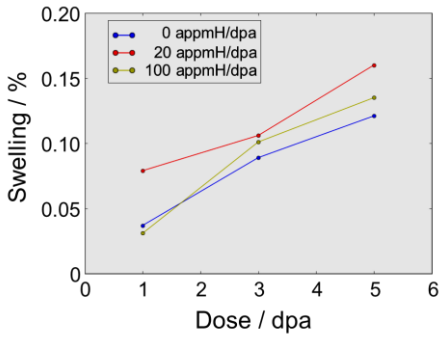

Fig. 11 Dose dependence of swelling at 0, 20, and 100 appmH/dpa.

IV. CONCLUSIONS

The hydrogen effect on void formation in F82H would be small compared with pure iron, while, the existence of hydrogen with helium seemed to enhance void formation (synergetic effect). In addition, the carbon in matrix appeared to control the formation of the secondary defects, such as void and dislocation loop.
The hydrogen effect on cavity formation in pure iron could be summarized that H^+ would enhance the growth but not the nucleation of cavities hence electron/H^+ irradiation exhibited the bimodal distribution of cavities without any increment of its densities. The increasing of dislocation density with increasing H^+ concentration would be due to smaller dislocation bias by H^+. There might be a peak of swelling value at a proper H^+ concentration, which leads to the highest flow of H^+ into cavities.

ACKNOWLEDGMENTS

We are grateful to Dr. T. Shibayama of Hokkaido University and H. Kinoshita of the Fukushima National Collage of Technology for operation of HVEM. This work was sponsored by Japan-US.

REFERENCES

[1] F. Gao, Huiqiu Deng, H.L. Heinisch, R.J. Kurtz, J. Nucl. Mater. **418** (2011) 115–120.
[2] E. Wakai, N. Hashimoto, Y. Miwa, J.P. Robertson, R.L. Klueh, K. Shiba, S. Jistukawa, J. Nucl. Mater. **283-287** (2000) 799-805.
[3] T. Tanaka, K. Oka, S. Ohnuki, S. Yamashita, T. Suda, S. Watanabe, E. Wakai J. Nucl. Mater. **329-333** (2004) 294-298.
[4] E. Wakai, K. Kikuchi, S. Yamamoto, T. Aruga, M. Ando, H. Tanigawa, T. Taguchi, T. Sawai, K. Oka, S. Ohnuki, J. Nucl. Mater. **318** (2003) 267–273.

4-6 Task2-3(1) Study on Stress Relaxation Behavior of Silicon Carbide by BSR Method

Kazuma Abe [1], Shuhei Nogami [1], Akira Hasegawa [1], Takashi Nozawa [2], Tatsuya Hinoki [3]

[1] Department of Quantum Science and Energy Engineering, Tohoku University
[2] Japan Atomic Energy Agency
[3] Institute of Advanced Energy, Kyoto University

Bend stress relaxation (BSR) experiments were performed on the two types of highly crystallized monolithic silicon carbide (SiC) produced by chemically vapor deposition (CVD) and liquid phase sintering (LPS) methods at the temperature of 600–1400°C for 1–100 hours. Small reduction of the BSR ratio with the time was observed in the relatively low temperature tests. While, the BSR ratio dropped rapidly during the first hour of the test and decreased gradually after that in the high temperature tests above 1200°C. Almost no difference of the time dependence was observed between those two materials. Small reduction of the BSR ratio was observed at the temperature from 600 to 1000°C. The BSR ratio of those two materials dropped steeply at the temperature from 1200 to 1400°C. The BSR ratio of the LPS–SiC was much smaller than that of the CVD–SiC at the temperature from 1200 to 1400°C.

1. Introduction

Silicon carbide (SiC) fiber reinforced SiC matrix (SiC/SiC) composite is one of the candidate structural materials for fusion reactor blanket because of its high temperature strength and low radioactivation [1]. The major load applied to the SiC/SiC composite as a blanket structural material in fusion environment is considered to be thermal stress induced by fusion plasma, therefore stress relaxation by thermally activated creep might occur under the deformation–controlled stress. Thus, the objective of this study is to investigate the stress relaxation behavior of monolithic SiC materials in order to clarify the fundamental deformation behavior under the practical temperature conditions of fusion blanket using SiC/SiC composites.

SiC/SiC composites fabricated by the chemical vapor infiltration (CVI) and the nano–infiltration transient–eutectic phase (NITE) are promising for the fusion reactor blanket because of their stoichiometric and highly crystallized SiC matrices [2]. Therefore, the chemically vapor deposited (CVD) SiC and the liquid phase sintered (LPS) SiC were examined in this study, which were equivalent to the matrices of the CVI–SiC/SiC and the NITE–SiC/SiC composites. Bend stress relaxation (BSR) method, which has been originally developed for the evaluation of creep properties of ceramic fibers, was employed in this study in order to investigate the stress relaxation behavior under the deformation–controlled stress [3-7].

2. Experimental

The CVD–SiC fabricated by Rohm and Haas and the LPS–SiC provided by the BA (Broad Approach) activity were employed for the BSR experiment. Purity and grain size of the CVD–SiC was >99.9995% and about 5 μm, respectively [8]. The LPS–SiC was sintered with the SiC nano powder and alumina and yittria particles as process additives. The grain size of the LPS-SiC was about 0.5–1 μm. The dimension of specimens was 40 mm x 1.2 mm x 50 μm. All the specimens of the CVD–SiC were machined with the longitudinal directions perpendicular to the CVD growth direction. Figure 1 shows a schematic illustration of the specimen and the fixture. The thin strip specimen was fixed within a narrow gap about 0.4 mm between curved surfaces of the pair loading plates. All the fixture parts were made of the CVD–SiC to avoid chemical reactions with the specimens. The bend radius and applied initial surface strains of the constrained specimens were 156 mm and 0.015%, respectively.

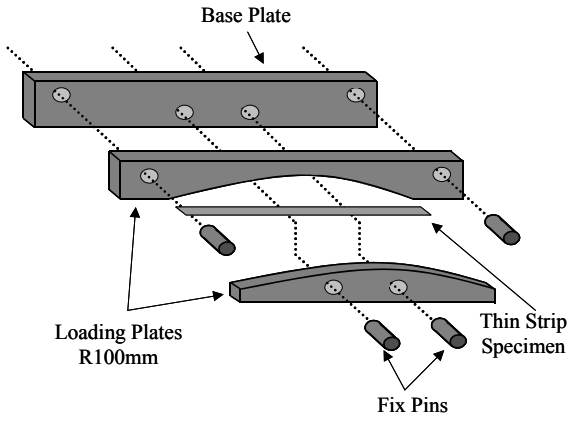

Fig. 1 Schematic illustration of specimen and fixture of BSR experiment.

The degree of the stress relaxation was evaluated by the BSR ratio (m) defined by the following equation [3,4].

$$m = 1 - R_0/R_a = 1 - \Phi_a/\Phi_0 \quad (1)$$

where Φ_o and Φ_a are the initial and final bend angle, and R_o and R_a are the initial and final curvature of the specimen as shown in Figure 2, respectively. The BSR ratio of 0 and 1 indicates full relaxation and no–relaxation, respectively. The BSR ratio in this study was decided by measuring the bend angles (Φ_o and Φ_a) using an optical microscope. The accuracy of the bend angle measurement was less than 0.3°. This gives a potential scatter less than 0.02 in the BSR ratio. The BSR experiments were carried out in high purity argon flow. The test temperature and time were from 600 to 1400°C and 1, 10 and 100 hours, respectively.

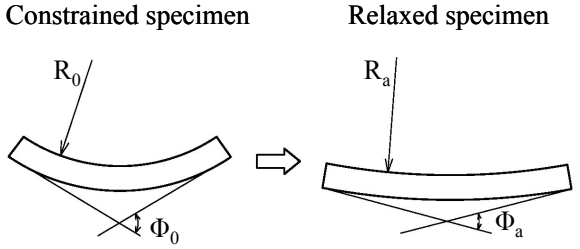

Fig. 2 The measurement of the bend radius of the constrained and relaxed specimens.

3. Results and Discussion

Figure 3 plots the BSR ratio, m, against the test time. The BSR ratio generally decreased with increasing the test temperature and the test time. Small reduction of the BSR ratio with the test time was observed in the relatively low temperature tests. While, the BSR ratio dropped rapidly during the first hour of the test and decreased gradually after that in the high temperature tests above about 1200°C. The observed stress relaxation behavior was similar to the result of the previous study on the polycrystal and single–crystal CVD–SiC [4]. This tendency was considered to be due to the primary creep, since the CVD–SiC is known to exhibit only primary creep at the temperature from 1100 to 1400°C [5]. Almost no difference of the test time dependence was observed between those two materials.

Figure 4 plots the BSR ratio against the reciprocal temperature. Small reduction of the BSR ratio was observed at the temperature from 600 to 1000°C. The BSR ratio of the CVD–SiC was almost the same as or a little smaller than that of the LPS–SiC at those temperature ranges. In contrast, the BSR ratio of those two materials dropped steeply at the temperature from 1200 to 1400°C. The BSR ratio of the LPS–SiC was much smaller than that of the CVD–SiC at those temperature ranges. From these results, those two materials have good creep resistance at the practical temperature (about 600–1000 °C) of fusion blanket using SiC/SiC composites [1].

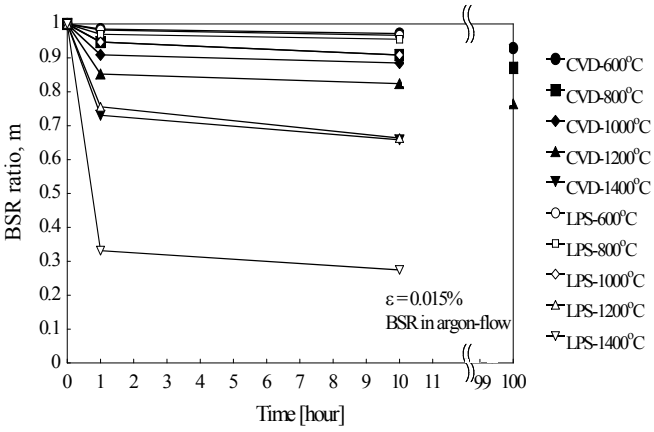

Fig. 3 Time dependency of the BSR ratio (m) in the CVD–SiC and LPS–SiC.

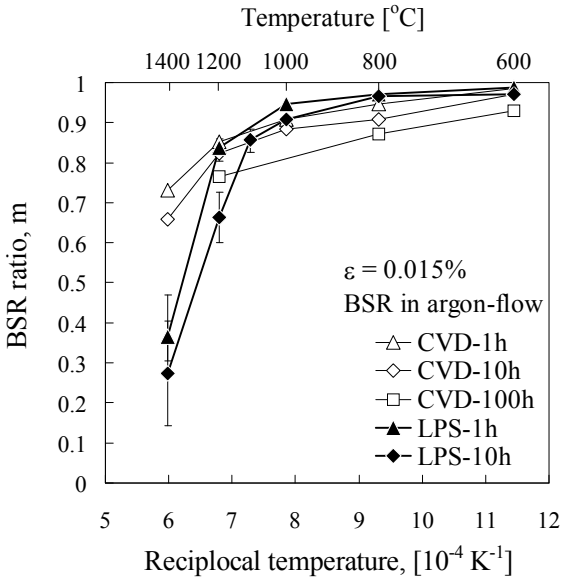

Fig. 4 The BSR ratio (m) of the CVD–SiC and LPS–SiC plotted against the reciprocal temperature.

Since the stress relaxation in this study might occur by the thermally activated process, the rate–controlling activation energy, Q, could be determined from the Δ(1/T) spacing between the curves at a constant BSR ratio in

Figure 4(cross–cut method)[3]. For one order of magnitude change in time, activation energy can be determined as below equation.

$$Q = 2.3R/\Delta(1/T) \quad (2)$$

where R is the gas constant (8.314 J/(mol·K)). Figure 5 shows the calculated activation energy at each range of the temperature from the space between 1 and 10 hours curves of Figure 4. The activation energy tended to increase with the test temperature. The activation energies ranged from 708 to 915 kJ/mol at the high temperature region from about 1200 to 1400°C. This is acceptable agreement with the calculated activation energy of the carbon self-diffusion (713–840 kJ/mol) and silicon the self-diffusion (695–910 kJ/mol) in β–SiC [9,10]. Therefore, it can be concluded that the main mechanism responsible for the stress relaxation of the CVD–SiC and the LPS–SiC at those temperature ranges was controlled by the grain boundary sliding (GBS) by the diffusion [3]. From these discussions, one of the reasons why the BSR ratio of the LPS–SiC was much smaller than that of the CVD–SiC at the temperature from 1200 to 1400°C was considered to be the grain size difference and the process additives in the LPS–SiC. The mechanisms of stress relaxation at the temperature below 1200°C were not clarified in this study. Those mechanisms will be studied in future work.

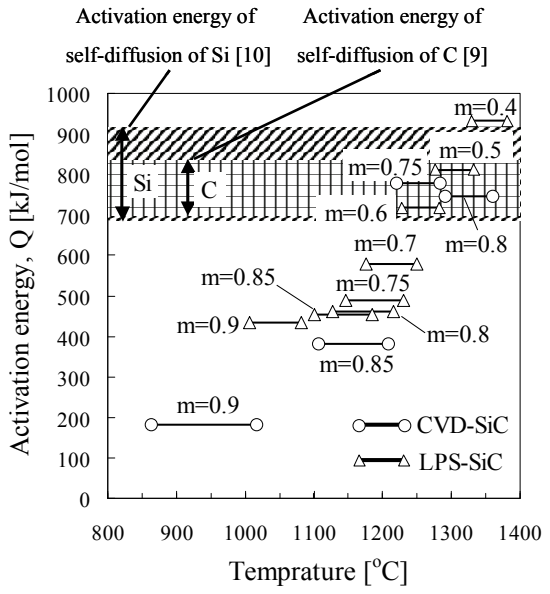

Fig. 5 The calculated activation energy of the stress relaxation at the each temperature region in the CVD–SiC and LPS–SiC.

4. Conclusions

The BSR experiments were performed on the two different types of highly crystallized monolithic SiC (CVD–SiC and LPS–SiC) at the temperature from 600 to 1400°C for 1, 10 and 100 hours in high purity argon flow in order to evaluate the stress relaxation behavior under the deformation–controlled stress at the practical operation temperatures of fusion blanket using SiC/SiC composites. The following results were obtained.

(1) Small reduction of the BSR ratio with the test time was observed in the relatively low temperature tests. While, the BSR ratio dropped rapidly during the first hour of the test and decreased gradually after that in the high temperature tests above about 1200°C. Almost no difference of the test time dependence was observed between the CVD–SiC and the LPS–SiC.

(2) Small reduction of the BSR ratio was observed at the temperature from 600 to 1000°C, which means the CVD–SiC and the LPS–SiC have good creep resistance at the practical temperature of fusion blanket using SiC/SiC composites. On the other hand, the BSR ratio of those two materials dropped steeply at the temperature from 1200 to 1400°C. The BSR ratio of the LPS–SiC was much smaller than that of the CVD–SiC at those temperature ranges.

(3) The activation energies of the CVD–SiC and the LPS–SiC calculated by cross cut method at the temperature from 1200 to 1400°C acceptably corresponded to the activation energy of self–diffusion of the silicon and the carbon in β–SiC, suggesting that the GBS controls the stress relaxation mechanism.

Acknowledgement

This work was mainly supported by the R&D on SiC/SiC composites for the DEMO R&D for the IFERC (International Fusion Energy Research Centre) project in BA (Broader Approach) activity. Authors are grateful to all the member of the TITAN (Tritium, Irradiation and Thermofluid for America and Nippon) task-II for their comments and discussion about the BSR experiments in this study.

References

[1] Y. Katoh, L.L. Snead, C.H. Henager Jr, A. Hasegawa, A. Kohyama, B. Riccardi, H. Hegeman, J. Nucl. Mater. 367–370 (2007) 659–671.

[2] K. Shimoda, T. Hinoki, Y. Katoh, A. Kohyama, J. Nucl. Mater. 384 (2009) 103–108.

[3] G.N. Morscher and J.A. Dicarlo, J. Am. Ceram. Soc. 75 (1992) 136–140.

[4] Y. Katoh and L.L. Snead, Fusion Reactor Materials Semannual Progress Report. DOE/ER–0313/35 (2005) 13–18.

[5] G.N. Morscher, C.A. Lewinsohn, C.E. Bakis, R.E. Tressler, T. Wagner, J. Am Ceram. Soc. 78 (1995) 3244–3252.

[6] J.J. Sha, J.S. Park, T. Hinoki, A. Kohyama, Mech. Mater. 39 (2007) 175–182.
[7] G.E. Youngblood, R.H. Jones, G.N. Morscher, A. Kohyama, Fusion Reactor Materials Semannual Progress Report. DOE/ER-0313/22 (1997) 81–86.
[8] Rohm and Haas HP, http://www.rohmhaas.com/
[9] J.D. Hon and M.H. Davis, J. Am. Ceram. Soc. 63 (1980) 546–552.
[10] J.D. Hong, R.F. Davis and D.E. Newbury, J. Mater. Sci. 16 (1981) 2485–2494.

Task2-3(2) IRRADIATION CREEP OF NANO-POWDER SINTERED SILICON CARBIDE AT LOW NEUTRON FLUENCES

T. Koyanagi[1,2*], K. Shimoda[1], S. Kondo[1], T. Hinoki[1], K. Ozawa[2], Y. Katoh[2]

[1]*Institute of Advanced Energy, Kyoto University, Gokasho, Uji, Kyoto 611-0011, Japan, koyanagit@ornl.gov, hinoki@iae.kyoto-u.ac.jp, k-simd@iae.kyoto-u.ac.jp*
[2]*Materials Science and Technology Division, Oak Ridge National Laboratory, P.O. Box 2008, Oak Ridge, TN 37831, USA, ozawak@ornl.gov, katohy@ornl.gov*

The irradiation creep behavior of nano-powder sintered silicon carbide was investigated using the bend stress relaxation method under neutron irradiation up to 1.9 dpa. The creep deformation was observed at all temperatures ranging from 380 to 1180 °C mainly from the irradiation creep but with the increasing contributions from the thermal creep at higher temperatures. The apparent stress exponent of the irradiation creep slightly exceeded unity, and instantaneous creep coefficient at 380 to 790 °C was estimated to be ~1 × 10^{-5} [MPa^{-1} dpa^{-1}] at ~0.1 dpa and 1 × 10^{-7} to 1 × 10^{-6} [MPa^{-1} dpa^{-1}] at ~1 dpa. The irradiation creep strain appeared greater than that for the high purity SiC. Microstructural observation and data analysis indicated that the grain-boundary sliding associated with the secondary phases contributes to the irradiation creep at 380–790 °C to 0.01–0.11 dpa.

I. INTRODUCTION

Silicon carbide (SiC) and its composites are considered to be attractive nuclear materials mainly because of their excellent resistance to neutron irradiation at high temperatures[1, 2]. The nano-infiltration and transient eutectic-phase (NITE) method, which is a specific type of liquid phase sintering (LPS) using SiC nano-powder and a reduced amount of sintering additives, is one of the fabrication possesses to obtain radiation-resistant SiC-matrix composites[3, 4]. The NITE SiC-matrix composites are candidates for components in fusion blankets system[5], because these composites show superior hermeticity and resistance to the matrix cracking as compared to the SiC composites through other fabrication routes[6, 7]. The LPS process with SiC nano-powder and additives is also applied for a fabrication of dense monolithic SiC with the microstructure similar to the matrix of the NITE-SiC composite. This nano-powder sintered monolithic SiC is referred to as the NITE-like sintered (NLS) SiC. The NLS SiC is used for applications such as irradiation-tolerant joint between SiC bodies[8, 9]. The NLS SiC is significantly different from the conventional LPS SiC in terms of the sintering process and the resultant microstructures and properties[10].

For nuclear fusion applications, SiC and its composites must withstand both the primary stress from the external loading and the thermal and swelling-induced stresses caused the temperature gradients. The irradiation creep is an important property for these materials not only because it often determines the design limits for temperature, stress loading, and neutron fluence but also it may mitigate the secondary stress issues. The objective of this study is to clarify the irradiation-creep behavior of NLS SiC, representing the matrix phase of the NITE SiC composites at various irradiation temperatures and applied stress levels.

The neutron irradiation creep of SiC materials is studied by the bend stress relaxation (BSR) method[11, 12]. The BSR method is useful for neutron irradiation experiments because it enables the application of stress to miniature specimens under irradiation and it requires only very simple post-irradiation measurement. Katoh et al. evaluated irradiation creep of chemical vapor deposition (CVD) SiC using the BSR method under collaborative TITAN program and reported that a likely mechanism of the transient irradiation creep at 380 to 790 °C is swelling-coupled creep caused by anisotropic evaluation of the multi-dimensional defect clsuters under applied stresses[12]. Kondo et al. studied irradiation creep of CVD SiC using an ion-irradiation technique and also mentioned that anisotropic distribution of self-interstitial atom clusters was suspected to be the governing creep mechanism[13]. Katoh et al. found grain boundary-related irradiation creep of CVD SiC at temperatures higher than 790 °C. Different creep behavior is expected between CVD SiC and NLS SiC at this temperature, because of the different grain boundary microstructures: the CVD SiC has a chemically clean grain-boundaries, whereas the NLS SiC generally contains thin grain-boundary oxide films and the secondary phases at the grain pockets[14].

To understand irradiation creep of materials at high temperature, information on the thermal creep is essential.

Insignificant thermal creep at low temperature (~1000 °C) during 10 h of heat treatment has been demonstrated in NLS SiC by the BSR method[15]. BSR was also used by Shimoda et al. to investigate the thermal creep behavior of two kinds of NLS SiC at 1000–1500 °C[16]. Analysis of the microstructure revealed that the secondary phases attributed to sintering additives at the grain boundaries and grain pockets likely played an important role in the thermal creep mechanism. However, there is currently a dearth of information on the long-term thermal creep behavior of NLS SiC. Therefore, the present study investigates the thermal creep as well as the neutron irradiation creep of NLS SiC.

II. EXPERIMENTAL

Two types of NLS SiC were fabricated as follows. SiC nano-powder (Sumitomo Osaka Cement Co. Ltd., Japan, T-1 grade) was mixed with the following sintering additives to a total amount of 12 or 22.5 wt.% additives: Al_2O_3 (Kojundo Chemical Laboratory Co. Ltd., Japan, mean diameter of 0.3 μm, 99.99% pure), Y_2O_3 (Kojundo Chemical Laboratory Co. Ltd., Japan, mean diameter of 1.0 μm, 99.99% pure), and SiO_2 (Kojundo Chemical Laboratory Co. Ltd., Japan, mean diameter of 1.0 μm, 99.9% pure). The mixtures were sintered by holding at 1850 or 1900 °C, for 1 or 2 h under a pressure of 20 MPa in flowing Ar atmosphere. In this study, these SiC ceramics fabricated with 12 and 22.5 wt% additives are called NITE1 and NITE2, respectively.

Irradiation creep and thermal creep were evaluated by BSR as follows. Specimens were machined into thin strips of 40 mm length × 1 mm width × 0.075–0.15 mm thickness and then polished to a mirror-like finish. The thin strips were attached to a fixture with a curvature radius of 100 or 150 mm to apply flexural stress, and then were irradiated or annealed. The fixture was fabricated from CVD SiC (Rohm and Haas, currently The Dow Chemical Co., USA) to avoid chemical reaction between the thin strips and the fixture. The initial flexural stress was 46 to 376 MPa. Relaxation creep was evaluated using the BSR ratio (m), which is the ratio of final stress (σ_a) to initial stress (σ_o). The BSR ratio can be expressed as Equation 1, where E, ε, and R are the elastic modulus, flexural strain, and curvature radius of the specimen, respectively.

$$m = \frac{\sigma_a}{\sigma_0} = \frac{E_a(\varepsilon_0 - \varepsilon_c)}{E_0\varepsilon_0} = \frac{E_a}{E_0}\left(1 - \frac{R_0}{R_a}\right) \quad (1)$$

The subscripts a, 0, and c stand for the initial state, final state, and creep, respectively. The BSR ratio varies between 0 and 1, where 0 indicates complete relaxation and 1 indicates no relaxation.

In this study, E_a/E_0 = 0.95 was adopted to represent the neutron irradiation experiments, based on the previously determined elastic modulus of NLS SiC following neutron irradiation[4]. The BSR ratio was evaluated by measuring the curvature radius of the specimen. The ratio of final to initial radius was evaluated using the initial and final bend angle at the end of the test strip. The uncertainty in the bend angle measurement was less than 0.1°. This gives a potential scatter of ~0.02 in the BSR ratio. The creep strain was obtained from the BSR ratio and initial flexural strain according to Eq. (1). Further details about the BSR testing procedure can be found elsewhere[17, 18].

Neutron irradiation was conducted at the High-Flux Isotope Reactor (HFIR) at Oak Ridge National Laboratory (Tennessee, USA). The specimens were irradiated at 380–1180 °C to 0.011–1.9 dpa for SiC (0.011–1.9 × 10^{25} n/m^2, E > 0.1 MeV; hereafter, 1.0 × 10^{25} n/m^2 = 1 dpa is assumed). The damage rate was 4.5–6.0 × 10^{-7} dpa/s. Experiments to determine the irradiation creep were conducted in a high-purity helium atmosphere.

The thermal creep experiments were conducted by holding the elastically bent specimens at temperatures 775 and 1180 °C for up to 100 h under a flow of high-purity argon. The time evolution of the BSR ratio was obtained for each sample by an iterative process of annealing and measurement of the bend angle.

The microstructure of the as-received specimens was observed with transmission electron microscope (JEOL-2200FS, 200 kV and Hitachi-H-9000UHR, 300 kV).

III. RESULTS

III.A. MICROSTRUCTURE OF MATERIALS BEFORE IRRADIATION

Figure 1 shows the TEM images of NITE1 and NITE2. Secondary phases comprising mainly Y, Al, and

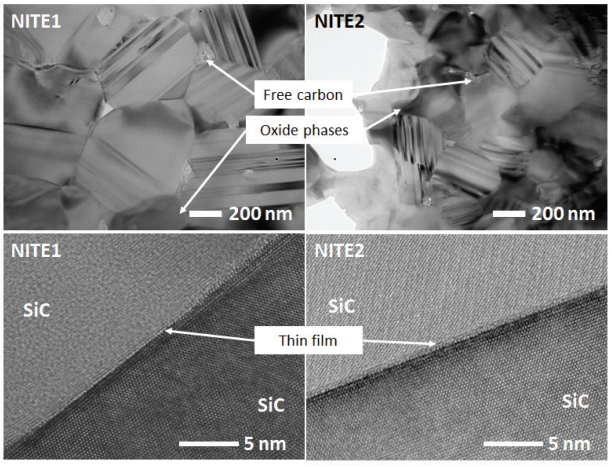

Fig. 1. TEM images for as-received NLS SiC.

O were observed at the grain pockets of both materials. Additionally, free carbon was identified at the grain boundaries and the grain pockets by the energy dispersive X-ray spectroscopy. The average SiC grain size of NITE1 was 414 nm and that of NITE2 was 226 nm, based on the evaluation of more than 100 grains. An amorphous-like film of typically ~1 nm thickness exists at SiC-SiC grain boundaries of both materials.

III.B. STRESS RELAXATION BY THERMAL ANNEALING

TABLE 1 summarizes the results of the thermal creep experiments for NLS SiC. Annealing at 775 °C produces insignificant stress relaxation; a BSR ratio of >0.9 was observed in both NITE1 and NITE2 after 100 h annealing. In contrast, obvious stress relaxation was observed at 1180 °C. After 100 h heat treatment, NITE1 and NITE2 both exhibit a decrease in the BSR ratio to 0.60 and 0.37, respectively. Analysis of the data reveals that the creep strain rate of NITE1 and NITE2 increased in proportion to the average flexural stress applied during annealing at 1180 °C; in other words, the apparent stress exponent (n) of the creep strain was almost unity at 1180 °C.

TABLE 1. Results of thermal creep experiments for NLS SiC. Parentheses indicate standard deviations.

Material	Annealing temperature (°C)	Annealing time (h)	Number of specimens	Initial flexural stress (MPa)	BSR ratio, m	Apparent stress exponent, n
NITE1	775	1	2	142–158	0.992 (0.004)	n.a.[1]
		10			0.982 (0.015)	
		30			0.974 (0.030)	
		100			0.966 (0.033)	
	1180	10	3	92.4–185	0.721 (0.042)	1.1
		30			0.667 (0.038)	0.84
		100			0.601 (0.053)	1.2
NITE2	775	1	1	74.4	0.991	n.a.
		10			0.991	
		30			0.973	
		100			0.944	
	1180	10	3	69.3–208	0.511 (0.075)	1.2
		30			0.458 (0.050)	0.99
		100			0.371 (0.070)	0.75

[1] Not available because of a limited number of specimens.

III.C. STRESS RELAXATION DURING NEUTRON IRRADIATION

Figure 2 shows the BSR ratios of NITE1 and NITE2 as a function of the applied flexural stress at various irradiation conditions. The highest and lowest values of the error bars indicate the initial and final flexural stresses, respectively. Below 790 °C, both materials exhibited obvious stress relaxation during irradiation, yet insignificant relaxation during annealing. The BSR ratios of both materials tended to decrease with higher applied stresses, indicating that the apparent stress exponent was larger than unity. This behavior appeared to be significant at higher neutron fluence. The NITE2 exhibits a smaller average BSR ratio than NITE1at low neutron fluence. Figure 3 shows stress dependence of the irradiation creep strain. The stress value plotted in the figure is an average flexural stress during irradiation. The highest and lowest values of the error bars indicate the initial and final stresses, respectively. The apparent stress exponent of the creep strain was obtained from the slope of the straight line for the each data set in log-log plot. The values of the apparent stress exponent are similar for NITE1 and NITE2, and mostly exceeds 1 in this irradiation conditions. The determination of the stress exponent is more reliable in case of lower neutron fluence because of the small gap between initial and final stress.

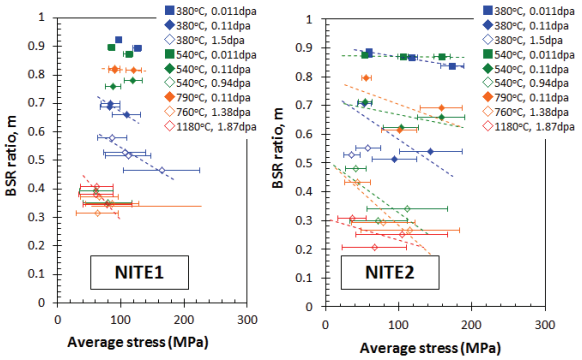

Fig. 2. BSR ratios of NITE1 and NITE2 as a function of the applied flexural stress under various irradiation conditions.

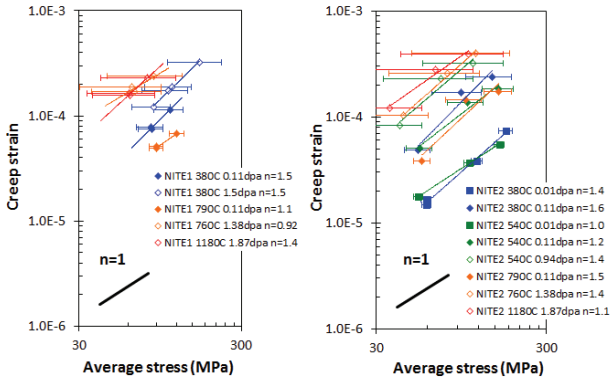

Fig. 3. Plots of creep strain vs. average applied stress of NITE1 and NITE2 specimens at various irradiation conditions. The apparent stress exponent (n), which is shown as the slope of the straight line in the graph, is indicated.

VI. DISCUSSION

VI.A. EFFECT OF THERMAL CREEP ON IRRADIATION CREEP

Figure 4 shows the time-dependent evolutions of the thermal creep strain and the irradiation creep strain, normalized to the average flexural stress at 760–790 and 1180 °C. It is reasonable to normalize the thermal creep strain to the stress, because the stress exponent was close to unity. In contrast, the average stress exponent of the irradiation creep strain was more than one. However, the irradiation creep strain normalized to the stress is used in this study, because the stress exponent of the irradiation creep did not significantly exceed unity. Assuming the stress exponent as unity is useful for a rough comparison of the creep behavior with reference materials showing unity of stress exponent.

The normalized thermal creep strain increased with exposure time, and its relationship to the exposure time can be described by a power law. The trend lines in Fig. 4 indicate the power law fits to the thermal creep data. This fitting appears reasonable for thermal primary-creep of materials[19]. The ratio of normalized thermal-creep strain to irradiation-creep strain was 16% and 10% in NITE1 and NITE2, respectively, at a radiation fluence of 0.11 dpa and a temperature of 760–790 °C. The ratio of thermal creep strain to irradiation creep strain was estimated to be 11% from the fitted line of thermal creep data for both NITE1 and NITE2 to 1.38 dpa at 760–790 °C. These results indicate that the contributions from the thermal creep strains to the total creep strains are insignificant below 790 °C for both NITE1 and NITE2.

In contrast, the thermal creep was significant after 100 h heating at 1180 °C. The irradiation creep of both NITE1 and NITE2 at 1180 °C is close to each power law fitting line for the thermal creep in Figure 4. The ratio of the thermal creep strain to the irradiation creep strain in NITE1 and NITE2 at 1.38 dpa was estimated to be 92% and 100%, respectively, indicating that the thermal creep

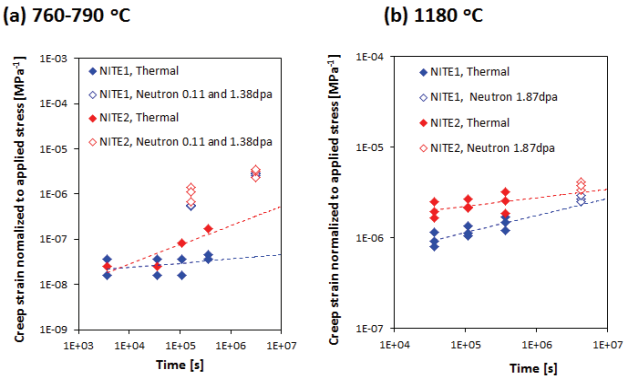

Fig. 4. Creep strain normalized to average applied strain under thermal treatment and neutron irradiation at (a) 760–790 °C, and (b) 1180 °C.

significantly affected the irradiation creep at 1180 °C. However, stress exponent of the irradiation creep in NTIE2 was slightly higher than that of thermal creep. This indicates that the creep mechanism of the irradiation creep was somewhat different from or more complex than that of thermal creep.

VI.B. IRRADIATION CREEP BEHAVIOR

Irradiation creep of NLS SiC was measured at 380–790 °C, where thermal creep was not dominant as described in section VI.A. The irradiation creep at low temperature is also observed in high-purity, polycrystalline and mono-crystalline CVD SiC[12]. Note that the creep strain of NITE1 and NITE2 tends to be ~1.5 and ~1.8 times larger comparing to CVD SiC for similar irradiation conditions, respectively. In addition, stress exponents of NLS SiC are also relatively high. These results indicate that irradiation creep mechanism of NLS SiC is different from that of CVD SiC or additional creep mechanism operates in NLS SiC. The supposed creep mechanism of CVD SiC is anisotropic swelling which is caused by anisotropy of self-interstitial cluster evolution due to the external stress[12]. This swelling-coupled creep can occur in NLS SiC, because NLS SiC consists mainly of 3C SiC grains.

Creep coefficient, which is normalized creep strain with respect to the stress and the fluence is used to compare creep behavior of different materials at low fluence level[20]. The instantaneous creep coefficient ($\overline{K}$) is defined by

$$\overline{K} \cong \frac{\varepsilon_2 - \varepsilon_1}{\overline{\sigma}(\gamma_2 - \gamma_1)} \qquad (2)$$

, where γ_1 and γ_2 ($\gamma_1 < \gamma_2$) are neutron fluences, $\overline{\sigma}$ is average stress during irradiation, and ε_1 and ε_2 are irradiation creep strains following irradiation at a fluence of γ_1 and γ_2, respectively. Figure 5 shows the fluence dependence of the instantaneous creep coefficient of NLS SiC. The highest and lowest error bars indicate the fluence of γ_2 and γ_1 for each data point, respectively. The figure also shows the instantaneous creep coefficient of CVD SiC[12], and the creep coefficients for the swelling-coupled creep model of CVD SiC at 380–540 °C[12] and the logarithmic creep model fit to present data. The logarithmic creep is generally observed in metals and ceramics in the initial stage of thermal creep. Both the swelling-coupled creep model and logarithmic creep model can represent the trend of the experimental data for the case of irradiation at 380–790 °C. For both NITE1 and NITE2, the creep coefficients have the values of ~1×10^{-5} [MPa^{-1} dpa^{-1}] at ~0.1 dpa and 1×10^{-7} to 1×10^{-6} [MPa^{-1} dpa^{-1}] at ~1 dpa, which is within one order of magnitude of that of CVD SiC. In other words, creep behavior was not dramatically different between CVD SiC and NLS SiC though NLS SiC exhibited somewhat larger magnitude of creep strain and stress exponent.

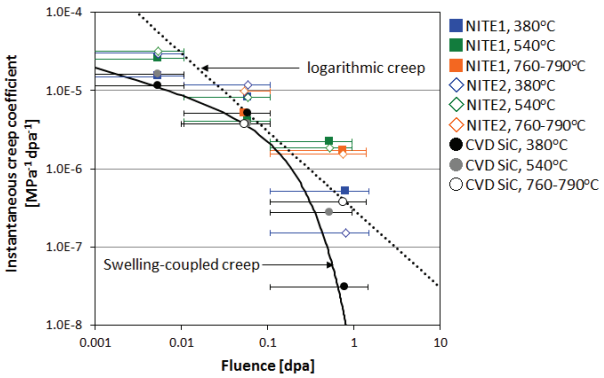

Fig. 5. Neutron fluence dependence of instantaneous creep coefficients of NLS SiC. The data of CVD SiC, and the creep coefficients of swelling-coupled creep and logarithmic creep are also presented.

Significant differences in microstructures of these two materials are grain size and presence of secondary phases. The typical average grain-size is more than 1 micron for CVD SiC and a few hundred nm for NLS SiC. Secondary phases in NLS SiC mostly existed at grain-boundaries as thin amorphous like films and grain-pockets as agglomerate formation as shown in Fig. 1. In contrast, CVD SiC is a high-purity material with clean grain-boundary. These microstructural differences suggest that grain-boundary related creep operates in NLS SiC.

The grain-boundary related creep mechanism in ceramics can be discussed using both stress exponent and grain-size exponent [21]. The grain-size exponent is helpful for discussion of the creep mechanism, because NITE1 and NITE2 exhibit qualitatively similar microstructure, featuring random grains, Y-Al oxides at the grain pockets, thin films of additives at the grain boundaries, and free carbon content. Figure 5 shows grain-size dependence of creep strain normalized to applied stress, under various radiation conditions. Data sets of irradiation creep for two kinds of CVD SiC are also plotted[12]. The grain-size exponent is determined from the negative slope of each data set in the log-log plots in Fig. 6. The absolute value is close unity for NLS SiC under irradiation to 0.01 and 0.11 dpa at all temperatures. Generally, the closeness of both grain-size exponent and stress exponent to unity indicates that thermal creep of ceramics involves grain-boundary sliding[21]. Therefore, the grain-size exponent and stress exponent of NLS SiC indicate that the grain boundary sliding contributes to the irradiation creep.

Regarding the irradiation creep of CVD SiC, the normalized creep strain was independent to grain-size at 380 and 540 °C. This result is reasonable because the creep mechanism of CVD SiC does not relate to grain boundary but to anisotropic irradiation-defect evolution. Under irradiation at 760–790 °C, creep behavior of CVD SiC exhibited grain-size exponent of ~1. As with NLS SiC, the creep mechanism of CVD SiC relates to grain-boundary sliding, based on the grain-size exponent and stress exponent at this temperature. However, the different trend line for creep date between NLS SiC and CVD SiC is shown in Fig. 6. This indicates that the type of grain-boundary mechanism is different among them and grain-boundary sliding in NLS SiC may relate to thin intergranular film and/or secondary phases at the grain pockets, since CVD SiC has clean grain-boundary.

At ~1 dpa, the material quality did not affect creep behavior of NLS SiC, in contrast to the behavior at low dpa, implying that a different creep mechanism operates at ~1 dpa than at 0.11 dpa. The creep mechanisms at high dpa might not be governed by grain boundary diffusion and/or sliding, because the grain-size exponent is close to zero.

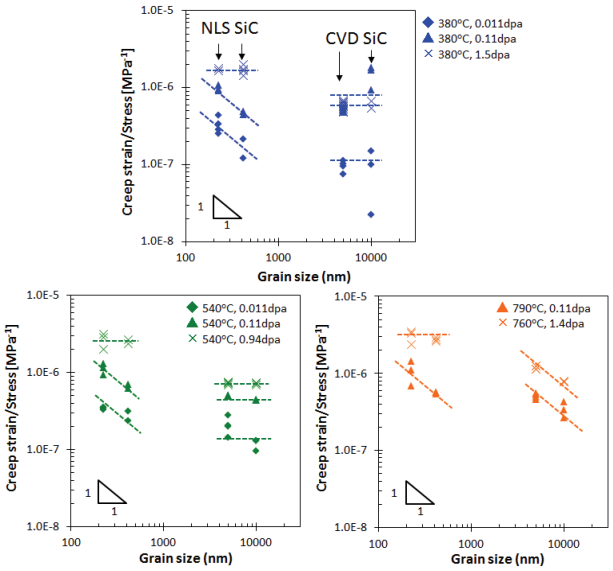

Fig. 6. Grain-size dependence of creep strain normalized to applied stress, under neutron irradiation at 380, 540 and 760–790 °C. Data correspond to NITE1 (average grain size: 414 nm), NITE2 (average grain size: 226 nm), and CVD SiC[12] (average grain size: ~5000 and ~10000 nm).

IV. CONCLUSIONS

The creep deformation of NLS SiC during neutron irradiation was dominated by the irradiation creep, with limited contributions from the thermal creep, at 380 to 790 °C. In contrast, at 1180 °C the thermal creep dominated in the irradiation-creep deformation. The stress exponent appeared approximately unity for both the thermal and irradiation creep.

The instantaneous creep coefficient at 380 to 790 °C was ~1 × 10^{-5} [MPa^{-1} dpa^{-1}] at ~0.1 dpa and 1 × 10^{-7} to 1 × 10^{-6} [MPa^{-1} dpa^{-1}] at ~1 dpa, which is within one order of

magnitude of that of high purity CVD SiC. However, irradiation creep strain of NLS SiC was 1.5–1.8 times larger than that of CVD SiC. In addition, the stress exponent slightly exceeds unity, which is also larger than that of CVD SiC.

At up to 0.11 dpa and 380–790 °C, difference of material quality such as grain size and the amount of secondary phases affected creep strain of NLS SiC. Microstructural observation and analysis indicates that grain-boundary sliding relating the secondary phases contributes to the irradiation creep. The effect of material quality was insignificant at ~1 dpa, in contrast to the behavior at less than 0.11 dpa.

ACKNOWLEDGMENTS

This work was supported by Office of Fusion Energy Sciences under contract DE-C05-00OR22725 with UT-Battelle, LLC, and US–Japan TITAN Collaboration on Fusion Blanket Technology and Materials. Research was supported in part by High Flux Isotope Reactor, which is sponsored by the Office of Basic Energy Sciences, U.S. Department of Energy.

REFERENCES

[1] L.L. SNEAD, T. NOZAWA and Y. KATOH et al.,"Handbook of SiC properties for fuel performance modeling", *J Nucl Mater*, **371**, 329, (2007).

[2] Y. KATOH, T. NOZAWA, and L.L. SNEAD KATOH et al.,"Stability of SiC and its composites at high neutron fluence", *J. Nucl. Mater.*, **417**, 400, (2011).

[3] Y. KATOH, S.M. DONG AND and A. KOHYAMA, "Thermo-mechanical properties and microstructure of silicon carbide composites fabricated by nano-infiltrated transient eutectoid process", *Fusion Eng Des*, **61**, 723, (2002).

[4] T. KOYANAGI, K. OZAWA and T. HINOKI et al., "Effects of neutron irradiation on mechanical properties of silicon carbide composites fabricated by nano-infiltration and transient eutectic-phase process", *J Nucl Mater*, (2013). http://dx.doi.org/10.1016/j.jnucmat.2013.10.005

[5] T. NOZAWA, T. HINOKI and A. HASEGAWA et al.,"Recent advances and issues in development of silicon carbide composites for fusion applications", *J Nucl Mater*, **386**, 622, (2009).

[6] K. SHIMODA, A. KOHYAMA and T. HINOKI, "High mechanical performance SiC/SiC composites by NITE process with tailoring of appropriate fabrication temperature to fiber volume fraction", *Compos Sci Technol*, **69**, 1623, (2009).

[7] T. HINO, E. HAYASHISHITA and Y. YAMAUCHI et al.,"Helium gas permeability of SiC/SiC composite used for in-vessel components of nuclear fusion reactor", *Fusion Eng. Des*. **73**, 51, (2005).

[8] H.-C. JUNG, T. HINOKI and Y. KATOH et al.," Development of a shear strength test method for NITE–SiC joining material", *J Nucl Mater*, **417**, 383, (2011).

[9] Y. KATOH, L.L. SNEAD and T. CHENG et al.,"Radiation-tolerant joining technologies for silicon carbide ceramics and composites", *J Nucl Mater*, (2013). http://dx.doi.org/10.1016/j.jnucmat.2013.10.002

[10] K. SHIMODA, N. EIZA and J.-S. PARK et al.,"High-Temperature Mechanical Property Improvements of SiC Ceramics by NITE Process", *Mater Trans*, **47**, 1204, (2006).

[11] Y. KATOH, L.L. SNEAD and T. HINOKI et al.,"Irradiation creep of high purity CVD silicon carbide as estimated by the bend stress relaxation method", *J Nucl Mater*, **367**, 758, (2007).

[12] Y. KATOH, L.L. SNEAD and C.M. PARISH et al.,"Observation and possible mechanism of irradiation induced creep in ceramics", *J Nucl Mater*, **434**, 141, (2013).

[13] S. KONDO, T. KOYANAGI and T. HINOKI, "Irradiation creep of 3C–SiC and microstructural understanding of the underlying mechanisms", *J Nucl Mater*, (2013). http://dx.doi.org/10.1016/j.jnucmat.2013.09.004

[14] T. KOYANAGI, S. KONDO and T. HINOKI, "MICROSTRUCTURAL ANALYSIS OF SECONDARY PHASES IN SILICON CARBIDE FABRICATED WITH SIC NANO-POWDER AND SINTERING ADDITIVES", *Ceram Eng Sci Proc*, **32**, 53, (2011).

[15] K. ABE, S. NOGAMI and A. HASEGAWA et al.,"Study on stress relaxation behavior of silicon carbide by BSR method", *J Nucl Mater*, **417**, 356, (2011).

[16] K. SHIMODA, S. KONDO and T. HINOKI et al.,"Thermal stress relaxation creep and microstructural evolutions of nanostructured SiC ceramics by liquid phase sintering", *J Eur Ceram Soc*, **30**, 2643, (2010).

[17] G.N. MORSCHER and J.A. DICARLO, "A Simple Test for Thermomechanical Evaluation of Ceramic Fibers", *J Am Ceram Soc*, **75**, 136, (1992).

[18] Y. KATOH and L.L. SNEAD, "Bend Stress Relaxation Creep of CVD Silicon Carbide", *Ceram Eng Sci Proc*, **26**, 265, (2005).

[19] R.W. HERTZBERG, R.P. VINCI and J.L. HERTZBERG, "Deformation and Fracture

Mechanics of Engineering Materials", J. Wiley & Sons, Inc., Hoboken, New Jersey, 1996.
[20] K. EHRLICH, "IRRADIATION CREEP AND INTERRELATION WITH SWELLING IN AUSTENITIC STAINLESS STEELS", *J Nucl Mater*, **100**, 149, (1981).
[21] W.R. CANNON and T.G. LANGDON, "Review Creep of ceramics", *J Mater Sci*, **18**, 1, (1983).

Task2-3(3) EFFECTS OF NEUTRON IRRADIATION ON MECHANICAL PROPERTIES OF SILICON CARBIDE COMPOSITES FABRICATED BY NANO-INFILTRATION AND TRANSIENT EUTECTIC-PHASE PROCESS

T. Koyanagi[1,2], K. Ozawa[2], T. Hinoki[1], K. Shimoda[1], Y. Katoh[2]

[1]*Institute of Advanced Energy, Kyoto University, Gokasho, Uji, Kyoto 611-0011, Japan, koyanagit@ornl.gov, hinoki@iae.kyoto-u.ac.jp, k-simd@iae.kyoto-u.ac.jp*
[2]*Materials Science and Technology Division, Oak Ridge National Laboratory, P.O. Box 2008, Oak Ridge, TN 37831, USA, ozawak@ornl.gov, katohy@ornl.gov*

Unidirectional silicon carbide (SiC)-fiber-reinforced SiC matrix (SiC/SiC) composites fabricated by a nano-infiltration and transient eutectic-phase (NITE) process were irradiated with neutrons at 830 °C to 5.9 dpa, and at 1270 °C to 5.8 dpa. The in-plane and trans-thickness tensile and the inter-laminar shear properties were evaluated at ambient temperature. The mechanical characteristics, including the quasi-ductile behavior, the proportional limit stress, and the ultimate tensile strength, were retained subsequent to irradiation. Analysis of the stress–strain hysteresis loop indicated the increased fiber/matrix interface friction and the decreased residual stresses. The inter-laminar shear strength exhibited a significant decrease following irradiation.

I. INTRODUCTION

The superior as-fabricated high-temperature mechanical properties and low-activation nuclear properties of silicon carbide (SiC)-fiber-reinforced SiC matrix (SiC/SiC) composites make them attractive as nuclear materials such as fusion blanket components[1]. Therefore, for nuclear applications, the mechanical performances of these materials must be retained under conditions of high temperature and neutron irradiation.

Among the industrially available SiC/SiC composites produced through various processing routes, chemically vapor-infiltrated (CVI) SiC matrix composites with the Generation III near-stoichiometric SiC fibers are presently considered as the reference nuclear grade materials. An extensive compilation of the neutron-irradiated properties for the CVI-SiC/SiC composites is now available[2]. Neutron-irradiated CVI-SiC/SiC composites, having less-crystalline SiC-based fibers and a highly crystalline matrix, reportedly exhibit interfacial debonding as a result of differential swelling between the fiber that densifies and swells under irradiation and the high-density matrix that only swells. Consequently, this results in degradation of the mechanical properties of the composite in the irradiated state[3]. In contrast, mechanical properties of the CVI-SiC/SiC composites that have highly crystalline fibers and matrices is not significantly altered subsequent to irradiation up to 40 dpa[4]. Thus, the combination of a highly crystalline fiber and matrix is essential for retention of mechanical properties during irradiation.

While CVI-SiC/SiC composites possess in general attractive properties, they are typified by 15 - 20% porosity. This translates into up to ~30% porosity in the matrix, considering the typical fiber volume fraction of ~35%, and is the major factor limiting the matrix cracking stress and thermal conductivity of these materials[2, 5]. Moreover, it is relatively challenging for CVI-SiC/SiC composites to achieve gas tightness that is required for certain applications. The quest for SiC/SiC composites in which these limitations are circumvented by achieving dense matrices has led to the development of a nano-infiltration and transient eutectic-phase (NITE) process[6]. The NITE process applied to SiC/SiC composite production involves sintering of SiC nano-powder, carbon-coated highly crystalline SiC fibers, and oxide additives. The porosity achieved with this process is typically less than 5%, and excellent proportional limit stress (PLS), reaching up to ~360 MPa, has been reported for laboratory-grade NITE-SiC/SiC composites[7]. The thermal conductivities of NITE-SiC/SiC composites were also reportedly significantly higher than those of CVI-SiC/SiC composites in unirradiated conditions[8].

There is currently a dearth of available information about the effects of irradiation on the mechanical properties of NITE-SiC/SiC composites, and the radiation stability of SiC sintered with oxide additives is not well understood. The objective of this study is to determine the effects of neutron irradiation on the mechanical properties of NITE-SiC/SiC composites. The irradiation strength of monolithic SiC, as the matrix material of the NITE-SiC/SiC composite, is also examined.

II. EXPERIMENTAL

Unidirectional Tyranno™-SA3 SiC fiber (product type: SA3-S1I16PX with nominal 7.5 μm diameter and 1600 filaments per yarn) reinforced NITE-SiC matrix composites (Pilot grade #3, Ube Industries, Ltd., Japan)

were used as the test materials. Pyrolytic carbon (PyC) of 200–300 nm thickness was chemically vapor-deposited onto the fiber surfaces. The fiber volume fraction and porosity were ~45% and ~5%, respectively. Al_2O_3, Y_2O_3, and SiO_2 were used as sintering additives. Monolithic SiC, used as the matrix of the NITE-SiC/SiC composite, was fabricated; this material is referred to as NITE-SiC hereafter. The NITE-SiC was fabricated from β-SiC nano-powder (Sumitomo Chemical Industries Ltd., Japan, mean diameter 30 nm), Al_2O_3 powder (Sumitomo Chemical Industries Ltd., Japan, mean diameter 0.3 μm, 99.99% purity), Y_2O_3 powder (Kojundo Chemical Industries Ltd., Japan, mean diameter 1.0 μm, 99.99% purity), and SiO_2 powder (Kojundo Chemical Industries Ltd., Japan, mean diameter 1.0 μm, 99.99% purity). The oxide additives, comprising a total of 12 wt%, were mixed with SiC powder and the combination was sintered by hot-pressing at 1800 °C, for 2 h, in an Ar atmosphere, under a pressure of 20 MPa. The porosity of NITE-SiC was less than 6%.

Neutron irradiation was conducted at the High-Flux Isotope Reactor (HFIR) located at Oak Ridge National Laboratory. The specimens were irradiated at 830–1270 °C to 5.8–5.9 dpa (5.8–5.9 × 10^{25} n/m^2, E > 0.1 MeV; hereafter, 1.0 × 10^{25} n/m^2 = 1 dpa is assumed) for HFIR-RB*-18J campaign.

The tensile properties were examined using straight bar specimens, the dimensions of which were 40 mm (l) × 4 mm (w) × 2 mm (t). The fiber orientation was parallel to the loading direction. The tensile test was conducted in the cyclic loading mode. The peak tensile stress was incremented by 25 MPa in the repeated unloading–reloading sequences. The experimental procedure follows the general guidelines of ASTM C1275, with the exception that cyclic loading was adopted. PLS was defined as the stress at 5% stress deviation from the extrapolated linear segment used for the modulus determination. The trans-thickness tensile strength was evaluated using a diametral compression test method[9]. Truncated disk specimens (diameter: 4 mm, thickness: 5 mm, width: 3 mm) were used for this test. The interlaminar layer in the specimen was oriented parallel to the direction of compressive loading. The interlaminar shear strength was evaluated by the compression of double-notched specimens[10], according to ASTM C1292. Notched specimens were loaded parallel to the fiber longitudinal direction. For evaluation of the Weibull statistical strength of the NITE-SiC monolith, 1/4-four point flexural tests with an outer span of 20 mm NITE-SiC were also conducted, as per ASTM C1161. The dimensions of the specimens were 24 or 25 mm (l) × 1 mm (w) × 1 mm (t). Dynamic Young's moduli of both the NITE-SiC/SiC composites and NITE-SiC were determined using the impulse excitation of vibration method in accordance with ASTM C1259. Microstructural observation of the unirradiated NITE-SiC and NITE-SiC/SiC composites was conducted using a field-emission scanning electron microscope (SEM, Ultra55, Zeiss). Three to six mechanical tests were performed under each condition (details of the valid test number are shown in TABLES 1), except in the case of the flexural tests (20–30) for the Weibull statistical analysis.

TABLE 1. Tensile properties of the non-irradiated and irradiated NITE-SiC/SiC composites. Numbers in parentheses indicate ± one standard deviation.

Irradiation condition	# of valid tests	Tensile modulus [GPa]	Sonic modulus [GPa]	Proportional limit Stress [MPa]	Ultimate tensile Strength [MPa]	Strain at maximum load [%]
Unirradiated	6	274 (15)	333 (5)	142 (26)	344 (25)	0.17 (0.02)
830°C 5.9dpa	5	289 (19)	332 (8)	152 (32)	388 (32)	0.18 (0.04)
1270°C 5.8dpa	3	282 (8)	345 (7)	181 (46)	404 (21)	0.19 (0.01)

III. RESULTS

Figure 1 shows the secondary electron and backscattered electron images of the NITE-SiC/SiC composite and the backscattered electron image of monolithic NITE-SiC in the unirradiated condition. The NITE-SiC and the matrix of the NITE-SiC/SiC composite consist primarily of polycrystalline β-phase SiC and small amounts of oxide ceramics as the remnants of the sintering additives. The oxide grains in the NITE-SiC were found at the multi-grain junctions of the β-phase SiC grains and appeared to be homogeneously distributed with the monolithic body. In the case of the NITE-SiC/SiC

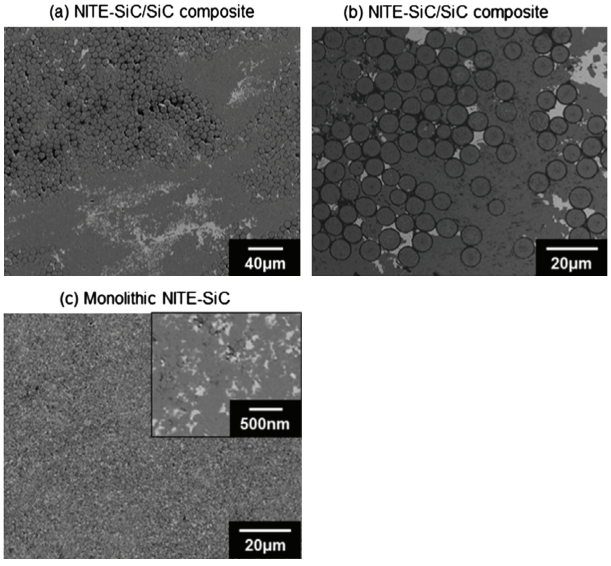

Fig. 1. SEM images for NITE-SiC/SiC composite and monolithic NITE-SiC: (a) secondary electron image, (b) and (c) backscattered electron image.

composite, pores were observed in the fiber inter-bundles, and the oxide phases attributed to the sintering additives were observed both in the matrix-rich area and to have segregated to occupy the spaces within the fiber bundles and at the inter-bundle pockets.

The typical stress–strain curves from the cyclic unloading–reloading sequences are compared for the unirradiated and irradiated NITE-SiC/SiC composites in Fig. 2. The unirradiated composites exhibited quasi-ductile failure behavior, and such behavior was also observed after irradiation. Figure 3 shows the maximum hysteresis loop width as a function of the matrix damage parameter[11], which was obtained from the composite modulus in each hysteresis loop. It should be noted that the maximum hysteresis loop width was significantly reduced subsequent to irradiation. For instance, decreases in the unirradiated loop width by 89, and 97% were observed at the matrix damage parameter of 0.15 following irradiation at the respective temperatures of 830 and 1270 °C. Despite this significant change in the loop width, the irradiation effects on the mechanical properties were not significant. The tensile properties before and after irradiation are summarized in Table 1. The PLS remained unchanged, within the limits of statistical uncertainty, subsequent to irradiation. The effects of irradiation on Young's modulus were generally insignificant. The ultimate tensile strength (UTS) was statistically unchanged upon irradiation at 830 °C, but increased by 17% following irradiation at 1270 °C.

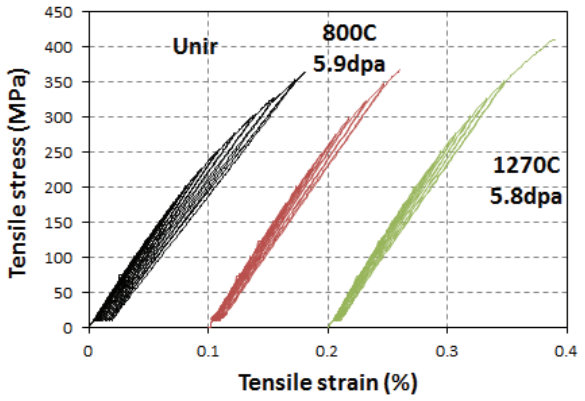

Fig. 2. Typical tensile stress-strain behaviors for the unirradiated and irradiated NITE-SiC/SiC composites. Each curve is offset horizontally for visibility.

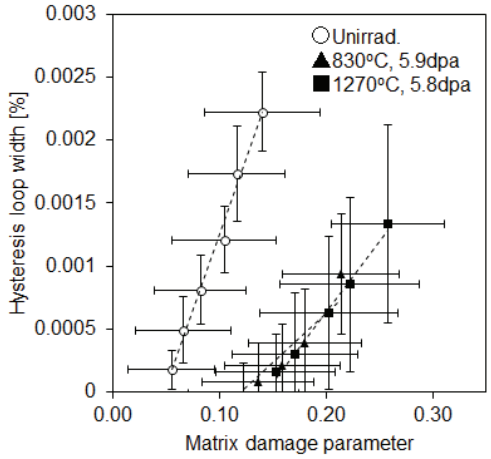

Fig. 3. The maximum hysteresis loop width as a function of matrix damage parameter before and after irradiation for the NITE-SiC/SiC composites.

Figure 4 shows a typical stress–displacement curve of the diametral compression test and a typical optical micrograph for an unirradiated test specimen. All of the evaluated specimens failed by propagation of a crack along the loaded direction. Nozawa et al. reported that the initial fracture stress determined from the maximum fracture stress in the diametral compression test was overestimated, and they found that execution of the diametral compression test using a pair of strain gauges or analysis using the slope of the stress–displacement curve facilitated more accurate determination of the initial fracture stress[12]. Herein, the analysis using the slope of the stress–displacement curves was adopted for unirradiated samples and those irradiated at 830 °C. The technique using the strain gauge was adopted for specimens irradiated at 1270 °C. The effects of irradiation on the trans-thickness tensile strength are summarized in TABLE 2. The trans-thickness tensile strength of 15 MPa for the unirradiated sample was not changed by irradiation at 830 and 1270 °C, considering the variability. However, the large variability obscures the irradiation effects on the trans-thickness tensile strength.

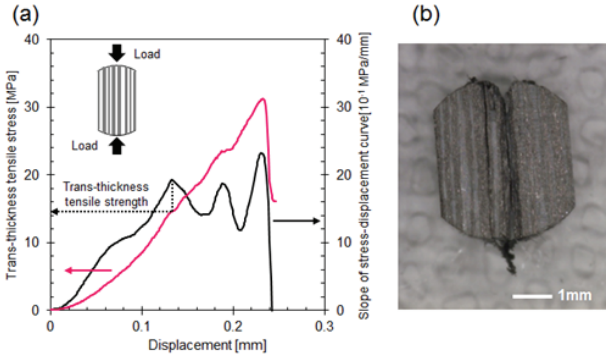

Fig. 4. (a) Typical fracture behavior of the NITE-SiC/SiC composite by the diametral compression test and (b) the typical image for the tested specimen in unirradiated condition.

A typical stress–displacement curve of the compression test for the double-notched specimen and a typical image for an unirradiated test specimen are shown in Fig. 5. Interlaminar shear fractures appeared in the stress–displacement curve in the instant that the load reached its maximum, and notch to notch fractures were observed in all of the specimens. The interlaminar shear strength (25.4 MPa) for irradiation at 5.9 dpa at 830 °C was approximately 30% lower than that for the unirradiated sample (37.2 MPa), as shown in TABLE 3. Cracks had propagated through the matrix pores along the interface in unirradiated condition.

TABLE 2. Effect of neutron irradiation on trans-thickness tensile strength of NITE-SiC/SiC composites. Average and ± one standard deviation are shown.

Irradiation condition	# of valid tests	Trans thickness tensile strength [MPa]	Change by irradiation [%]
Unirradiated	4	21.4 ±3.3	-
830°C 5.9 dpa	6	18.9 ±3.0	-11
1270°C 5.8 dpa	4	26.4 ±8.7	23

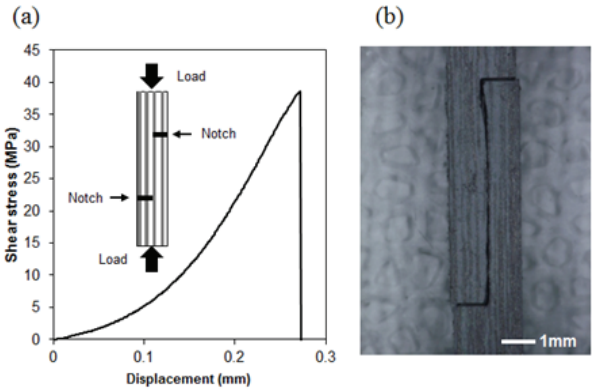

Fig. 5. (a) Typical fracture behavior of a double notched specimen of the NITE-SiC/SiC composite by the double notched shear test, and (b) the typical image for the tested specimen in unirradiated condition.

TABLE 4. Interlaminar shear strength of the non-irradiated and irradiated NITE-SiC/SiC composites. Average and ± one standard deviation are shown.

Irradiation Condition	# of valid tests	Interlaminar shear strength [MPa]	Change by irradiation [%]
Unirradiated	4	37.2 ±1.5	-
830°C 5.9 dpa	3	25.4 ±0.62	-31

Fig. 6 shows the 1/4-four point flexural strength of monolithic NITE-SiC. Significant degradation of the flexural strength as a result of irradiation was detected. For example, the characteristic strength was degraded by

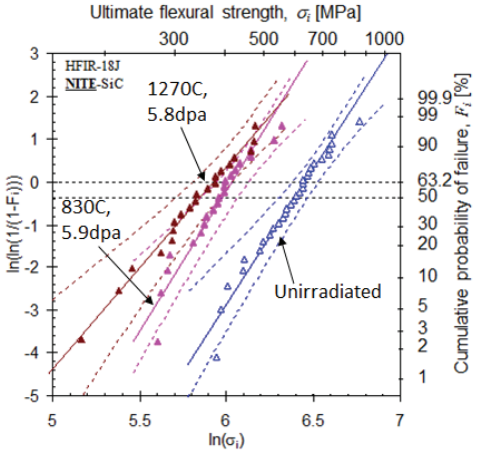

Fig. 6. Weibull statistical strength distribution of the monolithic NITE-SiC irradiated to relatively higher temperature and fluence (830~°C, 5.8~ dpa), irradiated at HFIR. Dotted lines indicate 95% confidence bounds.

respective values of 34 and 41% at 830 °C, 5.9 dpa and at 1270 °C, 5.8 dpa. The average dynamic Young's modulus of unirradiated NITE-SiC and the corresponding standard deviation were 344 and 7 GPa, respectively. The dynamic Young's modulus decreased by 5% following irradiation at 830 °C to 5.9 dpa, as well as at 1270 °C with irradiation to 5.8 dpa.

IV. DISCUSSION

IV.A. EFFECTS OF IRRADIATION ON PROPORTIONAL LIMIT STRESS

The PLS, which is an index of the matrix cracking stress, is in theory affected by the following parameters: (1) Young's moduli of the composite (E_c), fiber (E_f), and matrix (E_m); (2) the critical energy release rate for debonding at the fiber/matrix interface; (3) the critical mode-I matrix energy release rate; (4) the frictional stress at the fiber/matrix interface (τ); and (5) the thermal residual stress of the matrix in the tensile direction (σ_m) [13,14]. Thus, the PLS (σ_{PLS}) can be expressed as follows:

$$\sigma_{PLS} = \sigma - \sigma_m \frac{E_c}{E_m} \qquad (1)$$

where σ is a function of τ, E_f, E_m, the fiber volume fraction (V_f), the critical energy release rate for interfacial debonding, and the critical mode-I matrix energy release rate[13, 14]. Based on equation (1), it is clear that the residual stress of the matrix in the tensile direction exerts a significant effect on the PLS. The other parameters are relatively ineffective to PLS in theory. The following paragraphs discuss the effects of irradiation on these parameters, which strongly influence the PLS of the NITE-SiC/SiC composite.

The effect of irradiation on Young's modulus of SiC has been studied using chemical vapor deposition (CVD) SiC as the matrix phase of the CVI-SiC/SiC composite. It is believed that Young's modulus of CVD-SiC declines slightly in response to irradiation-induced lattice expansion[15]. Previous work by Katoh et al. revealed that Young's modulus of CVI-SiC/SiC composites containing Tyranno™-SA3 fibers remained statically unchanged following irradiation to 5.9 dpa at 800 °C and to 5.8 dpa at 1300 °C[16]. This result indicates that Young's modulus of the Tyranno™-SA3 fibers also remained unchanged, considering the marginal decrease in the matrix modulus. Given that the irradiation conditions in the reference[16] were similar to those used in this study, Young's modulus of the fibers in the NITE-SiC/SiC composites was expected to remain unchanged. On this basis, the insignificant effect of irradiation on Young's moduli of the NITE-SiC/SiC composites following irradiation both at 830 °C to 5.9 dpa and at 1270 °C to 5.8 dpa indicates that Young's modulus of the matrix was also maintained herein.

The effect of irradiation on the critical mode-I matrix energy release rate can be discussed using the strength and Young's modulus of monolithic NITE-SiC. If the effects of irradiation on the mechanical properties of monolithic NITE-SiC and the matrix of the NITE-SiC/SiC composite are similar, the critical matrix energy release rate should be decreased by irradiation at 830 and 1270 °C as a result of a significant reduction in the fracture strength and a minor reduction in the dynamic modulus of monolithic NITE-SiC. The effect of the decreased matrix energy release rate on the PLS is less certain, considering interfacial debonding at the fiber/matrix interface. In the case of very weak or strong interfacial debonding strength, the resulting decreased matrix energy release rate should contribute to the decreased PLS[13, 14]. The mechanism of degradation of the strength of monolithic NITE-SiC is discussed below.

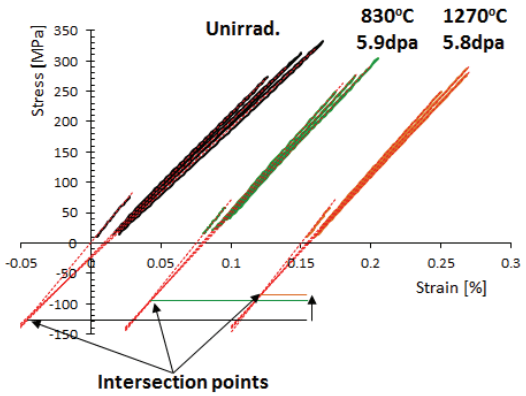

Fig. 7. Examples of the determination method for residual stress of tensile direction in matrix of the NITE-SiC/SiC composite.

The thermal residual stress in the NITE-SiC/SiC composites is generated by mismatch of the coefficient of thermal expansion (CTE) of the fiber and the matrix during fabrication. The residual stress in the tensile direction can be estimated from the point of intersection of the average linear regression line of the respective unload–reload curves[17], as shown in Fig. 7. The stress level at the intersection point is referred to as the misfit stress. The initial value of 146±22 MPa of stress in the unirradiated sample decreased to 94±22 and 83±12 MPa following irradiation at 830 and 1270 °C, respectively. The positive misfit stress observed herein is indicative of the tensile residual stress in the matrix. The relationship between the misfit stress (σ_T) and the residual stress of the matrix in the tensile direction (σ_m) is given as following[18].

$$\sigma_m = \frac{E_m}{E_c}\sigma_T \qquad (2)$$

From equations (1) and (2), the PLS is directly affected by the misfit stress, and a reduction in the misfit stress should effectively contribute to increasing the PLS. Therefore, reduction of the misfit stress, i.e., reduction of the tensile residual stress of the matrix in the fiber axial direction, is one of the factors accounting for the maintained PLS subsequent to irradiation. It is postulated that the mechanisms underlying this modification of the residual stress include thermal and/or irradiation creep, secondary stress caused by the relatively higher degree of swelling of the matrix compared to the fiber[19], and the effect of irradiation on CTE.

The frictional stress at the fiber/matrix interface (τ) relates to the inelastic strain parameter (H), which can be estimated from the width of the maximum hysteresis loop[20].

$$H = \frac{b_2(1-a_1V_f)^2 R\sigma_p^2}{4d\tau E_m V_f^2} \qquad (3)$$

Here, a_1 and b_2 are the Hutchinson and Jensen constants for Type II boundary conditions[20], V_f is the fiber volume fraction, R is the fiber radius, σ_p is the peak stress of the hysteresis loop, d is the matrix crack spacing, and E_m is Young's modulus of the matrix. The matrix crack spacing is theoretically inversely proportional to the matrix damage parameter (D) given by:

$$D = \frac{E_c - E^*}{E^*} \qquad (4)$$

where E_c and E^* are the modulus of the composite and the tangent modulus of the unloading curve, respectively, and D can be evaluated from each hysteresis loop[18]. Using the relationship between D and d, equation (2) can be rewritten as:

$$H = A\frac{D\sigma_p^2}{\tau} \qquad (5)$$

where A is almost constant when Young's moduli of the fiber and matrix are stable under irradiation. The inelastic strain parameter (H) of the NITE-SiC/SiC composite is plotted against $D\sigma_p^2$, before and after irradiation in Fig. 8;

the error bars show the standard deviations. Given that Young's moduli of the fiber and matrix were insensitive to irradiation at 830 and 1270 °C, as discussed above, the slope of the linear regression line should be inversely proportional to the interfacial frictional stress under these irradiation conditions. Figure 8 indicates approximately three- and 1.5-fold increases in the interfacial frictional stress following irradiation at 830 and 1270 °C, respectively, though there are large deviations possibly due to limited numbers of the tests. Theoretically, this increase should contribute to increasing the PLS[13, 14]. Interfacial frictional stress is defined as the product of multiplication of friction coefficient and clamping stress. One possible mechanism for the increased frictional stress involves increased friction coefficient caused by grain growth in the fibers and matrix. Another possible mechanism is locally increased clamping stress and friction coefficient derived from the larger swelling of the oxide phases around the fibers compared to swelling of the fibers and matrix. Previous evaluation of the irradiation-induced swelling of a monolithic SiC indicated larger swelling of Y-Al oxide as a secondary phase in monolithic NITE-SiC[21]. The larger swelling of the oxide phases are also indicated by neutron irradiation experiment[22]. However, additional experimental data are required to clarify the mechanism underlying the observed increase in the interfacial frictional stress caused by irradiation.

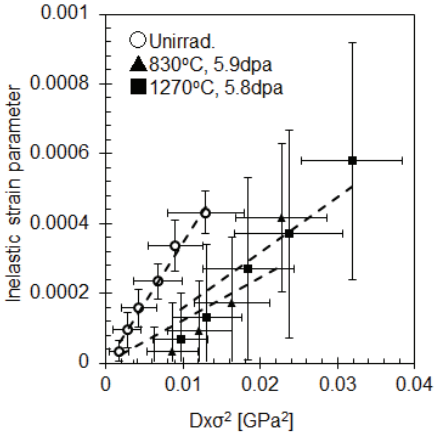

Fig. 8. Inelastic strain parameter as a function of matrix damage parameter multiplied by square of peak stress before and after irradiation for the NITE-SiC/SiC composites.

IV.B. EFFECT OF IRRADIATION ON THE ULTIMATE TENSILE STRENGTH

It is known that the UTS of unidirectional fiber-reinforced composites depends on the mechanical properties of the fiber and the interfacial frictional stress. When a matrix crack is ideally deflected at the fiber/matrix interface, the UTS (σ_u) is described by:

$$\sigma_u = f\sigma_0^{\frac{m}{m+1}}\left(\frac{\tau L_0}{R}\cdot\frac{2(m+1)}{(m+2)m}\right)^{1/(m+1)}\frac{m+1}{m+2} \quad (6)$$

where σ_0 is the Weibull mean strength, m is the Weibull modulus for the fiber strength, and L_0 is the gauge length[23]. The reported Weibull modulus for the strength of the Tyranno™-SA3 fiber was about 4 with and without irradiation to ~5.3 dpa at ~910 °C[18]. Thus, the fiber strength is a determining factor for the UTS. Katoh et al. demonstrated preservation of the UTS of a CVI-SiC/SiC composite containing Tyranno™-SA3 fibers subsequent to irradiation to 5.9 dpa at 800 °C, and to 5.8 dpa at 1300 °C, which are similar to the irradiation conditions used in this study[16]. This result implies the stability of the fiber strength under these irradiation conditions. Therefore, the excellent irradiation resistance of the UTS of the NITE-SiC/SiC composite is plausibly associated with the stable mechanical properties of the Tyranno™-SA3 fiber.

The UTS is also affected by the residual stress, given that the residual stress in the fiber radial direction affects the bonding strength at the fiber/matrix interface, with a consequent effect on the deflection of the matrix crack at the interface. The hysteresis loop analysis shown in Fig. 7 revealed the existence of tensile residual stress of the matrix in the fiber axial direction. This result is consistent with a larger CTE of the matrix relative to the fiber and the existence of compressive stress at the fiber/matrix interface in the fiber radial direction, based on the fiber–matrix concentric two-cylinder model[13]. Considering the decreased misfit stress following irradiation, it is expected that the residual compressive stress in the fiber radial direction was decreased as a result of irradiation. This decrease in the compressive stress should decrease the strength of interfacial bonding and consequently promote the deflection of the matrix crack, which should contribute to increasing the UTS. Therefore, the 17% increase in the UTS at 1270 °C may be explained in terms of a decrease in the strength of the interfacial debonding as a result of modification of the residual stress.

IV.C. EFFECT OF IRRADIATION ON THE MECHANICAL PROPERTIES OF NITE-SIC

The flexural strength of NITE-SiC was significantly degraded by irradiation in this study, which agrees with previous research on the effects of the irradiation strength on SiC containing a secondary phases[15]. As discussed above, the microstructure of NITE-SiC consists primarily of β-phase SiC with small amount of oxide ceramics. Since β-phase SiC in a high purity polycrystalline form is reportedly very stable in the irradiation conditions of this study[15], the observed detrimental effect of irradiation on

strength of NITE-SiC is attributed to the presence of the oxide secondary phases.

One known mechanism that explains the irradiation-induced strength deterioration for SiC with secondary phases involves micro-cracking caused by the misfit stress due to the differential swelling between the secondary phase and SiC. However, in the present case, an extensive micro-crack generation is unlikely given that only ~5% decrease in Young's modulus was observed following irradiation at 830 and 1270 °C. However, the misfit stress caused by differential swelling is a plausible cause of the degradation of the flexural strength as a result of irradiation. Other possible reasons include the strength degradation of the secondary phase itself and degradation of the grain boundary strength due to the likely presence of oxide films at the SiC grain boundaries.

IV.D. EFFECT OF IRRADIATION ON TRANS-THICKNESS TENSILE AND INTERLAMINAR SHEAR STRENGTHS

Based on the SEM image presented in Fig. 1, pores in the fiber bundle are the most probable origin of the fracture in the diametral compression test. Cracks originating at the fiber bundle plausibly propagated to the matrix-rich region surrounding the fiber bundle, with subsequent fracture of the matrix at the trans-thickness tensile strength region. Based on this consideration, the trans-thickness tensile strength should be closely-related to the fracture toughness of the matrix. Herein, the effects of irradiation on the trans-thickness tensile strength were insignificant at 830 and 1270 °C. Therefore, this result implies that there is no significant degradation of the fracture toughness of the matrix.

V. CONCLUSIONS

No significant effects of neutron irradiation on the tensile properties such as quasi-ductile behavior, PLS, and UTS of the unidirectional Tyranno™-SA3 fiber-reinforced NITE-SiC/SiC composites were observed subsequent to irradiation with 5.9 dpa at 830 °C, and with 5.8 dpa at 1270 °C. In contrast, hysteresis loop analysis indicates an increase in the frictional stress at the fiber/matrix interface at 830 and 1270 °C, which is possibly caused by the locally increased clamping stress and friction coefficient derived from the larger swelling of the secondary phase compared to swelling of the fibers and matrix. Hysteresis loop analysis also further indicated reduction of the tensile residual stress of the matrix in the fiber axial direction for all of the irradiation conditions considered.

Significant degradation of the flexural strength of monolithic NITE-SiC, which represented as the matrix of the NITE-SiC/SiC composite, was demonstrated following irradiation at 830 and 1270 °C, whereas the PLS of the NITE-SiC/SiC composites did not exhibit any degradation. Effectively contribution to increasing the PLS was theoretically brought form residual stress modification of the matrix as described above, which accounts in part for the excellent irradiation resistance of the PLS.

The excellent irradiation resistance of the ultimate tensile strength was plausibly attributed to the stable mechanical properties of the Tyranno™-SA3 fiber following irradiation.

ACKNOWLEDGMENTS

This work was supported by Office of Fusion Energy Sciences under contract DE-C05-00OR22725 with UT-Battelle, LLC, and US–Japan TITAN Collaboration on Fusion Blanket Technology and Materials. Research was supported in part by High Flux Isotope Reactor, which is sponsored by the Office of Basic Energy Sciences, U.S. Department of Energy, and International Research Center for Nuclear Materials Science, Institute for Materials Research, Tohoku University.

The authors thank Y.-B. Choi, L.T. Gibson, A.M. Williams, P.S. Tedder, A.D. Harrison, S.G. Beck, L.E. Reid, and B.D. Johnson for post-irradiation experiments in ORNL.

REFERENCES

[1] Y. KATOH, L. L. SNEAD, and I. SZLUFARSKA et al., "Radiation effects in SiC for nuclear structural applications", *Curr Opin Solid State Mater Sci*, **16**, 143, (2012)

[2] Y. KATOH, K. OZAWA, and C. SHIH et al., " Continuous SiC fiber, CVI SiC matrix composites for nuclear applications: Properties and irradiation effects", *J Nucl Mater* http://dx.doi.org/10.1016/j.jnucmat.2013.06.040, (2013)

[3] L. L. SNEAD, D. STEINER, and S. J. ZINKLE, "Measurement of the effect of radiation damage to ceramic composite interfacial strength", *J. Nucl. Mater.*, **191**, 566, (1992).

[4] Y. KATOH, T. NOZAWA, and L. L. SNEAD et al., "Stability of SiC and its composites at high neutron fluence", *J. Nucl. Mater.*, **417**, 400, (2011).

[5] J.A. DICARLO, H-M. YUN, and G.N. MORSCHER et al., SiC/SiC Composites for 1200°C and Above, in: N. P. Bansal (Eds.), Handbook of Ceramic Composites, Springer Science Business Media, Inc, New Yotk, 2005, pp. 77.

[6] Y. KATOH, S. M. DONG, and A. KOHYAMA, "Thermo-mechanical properties and microstructure of silicon carbide composites

fabricated by nano-infiltrated transient eutectoid process", *Fusion Eng. Des*., **61**, 723, (2002).

[7] K. SHIMODA, A. KOHYAMA, and T. HINOKI, "High mechanical performance SiC/SiC composites by NITE process with tailoring of appropriate fabrication temperature to fiber volume fraction", *Compos. Sci. Technol*., **69**, 1623, (2009).

[8] K. SHIMODA, J.S. PARK, and T. HINOKI et al., "Microstructural optimization of high-temperature SiC/SiC composites by NITE process", *J. Nucl. Mater*., **386**, 634, (2009).

[9] T. HINOKI, E. LARA-CURZIO, and L. L. SNEAD, "EVALUATION OF TRANSTHICKNESS TENSILE STRENGTH OF SiC/SiC COMPOSITES", *Ceram. Eng. Sci. Proc*., **24**, 401, (2003).

[10] E. LARA-CURZIO, D. BOWERS, and M. K. FERBER, "The interlaminar tensile and shear behavior of a unidirectional C-C composite", *J. Nucl. Mater*., **230**, 226, (1996).

[11] M.Y. HE, B.-X. WU, and A.G. EVANS et al., "Inelastic strains due to matrix cracking in unidirectional fiber-reinforced composites", *Mech. Mater*. **18**, 213, (1994).

[12] T. NOZAWA, K. OZAWA, and Y. B. CHOI et al., "Determination and prediction of axial/off-axial mechanical properties of SiC/SiC composites", *Fusion Eng. Des*., **87**, 803, (2012).

[13] B. BUDIANSKY, J. W. HUTCHINSON, and A. G. EVANS, "MATRIX FRACTURE IN FABER-REINFORCES CERAMICS", *J. Mech. Phys. Solids*, **34**, 167, (1986).

[14] M. SUTCU, and W. B. HILLIG, "THE EFFECT OF FIBER-MATRIX DEBOND ENERGY ON THE MATRIX CRACKING STRENGTH AND THE DEBOND SHEAR STRENGTH", *Acta Metall. Mater*., **38**, 2653, (1990).

[15] L. L. SNEAD, T. NOZAWA, and Y. KATOH et al., "Handbook of SiC properties for fuel performance modeling", *J. Nucl. Mater*., **371**, 329, (2007).

[16] Y. KATOH, K. OZAWA, and T. HINOKI et al., "Mechanical properties of advanced SiC fiber composites irradiated at very high temperatures ", *J. Nucl. Mater.,* **417**, 416, (2011) .

[17] M. STEEN, and J. L. VALLES, "Unloading-reloading sequence and the analysis of mechanical test results for constituents fiber ceramic composites", in: M. G. JENKINS, E. LARA-CURIZO, and S. T. GONCZY et al., (Eds.), "Thermal and mechanical test method and behavior of continuous fiber ceramic composites", ASTM STP 1309, ASTM, West Conshohocken, 1996, pp. 49.

[18] Y. KATOH, L. L. SNEAD, and T. NOZAWA et al., "Thermophysical and mechanical properties of near-stoichiometric fiber CVI SiC/SiC composites after neutron irradiation at elevated temperatures", *J. Nucl. Mater*., **403**, 48, (2010).

[19] T. KOYANAGI, S. KONDO, and T. HINOKI, "Effect of differential swelling between fiber and matrix on the strength of irradiated SiC/SiC composites", *J. Nucl. Mater.,* **442**, S380, (2013).

[20] J. W. HUTCHINSON, and H. M. JENSEN, "MODELS OF FIBER DEBONDING AND PULLOUT IN BRI'ITLE COMPOSITES WITH FRICTION", *Mech. Mater*., **9**, 139, (1990).

[21] T. KOYANAGI, S. KONDO, and T. HINOKI, "The influence of sintering additives on the irradiation resistance of NITE SiC", *J. Nucl. Mater*., **417**, 435, (2011).

[22] K. OZAWA, Y. KATOH, and L. L. SNEAD et al., "THE EFFECTS OF NEUTRON IRRADIATION ON DIMENSIONAL CHANGE IN ADVANCED SILICON CARBIDE COMPOSITES", *Fusion Materials Semiannual Progress Report* DOE/ER-0313/46, 4, (2009).

[23] W. A. CURTIN, B. K. AHN, and N. TAKEDA, "MODELING BRITTLE AND TOUGH STRESS-STRAIN BEHAVIOR IN UNIDIRECTIONAL CERAMIC MATRIX COMPOSITES", *Acta Mater.,* **46**, 3409, (1998).

Task2-3(4) Tritium Trapping in Silicon Carbide in Contact with Solid Breeder under High Flux Isotope Reactor Irradiation

*H. Katsui[1], Y. Katoh[2], A. Hasegawa[3], M. Shimada[4], Y. Hatano[5], T. Hinoki[6], S. Nogami[3], T. Tanaka[7], S. Nagata[1] and T. Shikama[1]

[1]Institute for Materials Research, Tohoku University, Sendai, Japan
[2]Materials Science and Technology Division, Oak Ridge National Laboratory, Oak Ridge, USA
[3]Department of Quantum Science and Energy Engineering, Tohoku University, Sendai, Japan
[4]Fusion Safety Program, Idaho National Laboratory, Idaho Falls, USA
[5]Hydrogen Isotope Research Center, University of Toyama, Japan
[6]Institute of Advanced Energy, Kyoto University, Kyoto, Japan
[7]Department of Helical Plasma Research, National Institute for Fusion Science, Toki, Japan

The trapping of tritium in Silicon carbide (SiC) injected from ceramic breeding materials was examined via tritium measurements using Imaging Plate (IP) techniques. Monolithic SiC in contact with ternary lithium oxide (lithium titanate and lithium aluminate) as a ceramic breeder was irradiated in the High Flux Isotope Reactor (HFIR), Oak Ridge, Tennessee, USA. The distribution of photo-stimulated luminescence (PSL) of tritium in SiC was successfully obtained. The tritium incident from ceramic breeders was retained in the vicinity of the SiC surface even after irradiation at 800 °C over the duration of ~3,000 h, while trapping of tritium was not observed in the bulk region.

1. Introduction

Silicon carbide (SiC) is a promising reduced activation structural material for DT fusion blankets because of its high-temperature operation capability and the chemical inertness, especially in the form of SiC fiber-reinforced SiC-matrix composites [1-3]. To establish an effective tritium recovery scheme, it is important to examine the behavior of tritium in SiC under irradiation with neutrons and energetic particles, including tritons created by nuclear reactions of ^{6}Li(n, α)T in breeder materials. The behavior of hydrogen isotopes, including tritium in SiC and its composites, has been discussed in the literature in which data showed six orders of magnitude deviation of the diffusion coefficient [4−8]. In these studies, the hydrogen isotopes retained in the bulk region of SiC have not been directly observed because the gaseous tritium, which is thermally released in the form of HTO, T_2O, HT and/or T_2, is detected in most cases. Because hydrogen isotopes in materials undergo several processes (e.g., trapping-detrapping, diffusion and recombination) before their release, the direct observation of tritium in the materials can extensively elucidate the underlying tritium behavior, including the effects of irradiation with energetic particles. The goal of this study is to evaluate tritium distribution in SiC under irradiation at high temperature using the imaging plate (IP) technique, which is a powerful tool for measuring the tritium distribution on and in the bulk region of materials [9].

Studies on tritium injected as energetic particles into SiC under neutron irradiation at high temperatures assuming fusion reactor conditions (e.g., the proposed design of the helium-cooled ceramic breeder blanket) are not available to date. In Japan-US collaboration program JUPITER-II, monolithic beta-phase SiC and lithium ceramics were irradiated in the High Flux Isotope Reactor (HFIR) to elucidate the compatibility, irradiation effects, and behavior of tritium created in lithium ceramics under neutron irradiation and injected into SiC as MeV energetic particles. In 2011, we reported the compatibility studies of the SiC and lithium ceramics[10]. In the present study, trapping of tritium in-situ injected into SiC samples from LAO and LTO during irradiation in the HFIR was examined, using the IP technique. To the best of our knowledge, this is the first study to successfully evaluate tritium in radioactive ceramic materials irradiated with neutrons and tritium.

2. Experimental

High purity monolithic SiC disc samples (3 mm diameter and ~1 mm in thick), fabricated by Rohm and Hass Co. Ltd. by chemical vapor deposition, were used. The SiC samples were loaded in a helium-filled TZM capsule in contact with discs of lithium aluminate ($Li_{1-x}AlO_{2-x}$: LAO) and lithium titanate ($Li_{2-x}TiO_{3-y}$: LTO) on one side. Irradiation was performed in HFIR of ORNL. The irradiation temperature was 1073 K and the fast neutron (E > 0.1 MeV) fluence was 5.9×10^{25} n/m^2, corresponding to 5.9 displacements by the fast neutrons per atom (dpa) for SiC [11].

After the irradiation, the SiC disk samples were cleaned by ultrasonic cleaning. They were then heated to 150 °C for 30 min to remove contaminants on the surface, prior to being cut in the cross-sectional direction and polishing. The cross-sectional face of the SiC sample was exposed to an IP film (GE Healthcare Japan, BAS-TR2040), as depicted in Fig. 1. The exposure time was 1 h. The photo-stimulated luminescence (PSL) intensity distribution was measured by an IP reader. In the exposure process, a thin polymer film (1.2 μm thick, ING Corporation) was placed between the SiC sample and IP film to avoid contamination from including tritium or other radioactive constituents on the IP film. Because the range of tritium β-rays in the polymer film was approximately 5 μm, the contribution of the thin polymer film to the PSL intensity distribution could be negligible. To separate the contribution of tritium β-rays to PSL signals from that of ^{14}C β-ray excitation, IP measurements were also performed on a reference SiC sample that was irradiated in the HFIR outside the TZM capsule at the same fluence and temperature to prevent irradiation with tritium created in ceramic breeder materials. The IP technique is useful for detecting β-rays from tritium because of the wide dynamic range of the technique, as demonstrated in various metal materials by Otsuka et al. [9]. However, the application of this technique to the measurement of tritium in radioactive materials has been limited because radiation from radionuclides can affect the memorizing system of IP film. Even at a high fluence of neutron irradiation, the low activity of SiC enabled the evaluation of tritium distribution owing to the lower background radiation.

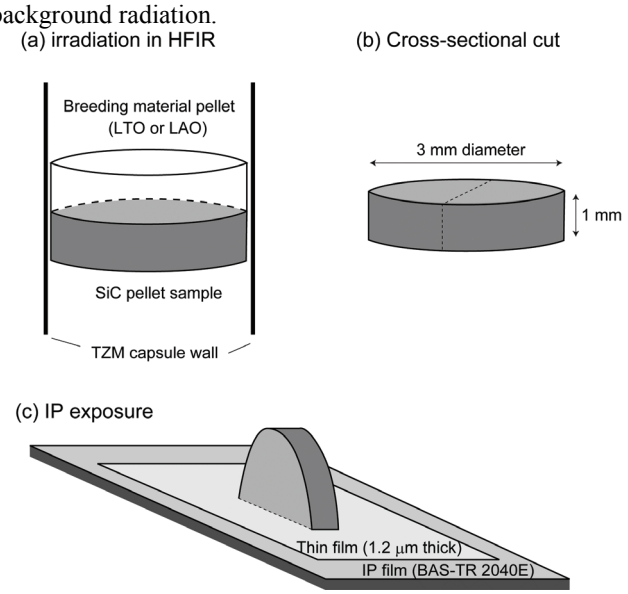

Fig. 1: Schematic of HFIR irradiation and tritium experimental procedures using IP

3. Results and discussion

IP images of cross sections of SiC irradiated in the HFIR with ceramic breeder materials are shown in Fig. 2. To clarify the effect of tritium injection from solid breeder materials, an image showing the reference SiC sample outside the TZM capsule is included in Fig. 2. The upper of the SiC samples in images of (a) and (b) corresponds to the face of SiC in contact with the solid breeder disc. A significantly higher PSL intensity is observed near the incident surface that had been in contact with LTO or LAO during the irradiation. The PSL in the bulk region was observed but was quite lower than that in the vicinity of the incident surface. Comparison of the PSL intensity profile from the reference SiC sample indicates that the PSL in the bulk region is derived primarily from ^{14}C, instead of tritium. Because the PSL extends beyond the SiC samples (green and light blue regions in Fig. 2) owing to the exposure of the IP to β-rays traveling in air from the surface, the PSL does not indicate the existence of tritium outside the SiC samples [12].

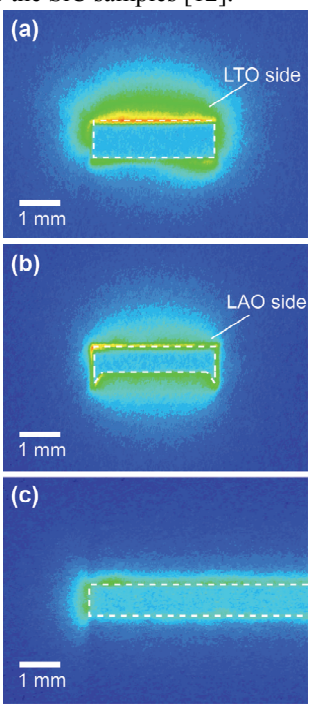

Fig. 2

Fig. 2: IP images of cross-section in SiC samples irradiated in HFIR at 1073 K to 5.9 dpa fluence. The edges on the upper side in the images are surfaces which had been in contact with LTO (a) and LAO (b) under the irradiation. For comparison, an IP image of a reference SiC is shown in (c).

In Figure 3, the PSL intensities of the SiC samples in the direction from the ceramic breeder side to the back faces approximately at the center vertical lines with

arbitrary origins in Fig. 2 are depicted. The thickness of each sample was different because grooves were etched on the posterior face to identify each sample. The PSL intensities in the near-surface regions on the sides of the solid breeders were significantly higher than those on the other sides for SiC samples with both LTO and LAO, although short-range depth profiles in the order of m^{-6}–m^{-5} could not be obtained from the IP measurement owing to its spatial resolution limitation of 25 m^{-6} and the contribution of β-rays traveling in air to the PSL intensities. In the bulk region of the SiC in contact with solid breeders, the PSL intensities were similar to those in the reference SiC sample. This means that the in-situ injected tritium did not undergo long-range diffusion into the bulk during the 1073 K irradiation over a duration of ~3,000 h. Here, all of the ^{6}Li in solid breeders was burned under the present irradiation conditions in the HFIR, according to the calculation obtained from the EASY-2001 inventory and activation calculation system [13].

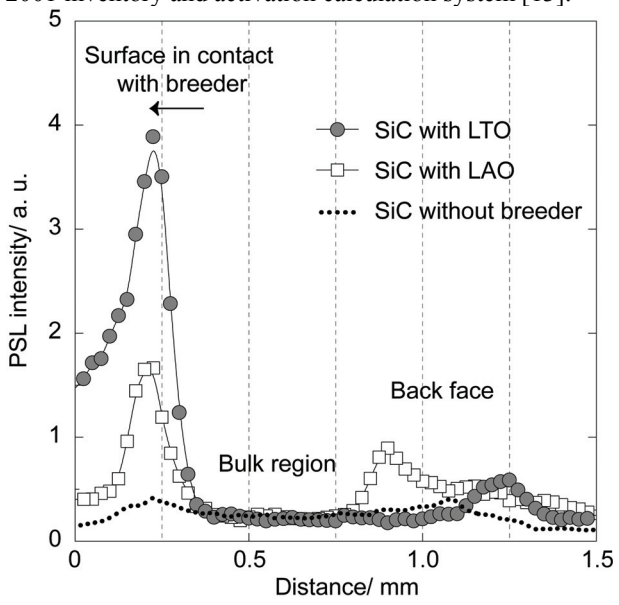

Fig. 3: The PSL intensity distribution on the SiC cross sections in the direction from upper sider to bottom side in the images.

Considering lithium burnup, the depth profiles of the ion ranges of the incident tritium in SiC samples were calculated by an iterative method in terms of its thickness in SiC samples and ceramic breeders (Fig. 4.). In the present experiment, the Li isotope ratio was natural in the solid breeders and tritium was created isotropically with an energy of 2.7 MeV by transformation from ^{6}Li. The stopping cross-sections of triton were based on the parameters reported by Andersen and Ziegler [14]. Because of differences in Li concentrations and stopping cross sections of tritons in solid breeders, the amount of tritium injected in the near surface region of SiC in contact with LTO was estimated to be slightly greater than that with LAO, resulting in higher PSL intensity at the SiC surface in contact with LTO.

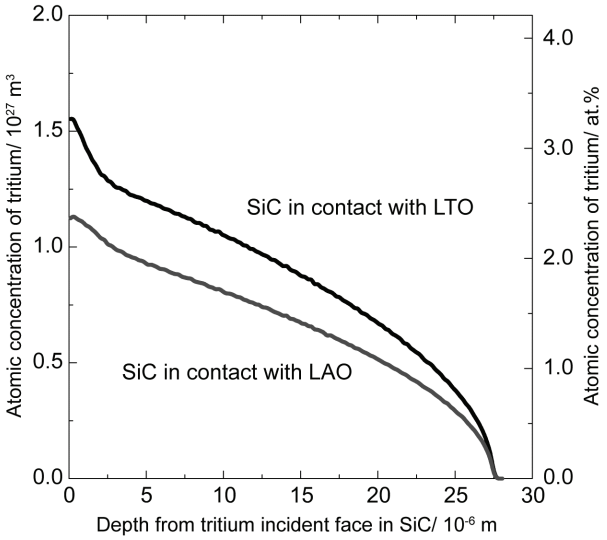

Fig. 4: Depth profiles of tritium ion ranges incident from LTO and LAO in SiC, calculated by an iterative method using semi-empirical parameters of stopping cross sections for hydrogen isotopes [14].

The diffusion of hydrogen isotopes in SiC has been studied by several research groups, and the reported results show deviation (e.g., diffusion coefficients are ranged from 10^{-14} to 10^{-19} m^2 s^{-1} at 1073 K) [6–8]. Assuming the diffusion coefficient to be higher than 10^{-15} m^2 s^{-1}, long-range (> m^{-4}) diffusion of tritium could be expected during annealing in the present experiment, which must be observable in the IP measurements. Causey et al. indicated that effective diffusivity might have been reduced by tritium traps induced by irradiation of tritons and α particles created from ^{6}Li(n, α)T [6, 8]. According to theoretical calculations, the trapping and detrapping of hydrogen by silicon vacancies results in an effective diffusion barrier in the range 4.0–5.3 eV, which is significantly higher than the reported activation energies of hydrogen diffusion in the undamaged SiC [15]. Nagata et al. reported that deuterium ion implanted in SiC single crystals could not be thermally released up to 1073 K owing to the formation of dangling bonds [16]. Given the calculated fluence of the incident tritium depicted in Fig. 4 and the displacement damage, which is based on a binary collision approximation [17], the accumulated damage by tritons could be estimated to be 3 dpa, which is approximately the same order of magnitude as that by neutron irradiation. However, most of the ^{6}Li in the solid breeders was burned, and tritons and α particles were injected into SiC at the initial stage of irradiation within

200 h, while the displacement damage by neutrons was accumulated over 3000 h. Therefore, the tritons and α particles (rather than neutrons) could induce defects, interacting with tritium trapping in the vicinity of the incident surface of SiC. The interaction between tritium and defects induced by the injection of MeV-energy tritons and α particles from the adjoining breeder material may result in the apparent tritium retention in the vicinity of the incident surface of SiC in the present IP study. The PSL intensity could not simply be converted to tritium concentration owing to the absorption of β-rays in SiC and β-rays traveling in air from the SiC surface before their detection by the IP. Further quantitative studies are required to explain the tritium transport processes, including detrapping, diffusion into bulk, and recombination.

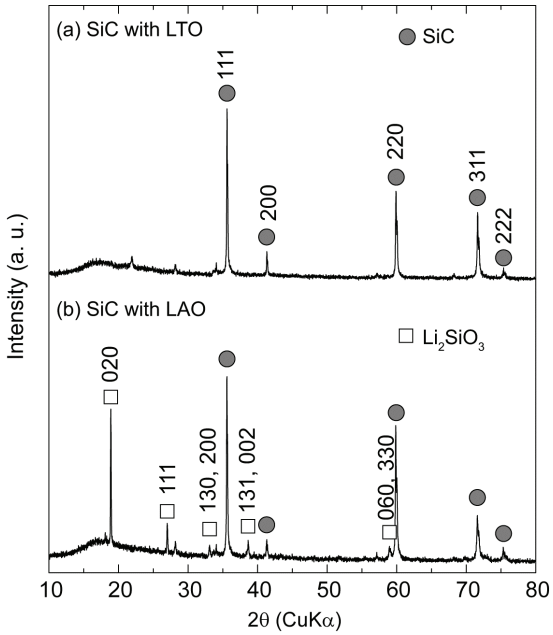

Fig. 5: XRD patterns in SiC samples irradiated in HFIR. During the irradiation, the samples were in contact with different ceramic breeders, (a): LAO, (b): LTO.

In Fig. 5, XRD spectra for SiC faces, which were in contact with the two ceramic breeders, after irradiation are shown. Intensive peaks were assigned to a SiC phase in the sample in contact with LTO (Fig.5 (a)). No significant change was induced by the irradiation on the SiC face in contact with LTO, although observed small peaks at 23° and 28° were assigned to the major peak of SiO_2 and TiO_2, respectively. On the other hand, apparent peaks other than those of a SiC phase were observed in the sample in contact with LAO. The change in the XRD pattern of SiC in contact with LAO indicated the formation of Li_2SiO_3 during the irradiation. Several research groups have reported the formation of Li_2SiO_3 on SiC surfaces with ceramic breeder materials at high temperature in out of-pile-tests [18–20]. Nogami et al. reported the formation of a Li_2SiO_3 layer and the diffusion of lithium and oxygen from solid breeders into SiC over the depth range of 15 μm by annealing tests at 1173–1273 K for 100 h [18]. In this study, the SiC–LTO system exhibited better compatibility than the SiC–LAO system under irradiation of neutrons at 1073 K in terms of the formation of a Li_2SiO_3 phase. Tritium created in Li_2SiO_3 by $^6Li(n,\alpha)T$ was reported to be released in the temperature range 800–1000 K [21]. The IP results, as described in Fig. 3, indicated that the PSL intensity in SiC in contact with LAO was considerably lower than that with LTO while the difference in the amount of the incident tritium was not significant in the calculation result depicted in Fig. 4. The release of tritium at 1073 K could be accompanied by Li_2SiO_3 formation, which would result in the considerably lower PSL intensity in SiC surface in contact with LAO.

4. Summary

PSL intensity distribution of tritium in SiC was successfully obtained using the IP technique that separated the contribution of ^{14}C β–rays to the PSL of IP films from that of tritium β-rays. The PSL intensity in the vicinity of the SiC surface in contact with LAO and LTO was significantly high, while PSL was not detected in the bulk region. The tritium incident from the adjoining breeding materials was retained in the vicinity of the SiC surface and did not diffuse into the bulk region even after irradiation at 1073 K over a duration of ~3,000 h. The PSL intensity near the SiC surface in contact with LTO was higher than that with LAO. Formation of a Li_2SiO_3 phase was identified in SiC in contact with LAO while no phase formation was observed in SiC in contact with LTO. The formation of the Li_2SiO_3 phase on SiC resulting from its reaction with LAO during irradiation and/or the smaller amount of incident tritium were considered to presumably caused significantly smaller PSL intensity near the SiC surfaces in contact with LAO.

References

[1] Y. Katoh et al., *J. Nucl. Mater.*, **403** (2010) 48-61.
[2] S.J. Zinkle and N.M. Ghoniem, *Fusion Eng. Des.*, **51-52** (2000) 55-71
[3] B. Riccardi et al., *J. Nucl. Mater.*, **329-333** (2004) 56-65.
[4] K. Isobe et al., *Fusion Eng. Des.*, **85** (2010) 1012-1015
[5] Y. Oya et al., *J. Nucl. Mater.*, **337-339** (2005) 595-599
[6] R.A. Causey et al., *J. Am. Ceram.* Soc. 61 (1978) 221-225
[7] G. A. Esteban et al., *J. Nucl. Mater.*, **307-311** (2002) 1430-1435

[8] R.A. Causey et al., *J. Nucl. Mater.*, **203** (1993) 196-205
[9] T. Otsuka et al., *J. Nucl. Mater.*, 415 (2011) S769-S772
[10] H.Katsui et al., *Fusion Science and Technology*., 60 (2011) 288-291
[11] G. Newsome et al., *J. Nucl. Mater.*, 371 (2007) 76-89
[12] K. Hashizume et al., *J. Nucl. Mater.*, **367-370** (2007) 876-881
[13] R.A. Forrest, *UKAEA FUS* 449 (2001).
[14] H. H. Andersen and J. F. Ziegler, New York: Pergamon Press (1977)
[15] B. Aradi et al., *Phys. Rev. B*, **69** (2004) 233202
[16] S. Nagata et al., *J. Nucl. Mater.*, **128&129** (1984) 760-763
[17] J. Ziegler, <http://www.srim.org>.
[18] S. Nogami et al., *J. Nucl. Mater.*, **386-388** (2009) 628-630
[19] T. Sample et al., *J. Nucl. Mater.*, **212-215** (1994) 1529-1533
[20] H. Kleykamp, J. *Nucl. Mater.*, **283-287** (2000) 1385-1389
[21] Y. Nishikawa et al., *J. Nucl. Mater.*, 367-370 (2007) 1371-1376

4-7 Common Task(1) INTEGRATED MATERIALSYSTEM MODELING OF FUSION BLANKET

A. Sagara[1], R. Nygren[2], M. Miyamoto[3], D. Nishijima[4],R. Doerner[4], S. Fukada[5],
Y. Oya[6], T. Oda[7], Y. Watanabe[8†], K. Morishita[8], F. Gao[9], T. Norimatsu[10], H. Hashizume[11]

[1]*National Institute for Fusion Science, Toki 509-5292, Japan, sagara.akio@LHD.nifs.ac.jp*
[2]*Sandia National Laboratories, Albuquerque, NM 87123-1129, USA, renygre@sandia.gov*
[3]*Shimane University,Matsue, Shimane 690-8504, Japan, miyamoto@riko.shimane-u.ac.jp*
[4]*University of Californian, San Diego, CA 92093-0417, USA, dnishijima@ferp.ucsd.edu, rdoerner@ucsd.edu*
[5]*Kyushu University, Fukuoka 812-8581, Japan, sfukada@nucl.kyushu-u.ac.jp*
[6]*Shizuoka University, Shizuoka 422-8529, Japan, syoya@ipc.shizuoka.ac.jp*
[7]*Department of Materials Science and Engineering, University of Tennessee, USA, oda@flanker.n.t.u-tokyo.ac.jp*
[8]*Institute of Advanced Energy, Kyoto University, Kyoto 611-0011, Japan, morishita@iae.kyoto-u.ac.jp*
([†] Current affiliation: Japan Atomic Energy Agency, Aomori 039-3212, Japan)
[9]*Pacific Northwest National Laboratory, Richland, WA 99352, USA, fei.gao@pnl.gov*
[10]*Institute of Laser Engineering, Osaka University, Suita, Osaka 5650871, Japan, norimats@ile.osaka-u.ac.jp*
[11]*Tohoku University,Sendai 980-8579, Japan, hidetoshi.hashizume@qse.tohoku.ac.jp*

The blanket of fusion reactors is a multifunctional system that breeds tritium, harvests heat from the burning plasma, and protects the other components and the environment.The common task in the US-J TITAN (Tritium, Irradiation and Thermofluid for America and Nippon) project identifies cross-linkedconsiderations in the blanket system modeling on the basis of the material research in each task. In this paper,we review the main outputs of this task:elucidation of the effect of helium on deuterium retention in the tungsten wall, analysis of tritium transfer in a Pb-Li liquid breeder, experimental and computational studies on the effects of radiation damage on hydrogen trapping, and modeling of the tritium barrier in a double-tube heat exchanger.

I. INTRODUCTION

Fusion systems of magnetically confined fusion energy (MFE) or inertial fusion energy (IFE) are enclosed within a blanket system that breeds tritium, converts the energy of fusion output into heat for power conversion, transfers this heat with high efficiency, and provides nuclear shielding to the in-vessel components and the environment. Thus, the blanket system must be optimized not as a single function but as an integrated multifunctional system incorporating the boundary conditions of burning core plasmas, plant requirements for power conversion, and tritium handling (involving safety issues and environmental protection). In this project, crosslinkingbetween taskswas regarded as a multi-physics modeling for the optimal design of a fusion blanket.

For each task, tritium transfer, thermofluid mechanisms, and irradiation synergy are investigated under typical reactor conditions: plasma-wall interactions with heat and particles, nuclear and chemical reactions in the blanket material, MHD effects in high magnetic field, heat and mass transfer in each subsystem of the heat exchanger and tritium separation system, and the intermittent effects of intense transient heat loads. The time constants for tritium and material behaviors are separated and evaluated from these tasks, and the characteristics of the system components are verified byanexperiment.

The common task createsa self-consistent modelby integrating the separate systems of tritium, heat, and thermofluid. At the same time, via feedback of importantconsiderationsto each task,the validity of our experimental results is assessed in the interfaces between research goals in each task,in order to promote the development of an integrated system modeling methodology.

In this review, we focus on material research in Tasks 1-1; 1-2; and 2-1, 2-2, 2-3. The common critical issue in MFE and IFE in terms of fuel self-sufficiency and environmental safety is tritium mass transfer through the heat exchangers. Therefore, a typical heat-exchanger system,designed to identify appropriate boundary conditions for material researches, is also discussed.

II. HELIUM (He) EFFECT ON DEUTERIUM (D) RETENTION IN TUNGSTEN

A critical consideration in fusion reactor design is the tritium recycling properties of the first wall of the fusion blanket. The effects of helium on the retention of hydrogen isotopes in tungsten have been extensively reported, but remain contentious. While some studies have reported that retention is enhanced by helium implantation, others have reported the opposite[2-10].

These discrepancies may be attributed to differences in experimental conditions. The results of several previous studies are shown in Figs. 1 and 2,and numerical data are summarized in Table 1. Results for D retention by energetic ion implantation (open symbols in Figs. 1 and 2) are consistent across studies, with D retention saturating at around 3×10^{20} D^+ m^{-2}, even for He^+fluenceas large as 10^{22} He^+ m^{-2}. Given that D retention in the absence of $He^+$is ~1×10^{20} D^+ m^{-2}, we observe that He^+ implantation enhances D retention by two- to three-fold. Abovea fluence of 1×10^{19} He^+ m^{-2}, He exerts no further enhancing effect on D retention. While He bubble formation and radiation damages create potential D trapping sites, higher density and larger He bubbles may enhance desorption of D by suppressing its diffusion toward the bulk tungsten. The lack of annealing effects in ion implantation experiments would have reduced the ion flux,thereby contributing to D retention in the implant region. In different plasma exposure experiments, D retention is quite scattered even at the same D^+fluence, as shown in Fig. 1. A strong mediator of D retention in tungsten is the formation of He bubbles and occupation of trap sites by He atoms. As previously mentioned[10],tungsten exposed to He plasma at a high temperature (1600 K)exhibits reduced He retention capacity,while additional exposure to D plasma exposure induces D trapping. However, exposure to lower-temperature He plasma enhances the formation of He bubbles and He retention, leading to reduced D retention.

Under Task 1-1, the effects of He on D retention of tungsten were clarified in D+He mixed plasma exposure experiments, conducted in the Plasma Interaction with Surface and Components Experimental Simulator(PISCES) facility at the University of California, San Diego [9,11]. Complementary ion irradiation experiments were performed at Shimane University [5]. Transmission electron microscopy (TEM) observations of prethinned W samples exposed to mixed D+He plasma in PISCES revealed the formation of high-density nanosized He bubbles in the near surface region, accompanied by suppression of blister formation and significantlyreduced D retention [9]. The volume fraction of bubbles, estimated from TEM cross-sectional observations and ellipsometric measurements, exceeds the percolation threshold, beyond which bubbles interconnect at the near surface region [11]. The percolating bubble clusters provide a diffusion path to the surface for D atoms exposed to the plasma, allowing them to escape. D retention is similarly reduced under the sequential irradiation of helium and deuterium ions. Preirradiation of 3 keVHe^+at high fluence (above 1.0×10^{23} He^+/m^2) results in a drastic reduction of D retention. On the other hand, at lower He fluences(up to 1.0×10^{22} He^+/m^2), retention increases with increasing He fluence [5]. This suggests that defects induced by He irradiation may trap D atoms at lower He fluences, where He bubbles are not yet interconnected.

To verify the abovementioned experimental observations, we consider that multiscale modeling,combined with various simulation techniques (e.g., molecular dynamics simulation and finite element method), is required.Multiscale modeling can capture a wide range of spatial and temporal phenomena occurring in real-time fusion reactors. For example, energy is transferred from implanted D to target W atoms in a femtosecond timeframe, while He bubbles are expected to form and migrate over a much longer period, given that the implantation depth of D in Wand the diffusion distance of D in W areon the order of several millimeters.

III. TRITIUM ABSORPTION AND DIFFUSION IN Pb-Li

Task 1-2 of the TITAN project is the quantitative analysis of tritium absorption and diffusion in a promising blanket cooling material (Pb-Li)[12-17]. First, the solubility of T in Pb-Li must be determined. Previous data of H isotope solubility in Pb-Li eutectic alloys are highly scattered. Therefore, in our study, solubility measurements were carried out by two different methods: 1) a constant volume method at the Idaho National Laboratory (INL) and 2) a transient permeation method at Kyushu University. The former experiment determined T solubility in Pb-Li,while the latter determined the solubility and diffusivity of H and D in Pb-Li. The results are presented in a separate Task 1-2 paper of the special issue: “Clarification of tritium behavior in Pb-Li blanket system” [18].

The second task is system design integration, with the application of aPb-Li breeding material to the fusion reactor systems.Pb-Li is proposed as a test blanket module (TBM) in ITER, although other candidates, such as He-cooled lithium lead(HCLL) and dual coolant lithium lead(DCLL),have been proposed by the European Unionand United States. In Japan, a water-cooled ceramic (Li_2TiO_3) breeder blanket is used as the ITER–TBM.Blanket designs using Pb-Li as coolant and breeder of magnetic fusion have not been considered previously. On the other hand, a wet-wall Pb-Li design is proposed for the Koyo-fast commercial fusion reactor.A schematic of this design, with a list of design parameters, is shown in Fig. 3. Pb-Li flows intothe top of the reactor chamber to protect the metal chamber from damage by heavy neutron irradiation. Besides its role asa tritium breeder, Pb-Li receives heat from particles created by D-T fusion and the n-^{6}Li reaction within the blanket.The energy conversion and tritium recovery systems in the external Pb-Li flow for IFE are essentiallysame as those for MFE, except that the flowing Pb-Li directly comes in contact with the high-temperature plasma on the wet wall ofthe vacuum chamber. Tritium concentration in the Pb-Li flow is controlled by the tritium generation rate in the chamber and by the Pb-Li flow rate. The Pb-Li temperature is maintained between 300 and 500°C. Majority of the tritium is recovered by a Pb-Li-He counter-current flowing system, but a small portion escapes from the outlet of the recovery system into the heat exchanger.

Tritium balance and permeation rate through heat-exchanger tubes were initially estimated as 255 Ci/day. We consider that this comparatively high tritium permeation rate can be mitigated by coating the heat exchanger tubes with ceramic. A 1000-fold reduction in permeation implies a tritium leakage ratebelow 1 Ci/day, which complies withthe safety standards. Experimental verification of permeation reduction is presented in the Task 1-2 section of the abovementioned paper.

IV. EFFECTOF RADIATION ON TRITIUM RETENTION IN TUNGSTEN EXPOSED TO ION AND NEUTRON IRRADIATIONS

The effect of radiation on tritium accumulation in tungsten (a promising candidate for the first wall of fusion blankets) has attracted much attention since radiation damage is likely to increase tritium retention. Most previous research has focused on ion irradiation rather than neutron irradiation; however, the formation of radiation damage structures depends on the irradiation conditions. Hence,accurate prediction of tritium retention in fusion reactors requires careful analysis and interpretation of these experimental results, which has not necessarily been accomplished to date. In Task 2-1, the effects of neutron and ion irradiation were investigated by computer simulations [19] as well as by irradiation experiments with neutrons and ions[20-22].

We developed a simulation code based on the Monte Carlo technique for modeling the accumulation and release behaviors of hydrogen isotopes interacting with vacancies in tungsten[19]. The code utilizes the results of first-principle calculations as well as data obtained in previous experiments.It can integrate systems containing vacancies from external sources, for example, from TRIM code.We then evaluated the behavior of hydrogen loaded by plasma exposure or ion irradiation.The results are presented as depth profiles in tungsten and thermal desorption spectra. From the simulation results, hydrogen introduced by plasma exposure was found to be localized ina region of high defect density created by ion irradiation of tungsten. In contrast, in neutron-irradiated tungsten, hydrogen was spread over a wide region(Fig. 4). Thermal desorption behavior of introduced hydrogen also differed between ion-irradiated and neutron-irradiated samples, consistent withthe experiment [20]. These differences are attributed to a difference in the vacancy distribution between ion-irradiated (localized distribution) and neutron-irradiation (uniform distribution) systems. In future work, the accuracy of simulation results will be improved by(1) balancinglong-time irradiation processes with a rapid diffusion process, (2) preventing unrealistic accumulation of hydrogen, and (3) modeling the release of hydrogen forcibly loaded into a region alreadycontaining high hydrogen density.

V. MULTISCALE MODELING OF MICROSTRUCTURAL CHANGE IN SiC DURING IRRADIATION

The main component of SiC/SiC composites,used as blanket structural materials for nuclear fusion reactors, is cubic silicon carbide (β-SiC). Fusion reactor materials are subject to various point defects such as vacancies (V), self-interstitial atoms (SIAs), and those induced by helium and hydrogen atoms displaced by high-energy incident neutrons from the fusion core plasma.These processes occur on picosecond-ordertimeframes and across nanometer-orderdistances. The resulting defects thermally migrate and form defect clusters (SIAclusters, Vclusters, and cavities) over submicrosecondtimes and acrosssubmicrometerdistances. The microstructural changes caused by defect clustersdegrade the performance of the material; therefore,such changes should be accurately predicted and controlled. Material response to irradiation is inherently a multiscale phenomenon, as described above, and should be modeled by multiple complementation of experimental and computational techniques over appropriate time and distance scales [23,24]. To understand the microstructural changes in β-SiC during irradiation, a variety of transmission electron microscopy experiments have been conductedon material test fission reactors and ion accelerators. While these experiments have elucidated the species and sizes of defect clusters under various irradiation conditions [25,26], the formation mechanism of defect clusters remains poorly understood. In the present study, the kinetics of defect cluster formation in β-SiCwere numerically evaluated through a multiscale modeling approach, focusing on the nucleation and growth processes of SIAclusters. We note thatSiC is a binary compound comprising silicon and carbon atoms; therefore, defect clusters of various chemical compositions could be formed, depending on the irradiation conditions. Modeling defect cluster formation in a compound material requires special care, as discussed below.

First, the formation, binding, and migration energetics of β-SiCdefects were investigated by classical molecular dynamics (MD) and molecular statics (MS), combined with the method of Gao–Weber empirical interatomic potential [27], which employs not only experimental observations but also ab-initio calculations. In the MD and MS calculations, the formation energy of the most energeticallyfavorable SIAclusters was derived as a function of size and chemical composition ratio (Si/C) of the clusters [28,29]. Knowledge of the formation energy is crucial forevaluating binding energy between defects since the binding energy corresponds to the thermal stability of the defects. Migration energies of isolated silicon and carbon interstitials(SIAs) were also derived[30].

On the basis ofthe defect energetics obtained from the atomistic calculations, the nucleation and growth processes of SIAclusters were then investigated by the kinetic MonteCarlo (KMC) method. Here the KMC model constructed allows for statistical fluctuationsin the inflow/outflow of isolated SIAs into/from an SIAcluster. In the KMC simulations, the ratios of the diffusion

fluxesbetween silicon and carbon interstitials ($D_I^{Si}C_I^{Si}$:$D_I^{C}C_I^{C}$) were set as 1:1, 1:10, and 1:100, while the total diffusion flux ($D_I^{Si}C_I^{Si}$ + $D_I^{C}C_I^{C}$) was kept constant at 1.0×10^{19} m^2/s. The formation kinetics of SIAclusters in β-SiC during irradiation wereroughly classifiable into two temperature-dependent classes [31]. At relatively high temperatures, the thermal stability of an SIAcluster is crucial, and the chemical composition of the cluster is almost stoichiometric (i.e., Si/C=1), as shown in Fig. 5-(a). In contrast, at relatively low temperatures, where cluster thermal stability is no longer crucial, the composition of SIAclusterscan deviate markedly from stoichiometric(Fig. 5-(b)). Such information is very important for prediction of the microstructural changes in compound materials during irradiation. As such, it will form thebasis of a model incorporating reaction-rate-theory analysis and phase-field method, for evaluating microstructural changesover aprolonged time and lengthscales.

VI. LEAKAGE CONTROL OF TRITIUM THROUGH HEAT CYCLES OF FUSION REACTOR

Tritium leakage by diffusion through heat exchangers occurs in both MCF and IFE. While retaining the system efficiency, the tritium leakage must be reduced by a factor of $1/10^{10}$ to reach that of a current fission plant. To reduce tritium permeation from the primary liquid metal or sodium loop into the secondary water loop, a heat exchanger incorporating small-diameter tubes containing an oxidizer was proposed [32]. An inert gas containing a small amount of oxidizer flows through the tubes, oxidizing tritium intercepted from the primary liquid metal coolant. The tritiated water was conveyed to a tritium recovery system, minimizing leakage into the secondary water loop. Evaluation of this design indicated that the tritium leakage through the heat exchanger was reduced by $1/10^5$, with an acceptable increase in the size ofthe heat exchanger. This scheme is compatible with the coating technique, using compounds such as Er_2O_3 and ZrO_2,which may further reduce permeation by a factor of $1/10^{4,18)}$.

The permeation rate and chemical form of tritium after permeation are known to depend on surface conditions and temperature. Figure 6 shows a simplified model of tritium permeation through the wall of a heat exchanger. A virtual gap with zero thickness between the wall and the liquid LiPbis assumed. Thetritium concentration in metals and the tritium partial pressure in the gapare assumedto be related by Sieverts' law. Following the permeation of wet surfaces, almost all of the tritium atoms form HTO through isotope exchange reactions. However,some tritium forms $T_2$when the surface is dry and the temperature is high. Henry's law is assumed to relate the tritium concentration in pressurized water to the T_2 in the vapor phase.

Figure 7 shows cross sections of the steam tube proposed in this study. The thick walls of the tube are fitted with small-diameter tubes filled with an oxidizer and carrier gas. Tritium permeating from the outer LiPb will be oxidized on the surfaces of the small tubes and conveyed to the tritium recovery system, thereby reducing the amount of tritium reaching the inner surface of the steam pipe.

In the following calculations, the partial pressures of tritium in the outer and inner virtual gaps are assumed as 1 Pa and zero, respectively. The permeation rate is 8.3×10^{12} atoms m/m^2 $Pa^{1/2}$ s at 745K. The solubility and thermal conductivity are 7×10^{21} atoms/m^3 $Pa^{1/2}$ and 20 W/m K, respectively. The apparent thermal conductivity and permeation of tritium from outer to inner surfaces are calculated using a commerciallyavailable finite element code (ANSYS).

Figure 8 shows the normalized tritium permeation through a heat exchanger maintained at a constant heat flow. The expected reduction of tritium flow is approximately $1/10^5$.

Applying this system to the heat cycle of a 1 GWe plant, the tritium concentration in the second water loop is predicted as 400MBq/cm^3 afterone year of full power operation. Therefore, for safety reasons, a tritium recovery system must be designed for the second loop. Almost all of the injected tritium can be recovered and reused asfuel after isotope separation.

VII. SUMMARY[33]

The common task in the US-J TITAN project identifies cross-linked considerations in the blanket system modeling on the basis of the material research in each task. The results are summarized as follows:

(1) The helium effects on hydrogen isotope retention in tungsten were investigated by reviewing the results of previousstudies and by conducting D+He mixed plasma exposure experiments in PISCES. These results reveal that D retention is reduced by high-density He bubbles forming in the near surface region.

(2) Research into permeability, diffusivity, and solubility of hydrogen isotopes in aPb-Li alloy as a tritium breeder is summarized. The blanket design must achieve a low tritium leak to the outside and high tritium recovery from a breeder loop.

(3) A simulation code to model the accumulation and release of hydrogen isotopes interacting with vacancies in tungsten was developed using a Monte Carlo technique. Simulation results revealedthat the behavior of hydrogen isotopes depends strongly on the mode of irradiation (i.e., whether the specimen is ion- or neutron-irradiated).

(4) Multiscale modeling of microstructural changes in a binary compound material during irradiation has elucidated the nucleation and growth processes of defect clusters.

(5) Tritium permeation through a heat exchanger equipped with double tubes filled with an oxidizer can be reduced to $1/10^4$ that of bare stainless tubes, without degrading the heat exchange rate.

ACKNOWLEDGMENT

This work is supported by the Japan–US cooperation program TITAN sponsored by Japan-MEXT and US-DOE.

REFERENCES

[1] T. Muroga, D.K. Sze, K. Okuno, T. Terai, A. Kimura, R.J. Kurtz, A. Sagara, R. Nygren, Y. Ueda, R.P. Doerner, J.P. Sharpe, T. Kunugi, N.B. Morley, Y. Hatano, M.A. Sokolov, et al., Midterm Summary of Japan–US Fusion Cooperation Program TITAN: Fusion Sci. Technol. 60 (2011) 321–328.

[2] Y.Oya, M Kobayashi, R. Kurata, W. Wang, N. Ashikawa, A. Sagara, N. Yoshida, Y. Hatano, K. Okuno: J. Nucl. Mater. 415 (2011) S701–S704.

[3] S.Nagata, K. Takahiro: J. Nucl. Mater. 290–293 (2001) 135–139.

[4] H.Iwakiri, K. Morishita, N. Yoshida: J. Nucl. Mater. 307-311 (2002) 135–138.

[5] Y.Sakoi, M. Miyamoto, K. Ono and M. Sakamoto: J. Nucl. Mater., in press, http://dx.doi.org/10.1016/j.jnucmat.2012.10.003.

[6] H.T.Lee, A.A. Haasz, J.W. Davis, R.G. Macaulay-Newcombe, D.G. Whyte, G.M. Wright: J. Nucl. Mater. 363–365 (2007) 898–903.

[7] B.I.Khripunov, A.N. Brukhanov, V.M. Gureev, V.S. Koidan, S.N. Kornienko, S.T. Latushkin, V.B. Petrov, A.I. Ryazanov, E.V. Semenov, V.G. Stolyarova, V.N. Unezhev, L.S. Danelyan, V.S. Kulikauskas, V.V. Zatekin, V.G. Vostrikov, E.A. Romanovsky: J. Nucl. Mater. 415 (2011) S649–S652.

[8] H.T.Lee, A.A. Haasz, J.W. Davis, R.G. Macaulay-Newcombe: J. Nucl. Mater. 360 (2007) 196–207.

[9] M. Miyamoto, D. Nishijima, Y. Ueda, R.P. Doerner, H. Kurishita, M.J. Baldwin, S. Morito, K. Ono and J. Hanna: Nucl. Fusion 49 (2009) 065035.

[10] D.Nishijima, T. Sugimoto, H. Iwakiri, M.Y. Ye, N. Ohno, N. Yoshida, S. Takamura: J. Nucl. Mater. 337–339 (2005) 927–931.

[11] M. Miyamoto, D. Nishijima, M.J. Baldwin, R.P. Doerner, Y. Ueda, K. Yasunaga, N. Yoshida and K. Ono: J. Nucl. Mater. 415 (2011) S657–S660.

[12] Y. Edao, S. Fukada, S. Yamaguchi, H. Nakamura: Fus. Engng. Des.,85 (2010) 53–57.

[13] Y. Edao, H. Okitsu, H. Noguchi and S. Fukada: Fus. Sci. Technol., 60 (2011) 1163–1166.

[14] Y. Edao, H. Noguchi, S. Fukada:J. Nucl. Mater., 417 (2011) 723–726.

[15] S. Fukada, Y. Edao: J. Nucl. Mater.,417 (2011) 727–730.

[16] D. Matsuyama, T. Oda, S. Fukada: Chem. Phys. Lett., 483 (2009) 214–217.

[17] Y. Edao, S. Fukada, H. Noguchi, Y. Maeda, K. Katayama: Fus. Sci. Technol. 56 (2009) 831–835.

[18] S. Fukada, T. Terai, S. Konishi, K. Katayama, T. Chikada, Y. Edao, T. Muroga, M. Shimada, B. Merrill, D. K. Sze: Mater. Trans. this special issue.

[19] T. Oda, M. Shimada, K. Zhang, P. Calderoni, Y. Oya, M. Sokolov, R. Kolasinski, J.P. Sharpe, Y. Hatano: Fus. Sci. Technol. 60 (2011) 1455–1458.

[20] M. Shimada, Y. Hatano, P. Calderoni, T. Oda, Y. Oya, M. Sokolov, K. Zhang, G. Cao, R. Kolasinski, J.P. Sharpe: J. Nucl. Mater. 415 (2011) S667–S671.

[21] Y. Oya, M. Shimada, M. Kobayashi, T. Oda, M. Hara, H. Watanabe, Y. Hatano, P. Calderoni, K. Okuno: PhysicaScripta T145 (2011) 014050.

[22] Y. Shimada, G. Cao, Y. Hatano, T. Oda, Y. Oya, M. Hara, P. Calderoni: PhysicaScriptaT145 (2011) 014051.

[23] S. Sharafat and K. Morishita: J. At. Energy Soc. Jpn. 50 (11) (2008) 724.

[24] K. Morishita and S. Sharafat: J. At. Energy Soc. Jpn. 50 (12) (2008) 803.

[25] Y. Katoh, N. Hashimoto, S. Kondo, L.L. Snead, A. Kohyama: J. Nucl. Mater. 351 (2006) 228–240.

[26] T. Yano and T. Iseki: Philos. Mag. A 62 (1990) 421–430.

[27] F. Gao and W.J. Weber: Nucl. Instrum. Meth. B 191 (2002) 504–508.

[28] Y. Watanabe, K. Morishita, A. Kohyama: J. Nucl. Mater. 417 (2011) 1119–1122.

[29] K. Morishita, Y. Watanabe, A. Kohyama, H.L. Heinisch, F. Gao: J. Nucl. Mater. 386–388 (2009) 30–32.

[30] Y. Watanabe, K. Morishita, A. Kohyama, H.L. Heinisch, F. Gao: Nucl. Instrum. Meth. B 267 (2009) 3223–3226.

[31] Y. Watanabe, K. Morishita, Y. Yamamoto: Nucl. Instrum. Meth. B 269 (2011) 1698–1701.

[32] T. Norimatsu, H. Saika, H. Homma, M. Nakai, S. Fukada, A. Sagara and H. Azechi: Fus. Sci. Technol. 60 (2011) 893–896.

[33] A. Sagara, R. Nygren, M. Miyamoto, D. Nishijima, R. Doerner, S. Fukada, Y. Oya, T. Oda, Y. Watanabe, K. Morishita, F. Gao, T. Norimatsu: Materials Transactions, 54 (2013) 477–483.

Table 1 Summary of conditions of various He+ and D+ implantation and plasma exposure experiments.

	Ion energy: He D	Ion flux: $\Gamma_{He}/He^+ m^{-2} s^{-1}$ $\Gamma_D/D^+ m^{-2} s^{-1}$	Ion fluence: $\Phi_{He}/He^+ m^{-2}$ $\Phi_D/D^+ m^{-2}$	Implantation temperature
○Y. Oya	3.0 keV 3.0 keV	$(0.2–1.8) \times 10^{18}$ 1.0×10^{18}	$(0.2–1.8) \times 10^{22}$ 1.0×10^{22}	R.T.
◇S. Nagata	10 keV 1 keV	— —	$4.2 \times 10^{18}–6.0 \times 10^{21}$ 3.0×10^{21}	R.T.
☆H. Iwakiri	8 keV 4 keV	— —	$(0.1–2.0) \times 10^{21}$ $10^{19}–10^{22}$	R.T.
△Y. Sakoi	3 keV 3 keV	5.0×10^{18} 1.0×10^{18}	1.0×10^{21} 1.0×10^{21}	R.T.
●H. T. Lee	500 eV 500 eV	$10^{18}–10^{19}$ 1.0×10^{19}	$10^{21}–10^{23}$ $(0.5–2.0) \times 10^{23}$	300 K
◆B. I. Khripunov	4 MeV 250 eV	— —	$(1.0–3.0) \times 10^{22}$ $(0.27–1.3) \times 10^{26}$	373 K
★H. T. Lee	500 eV 500 eV	$10^{18}–10^{19}$ 1.0×10^{19}	3.0×10^{21} 2.0×10^{23}	300 K
▲M. Miyamoto	120 eV 120 eV	5.0×10^{20} 1.0×10^{22}	2.5×10^{24} 5.0×10^{25}	573 K
▼D. Nishijima	20–25 eV 80 eV	$(0.25–4.8) \times 10^{22}$ 4.0×10^{21}	$(1.8–9.0) \times 10^{21}$ 3.0×10^{25}	700–1600 K (He) 550 K (D)
◧Y. Sakoi	10 eV 3 keV	1.0×10^{21} 1.0×10^{18}	3.0×10^{22} 1.0×10^{21}	573 K (He) R.T. (D)

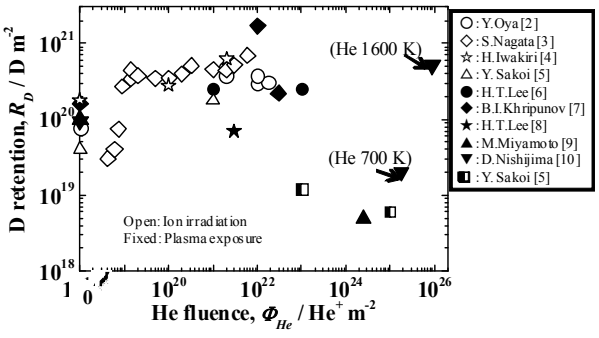

Fig. 1D retention in ion-implanted or plasma-exposed tungsten, as a function of He^+ fluence.

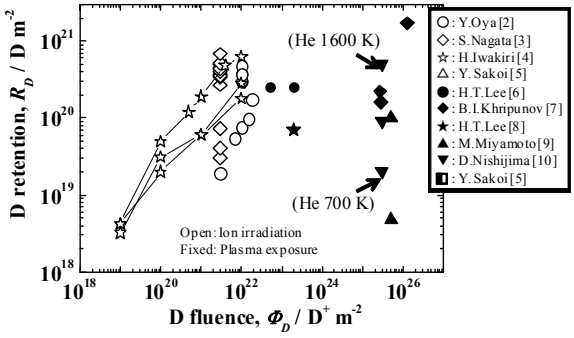

Fig. 2D retention in ion-implanted or plasma-exposed tungsten, as a function of D^+ fluence.

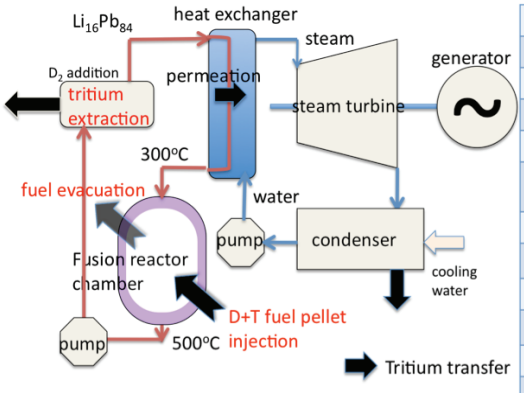

Total power	1 GWt
$Li_{16}Pb_{84}$ inlet temp.	300 °C
$Li_{16}Pb_{84}$ outlet temp.	500 °C
$Li_{16}Pb_{84}$ mass flow rate	18.4 t/s
T generation rate	1.43 MCi/day
T concentration in $Li_{16}Pb_{84}$	8.6×10^{-9} T/$Li_{16}Pb_{84}$
T partial pressure in LiPb	1.8×10^{-3} Pa
Heat transfer coefficient of heat exchanger	5.0×10^3 W/m^{2}K
Surface area of het exchanger	690 m^2
Logarithmic temperature difference in heat exchanger	290 °C
Estimated T leak rate	255 Ci/day
Rate-determining step	T permeation through tube wall

Fig. 3$Li_{16}Pb_{84}$ loop and steam Rankine cycle in a laser fusion reactor.

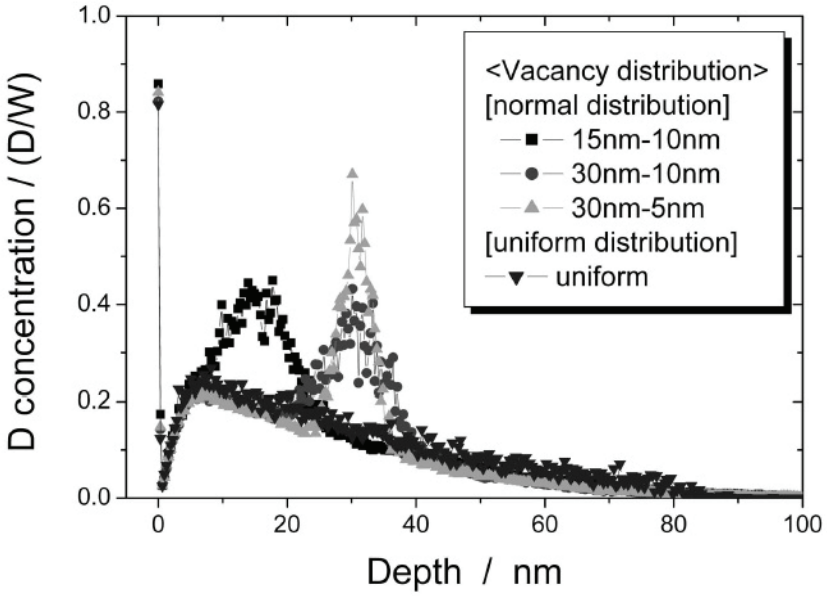

Fig. 4Monte Carlo simulation results on distribution of deuterium implanted into ion-irradiated or neutron irradiated tungsten at 473 K. Deuterium implantation depth is around 5 nm, corresponding to a plasma exposure of 200 eV deuterium. The label "15–10 nm" signifies that the vacancy distribution is centrally localized at 15 nm with FWHM 10 nm (assuming normal distribution), and "uniform" signifies a uniform distribution of defects. The localized and uniform distributions correspond to ion and

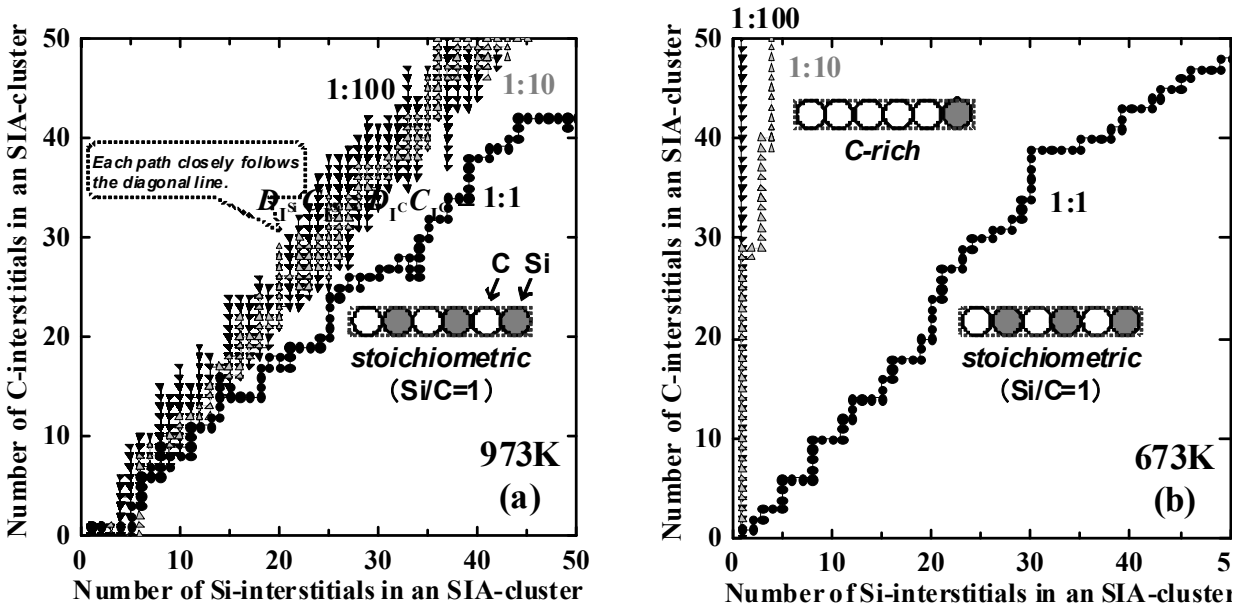

Fig. 5KMC simulations of nucleation and growth path of SIA clusters in β-SiC at (a) 973 K and (b) 673 K.

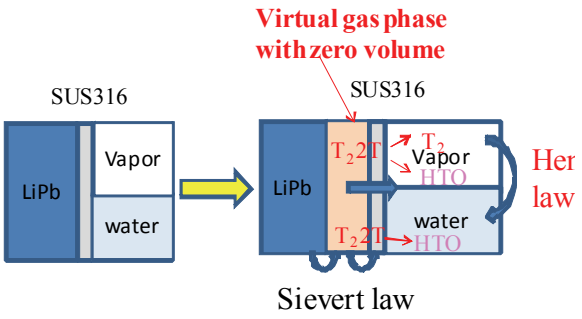

Fig. 6Model of tritium permeation through a wall of a heat exchanger.

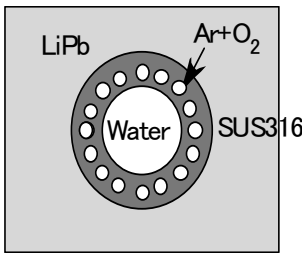

(a)

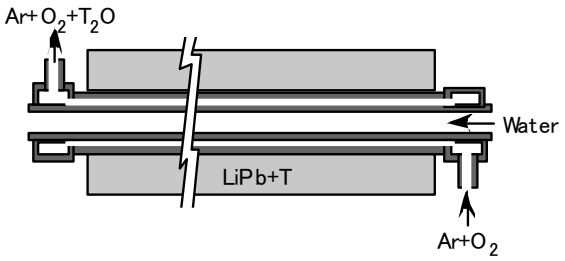

(b)

Fig. 7Double tube design for the heat exchanger. Cross section (a) perpendicular to the water flow (a) and (b) parallel to the flow.

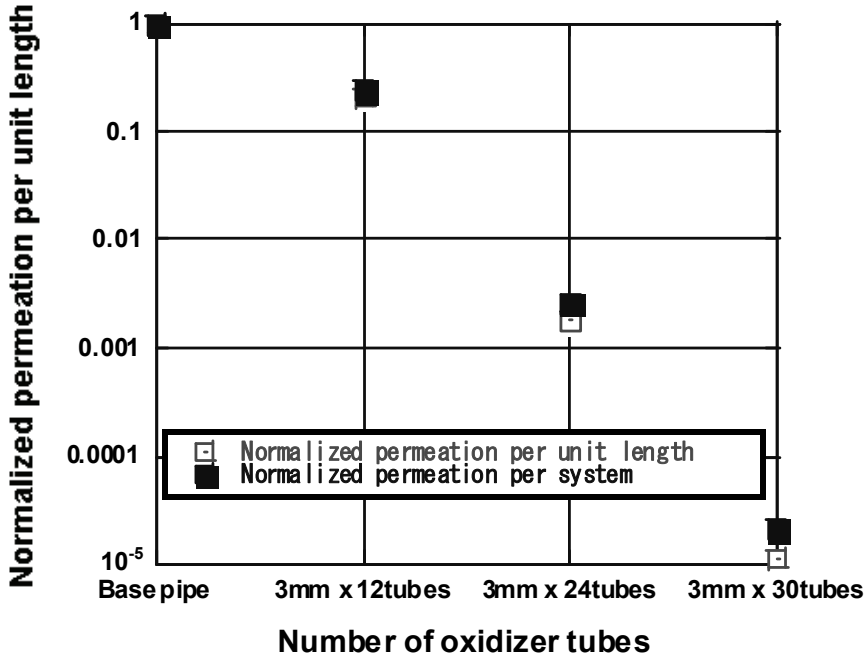

Fig. 8Normalized tritium permeation through a heat exchanger equipped with different configurations of double pipes. The heat flow through the exchanger is constant.

5. List of publications

Overview

[1] T. Muroga, D.K. Sze, K. Okuno, T. Terai, A. Kimura, R. Kurtz, A. Sagara, R. Nygren, Y. Ueda, R. Doerner, P. Sharpe, T. Kunugi, N. Morley, Y. Hatano, M. Sokolov, T. Yamamoto, A. Hasegawa, Y. Katoh, N. Ohno, K. Tokunaga, S. Konishi, S. Fukada, P. Calderoni, T. Yokomine, K. Messadek, Y. Oya, N. Hashimoto, T. Hinoki, H. Hashizume, T. Norimatsu, T. Shikama, R. Stoller, K.A. Tanaka, M. Tillack, "Midterm Summary of Japan-US Fusion Cooperation Program TITAN" Fusion Sci. & Tech. 60 (2011) 321-328.

[2] T. Muroga, D.K. Sze, K. Okuno, " Overview of TITAN project" Fusion Eng. Des. 87 (2012) 613-619.

Task 1-1 Tritium and Mass Transfer in first wall

[1] K. Tokunaga M.J. Baldwin, R.P. Doerner, D. Nishijima, H. Kurishita, T. Fujiwara, K. Araki, Y. Miyamoto, N. Ohno, Y. Ueda, "Nanoscale surface morphology of tungsten materials induced by Be-seeded D-He plasma exposure" J. Nucl. Mater. 417,528 (2011).

[2] K. Tokunaga, M.J. Baldwin, D. Nishijima, R.P. Doerner, S. Nagata, B. Tsuchiya, H. Kurishita, T. Fujiwara, K. Araki, Y. Miyamoto, N. Ohno, Y. Ueda, "Properties of deposited layer formed by interaction with Be seeded D–He mixture plasma and tungsten", J. Nucl. Mater. 442, S313 (2013).

[3] M. Miyamoto, D. Nishijima, M.J. Baldwin, Russell P. Doerner, UEDA Yoshio, KURISHITA Hiroaki, YOSHIDA Naoaki and SAGARA Akio, "Microstructure and Deuterium Retention Property of W in D-He-Be Mixture Plasma Environment", J. Plasma Fusion Res. 89, 335 (2013), in Japanese.

[4] M. Shimada, R. D. Kolasinski, J. P. Sharpe, R. Causey, "Tritium plasma experiment: Parameters and potentials for fusion plasma -wall interaction studies", Rev. Sci. Instrum. 82, 083503 (2011);

[5] T, Otsuka, T. Tanabe, K. Tokunaga, N. Yoshida, K. Ezato, S. Suzuki, M. Akiba, "Application of tritium tracer techniques to observation of hydrogen on surface and in bulk of F82H", J. Nucl. Mater., 417 issue 1-3 1135-1138, (2011).

[6] T. Otsuka, M. Shimada, T. Tanabe, P. Sharpe., "Behavior of Tritium near Surface Region of Metals Exposed to Tritium Plasma", Fusion Sci. Technol., 60, 1539-1542 (2011).

[7] T Otsuka, T Tanabe and K Tokunaga, “Behaviour of tritium in plasma-sprayed tungsten coating on steel exposed to tritium plasma”, Phys. Scr. T145 (2011) 014035 (4pp).

[8] Shin Kajita, Daisuke Nishijima, Russ Doerner, Karl Umstadter, Jonathan Yu, Noriyasu Ohno, Yoshio Ueda, “Beryllium erosion induced by transient heat loads and subsequent reactions in a deuterium plasma”, J. Nucl. Mater. 420 (2012) 252–257.

[9] M. Miyamoto, D. Nishijima, Y. Ueda, R.P. Doerner, H. Kurishita, M.J. Baldwin, S. Morito, K. Ono and J. Hanna, “Observations of suppressed retention and blistering for tungsten exposed to deuterium–helium mixture plasmas”, Nucl. Fusion 49 (2009) 065035 (7pp).

[10] M. Miyamoto, D. Nishijima, M.J. Baldwin, R.P. Doerner, Y. Ueda, K. Yasunaga, N. Yoshida, K. Ono, “ Microscopic damage of tungsten exposed to deuterium–helium mixture plasma in PISCES and its impacts on retention property”, Journal of Nuclear Materials 415 (2011) S657–S660.

[11] Mitsutaka Miyamoto, Daisuke Nishijima, Matthew J. Baldwin, Russell P. Doerner, Yoshio Ueda, Akio Sagara and Hiroaki Kurishita, “Microstructures and Deuterium-Retention Behavior of Tungsten Exposed to D+(He and/or Be) Mixture Plasmas”, Materials Transactions, Vol. 54, No. 4 (2013) pp. 420 to 424.

[12] M. Miyamoto, D. Nishijima, M.J. Baldwin, R.P. Doerner, Y. Ueda, A. Sagara, “Influence of Be seeding on microstructures of tungsten exposed to D-He mixture plasmas in PISCES and its impacts on retention properties”, Journal of Nuclear Materials 438 (2013) S216–S219.

Task 1-2 Tritium transfer in fusion reactor blanket

[1] Masuyama, D., Oda, T., Fukada, S., Tanaka, S., “Chemical state and diffusion behavior of hydrogen isotopes in liquid lithium-lead”, Chem. Phys. Lett. vol. 483 (2009) pp. 214-218.

[2] Yao, Z., Suzuki, A., Levchuk, D., Chikada, T., Tanaka, T., Muroga, T., Terai, T., “Hydrogen permeation through steel coated with erbium oxide by sol-gel method”, Journal of Nuclear Materials, Volumes 386-388 (2009) 700-702.

[3] Chikada, T., Suzuki, A., Yao, Z., Levchuk, D., Maier, H., Terai, T., Muroga, T., “Deuterium permeation behavior of erbium oxide coating on austenitic, ferritic, and ferritic/martensitic steels”, Fusion Engineering and Design, Volume 84 (2009) 590-592.

[4] Chikada, T., Suzuki, A., Kobayashi, T., Yao, Z., Levchuk, D., Maier, H., Terai, T., Muroga, T., "Thermal influence on erbium oxide coating for tritium permeation barrier", Fusion Science and Technology, Volume 56 (2009) 309-313.

[5] Yagi, J., Suzuki, A., Terai, T., Muroga, T., Tanaka, S., "In-situ observation of hydrogen hot trapping from molten lithium with yttrium", Fusion Engineering and Design, Volume 84 (2009) 1993-1996.

[6] Chikada, T., Suzuki, A., Tanaka, T., Terai, T., Muroga, T., "Microstructure control and deuterium permeability of erbium oxide coating on ferritic/martensitic steels by metal-organic decomposition", Fusion Engineering and Design, Volume 85 (2010) 1537-1541.

[7] Edao, Y., Fukada, S., Yamaguchi, S., Nakamura, H., "Tritium removal by Y hot trap for Li purification of IFMIF target", Fusion Engineering and Design, Vol. 85 (2010) pp. 53-57.

[8] Wu, Y., Edao, Y., Fukada, S., Nakamura, H., Kondo, H., "Removal rates of hydrogen isotope from liquid Li by HF-treated Y plate", Fusion Engineering and Design, Vol. 85 (2010) pp. 1484-1487.

[9] Edao, Y., Noguchi, H., Fukada, S., "Isotopic exchange rate between hydrogen and deuterium in the process of permeating through $Li_{0.17}Pb_{0.83}$", Fusion Engineering and Design, Vol. 85 (2010) pp. 1225-1228.

[10] Fukada, S., Edao, Y., Sagara, A.,"Effects of simultaneous transfer of heat and tritium through Li-Pb or Flibe blanket", Fusion Engineering and Design, Vol. 85 (2010) pp. 1314-1319.

[11] Fukada, S., Edao, Y., "Unresolved issues on tritium mass transfer in Li-Pb liquid blankets J. Nucl. Mater. Vol. 417 (2011) pp. 727-730.

[12] Chikada, T., Suzuki. A., Kobayashi. T., Maier, H., Terai, T., Muroga, T., "Microstructure change and deuterium permeation behavior of erbium oxide coating", Journal of Nuclear Materials, Volume 417 (2011) 1241-1244.

[13] Chikada, T., Suzuki, A., Maier, H., Terai, T., Muroga, T., "Modeling of tritium permeation through erbium oxide coatings", Fusion Science and Technology, Volume 60 (2011) 378-393.

[14] Chikada, T., Suzuki, A., Adelhelm, C., Terai, T., Muroga, T., "Surface behaviour in deuterium permeation through erbium oxide coatings" Nuclear Fusion, Volume 51 (2011) 063023.

[15] Edao, Y., Okitsu, H., Noguchi, H., Fukada, S., "Permeation of two-component hydrogen isotopes in lithium-lead eutectic alloy, Fus. Sci. Technol. Vol. 60 (2011) pp. 1163-1166.

[16] Edao, Y., Noguchi, H., Fukada, S., Experiment of hydrogen isotopes permeating through Li-Pb with diffusion, dissolution and isotopic exchange J. Nucl. Mater. Vol. 417 (2011) pp. 723-726.

[17] Norimatsu, T., Saika, H., Homma, H., Nakai M., and Fukada, S., “Leakage control of tritium through heat cycles of conceptual-design, laser-fusion reactor Koyo-F”, Fus. Sci. Technol. Vol. 60 (2011) pp. 893-896.

[18] Okitsu, H., Edao, Y., Okada, M., Fukada, S., “Analysis of diffusion and dissolution of two-component hydrogen (H+D) in lead lithium”, Fusion Engineering and Design”, vol. 87 (2012) pp.1324-1328.

[19] Fukada, S., Edao, Y., Katekari, K., Okitsu, H., Hatachi, Y., Okada, M., Tamari, K., “Tritium recovery from liquid blanket systems for fusion reactor”, Fus. Sci. Technol. Vol. 61 (2012) pp. 58-63.

[20] Hatachi Y., Shigeharu S., Katekari K., Edao Y., Fukada S., “Analysis of hydrogen isotopes absorption between liquid lithium and yttrium under dynamic conditions”, Fusion Engineering and Design, Vol. 87 (2012) pp.1457-1460.

[21] Fukada S., Okada M., Yoshimura S., Edao Y., “Chemical activity of hydrogen isotopes in Pb-Li eutectic alloy blanket”, Journal of Applied Nuclear Science and Technology, Vol 5 (2012) pp. 27-31.

[22] Shigeharu S., Hiromoto T., Sugie K., and Fukada S., “Determination of distribution coefficient of hydrogen isotopes between Y and Li”, Journal of Applied Nuclear Science and Technology, Vol. 5 (2012) pp. 54-58.

[23] Yagi, J., Suzuki, A., Terai, T., “Nitrogen contamination effect on yttrium gettering of hydrogen in liquid lithium”, Journal of Nuclear Materials, Volume 417 (2011) 710-712.

[24] Yagi, J., Suzuki, A., Terai, T., “Tritium monitoring for liquid lithium by permeation through iron window” Fusion Science and Technology, Volume 60 (2011) 1014-1017.

[25] Yagi, J., Suzuki, A., Terai, T., Nakamura, K., Kondo, H., Ida, M., Kanemura, T., Furukawa, T., Hirakawa, Y., “Material improvement of hydrogen isotope permeation monitor for liquid lithium”, Fusion Science and Technology, Volume 62 (2012) 204-209.

[26] Suzuki, A., Yagi, J., Nagura, M., Komiyama, D., Terai, T., “Tritium release from PbLi natural convection loop under neutron irradiation”, Fusion Science and Technology, Volume 62 (2012) 295-299.

[27] Okada M., Yoshimura S., Okitsu H., Edao Y., Fukada S., “Study on hydrogen isotopes permeation under lithium-lead thermal convection”, Journal of Applied Nuclear Science and Technology, Vol. 5 (2012) pp. 117-121.

[28] Mao, W., Chikada, T., Suzuki, A., Terai, T., Yamaguchi, K., “Experimental and computational studies on tritium permeation mechanism in erbium oxide” Journal of Plasma and Fusion Research SERIES, Volume 10 (2013) 27-32.

[29] Chikada, T., Suzuki, A., Koch, F., Maier, H., Terai, T., Muroga, T., “Fabrication and deuterium permeation properties of erbia-metal multilayer coatings” Journal of Nuclear Materials, Volume 442 (2013) S592-S596.

[30] Mao, W., Chikada, T., Shimura, K., Suzuki, A, Yamaguchi, K., Terai, T., “Adsorption of H atoms on cubic Er_2O_3 (001) surface: A DFT Study” Journal of Nuclear Materials, Volume 443 (2013) 555-561.

[31] Chikada, T., Suzuki, A., Terai, T., Muroga, T., Koch F., “Compatibility of erbium oxide coating with liquid lithium-lead alloy and corrosion protection effect of iron layer” Fusion Engineering and Design, Volume 88 (2013) 640-643.

[32] Chikada, T., Naitoh, S., Suzuki, A., Terai, T., Tanaka, T., Muroga, T, “Deuterium permeation through erbium oxide coatings on RAFM steels by a dip-coating technique” Journal of Nuclear Materials, Volume 442 (2013) 533-537.

[33] Mao, W., Chikada, T., Shimura, K., Suzuki, A., Terai, T., “Energetics and diffusion of hydrogen in α-Al_2O_3 and Er_2O_3” Fusion Engineering and Design, Volume 88 (2013) 2646-2649.

[34] Fukada, S., Terai, T., Konishi, S., Katayama, K., Chikada, T., Edao, Y., Muroga, T., Shimada, M., Merrill, B., Sze, D.K., “Clarification of Tritium Behavior in Pb-Li Blanket System (Overview)” Materials Transaction, Volume 54 (2013) 425-429.

[35] Fukada S., Okada M., Edao Y., Okitsu H., Yoshimura S., “Overall hydrogen permeation through fluidized PbLi alloy under natural convection”, Fusion Science and Technology, Vol. 64(3) (2013) pp. 636-642.

[36] Terai, T., Fukada, S., Konishi, S., Katayama, K., Yamamoto, Y., Noborio, K., Edao, Y., Chikada, T., “Tritium transfer in fusion reactor blanket” Journal of Japan Society of Plasma Science and Nuclear Fusion Research, Volume 89 (2013) 714-718.

[37] Chikada, T., Shimada, M., Pawelko, R.J., Terai, T., Muroga, T., “Tritium permeation experiments using reduced activation ferritic/martensitic steel tube and erbium oxide coating” Fusion Engineering and Design, submitted.

[38] Mao, W., Chikada, T., Suzuki, A., Terai, T., “First-principles study of hydrogen adsorption and permeation in the reconstructed cubic erbium oxide” Fusion Engineering and Design, submitted.

[39] Sato, R., Chikada, T., Matsuzaki, H., Suzuki, A., Terai, T., Sugiyama, K., Maier, H., “Measurement of hydrogen isotope concentration in erbium oxide coatings” Fusion Engineering and Design, submitted.

[40] Pavelko, R., Shimada, M., Katayama, K., Fukada, S., Terai, T.,, “development of a low tritium partial pressure permeation system for mass transport measurement in lead lithium eutectic”, Fus. Sci. Technol., in contribution.

Task 1-3 Flow control and thermofluid modeling

[1] J. Takeuchi, S. Satake, T. Kunugi, T. Yokomine, N. Morley, M. Abdou, “Development Of PIV Technique Under Magnetic Fields And Measurement Of Turbulent Pipe Flow Of Flibe Simulant Fluid”, Fusion Sci. Technol., vol. 52 (2007) pp. 860-864.

[2] T. Yokomine, J. Takeuchi, H. Nakaharai, S. Satake, T. Kunugi, N. Morley, M. Abdou, “Experimental Investigation Of Turbulent Heat Transfer Of High Prandtl Number Fluid Flow Under Strong Magnetic Field”, Fusion Sci. Technol. vol. 52 (2007) pp.625-629.

[3] H. Nakaharai, J. Takeuchi, T. Yokomine, T. Kunugi, S. Satake, N. Morley, M. Abdou, “The influence of a magnetic field on turbulent heat transfer of high Prandtl number fluid”, Experimental Thermal and Fluid Science, vol. 32 (2007) pp.23–28.

[4] S. Smolentsev, R. Moreau, “One-Equation Model for Quasi-Two-Dimensional Turbulent Magnetohydrodynamic Flows”, Physics of Fluids, 19 (2007) 078101.

[5] T. Satoh, K. Yuki, S. Chiba, H. Hashizume, A. Sagara, “Heat Transfer performance for high Prandtl and high temperature molten salt flow in sphere-packed pipes”, Fusion Sci. Technol. vol.52, no.3 (2007) pp. 618-624.

[6] M. Satake, K. Yuki, H. Hashizume, “Reproduction of behavior of 2-D channel flow with two rods by using k-e model”, Fusion Sci. Technol. vol.52, no.4 (2007) pp. 821-826.

[7] A. Beltrán, S. Cuevas, S. Smolentsev, “Instabilities in the Flow past Localized Magnetic Fields”, Journal of Physics: Conference Series, 64 (2007) 012009.

[8] J. Takeuchi, S. Satake, N.Morley, T. Kunugi, T. Yokomine, M.Abdou, “Experimental study of MHD effects on turbulent flow of Flibe simulant fluid in a circular pipe”, Fusion Eng. Des., vol. 83 (2008) pp.1082–1086.

[9] Y. Yamamoto, T. Kunugi, S. Satake, S. Smolentsev, “DNS and k–ε model simulation of MHD turbulent channel flows with heat transfer”, Fusion Eng. Des., vol. 83(2008) pp.1309-1312.

[10] K. Yuki, M. Okumura, H. Hashizume, S. Toda, N. Morley, A. Sagara, “Flow visualization and heat transfer characteristics for sphere-packed pipes”, Journal of Thermophysics and Heat Transfer”, vol. 22, no. 4 (2008) pp. 638-648.

[11] S. Satake, N. Yoshida, T. Kunugi, K. Takase, Y. Ose, T. Kano, “DNS of turbulent heat transfer under a uniform magnetic field at high Reynolds number”, Fusion Eng. Des., vol. 83 (2008) pp.1092-1096.

[12] S. Smolentsev, N.B. Morley, C. Wong and M. Abdou, “MHD and heat transfer considerations for the US DCLL blanket for DEMO and ITER TBM”, Fusion Eng. Des., vol. 83 (2008) pp.1788-1791.

[13] S. Smolentsev, R. Moreau, M. Abdou, “Characterization of key magnetohydrodynamic phenomena in PbLi Flows for the US DCLL Blanket”, Fusion Eng. Des., vol. 83 (2008) pp.771-783.

[14] N. Morley, Y. Katoh, S. Malang, B.A. Pint, A.R. Raffray, S. Sharafat, S. Smolentsev, G.E. Youngblood, “Recent Research and Development for the Dual-Coolant Blanket Concept in the US”, Fusion Eng. Des., vol. 83,(2008), pp.920-927.

[15] N. Morley, M.-J. Ni, R. Munipalli, P. Huang, M. Abdou, “MHD simulations of liquid metal flow through a toroidally-oriented manifold”, Fusion Eng. Des., vol. 83 (2008) pp.1335-1339.

[16] N. Seto, K. Yuki, H. Hashizume, A. Sagara, “Heat transfer enhancement in sphere-packed pipes under high Reynolds number conditions”, Fusion Eng. Des., vol.83 (2008) pp. 1102-1107.

[17] S. Smolentsev, “MHD Duct Flows under Hydrodynamic “Slip” Condition”, Theor. Comput. Fluid Dyn., 23 (2009) pp. 557-570.

[18] Y. Ueki, M. Hirabayashi, T. Kunugi, T. Yokomine and K. Ara, “Acoustic Properties of Pb-17Li Alloy for Ultrasonic Doppler Velocimetry”, Fusion Sci. Technol., vol. 56 (2009) pp. 846-850.

[19] N .Morley, A. Medina, M. Abdou, “Measurement of Specific Electrical Contact Resistance between SiC and Lead-Lithium Eutectic Alloy”, Fusion Sci. Technol., vol. 56 (2009) pp. 195-200.

[20] S. Smolentsev, S. Malang, “Double-Layer Flow Channel Insert for Electric and Thermal Insulation in the Dual-Coolant Lead-Lithium Blanket”, Fusion Sci. Technol., vol. 56 (2009) pp. 201-205.

[21] N. Vetcha, S. Smolentsev, M. Abdou, “Theoretical Study of Mixed Convection in Poloidal Flows of DCLL Blanket”, Fusion Sci. Technol., vol. 56 (2009) pp. 851-855.

[22] K. Messadek, M. Abdou, “Experimental study of the MHD flow in a prototypic inlet manifold section of the DCLL blanket”, Magnetohydrodynamics, vol. 45 (2009) pp.233-238.

[23] S. Smolentsev, “MHD Turbulent and Buoyant Flow in Fusion Blankets”, J. Plasma Fusion Res., 85 (2009) pp. 556-557.

[24] R. Moreau, S. Smolentsev, S. Cuevas, “Flow in an Insulating Rectangular Duct at the Entry of a Magnet”, Magnetohydrodynamics, vol. 45, (2009) pp.181-192.

[25] H. Hashizume, K. Yuki, N. Seto, A. Sagara, “Feasibility Study for Flibe TBM Based on Thermofluid Analysis”, Fusion Sci. Technol., vol. 56, no 2 (2009) pp. 892-896.

[26] S. Smolentsev, S. Cuevas, A. Beltrán, “Induced Electric Current-Based Formulation in Computations of Low Magnetic Reynolds Number Magnetohydrodynamic Flows”, J. Comput. Phys, 229 (2010) pp.1558-1572.

[27] S. Smolentsev, Z.Xu, Ch.Pan, M.Abdou, “Numerical and Experimental Studies of MHD flow in a Rectangular Duct with a Non-Conducting Flow Insert”, Magnetohydrodynamics, 46 (2010) pp.99-111.

[28] Y .Ueki, T. Kunugi, M. Kondo, A. Sagara, N.Morley, M. Abdou, “Consideration of Alumina Coating Fabricated by Sol-gel Method for PbLi Flow”, Zero-Carbon Energy Kyoto 2009, Springer (2010) pp.373-379.

[29] Y. Ueki, T. Kunugi, N.B. Morley, M.A. Abdou, “Electrical Insulation Test of Alumina Coating Fabricated by Sol-gel Method in Molten PbLi Pool”, Fusion Eng. Des., vol.85 (2010) pp. 1826-1830.

[30] S. Smolentsev, R. Moreau, L. Bühler, C. Mistrangelo, “MHD thermofluid issues of liquid-metal blankets: Phenomena and Advances”, Fusion Eng. Des., vol.86 (2010) pp. 1196-1205.

[31] S. Smolentsev, C. Wong, S. Malang, M. Dagher, M. Abdou, “MHD Considerations for the DCLL Inboard Blanket and Access Ducts", Fusion Eng. Des., vol.85 (2010) pp.1007-1011.

[32] C.P.C. Wong, M. Abdou, M. Dagher, Y. Katoh, R.J. Kurtz, S. Malang, E.P. Marriott, B.J. Merrill, K. Messadek, N.B. Morley, M.E. Sawan, S. Sharafat, S. Smolentsev, D.K. Sze, S. Willms,

A. Ying, M.Z. Youssef, “An Overview of the US DCLL ITER-TBM Program”, Fusion Eng. Des., vol.85 (2010) pp.1129-1132.

[33] M. Aoyagi, S. Ito, H. Hashizume, T. Muroga, “MHD pressure drop characteristics in a three-surface-multi-layered channel under a strong magnetic field,” Fusion Eng. Des., vol.85 (2010) pp. 1181-1184.

[34] S. Satake, H. CHikamasa, T. Kunugi, K. Takase, “Direct numerical simulation of unstable stratified turbulent flow under a magnetic field,” Fusion Eng. Des., vol.85 (2010) pp.1326-1330.

[35] Y. Ueki, K. Nagai, T. Kunugi, M. Hirabayashi, K. Ara, Y. Yonemoto, T. Hinoki, “Contact Angle Measurement of Molten Lead-Lithium on Silicon Carbide Surfaces”, Fusion Eng. Des., vol.86 (2011) pp. 2297-2300.

[36] Y. Ueki, M. Hirabayashi, T. Kunugi, K. Nagai, J. Saito, K. Ara, N.B. Morley, “Velocity Profile Measurement of Lead-Lithium Flows by High-Temperature Ultrasonic Doppler Velocimetry”, Fusion Sci. Technol., vol. 60 (2011) pp 506-510.

[37] N. Vetcha, S. Smolentsev, M. Abdou, “Stability Analysis for Buoynacy-Opposed Flows in Poloidal Ducts of the DCLL Blanket”, Fusion Sci. Technol., vol.60 (2) (2011) pp. 518-522.

[38] Y. Ueki, T. Kunugi, K. Nagai, M. Hirabayashi, K. Ara, Y. Yonemoto, T. Hinoki, “Experimental Investigation on Contact Angeles of Molten Lead-Lithium on Silicon Carbide Surfaces”, Zero-Carbon Energy Kyoto 2010, Springer (2011) pp.271-277.

[39] M. Aoyagi, S. Ito, S. Ebara, T. Muroga, H. Hashizume, “Thermo-Fluid Simulation in a Liquid Metal Blanket with Three-Surface-Multi-Layered Channel,” Fusion Sci. Technol., vol. 60 (2011) pp. 283-287.

[40] S. Satake, K. Furumi, H. Chikamasa, T. Kunugi, “DNS of MHD Turbulent Flow with Buoyancy,” Progress in NUCLEAR SCIENCE and TECHNOLOGY, Vol.2 (2011) pp.90-94.

[41] S. Smolentsev, T. Kunugi, K. Messadek, T. Yokomine, J. Young, K. Yuki, Y. Ueki, T. Sketchley, F.-C. Li, N. Morley, M. Abdou, “Status of “TITAN” Task 1-3 “Flow Control and Thermofluid Modeling”, Fusion Eng. Des., vol.87 (2012) pp. 777-781.

[42] S. Smolentsev, N. Vetcha, R. Moreau, “Study of Instabilities and Transitions for a Family of Quasi-Two-Dimensional Magnetohydrodynamic Flows Based on a Parametric Model”, Physics of Fluids, vol.24 (2012) 024101.

[43] N. Vetcha, S. Smolentsev, M. Abdou, “Stability analysis for the Hartmann flow with interfacial slip”, Magnetohydrodynamics, vol.48 (1) (2012) pp. 147-155.

[44] Y. Ueki, T. Kunugi, M. Hirabayashi, K. Nagai, J. Saito, K. Ara, N.B. Morley, T. Yokomine, “High-Temperature Ultrasonic Doppler Velocimetry for Lead-Lithium Flows”, Zero-Carbon Energy Kyoto 2011, Springer (2012) pp. 267-272.

[45] M. Aoyagi, Y. Inage, S. Ito, S. Ebara, Y. Ueki, K. Yuki, F.-C. Li, S. Smolentsev, T. Yokomine, T. Kunugi, T. Sketchley, M. Abdou, H. Hashizume, “Verification Test of a Three-Surface-Multi-Layered Channel to Reduce MHD Pressure Drop”, The Eighth Japan-Korea Symposium on Nuclear Thermal Hydraulics and Safety, N8P1089, Beppu, Japan, (Dec., 2012).

[46] N. Vetcha, S. Smolentsev, M. Abdou, R. Moreau, “Study of Instabilities and Quasi-Two-Dimensional Turbulence in Volumetrically Heated MHD Flows in a Vertical Rectangular Duct”, Physics of Fluids, in press (2013).

[47] T. Kunugi, S. Smolentsev, T. Yokomine, F.-C. Li, Y. Ueki, K. Yuki, M. Aoyagi, T. Sketchley, M. Abdou, “Current Status of TITAN Task 1-3 “Flow Control and Thermofluid Modeling”, Journal of Applied Nuclear Science and Technology, vol. 5, Supplement (2012) pp. 72-75.

[48] T. Kunugi, S. Smolentsev, T. Yokomine, F.-C. Li, Y. Ueki, K. Yuki, M. Aoyagi, T. Sketchley, M. Abdou, “Current Status of TITAN Task 1-3 “Flow Control and Thermofluid Modeling Journal of Applied Nuclear Science and Technology, vol. 5, Supplement (2012) pp. 72-75.

[49] N. Vetcha, S. Smolentsev, M. Abdou, R. Moreau, “Study of Instabilities and Quasi-Two-Dimensional Turbulence in Volumetrically Heated MHD Flows in a Vertical Rectangular Duct”, Physics of Fluids, vol.25, 024102 (2013).

[50] S. Smolentsev, F.-C. Li, N. Morley, Y. Ueki, M. Abdou, T. Sketchley, “Construction and initial operation of MHD PbLi facility at UCLA”, Fusion Eng. Des., vol.88 (2013) pp. 317-326.

[51] M. Aoyagi, S. Ito, T. Muroga, H. Hashizume, Three-dimensional MHD flow simulation in an L-shape elbow of a three-surface-multi-layered channel, Submitted to Fusion Eng. Des.

Task 2-1 Irradiation-Tritium Synergism

[1] Shimada, M., Hatano, Y., Calderoni, P., Oda, T., Oya, Y., Sokolov, M. A., Zhang, K., Cao, G., Kolasinski, R. and Sharpe, J. P., “First Result of Deuterium Retention in Neutron-Irradiated Tungsten Exposed to High Flux Plasma in TPE”, Journal of Nuclear Materials, Vol.415, 2011, pp. 667-671

[2] Oya, Y., Shimada, M., Kobayashi, M., Oda, T., Hara, M., Watanabe, H., Hatano, Y., Calderoni, P. and Okuno, K., “Comparison of Deuterium Retention for Ion-Irradiated and Neutron-Irradiated Tungsten”, Physica Scripta, Vol. 145, 2011, 014050

[3] Shimada, M., Cao, G., Hatano, Y. , Oda, T., Oya, Y. , Hara, M. and Calderoni, P. , “Deuterium Depth Profile in Neutron-Irradiated Tungsten Exposed to Plasma”, Physica Scripta, Vol.145, 2011, 014051

[4] Calderoni, P., Sharpe, J., Shimada, M., Denny, B., Pawelko, R., Schuetz, S., Longhurst, G., Hatano, Y., Hara, M., Oya, Y., Otsuka, T., Katayama, K., Konishi, S., Noborio, K. and Yamamoto, Y. “An Overview of Research Activities on Materials for Nuclear Applications at the INL Safety, Tritium and Applied Research Facility”, Journal of Nuclear Materials, Vol. 417, 2011, pp.1336-1340

[5] Oda, T., Shimada, M., Zhang, K., Calderoni, P., Oya, Y., Sokolov, M. A., Kolasinski, R., Sharpe , J. P. and Hatano, Y., “Development of Monte Carlo Simulation Code to Model Behavior of Hydrogen Isotopes Loaded into Tungsten Containing Vacancies”, Fusion Science and Technology, Vol. 60, 2011, pp.1455-1458

[6] Shimada, M., Hatano, Y., Oya, Y., Oda, T., Hara, M., Cao, G., Kobayashi, M., Sokolov, M. A., Watanabe, H., Tyburska-Püschel, B., Ueda, Y., Calderoni, P. and Okuno, K., “Overview of the US-Japan Collaborative Investigation on Hydrogen Isotope Retention in Neutron-Irradiated and Ion-Damaged Tungsten”, Fusion Engineering and Design, Vol. 87, 2012. pp.1166-1170

[7] Hatano, Y., Shimada, M., Otsuka, T., Oya, Y., Alimov, V. Kh., Hara, M., Shi, J., Kobayashi, M., Oda, T., Cao, G., Okuno, K., Tanaka, T., Sugiyama, K., Roth, J., Tyburska-Püschel, B., Dorner, J., Yoshida, N., Futagami, N., Watanabe, H., Hatakeyama, M., Kurishita, H., Sokolov, M. A. and Katoh, Y., “Hydrogen Isotope Trapping at Defects Created with Neutron- and Ion-Irradiated Tungsten”, Proceedings of 24th IAEA Fusion Energy Conference, October 8-13, 2012, San Diego, USA

[8] Hatano, Y. , Shimada, M., Oya, Y., Cao, G. , Kobayashi, M., Hara, M., Merrill, B. J., Okuno, K., Sokolov, M. A. and Katoh, Y., “Retention of Hydrogen Isotopes in Neutron Irradiated Tungsten (Overview)”, Materials Transactions, Vol. 54, 2013, pp.437-441

[9] Kobayashi, M., Shimada, M., Hatano, Y., Oda, T., Merrill, B., Oya, Y. and Okuno, K., “Deuterium Trapping by Irradiation Damage in Tungsten Induced by Different Displacement Processes”, Fusion Engineering and Design, Vol. 88, 2013, pp. 1749–1752

[10] Hatano, Y., Shimada, M., Otsuka, T., Oya, Y., Alimov, V. Kh., Hara, M., Shi. J., Kobayashi, M., Oda, T., Cao, G., Okuno, K., Tanaka, T., Sugiyama, K., Tyburska-Püschel, B., Roth, J., Dorner, J., Yoshida, N., Futagami, N., Watanabe, H., Hatakeyama, M., Kurishita, H., Sokolov and M. A., Katoh,

Y. “Deuterium Trapping at Defects Created with Neutron and Ion Irradiations in Tungsten”, Nuclear Fusion, Vol.53, 2013, 073006

[11] Hatano, Y., Shimada, M., Alimov, V. Kh., Shi, J., Hara, M., Nozaki, T., Oya, Y. Kobayashi, M., Okuno, K., Oda, T., Cao, G., Yoshida, N., Futagami, N., Sugiyama, K., Roth, J., Tyburska-Püschel, B., Dorner, J., Takagi, I, Hatakeyama, M., Kurishita, H.and Sokolov, M. A., “Trapping of Hydrogen Isotopes in Radiation Defects Formed in Tungsten by Neutron and Ion Irradiations”, Journal of Nuclear Materials, Vol. 438, 2013, pp.114-119

[12] Oya, Y., Shimada, M., Tokunaga, T., Watanabe, H., Yoshida, N., Hatano, Y., Kasada, R., Nagasaka, T., Kimura, A. and Okuno, K., “Behavior of Deuterium Retention and Surface Morphology for VPS-W/F82H”, Journal of Nuclear Materials, Vol. 442, 2013, pp.242-245

Task 2-2 Joining and coating integrity

[1] H. Kishimoto, K. Yutani, R. Kasada, O. Hashitomi and A. Kimura, “Heavy-ion Irradiation Effects on the Morphology of Complex Oxide Particles in Oxide Dispersion Strengthened Ferritic Steels”, J. Nucl. Mater. 367-370 (2007) 179-184.

[2] K. Yutani, H. Kishimoto, R. Kasada and A. Kimura, “Evaluation of Helium effects on Swelling Behavior of Oxide Dispersion Strengthened Ferritic Steels under Ion Irradiation”, J. Nucl. Mater. 367-370 (2007) 423-427.

[3] M.A. Sokolov, A. Kimura, H. Tanigawa and S. Jitsukawa, “Fracture Toughness Characterization of JLF-1 Steel after Irradiation in HFIR to 5 dpa”, J. Nucl. Mater. 367-370 (2007) 644-647.

[4] R.J. Kurtz, A. Alamo, E. Lucon, Q. Huang, S. Jitsukawa, A. Kimura, R.L. Klueh, G.R. Odette, C. Petersen, M.A. Sokolov, P. Spätig, J.-W. Rensman, “Recent progress toward development of reduced activation ferritic/martensitic steels for fusion structural applications”, J. Nucl. Mater. 386-388 (2009) 411-417.

[5] T. Nagasaka, R. Kasada, A. Kimura, Y. Ueda, T. Muroga, “Thermophysical properties and microstructure of plasma-sprayed tungsten coating on low activation materials”, Fusion Sci. Technol. 56(2) (2009) 1053-1057.

[6] S.H. Noh, R. Kasada, N. Oono, N. Iwata, A. Kimura, “Relationship between Microstructure and Mechanical Property of Transient Liquid Phase Bonded ODS steels”, Zero-Carbon Energy Kyoto (2009) 339-345.

[7] S. Noh, R. Kasada, N. Oono, T. Nagasaka, A. Kimura, “Joining of ODS steels and tungsten for fusion applications”, Materials Science Forum 654-656 (2010) 2891-2894.

[8] S.H. Noh, R. Kasada, N. Oono, N. Iwata, A. Kimura, “Evaluation of microstructure and mechanical properties of liquid phase diffusion bonded ODS steels”, Fusion Eng. Des. 85 (2010) 1033-1037.

[9] Sanghoon Noh, Ryuta Kasada, Akihiko Kimura, “Solid-state diffusion bonding of high-Cr ODS ferritic steel”, Acta Materialia 59(8) (2011.05) 3196-3204.

[10] Takuya Nagasaka, Takeo Muroga, Hideo Watanabe, Ryuta Kasada, Noriyuki Iwata, Akihiko Kimura, “Mechanical properties of V–4Cr–4Ti alloy after first-wall coating with tungsten”, J. Nucl. Mater. 417 (2011) 306-309.

[11] Sanghoon Noh, Ryuta Kasada, Akihiko Kimura, Seung Hwan C. Park, Satoshi Hirano, “Microstructure and mechanical properties of friction stir processed ODS ferritic steels”, J. Nucl. Mater. 417(1-3) (2011) 245-248.

[12] Naoko Oono, Sanghoon Noh, Noriyuki Iwata, Takuya Nagasaka, Ryuta Kasada, Akihiko Kimura, “Microstructures of brazed and solid-state diffusion bonded joints of tungsten with oxide dispersion strengthened steel”, J. Nucl. Mater. 417 (2011) 253-256.

[13] Sanghoon Noh, Byungjun Kim, R. Kasada, A. Kimura, “Diffusion bonding between ODS ferritic steel and F82H steel for fusion applications”, J. Nucl. Mater. 426(1-3) (2012) 208-213.

[14] Naoyuki Hashimoto, Hiroshi Oka, Takeo Muroga, Takuya Nagasaka, Akihiko Kimura, Shigeharu Ukai, Takuya Yamamoto and Michail A. Sokolov, “Irradiation Effect on Tensile Property of F82H IEA and Its Joint in TITAN Project (Overview)”, Materials Transactions 54(4) (2013) 442-445.

[15] Y. Himei, K. Yabuuchi, R. Kasada, S. Noh, H. Noto, T. Nagasaka, S. Nogami and A. Kimura, “Ion-Irradiation Hardening of Brazed Joints of Tungsten and Oxide Dispersion Strengthened (ODS) Ferritic Steel”, Materials Transactions 54(4) (2013) 446-450.

[16] Hiroyuki Noto, Akihiko Kimura, Hiroaki Kurishita, Satoru Matsuo and Shuhei Nogami, “Evaluation of Feasibility of Tungsten/Oxide Dispersion Strengthened Steel Bonding with Vanadium Insert”, Materials Transactions 54(4) (2013) 451-455.

[17] K. Tokunaga, T. Hotta, K. Araki, Y. Miyamoto, T. Fujiwara, M. Hasegawa, K. Nakamura, K. Ezato, S. Suzuki, M. Enoeda, M. Akiba, T. Nagasaka, R. Kasada, A. Kimura, “High heat loading properties of vacuum plasma spray tungsten coatings on reduced activation ferritic/martensitic steel”, J. Nucl. Mater. 438 (2013) S905-S908.

[18] Yoshio Ueda, Kazuhiro Uekita, Makoto Oya, Yusuke Ohtsuka, Takuya Nagasaka, Ryuta Kasada, Akihiko Kimura, Tomonori Tokunaga, Naoaki Yoshida “Deuterium retention in VPS-W coated vanadium alloy (V–4Cr–4Ti)”, J. Nucl. Mater. 438 (2013) S1125-S1128.

[19] S. Wurster, N. Baluc, M. Battabyal, T. Crosby, J. Du, C. García-Rosales, A. Hasegawa, A. Hoffmann, A. Kimura, H. Kurishita, R.J. Kurtz, H. Li, S. Noh, J. Reiser, J. Riesch, M. Rieth, W. Setyawan, M. Walter, J.-H. You, R. Pippan, “Recent progress in R&D on tungsten alloys for divertor structural and plasma facing materials”, J. Nucl. Mater. 442 (2013) S181-S189.

[20] Kiyohiro Yabuuchi, Ryuta Kasada, Akihiko Kimura, “Effect of alloying elements on irradiation hardening behavior and microstructure evolution in BCC Fe ”, J. Nucl. Mater. 442 (2013) S790-S795.

[21] Q. Huang, N. Baluc, Y. Dai, S. Jitsukawa, A. Kimura, J. Konys, R.J. Kurtz, R. Lindau, T. Muroga, G.R. Odette, B. Raj, R.E. Stoller, L. Tan, H. Tanigawa, A.-A.F. Tavassoli, T. Yamamoto, F. Wan, Y. Wu, “Recent progress of R&D activities on reduced activation ferritic/martensitic steels ”, J. Nucl. Mater. 442 (2013) S2-S8.

[22] Hiroyuki Noto, Ryuta Kasada, Akihiko Kimura, Shigeharu Ukai, “Grain refinement of transient liquid phase bonding zone using ODS insert foil”, J. Nucl. Mater. 442 (2013) S567-S571.

[23] Tomonori Tokunaga, Hideo Watanabe, Naoaki Yoshida, Takuya Nagasaka, Ryuta Kasada, Young-Ju Lee, Akihiko Kimura, Masayuki Tokitani, Masatoshi Mitsuhara, Tatsuya Hinoki, Hideharu Nakashima, Suguru Masuzaki, Takeshi Takabatake, Nobuyoshi Kuroki, Koichiro Ezato, Satoshi Suzuki, Masato Akiba, “Development of high-grade VPS-tungsten coatings on F82H reduced activation steel”, J. Nucl. Mater. 442 (2013) S287-S291.

[24] Yasuhisa Oya, Masashi Shimada, Tomonori Tokunaga, Hideo Watanabe, Naoaki Yoshida, Yuji Hatano, Ryuta Kasada, Takuya Nagasaka, Akihiko Kimura, Kenji Okuno, “Behavior of deuterium retention and surface morphology for VPS–W/F82H”, J. Nucl. Mater. 442 (2013) S242-S245.

Task 2-3　Dynamic Deformation Behavior

[1] J.J. Sha, J.S. Park, T. Hinoki, A. Kohyama, “Bend stress relaxation of advanced SiC based fibers and its prediction to tensile creep”, MECHANICS OF MATERIALS, Vol.39[2], 2007, pp.175-182

[2] J.J. Sha, J.S. Park, T. Hinoki, A. Kohyama, “Tensile behavior and microstructural characterization of SiC fibers under loading”, MATERIALS SCIENCE AND ENGINEERING

A-STRUCTURAL MATERIALS PROPERTIES MICROSTRUCTURE AND PROCESSING, Vol.456[1-2], 2007, pp.72-77

[3] J.J. Sha, T. Hinoki, A. Kohyama, "Microstructural characterization and fracture properties of SiC-based fibers annealed at elevated temperatures", JOURNAL OF MATERIALS SCIENCE, Vol.42[13], 2007, pp.5046-5056

[4] Y. Katoh, T. Nozawa, L.L. Snead, T. Hinoki, "Effect of neutron irradiation on tensile properties of unidirectional silicon carbide composites", Journal of Nuclear Materials, Vol.367, 2007, pp.774-79

[5] S. Kondo, A. Kohyama, T. Hinoki, "Anisotropic evolution of Frank loops in ion-irradiated silicon carbide", Journal of Nuclear Materials, Vol.367, 2007, pp.764-68

[6] Y. Katoh, L.L. Snead, T. Hinoki, S. Kondo, A. Kohyama, "Irradiation creep of high purity CVD silicon carbide as estimated by the bend stress relaxation method", Journal of Nuclear Materials,Vol.367, 2007, pp.758-763

[7] K. Ozawa, T. Nozawa, Y. Katoh, T. Hinoki, A. Kohyama, "Mechanical properties of advanced SiC/SiC composites after neutron irradiation", Journal of Nuclear Materials, Vol.367, 2007, pp.713-718

[8] K.H. Park, T. Hinoki, A. Kohyama, " Influence of irradiation-induced defects on fracture behavior in highly pure SiC Journal of Nuclear Materials", Vol.367,2007, pp.703-07

[9] K. Shimoda, J.S. Park, T. Hinoki, A. Kohyama, "Influence of surface structure of SiC nano-sized powder analyzed by X-ray photoelectron spectroscopy on basic powder characteristics2, APPLIED SURFACE SCIENCE, Vol.253[24],2007, pp.9450-9456

[10] K. Shimoda, J.S. Park, T. Hinoki, A. Kohyama, "Influence of pyrolytic carbon interface thickness on microstructure and mechanical properties of SiC/SiC composites by NITE process", COMPOSITES SCIENCE AND TECHNOLOGY, Vol.68[1], 2008, pp.98-105

[11] K. Shimoda, J.S. Park, T. Hinoki, A. Kohyama, "Development of novel fabrication process for highly-dense & porous SiC/SiC composites with excellent mechanical properties", Ceramic Engineering & Science Proceedings, Vol.28[2],2008, pp.207-212

[12] Y. Katoh, T. Hinoki, H.C. Jung, J.S. Park, S. Konishi, M. Ferraris, "DEVELOPMENT AND EVALUATION OF SILICON CARBIDE JOINTS FOR APPLICATIONS IN RADIATION ENVIRONMENT", Fusion Materials Semi-Annual Progress Reports, DOE/ER-0313/44, 2008, pp.26-32

[13] J.J. Sha, T. Hinoki, A. Kohyama, “Thermal and mechanical stabilities of Hi-Nicalon SiC fiber under annealing and creep in various oxygen partial pressures”, CORROSION SCIENCE, Vol.50[11],2008, pp.3132-3138

[14] Y. Katoh Y.B. Choi, T. Hinoki, “TITAN TASK 2-3 SILICON CARBIDE BEND STRESS RELAXATION CREEP EXPERIMENT”, Fusion Materials Semi-Annual Progress Reports, DOE/ER-0313/45, 2008, pp.140-145

[15] Y. Katoh, K. Ozawa, L.L. Snead, Y.B.Choi, T. Hinoki, A. Hasegawa, “MECHANICAL CHARACTERIZATION OF SILICON CARBIDE COMPOSITES FOR HFIR-18J EXPERIMENT IN UNIRRADIATED CONDITION”, Fusion Materials Semi-Annual Progress Reports, DOE/ER-0313/45, 2008, pp.21-34

[16] M.K. Kim, T. Hinoki, A. Kohyama, J.S. Park, H. Kishimoto, “Process optimization for high performance SiC fibers from polymer-driven pre-ceramics”, Proceedings - Symposium on Fusion Engineering, 5226455, 2009

[17] K. Shimoda, T. Hinoki, Y. Katoh, A. Kohyama, “Development of the tailored SiC/SiC composites by the combined fabrication process of ICVI and NITE methods”, Journal of Nuclear Materials, Vol.384[2], 2009, pp.103-108

[18] J.J. Sha, T. Hinoki, A. Kohyama, “Microstructure and mechanical properties of Hi-Nicalon™ Type S fibers annealed and crept in various oxygen partial pressures”, Materials Characterization, Vol.60[8],2009, pp.796-802

[19] H.C. Jung, Y.H. Park, J.S. Park, T. Hinoki, A. Kohyama, “R&D of joining technology for SiC components with channel”, Journal of Nuclear Materials, Vol.386,2009, pp.847-851

[20] K. Shimoda, J.S. Park, T. Hinoki, A. Kohyama, “Microstructural optimization of high-temperature SiC/SiC composites by NITE process”,Journal of Nuclear Materials, Vol.386, 2009, pp.634-638

[21] T. Nozawa, T. Hinoki, A. Hasegawa, A. Kohyama, Y. Katoh, L.L. Snead, C.H. Henager, J.B.J. Hegeman, “Recent advances and issues in development of silicon carbide composites for fusion applications”, Journal of Nuclear Materials, Vol.386, 2009, pp.622-627

[22] K. Shimoda, A. Kohyama, T. Hinoki, “High mechanical performance SiC/SiC composites by NITE process with tailoring of appropriate fabrication temperature to fiber volume fraction”, COMPOSITES SCIENCE AND TECHNOLOGY, Vol.69[10], 2009, pp.1623-1628

[23] K. Shimoda, S. Kondo, T. Hinoki, A. Kohyama, “ Thermal stress relaxation creep and microstructural evolutions of nanostructured SiC ceramics by liquid phase sintering”, JOURNAL OF THE EUROPEAN CERAMIC SOCIETY, Vol.30[12],2010, pp.2643-52

[24] K. OzawaY. Katoh, T. Nozawa, T. Hinoki, L.L. Snead, “Evaluation of Damage Tolerance of Advanced SiC/SiC Composites after Neutron Irradiation”, IOP Conference Series-Materials Science and Engineering, 18, 162005, 2011

[25] T. Koyanagi, S. Kondo, T. Hinoki, “Internal residual stress analysis of SiC/SiC composites following ion irradiation”, IOP Conference Series-Materials Science and Engineering 18, 162008, 2011

[26] S. Kondo T. Koyanagi, T. Hinoki, “Development and Testing of Ion-Irradiation under the Applied Stress for Nuclear Ceramics”, IOP Conference Series-Materials Science and Engineering 18, 62004, 2011

[27] K. Shimoda, T. Hinoki, H. Kishimoto, A. Kohyama, “Enchanced high-temperature performances of SiC/SiC composites by high densification and crystalline structure”, COMPOSITES SCIENCE AND TECHNOLOGY, Vol.71[3], 2011, pp.326-32

[28] K. Shimoda, T. Hinoki, A. Kohyama, “Effect of additive content on transient liquid phase sintering in SiC nanopowder infiltrated SiCf/SiC composites”, COMPOSITES SCIENCE AND TECHNOLOGY, Vol.71[5], 2011, pp.609-615

[29] H. Katsui, A. Hasegawa, Y. Katoh, Y. Hatano, T. Tanaka, S. Nogami, T. Hinoki, T. Shikama, ”STUDY ON COMPATIBILITY BETWEEN SILICON CARBIDE AND SOLID BREEDING MATERIALS UNDER NEUTRON IRRADIATION”, FUSION SCIENCE AND TECHNOLOGY, Vol.60[1],2011, pp.288-91

[30] T. Koyanagi, S. Kondo, T. Hinoki, “The influence of sintering additives on the irradiation resistance of NITE SiC”, JOURNAL OF NUCLEAR MATERIALS, Vol.417[1-3], 2011, pp.435-439

[31] Y. Katoh, K. Ozawa, T. Hinoki, Y. Choi, LL. Snead, A. Hasegawa, “Mechanical properties of advanced SiC fiber composites irradiated at very high temperatures”, JOURNAL OF NUCLEAR MATERIALS, Vol.417[1-3], 2011, pp.416-420

[32] HC. Jung, T. Hinoki, Y. Katoh, A. Kohyama, “Development of a shear strength test method for NITE-SiC joining material”, JOURNAL OF NUCLEAR MATERIALS, 417[1-3], 2011, pp.383-386

[33] K. Abe, S. Nogami, A. Hasegawa, T. Nozawa, T. Hinoki, “Study on stress relaxation behavior of silicon carbide by BSR method”, JOURNAL OF NUCLEAR MATERIALS, Vol.417[1-3],2012, pp.356-358

[34] Y.B. Choi, T. Hinoki, K. Ozawa, Y. Katoh, K. Matsugi, T. Kelimu, “Strength Anisotropy of NITE-SiC/SiC Composite by Various Failure Modes”, MATERIALS TRANSACTIONS, Vol.53[11], 2012, pp.2060-2063

[35] H. Katsui, Y. Katoh, A. Hasegawa, M. Shimada, Y.Hatano, T. Hinoki, S. Nogami, T. Tanaka, S. Nagata, T. Shikama, ”Tritium trapping in silicon carbide in contact with solid breeder under high flux isotope reactor irradiation”, Journal of Nuclear Materials, accepted in 2012

[36] T. Hinoki, Y. Katoh, L.L. Snead, H.C. Jung, K. Ozawa, H. Katsui, Z.H. Zhong, S. Kondo, Y.H. Park, C.H. Shin, C.M. Parish, R.A. Meisner, A. Hasegawa, “Silicon Carbide and Silicon Carbide Composites for Fusion Reactor Application”, MATERIALS TRANSACTIONS, Vol.54[4], 2013, pp472-476

[37] Y. Katoh, L.L. Snead, C.M. Parish, T. Hinoki, “Observation and possible mechanism of irradiation induced creep in ceramics”,JOURNAL OF NUCLEAR MATERIALS, Vol.434[1-3], 2013, pp141-151

[38] Yutai Katoh, Kazumi Ozawa, Chunghao Shih, Takashi Nozawa, Robert J. Shinavski, Akira Hasegawa, Lance L. Snead, “ Continuous SiC fiber, CVI SiC matrix composites for nuclear applications: Properties and irradiation effects” , Journal of Nuclear Materials, accepted in 2013

Common Task：MFE/IFE system integration modeling

[1] Y. Oya, M Kobayashi, R. Kurata, W. Wang, N. Ashikawa, A. Sagara, N. Yoshida, Y. Hatano, K. Okuno: J. Nucl. Mater. 415 (2011) S701–S704.

[2] Y. Sakoi, M. Miyamoto, K. Ono and M. Sakamoto: J. Nucl. Mater., in press, http://dx.doi.org/10.1016/j.jnucmat.2012.10.003.

[3] M. Miyamoto, D. Nishijima, Y. Ueda, R.P. Doerner, H. Kurishita, M.J. Baldwin, S. Morito, K. Ono and J. Hanna: Nucl. Fusion 49 (2009) 065035.

[4] M. Miyamoto, D. Nishijima, M.J. Baldwin, R.P. Doerner, Y. Ueda, K. Yasunaga, N. Yoshida and K. Ono: J. Nucl. Mater. 415 (2011) S657–S660.

[5] Y. Edao, S. Fukada, S. Yamaguchi, H. Nakamura: Fus. Engng. Des., 85 (2010) 53–57.

[6] Y. Edao, H. Okitsu, H. Noguchi and S. Fukada: Fus. Sci. Technol., 60 (2011) 1163–1166.

[7] Y. Edao, H. Noguchi, S. Fukada: J. Nucl. Mater., 417 (2011) 723–726.

[8] S. Fukada, Y. Edao: J. Nucl. Mater., 417 (2011) 727–730.

[9] D. Matsuyama, T. Oda, S. Fukada: Chem. Phys. Lett., 483 (2009) 214–217.

[10] Y. Edao, S. Fukada, H. Noguchi, Y. Maeda, K. Katayama: Fus. Sci. Technol. 56 (2009) 831–835.

[11] T. Oda, M. Shimada, K. Zhang, P. Calderoni, Y. Oya, M. Sokolov, R. Kolasinski, J.P. Sharpe, Y. Hatano: Fus. Sci. Technol. 60 (2011) 1455–1458.

[12] M. Shimada, Y. Hatano, P. Calderoni, T. Oda, Y. Oya, M. Sokolov, K. Zhang, G. Cao, R. Kolasinski, J.P. Sharpe: J. Nucl. Mater. 415 (2011) S667–S671.

[13] Y. Oya, M. Shimada, M. Kobayashi, T. Oda, M. Hara, H. Watanabe, Y. Hatano, P. Calderoni, K. Okuno: Physica Scripta T145 (2011) 014050.

[14] Y. Shimada, G. Cao, Y. Hatano, T. Oda, Y. Oya, M. Hara, P. Calderoni: Physica Scripta T145 (2011) 014051.

[15] S. Sharafat and K. Morishita: J. At. Energy Soc. Jpn. 50 (11) (2008) 724.

[16] K. Morishita and S. Sharafat: J. At. Energy Soc. Jpn. 50 (12) (2008) 803.

[17] Y. Watanabe, K. Morishita, A. Kohyama: J. Nucl. Mater. 417 (2011) 1119–1122.

[18] K. Morishita, Y. Watanabe, A. Kohyama, H.L. Heinisch, F. Gao: J. Nucl. Mater. 386–388 (2009) 30–32.

[19] Y. Watanabe, K. Morishita, A. Kohyama, H.L. Heinisch, F. Gao: Nucl. Instrum. Meth. B 267 (2009) 3223–3226.

[20] Y. Watanabe, K. Morishita, Y. Yamamoto: Nucl. Instrum. Meth. B 269 (2011) 1698–1701.

[21] T. Norimatsu, H. Saika, H. Homma, M. Nakai, S. Fukada, A. Sagara and H. Azechi: Fus. Sci. Technol. 60 (2011) 893–896.

[22] A. Sagara, R. Nygren, M. Miyamoto, D. Nishijima, R. Doerner, S. Fukada, Y. Oya, T. Oda, Y. Watanabe, K. Morishita, F. Gao, T. Norimatsu: Materials Transactions, 54 (2013) 477– 483.

6. List of academic degrees

Task	Degree obtained in (Month/Year)	Degree (B,M,D)	Name	University	Title of theThesis
1-1	3/2008	M	Hideyuki Sasagawa	Shimane U.	Thermal desorption of helium from Fe-9Cr-2W ferritic alloy irradiated with low energy helium ions
1-1	3/2008	B	Masato Yamagiwa	Nagoya U.	Helium bubble formation on tungsten in dependence of fabrication method
1-1	3/2008	M	Takashi Yamada	Nagoya U.	Study of dust partcles' transport in the troidal diverter plasma sumulator
1-1	3/2009	B	Yuki Sakoi	Shimane U.	Thermal Desorption and Retention properties of Deuterium from HeirradiatedPlasma facing materials
1-1	3/2009	B	Satoshi Kumode	Shimane U.	Microstructure of tungsten exposed to Deuterium-Helium mixture plasmas
1-1	3/2009	D	Masakatsu Fukumoto	Osaka U.	Study on hydrogen isotope behavior in tungsten damaged by high energy hydrogen ion beam
1-1	3/2009	M	Akifumi Yamawaki	Osaka U.	Temperature dependence of carbon deposition on high Z materials by D/C mixed ion irradiation
1-1	3/2009	M	Jun Watanabe	Osaka U.	Tungsten Deposition Distribution in Divertor Region in JT-60U
1-1	3/2009	B	Tsubasa Saeki	Nagoya U.	Degradation of optical reflectivity of metals by helium bombardment
1-1	3/2009	B	Takanori Yokochi	Nagoya U.	Deuterium retention in SUS316 exposed to deuterium plasma
1-1	3/2009	M	Wataru Sakaguchi	Nagoya U.	Formation of nano structured W due to helium plasma irradiation
1-1	3/2010	B	Taku Gohara	Shimane U.	Simultenious irradiation effects of D and He ions on D retention in plasma facing materials
1-1	3/2010	M	Hidemasa Kurehashi	Osaka U.	Effects of repeated laser heat pulses on tungsten
1-1	3/2010	M	Hirotaka Tanaka	Osaka U.	Ion driven permeation in tungsten by D/He mixed ion irradiation
1-1	3/2010	M	Ken Tanimoto	Osaka U.	Effect of Radiation Damage on Deuterium Retention in Tungsten
1-1	3/2010	B	Yuki Hirahata	Nagoya U.	Influence of crystal orientation on damages of angle crystal tungsten exposed to helium plasma
1-1	3/2010	M	Masato Yamagiwa	Nagoya U.	In-situ Measurement of Hydrogen Isotope Retention under Plasma Exposure by using Ion Beam Analysis
1-1	3/2011	M	Yuki Sakoi	Shimane U.	Helium irradiation effects on deuterium retention in tungsten
1-1	3/2011	M	Kosuke Tsukatani	Osaka U.	Deuterium retention in damaged tungsten
1-1	3/2011	M	Koichi Miyato	Osaka U.	Effects of tungsten nano-structure on carbon deposition
1-2	3/2008	M	Takumi Chikada	U. of Tokyo	Characterization of erbium oxide coatings for hydrogen permeation barrier
1-2	3/2009	M	Yuki Edao	Kyushu U.	Study on tritium recovery from liquid blanket in fusion reactor
1-2	3/2010	D	Juro Yagi	U. of Tokyo	Trap behavior and modeling of nitrogen and hydrogen in hot-trap materials for liquid lithium blankets
1-2	3/2011	M	Lenichi Katekari	Kyushu U.	Study of hydroge isotopes from liquid lithium under fludized conditions

1-2	3/2011	M	Wu Gu	Kyushu U.	Study on tritium recovery from neutron irradiated lithium
1-2	3/2011	D	Takumi Chikada	U. of Tokyo	Study on hydrogen permeation behavior in erbium oxide coatings
1-2	3/2012	D	Yuki Edao	Kyushu U.	Study on hydrogen isotopes behavior in liquid breeder materials of fusion reactor
1-2	3/2012	M	Hiroaki Okitsu	Kyushu U.	Tritium recovery from liquid lithium lead in fusion reactor
1-2	3/2012	M	Yusuke Hatachi	Kyushu U.	Analysis of hydrogen isotopes absorption between liquid lithium and yttrium underdynamic conditions
1-2	3/2013	M	Makoto Okada	Kyushu U.	Study on tritium transfer in liquid lithium-lead blanket
1-2	3/2013	M	Satoshi Shigeharu	Kyushu U.	Study on hydrogen isotope transfer between yttrium and lithium under fludized condition
1-2	3/2013	M	Tetsushi Hiromoto	Kyushu U.	Recovery of hydrogen isotope from liquid lithium by Y and analysis of using chemical solution method
1-3	6/2012	D	N. Vetcha	UCLA	Study of instability and transition in MHD flows as applied to liquid metal blankets
1-3	9/2012	D	Yoshitaka Ueki	Kyoto U.	Development of high-temperature ultrasonic Doppler velocimetry for lead-lithium flow
1-3	3/2013	D	Mitsuhiro Aoyagi	Tohoku U.	Evaluation of the applicability of a three-surface-multi-layered channel to the first wall cooling of a fusion reactor
2-1	3/2009	M	Yohei Kikuchi	Shizuoka U.	D retention for simultaneous C+ and D2+ implanted W
2-1	3/2009	B	Miyuki Yajima	U. Toyama	Hydrogen isotope retention in porous nuclear materials
2-1	3/2010	B	Junya Osuo	Shizuoka U.	D retention for simultaneous D2+, C+ and He+ implanted W
2-1	3/2010	B	Akiko Hamada	Shizuoka U.	Hydrogen permeation behavior for stainless steel
2-1	3/2011	B	Kensuke Toda	Shizuoka U.	D retention in C+ implanted W
2-1	3/2012	B	Kenshin Masuda	U. Toyama	Hydrogen isotope retention in vacuum-plasma spray W
2-1	3/2012	B	Eriko Sano	Shizuoka U.	C+ irradiation effect on hydrogen isotope retention in W
2-1	3/2012	M	Masato Suzuki	Shizuoka U.	Qualitative analysis of hydrogen isotope recycling for C+ implanted W
2-1	3/2013	M	Kiyotaka Kawasaki	Shizuoka U.	Temperature dependence on co-deposition formation on C+ implanted W
2-1	3/2013	M	Tetsuo Fujishima	Shizuoka U.	Irradiation defect and deposition layer effect on hydrogen isotope retention and diffusion in W
2-2	7/2009	D	Jaehoon Lee	Kyoto Univ.	Roles of oxide particles dispersion and grain refinement in the high performance of ODS ferritic steels
2-2	9/2010	D	Sanghoon Noh	Kyoto Univ.	Welding and Joining Technology Development of Oxide Dispersion Strengthened Ferritic Steels
2-2	3/2011	M	Yoshiyuki Takayama	Kyoto Univ.	Development hardness evaluation method of ion-irradiated Fe-base alloys

2-2	9/2011	D	Kiyohiro Yabuuchi	Kyoto Univ.	Mn effect on irradiation hardening behavior and microstructural evolution in BCC Fe
2-2	3/2012	M	Yoshimasa Himei	Kyoto Univ.	Evaluation of bonding shear strength and ion-irradiation effect in W-ODS joints
2-2	3/2013	M	Naoto Tsuda	Kyoto Univ.	Evaluation of bonding shear strength and ion-irradiation effect in Friction stir welded ODS joints
2-2	3/2013	M	Kiyoshi Maekawa	Kyoto Univ.	Temperature dependence of tensile properties of tungsten
2-3	3/2008	D	Kazuya Shimoda	Kyoto U.	Fabrication technique of SiC/SiC composites utilizing SiC nano-powder for severe environment
2-3	5/2008	D	Kazumi Ozawa	Kyoto U.	Effect of irradiation on mechanical properties of advanced SiC/SiC composites
2-3	9/2008	D	Jung Hun-Chea	Kyoto U.	Development of joining technique for SiC ceramic material using hot-pressing
2-3	3/2010	D	Zhihong Zhong	Kyoto U.	Development of Technologies for Joining of Silicon Carbide Materials to Metals
2-3	9/2010	D	Hirokazu Katsui	Tohoku U.	Hydrogen Behavior in Ion-Irradiated Ternary Lithium Oxides
2-3	9/2011	D	Youngju Lee	Kyoto U.	Development of functional SiC material and understanding of its physical properties
2-3	9/2012	D	Kazuoki Toyoshima	Kyoto U.	Understanding of fracture behavior of continuous fiber reinforced composites by multilateral approach
2-3	3/2013	D	Takaaki Koyanagi	Kyoto U.	Modeling of mechanical properties of SiC composites under neutron irradiation by irradiated constitutive properties